UNIVERSITY OF GRANADA

DOCTORAL THESIS

Dark Matter and Solar Atmospheric Neutrino Searches with the KM3NeT-ORCA and ANTARES Neutrino Telescopes

---

Daniel López Coto

Thesis submitted for the degree of

Doctor of Philosophy

Programa de Doctorado en Física y Ciencias del Espacio
Dpto. de Física Teórica y del Cosmos
Facultad de Ciencias

March 02, 2022

Supervisor:
Dr. Sergio Navas Concha

Editor: Universidad de Granada. Tesis Doctorales
Autor: Daniel López Coto
ISBN: 978-84-1117-343-8
URI: http://hdl.handle.net/10481/74967

Declaration of Authorship

I, Daniel López Coto, declare that this thesis titled, "Dark Matter and Solar Atmospheric Neutrino Searches with the KM3NeT-ORCA and ANTARES Neutrino Telescopes" and the work presented in it are my own. I confirm that:

- This work was done wholly or mainly while in candidature for a research degree at this University.
- Where any part of this thesis has previously been submitted for a degree or any other qualification at this University or any other institution, this has been clearly stated.
- Where I have consulted the published work of others, this is always clearly attributed.
- Where I have quoted from the work of others, the source is always given. With the exception of such quotations, this thesis is entirely my own work.
- I have acknowledged all main sources of help.
- Where the thesis is based on work done by myself jointly with others, I have made clear exactly what was done by others and what I have contributed myself.

Signed:

Date:

Acknowledgements

I could not start this section without mentioning my complete and sincere gratitude to my supervisor, **Pr. Sergio Navas**. To him is that I owe the opportunity I had of working with the ANTARES and KM3NeT Collaborations. I can't thank him enough for its patience, guidance and support over these years. Thank you once again for everything you have done for me and, specially for reviewing countless times this document to get the best out of it.

I'm also grateful to the members of my doctoral committee: **XYZ**, **ABC** and **MNP** for spending their valuable time on reviewing and assessing my dissertation and giving me invaluable advices.

To my office colleagues and friends, **Dr. Alejandro Jiménez**, **Jose María Poyatos**, **Juan Silverio** and **Carlos Ruíz**. Thank you so much for all the joyfull moments at the office, and good luck with your theses!

I would like to thank to the whole team of the **ANTARES and KM3NeT Collaborations** for their closeness but, specially to the **Dark Matter & Exotics working group**, with whom I have shared countless discussions, doubts and concerns about my research.

An special mention to **Pr. Juande Zornoza**, **Dr. Rebecca Gozzini**, **Dr. Luigi Fusco** and **Dr. Arturo Nuñez** for all the help and guidance you have provided me. This thesis would not have been possible without you.

I could not miss the opportunity to show my gratitude to **Dr. Vincent Bertin** for inviting me to do my research stay at the CPPM in Marseille and for giving me the opportunity to be onboard the *Castor* ship, in which the sea operation that deployed 4 additional ORCA detection units was performed. This was a very exciting and unique opportunity. I would like to also thanks all the members at the CPPM (doctors, PhD students and personal) for being kind and make my stay more comfortable.

To my all-life friends, **Alejandro Rodríguez**, **Juanjo Mata** and **Rodrigo Martín**. Despite the distance, I have never felt closer to you.

To my friends of Granada, **Miguel Barrales**, **Cristina Martínez**, **Lucía Gómez**, **Marina Muñoz**, **Ester Ávila** the ones who have endure my joys and my sorrows along these 4 years. Thank you for sharing with me all those moments, all those dance congresses and all those unforgettable moments together.

To my partner **María Ponce**, thanks to you for sharing all those moments during the last period of my thesis. Your support has always been like the light from a guiding lighthouse. I only have to tell you one more thing: *3, 8, 18, . . .*
I hope you got that.

I also want to say thanks to *my radioactive girls*, **Beatriz Mato** and **María de los Ángeles Millán**. We shared a lot during the Master, and I am glad that our relationship has lasted to this day.

Por último, pero más importante, a mi familia. A mis padres, **Manuel** y **María de los Ángeles**, les quiero agradecer todas sus enseñanzas, las cuales han hecho que hoy sea quien soy, y esté donde estoy. Gracias por vuestro apoyo incesante, aunque no siempre hayamos estado de acuerdo y algunas decisiones que he tomado no os hayan gustado del todo. A mis hermanos **Israel** y **Mariann**. Ambos habéis sido siempre un modelo a seguir, aunque también me habéis mostrado qué caminos no tomar, y eso es aún más de agradecer. Isra gracias a ti (o por tu culpa), es por lo que he acabado siendo *Físico* y, en parte, por lo que me he metido en este *lío* de hacer un doctorado... Mariann, tu perseverancia y ganas de perseguir tu sueño me han inspirado siempre a luchar por lo que he querido.

Contents

Abstract

Dpto. de Física Teórica y del Cosmos

Facultad de Ciencias

UNIVERSITY OF GRANADA

Dark Matter and Solar Atmospheric Neutrino Searches with the KM3NeT-ORCA and ANTARES Neutrino Telescopes

by Daniel López Coto

The ANTARES neutrino telescope and its successor, KM3NeT, located in the sea bed of the Mediterranean, have been designed to study neutrinos from a variety of sources over a wide energy range. Both neutrino telescopes have a very broad scientific scope: the measurement of the diffuse flux of cosmic neutrinos, unveiling the origin of cosmic-rays, the study of point–like astrophysical sources of neutrinos or the discovery of the mysterious nature of dark matter.

This thesis collects the results of two different but related researches. On the one hand, 11 years of ANTARES data have been analyzed to perform a search for Solar Atmospheric neutrino (SAνs). The study and understanding of SAνs is crucial at different levels. First, the detection of SAνs can give indirect information about the primary cosmic-ray composition, the propagation of charged particles in the solar medium and, consequently, help the scientific community to understand the density and chemical structure of the Sun. Second, these neutrinos could be used as a *standard neutrino flux* for detector calibration. Last but not least, SAνs represent an unavoidable background for dark matter searches. On the other hand, the performance of the KM3NeT-ORCA detector to perform dark matter searches towards the Sun is studied. ORCA is the low energy component of KM3NeT, optimized for the study of neutrinos created by cosmic–rays in the Earth's atmospere. In this thesis, dark matter is assumed to be made of Weakly Interactive Massive Particles (WIMPs) that accumulate in celestial bodies. The privileged proximity of the Sun to the Earth makes it a perfect candidate to perform indirect dark matter searches.

The Monte Carlo simulation framework in both detectors (ANTARES and KM3NeT), which includes the simulation of neutrino interactions, particle generation and light propagation, event selection and reconstruction, as well as the statistical treatment of data and systematic uncertainties have been described in great detail.

The search of SAνs with 11 years of ANTARES data, based in a likelihood method, gives no evidence for a solar atmospheric neutrino signal above the expected background. An upper limit at 90% confidence level on the flux of solar atmospheric neutrinos is obtained to be equal to 7×10^{-11} [TeV^{-1}cm^{-2}s^{-1}] at $E_\nu = 1$ TeV for the reference model assumed.

In the second part of the thesis, the discovery potential of the ORCA detector is evaluated. Our results show that ORCA is potentially competitive in the search for dark matter in the Sun, surpassing the previous results from the ANTARES and SK searches, and being close to the IceCube results.

To those whom always have supported me: my family, my friends and my partner.

Part I

Introduction

1 Neutrinos: The Ghost Messengers of the Universe

"I have done a terrible thing, I have postulated a particle that cannot be detected."

Wolfgang Pauli

The problem of energy conservation in the β decay process made the scientific community hypothesize the existence of a new particle, the "neutrino". This particle was not discovered until 1956 by F. Reines and C. Cowan. The history of this elusive particle is presented in this chapter, which is organized as follows. In Sec. 1.1 an historical review of the neutrino is presented. Sec. 1.3 describes some of the sources of high energy neutrinos within the energy range of the ANTARES and ORCA neutrino detectors. Neutrino interactions and detection techniques are described in Sec. 1.4 and 1.5, respectively. Finally, a brief summary of the first projects and the existing neutrino telescopes is given in Sec. 1.6.

1.1 The Neutrino

According to the Standard Model (SM) of particle physics, the neutrino is a massless, electrically neutral particle that comes with three different lepton flavours (electron, muon and tau neutrino). As we discuss further in this section, the discovery of the neutrino flavour oscillation is a clear indicator of the existence of neutrino masses, opening a new window beyond the Standard Model.

The low interaction probability of neutrinos, along with their lack of electrical charge, makes them travel in straight paths from the point where they are produced to their interaction site. This property makes their detection very difficult, needing large volume detectors, a great amount of neutrino flux and a big amount of exposure time to increase the interaction probability inside the sensitive volume of the detector. However, these properties are also very useful and can be exploited to study the interior of stellar bodies as well as sites very far away from Earth.

1.1.1 The Neutrino Proposal

In contrast with the monochromatic spectrum of α and γ-decay processes, in which α and γ particles are emitted always with the same energy, the energy of the electrons emitted in a β-decay shows a continuous spectrum. In 1914, J. Chadwick demonstrated the continuous spectrum of the β-decay studying the decay of the radium E [1], result which was subsequently confirmed years later, in 1927, by C. D. Ellis and W. A. Wooster [2]. L. Meitner later demonstrated that the missing energy could not be ascribed to neutral γ-rays, which led to the idea that the missing energy could be explained by the existence of a new particle or, as N. Bohr suggested, perhaps energy conservation held only in a statistical sense.

In 1930, as a desperate solution to the energy conservation problem, W. Pauli proposed in an open letter to a physics conference at Tubingen [3] the existence of a new undetected particle emitted in β-decay. This new particle had to be a fermion electrically neutral, with a mass of the order of the electron. He called this particle *a neutron*.

When J. Chadwick discovered in 1932 the neutron as we know it today [4], E. Fermi renamed the W. Pauli particle the *neutrino*. The first published reference to the neutrino is in the Proceedings of the Solvay Conference of October 1933. E. Fermi [5] and F. Perrin [6] independently concluded in 1933 that neutrinos could be massless.

In the early 1950s, F. Reines and C. L. Cowan searched for a way to measure inverse β-decay, in which an antineutrino can produce a positron. After considering several methods, including a nuclear explosion, they settled on using the large flux of antineutrinos from a nuclear reactor and 10 ton of equipment, including 1400 liters of liquid scintillators. This experiment was the first reactor-neutrino experiment. In June of 1956, F. Reines and C. L. Cowan sent a telegram informing W. Pauli of the discovery. The antineutrino absorption reaction $p(\bar{\nu}, \beta^+)n$ was observed in two 200-liter water targets each placed between large liquid scintillation detectors and located near a powerful production fission reactor in an antineutrino flux of 1.2×10^{13} cm^{-2}s^{-1}. The signal, a delayed-coincidence event consisting of the annihilation of the positron followed by the capture of the neutron in cadmium which was dissolved in the water target, was subjected to a variety of tests. These tests demonstrated that reactor-associated events occured at the rate of 3.0 hr^{-1} for both targets taken together, consistent with expectations [7]. F. Reines (Cowan passed away in 1974) was awarded the Nobel prize in 1995, 40 years later of their discovery [8]. The interested reader can see refs. [9, 10] for further information about the neutrino history.

1.1.2 The Neutrino in the Standard Model and Beyond

The neutrino, within the framework of the Standard Model of particle physics, is a massless neutral particle with spin 1/2 that only couples to other SM particles through weak interactions mediated by Z and W bosons [11]. Neutrinos are three of the seventh fundamental particles that make up the SM (see Fig. 1.1). In all the

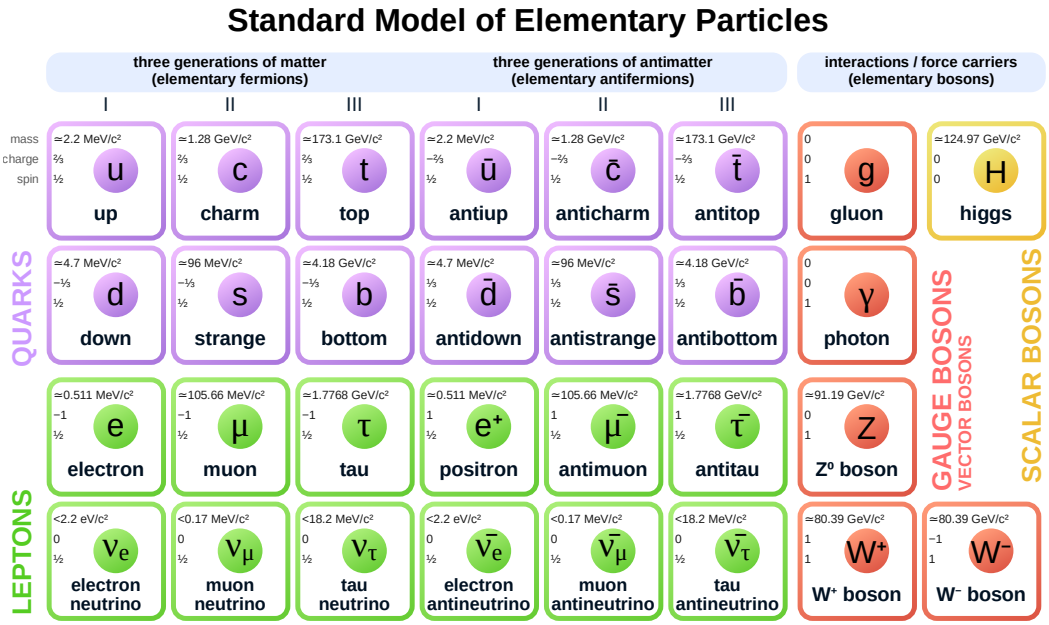

Figure 1.1: Scheme of the fundamental particles of the Standard Model of Particle Physics. From Wikimedia.

SM interactions, the difference between the number of leptons and the number of anti-leptons is preserved (lepton number conservation), and hence neutrinos are always associated with charged leptons of the same generation or produced as particle-antiparticle pairs.

In addition to the basic properties described above, in 1957, B. Pontecorvo postulated that neutrinos can change their lepton flavour [12], and hence, an electronic neutrino can be converted to a muon neutrino, even when they propagate through free space. This fenomena is so-called *neutrino oscillation*. However, this process can occur only if neutrinos are massive particles, because the flavour states (ν_e, ν_μ and ν_τ) are a non-trivial mixing of the neutrino mass states (ν_1, ν_2 and ν_3) through the PMNS mixing matrix [11]. For simplicity, here is only highlighted the two flavour scenario in which the oscillation is expressed in terms of transition probabilities between any two neutrino flavours, noted in the following equation by α and β:

$$P(\nu_\alpha \to \nu_\beta) = \sin^2(2\theta)\sin^2(1.27\Delta m^2 \frac{L}{E}),$$
$$P(\nu_\alpha \to \nu_\alpha) = 1 - \sin^2(2\theta)\sin^2(1.27\Delta m^2 \frac{L}{E}), \quad (1.1)$$

where Δm^2 is the mass difference between the two neutrino flavours, θ is the mixing angle, L is the neutrino path length and E is the neutrino energy. As stated before, equation 1.1 stands only for the two family neutrino scenario. The three family mixing scenario is more complicated and is left for the interested reader in refs. [11, 13, 14]. By measuring the appearance and disappearance of different neutrino flavours over different energy ranges and baselines, measurements of the mixing angles and mass splittings can be made and hence provide an insight into physics Beyond the Standard Model. Additionally, the nature of the neutrino with definite mass remains unknown, and great efforts are being carried out by the scientific community to determine if neutrinos are Majorana (neutrinos are their own anti-particle, and they have the same lepton number) or Dirac (neutrino and antineutrino have different lepton numbers) particles [15–19].

The first experimental measurement able to detect the effect of neutrino oscillation was the *Homestake experiment* carried by R. Davis in the late 1960s [20]. The experiment observed a deficit in the flux of solar neutrinos with respect the prediction of the SM, which was called the *solar neutrino problem*. However, it was not until 1998 at Super-Kamiokande (SK) [21] and 2001 at the Sudbury Neutrino Observatory (SNO) [22], that clear evidence to neutrino oscillations was provided. Nowadays, there is a huge variety of experiments making measurements of the neutrino properties. The results of the measurements of these experiments allowed to establish the world-best fit values for neutrino's properties, which are summarized in [11].

1.2 Diffuse Neutrino Flux

The diffuse neutrino flux is defined as the sum of neutrino fluxes produced by sources that cannot be identified accurately (yet). This diffuse flux comprises a background source for other neutrino searches. Therefore, the characterisation of this flux is of paramount importance. The identification of the source of these diffuse flux of neutrinos is one of the main scientific targets for the astroparticle physics community. In 2013, the IceCube collaboration discovered high energy neutrinos which were compatible with an extraterrestrial source [23]. This discovery showed the scientific potential of neutrino telescopes, establishing solid grounds for the development of a great variety of neutrino telescope projects. The ANTARES neutrino telescope is an example of the different searches that have been carried out after the outstanding discovery of IceCube [24–26].

1.3 High Energy Neutrino Astrophysics

Neutrinos can be artificially produced in accelerators [27–29] or produced by natural processes such as interactions and radioactive decays [1, 30], particle annihilations or fusion processes inside stellar bodies. In this thesis we will focus in

neutrinos from astrophysical sources [31–33], specially in neutrinos from cosmic-ray interactions with the solar atmosphere and from dark matter annihilations (see chapters 3 and 5, respectively).

There are important advantages when using high-energy neutrinos as cosmic messengers in contrast to cosmic-rays or very high energy photons. Very high-energy photons ($> 10^{12}$ eV) have a maximum visible distance of about 0.03 and 200 Mpc due to its interaction with the Cosmic Microwave Background (CMB) and infrared radiation. On the other hand, Cosmic-rays interacts with the ordinary matter and they are affected by the galactic magnetic fields, deflecting their trajectories and hence, missing the information of their source. High-energy neutrinos do not present any of these problems. Since they only interact weakly, neutrinos are able to probe the interior of dense sources and, as long as they are neutral electrically, they point back directly to their sources. These properties make the Universe *transparent* to neutrinos.

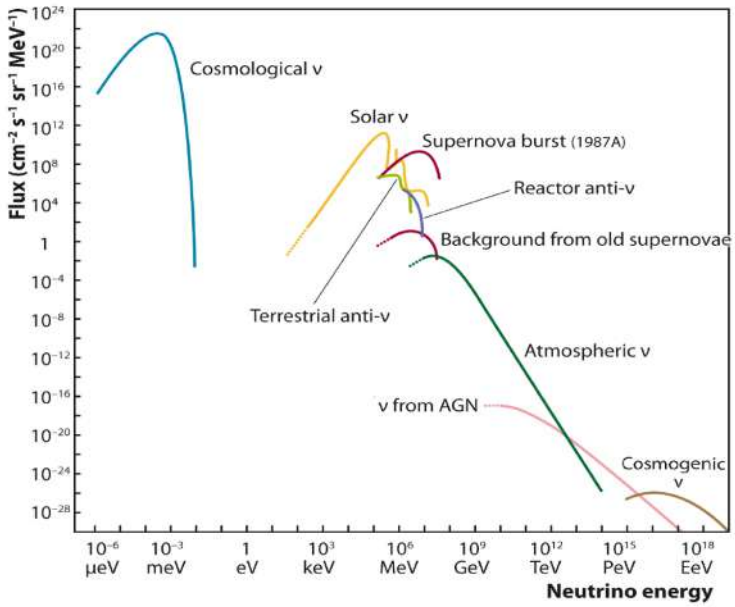

Figure 1.2: Observed and estimated neutrino fluxes as function of energy. Neutrino telescopes like ANTARES and KM3NeT explore neutrino energies above few GeV. From [34].

In Fig. 1.2 is shown a summary of the observed and estimated neutrino flux for different sources, as a function of the energy of the neutrinos. In this chapter, the proposed mechanisms and sources in the GeV-PeV range are described.

1.3.1 Shell-Type Supernova Remnants

Supernova remnants (SNRs) are powerful blast waves driven into the interstellar medium (ISM) [35] by the collapses of the cores of massive stars (supernovae). The morphology of this kind of SNR presents an expanding outer-shell dominated by light emission [36]. The outer-shell of the SNR is formed by the expansion of the shock-wave from the explosion of the supernova, heating the material it encounters. The supernovae are powerful sources of gamma-rays and neutrinos at nuclear energies, as demonstrated by the discovery of neutrinos from SN1987A [37].

SNRs represent the leading candidate for the origin of the bulk of cosmic-rays up to $\sim 10^6$ GeV [38], since (a) they show strong non-thermal power-law spectra indicating the presence of relativistic electrons [39, 40], (b) they inject enough power to be able to sustain the cosmic-ray flux for a reasonable particle acceleration efficiency of $\sim 1 - 10\%$, and (c) they have the chemical abundances found in cosmic-rays. Nevertheless, few TeV gamma-ray emission at the level expected from π^0 production in SNRs has not been found, except possibly in Cas A [41, 42]. TeV gamma-rays have been observed from the Crab nebula and from SN1006, but in both cases these gamma-rays seem to originate from inverse-Compton scattering of low-energy photons by accelerated electrons rather than from π^0 production by accelerated protons. Furthermore, in the case of the Crab nebula, the TeV gamma-ray emission is most likely pulsar-wind-driven and due to the acceleration of electron-positron pairs in the plerion.

1.3.2 Atmospheric Neutrinos

Neutrinos are produced in abundance by high-energy cosmic-rays impinging on the atmosphere of the Earth. These neutrinos, spanning energies from a few MeV to the highest-energy cosmic-rays, provide a background against which one must discriminate to detect extraterrestrial sources, but they have been enormously useful as a test beam in which muon neutrino oscillations were discovered, providing the first convincing evidence for neutrino mass.

The atmosphere is constantly and uniformly bombarded with cosmic-rays. These consist mostly of protons, but also heavy nuclei (9% alpha particles, 1% heavier nuclei), electrons and neutral particles. The neutrinos arise from the decay of pions and other mesons in the atmosphere and from the decay of muons [43]. The magnetic field of the Earth and other magnetic fields cut off the lower-energy particles from the Sun and more distant sources, so that the mean incoming kinetic energy is around 1 GeV.

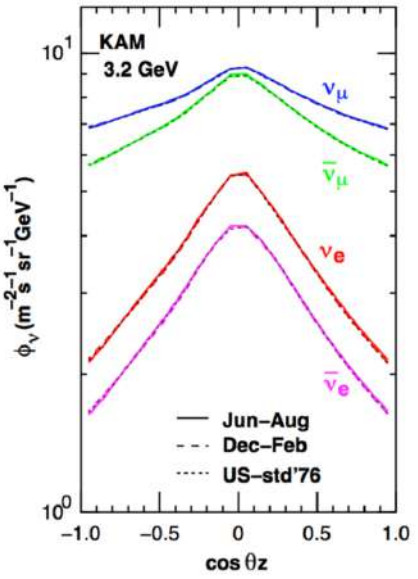

Figure 1.3: Arrival zenith-angle-dependent atmospheric neutrino fluxes at $E_\nu = 3.2$ GeV. As a reminder: $\cos\theta_z = -1$ is for upward–going, $\cos\theta_z = 0$ is for horizontal, and $\cos\theta_z = 1$ is for downward–going particles.
This is for the Super-Kamiokande site in Kamioka, Japan. For other sites, e.g. the ORCA site in the Mediterranean Sea, the angular dependence looks slightly different, as the exact angular dependence is influenced by the local atmosphere density and the geomagnetic effects at the interaction point. However, general characteristics are very similar for the ANTARES and ORCA sites. From [32, 44].

At energies above GeV, the atmospheric muon neutrino (differential) flux can be approximated as a power law with a spectral index of about -3.7 up to 1 PeV and -4.0 above 1 PeV. The electron neutrinos, which arise largely from muon decays, decline more swiftly above several GeV, decreasing to about 1% of the muon neutrino flux at the higher energies (TeV), where they arise mostly from kaon decay.

There is an angular variation in the neutrino flux, more prominent at higher energies, called *the secant theta effect*. This effect occurs because pions and muons that are produced nearly tangent to the Earth have more flight time in less dense atmosphere, so they have more chance to decay and make neutrinos. Hence, there is a peak near the horizontal arrival direction in the atmospheric neutrino angular distribution (see Fig. 1.3). This peak is symmetric about the horizon for any location (except at the lowest neutrino energies, below around 400 MeV, where geomagnetic effects spoil the symmetry) [45].

1.3.3 Active Galactic Nucleai

The presence of a supermassive black hole ()$M_{BH} > 10^5 M_\odot$) at the centre of some galaxies produce a matter accretion phenomena, which is assummed to be the reason of the light and gas emission. These galaxies are know as Active Galactic Nucleai (AGNs) [46, 47]. To classify a galaxy as an AGN, the bolometric luminosity must be $L_{\rm Bol}/L_{\rm Edd} \geq 10^{-5}$, where $L_{\rm Edd} \approx 1.5 \times 10^{31} W\ (M/M_\odot)$ is the luminosity of a source in hydrostatic equilibrium (Eddington luminosity). A common classification of AGNs is done according to the strength of its radio signal [48]. AGNs are also classified according to its orientation with respect to the Earth.

Among the AGNs, Blazars are a particularly interesting type of AGNs for neutrino detection. This special type of AGNs have a jet pointing towards the Earth (within an angular distance below 12°) and hence, present higher fluxes. It is though that the synchrotron acceleration mechanism is the responsible for the production of radio to X-ray flux.

Different hadronic [49] and leptonic [49–51] models have been used to fit the photon spectral energy distribution of Blazards that have been observed by FERMI [52, 53].

1.4 Neutrino Interactions

In this section, a brief overview of different neutrino interactions are presented (for a detailed review see Ref. [54]).

Neutrinos participate in interactions by exchange of weak bosons. Interactions with an exchange of $W^\pm$ boson are called Charged Current (CC) whereas the Neutral Current (NC) interactions are via Z^0 boson. Both reactions are presented schematically in Fig. 1.4. While in CC interactions a high energy lepton is produced along with hadronic shower, NC interactions (of all neutrino flavours) induce an hadronic shower and a scattered neutrino without changing the flavour.

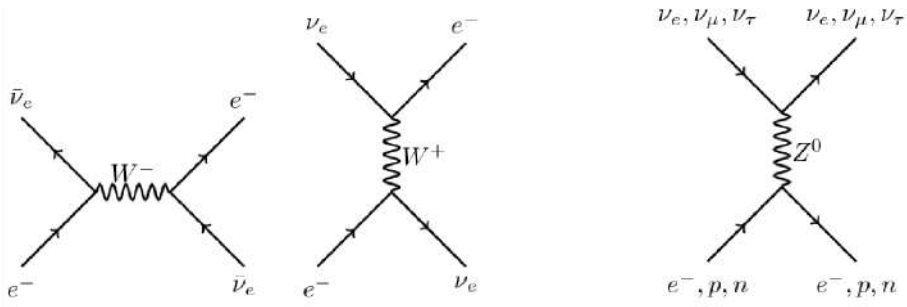

Figure 1.4: Diagram of a neutrino Charged Current (CC) interaction (left and center) and Neutral Current (NC) interaction (right).

In the range $E_\nu \sim 0.1 - 1$ MeV there are two processes:

- **Coherent scattering** involves the neutral current exchange where a neutrino interacts coherently with the nucleus:

$$\nu + {}^{A}_{Z}X \rightarrow \nu + {}^{A}_{Z}X^{*}, \tag{1.2}$$

  where A is the mass number, Z is the atomic number and the X^* represents the nucleus in an excited state.

- **Neutrino capture on radioactive nuclei** is also referred to as enhanced or stimulated beta decay emission. This process is similar to the ordinary beta decay with the difference that the neutrino is interacting with the target nucleus:

$$\nu_e + {}^{A}_{Z}X \rightarrow e^{-} + {}^{A}_{Z+1}X. \tag{1.3}$$

Energies about $E_\nu \sim 1 - 100$ MeV allow the neutrino to access nucleons individually. These reactions depend on the targets and can be summarised as:

- **Inverse beta decay.** This reaction allowed the confirmation of the neutrino existence by Reines and Cowan [9]. The products of the reaction can be well detected as a two light flashes arriving in coincidence: one is due to the positron annihilation (together with an electron quickly found in the matter it produces two gamma-rays) and a slightly delayed signal from the photon emission due to the neutron capture by cadmium for example. The reaction takes the form:

$$\bar{\nu}_e + p \rightarrow e^{+} + n. \tag{1.4}$$

- **Neutrino-deuterium interactions.**

$$\nu_e + d \xrightarrow{CC} e^{-} + p + p, \tag{1.5}$$

$$\nu + d \xrightarrow{NC} \nu + n + p. \tag{1.6}$$

  The first one goes via charged current and it is available only for electron neutrinos at $E_\nu < m_\mu$. The second, instead, goes with neutral current and it is the same for all neutrino flavours. Both reactions allowed the SNO experiment with a heavy water target to simultaneously measure the electron and non electron component of the solar neutrino spectrum and confirm the neutrino oscillations [22].

- **Other nuclear targets.** For other nuclear targets the reaction has the form:

$$\nu(\bar{\nu}) + {}^{A}_{Z}X \rightarrow l^{\mp} + {}^{A}_{Z\pm1}X, \tag{1.7}$$

  where lepton l corresponds to the neutrino flavour. This reaction was of particular importance for the first solar neutrino detection using a ^{37}Cl target at the Homestake experiment [55].

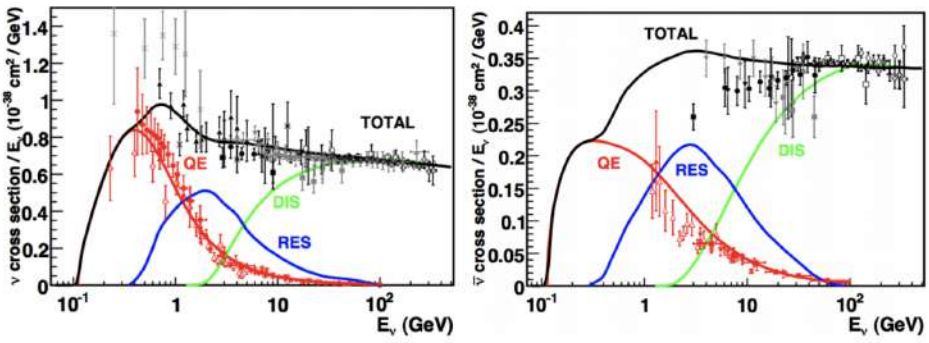

Figure 1.5: Muon neutrino (left) and antineutrino (right) CC cross section measurements and predictions from the NUANCE generator [56] as a function of neutrino energy. The contributing processes in this energy region include quasi-elastic (QE) scattering, resonance production (RES) and deep inelastic scattering (DIS). The error bars (typically 10–40%, depending on the channel) reflect the uncertainties on these cross sections. Mind the scale on Y-axis. From [57].

As the neutrino energy grows, the description of a neutrino scattering becomes more diverse. For energies about the GeV range there are three main categories:

- **Elastic and quasi-elastic scattering (QE).** Neutrinos can elastically scatter off an entire nucleon liberating a nucleon (or multiple nucleons) from a target. In the case of charged current neutrino scattering, this process is referred to as *quasi-elastic scattering* whereas for neutral current scattering this is traditionally referred to as *elastic scattering*. QE scattering dominates at energies ≤ 1 GeV.
- **Resonance Production (RES).** Neutrinos can excite the target nucleon to a resonance state. The resultant baryonic resonance decays to a variety of possible mesonic final states producing combinations of nucleons and mesons. This process dominates in the energy range $[1 - 4]$ GeV.
- **Deep inelastc scattering (DIS).** Given enough energy, the neutrino can resolve the individual quark constituents of the nucleon. This is called *deep inelastic scattering* and manifests in the creation of a hadronic shower. This process dominates for energies over about 4 GeV.

Fig. 1.5 shows the muon neutrino and muon anti-neutrino interaction cross section, as a function of the energy, and how QE, RES and DIS processes contribute. It is important to note that each of the previously mentioned processes have CC and NC analogues, the CC interaction cross section is $\sim$3 times larger than the associated NC interaction cross sections. Moreover, the cross section for antineutrinos is about a factor 2 smaller than those for neutinos.

1.5 Neutrino Detection

Neutrinos are weakly interacting particles. Their detection is possible by an identification of the interaction products with the matter. As the cross-sections of the interactions are on the weak scale, large detector volumes and long data taking periods are required. The interactions can be detected using the light, radio or acoustic emission.

- The *Cherenkov radiation* is the process of coherent light emission that happens when charged particles travels through a dielectric faster than the speed of light in that medium. This effect is the main process for neutrino detection used by under-water (ANTARES and KM3NeT) and under-ice (IceCube) detectors. See Sec. 1.5.1 for a detailed description.
- The radio emission due to the *Askaryan effect* [58] is similar to the Cherenkov radiation: a particle traveling faster than the phase velocity of light in a dielectric (such as salt, ice or air) produces a shower of secondary charged particles which contain a charge anisotropy and thus emits a cone of coherent radiation in the radio or microwave part of the electromagnetic spectrum. The Antarctic Impulsive Transient Antenna (ANITA) experiment exploits this effect to search for ultra-high energy neutrinos [59].
- *Acoustic emission* happens due to the instantly heated matter at the local area of the interaction and the fast expansion with a propagation of the pressure wave. The technique of acoustic neutrino detection is a promising approach for future large-scale ultra-high energy neutrino detectors in water. To investigate this technique in the deep sea, the AMADEUS system has been integrated into the ANTARES neutrino telescope in the Mediterranean Sea [60].

In this thesis only the Cherenkov radiation will be treated, as it is the main detection mechanism exploited by the ANTARES (chapter 2) and ORCA (chapter 4) detectors.

1.5.1 Cherenkov Radiation

When a fast charged particle travels at a uniform velocity in a dielectric medium, the associated electromagnetic field close to the particle polarizes the medium along its track, so that the electrons attached to the atoms follow the waveform of the pulse as the particle goes by. In the general case, when the particle is slow, the radiation from the displaced electrons is not observed, owing to destructive interference. If, however, the velocity of the particle in the medium is faster than the phase velocity of light in the medium, the wavelets from all portions of the track are in phase with one another on a wavefront inclined to the direction of the track, and a coherent radiation is then observed, which is called *Cherenkov radiation* [61–63].

The emission of the Cherenkov light is produced in a cone around the direction of the particle with a characteristic opening angle, θ_c. The particle that emits the

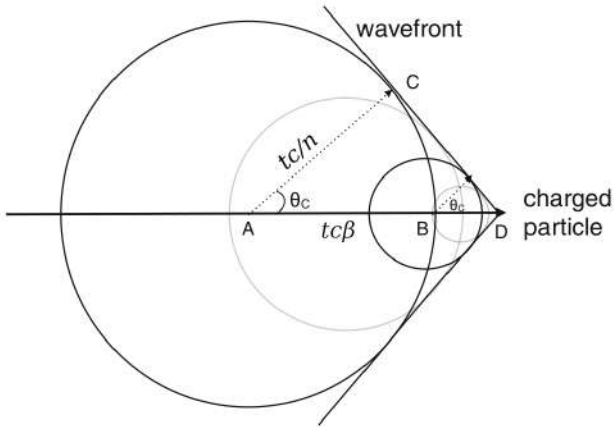

Figure 1.6: Scheme of the Cherenkov radiation for a particle moving from left to right at a speed faster than the speed of light in a media with refraction index n. Emission of the Cherenkov light from each point along the track has a spherical wavefront which produces a cone-shape wavefront for the whole track. The line $\overline{AC}$ is the distance traveled by the light with a speed of c/n in a time t. The segment $\overline{AD}$ is the distance traveled by the charged particle with a speed $\beta c = v$ in the same time t. Adapted from [64].

radiation lies at the vertex of the cone. At the edges of the cone, the emitted radiation overlaps and interferes constructively. In Fig. 1.6 the Cherenkov light emission is illustrated: the spherical wave emitted at the point A will reach the point C at the same time as the charged particle arriving time at the point D. The cosine of the angle θ_c is given by:

$$\cos\theta_c = \frac{\overline{AC}}{\overline{AD}} = \frac{tc/n}{t\beta c} = \frac{1}{\beta n}, \tag{1.8}$$

For a highly relativistic particle ($\beta \approx 1$), the Cherenkov angle becomes independent of the energy of the particle. The refraction index for sea water is $n \approx 1.35$, which results in a opening angle of $\theta_c \approx 42^\circ$.

Due to the dispersion properties of water, the majority of the observed Cherenkov radiation falls within the blue band of the visible spectrum and the ultraviolet region. Eq. 1.9 gives the number of photons N emitted within a wavelength interval $d\lambda$ by a charged particle per path length dx.

$$\frac{d^2N}{dxd\lambda} = \frac{2\pi\alpha}{\lambda^2}\left(1 - \frac{1}{\beta^2 n^2}\right), \tag{1.9}$$

where $\alpha \approx \frac{1}{137}$ is the fine-structure constant and λ is the wavelength of the Cherenkov photon. The range of the wavelength goes from 300 to 600 nm, which is the relevant range to water-based neutrino telescopes. The equation above provides an estimate of the expected number of Cherenkov per track length:

$$\frac{dN}{dx} \approx 340 \text{ cm}^{-1}. \tag{1.10}$$

The Cherenkov threshold for a particle with rest mass m_0 is given by:

$$E_c = \frac{m_0}{\sqrt{1 - 1/n^2}}. \tag{1.11}$$

This translates into a kinetic energy ($T_c = E_c - m_0c^2$) of $T_c(e) \approx 0.25$ MeV for electrons and $T_c(\mu) \approx 53$ MeV for muons in sea water [44, 65].

1.5.2 Particle Propagation

The Cherenkov light emission, even though being the main process to detect muons in neutrino telescopes, is not the main energy loss process for muons that travels through an optical medium. The main mechanism of energy loss for muons traveling in water is ionization (dominant at $E_\mu < 1$ TeV), e^+e^- pair production (dominant at $E_\mu > 1$ TeV), bremsstrahlung and nuclear interactions. The total contribution can be parameterised as:

$$-\frac{dE_\mu}{dx} = a + b \cdot E_\mu, \tag{1.12}$$

where the ionization (a) and stochastic loss (b) terms are assumed to be independent of the muon energy, E_μ. In water, the usual values are: $a = 0.274$ GeV m^{-1} and $b = 3.492 \times 10^{-2}$ m^{-1} [66, 67]. Muons of few-GeV crossing sea water leave a single uniform track (the so-called *track-like topology*). The range (R) of the track can be obtained from:

$$R = \frac{1}{b} \cdot \ln\left(1 + \frac{b \cdot E_0}{a}\right). \tag{1.13}$$

The muon track length is $\sim$4 m per GeV. Eventually, the muon decays ($T_\mu^{\text{rest}} \sim 2.2$ μs) into an electron, which initiates an electromagnetic shower, and two neutrinos.

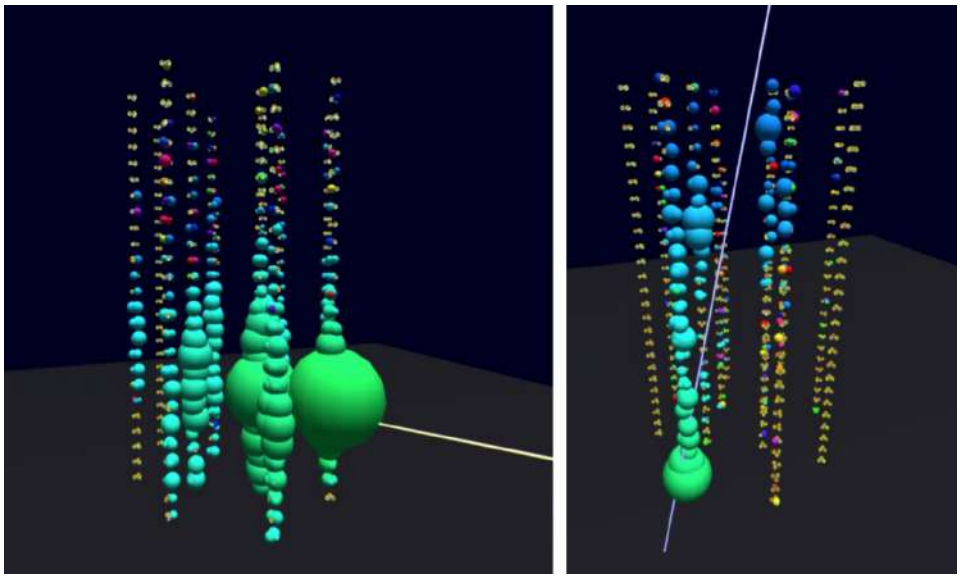

Figure 1.7: Event display of two events observed by the ANTARES neutrino telescope. The picture on the left shows a shower-like event topology and the right one shows a track-like. In both event displays, the size of the colored spheres represents the amount of photoelectrons collected on a PMT and the color code shows the arrival time of the photons. The straight lines that cross the detector indicate the reconstructed direction of the incoming neutrino. From [68].

The main energy loss mechanisms of electrons are bremsstrahlung and ionisation. The emitted photons undergo Compton scattering off electrons or pair production. These products result in an electromagnetic cascade (EM) of electrons and positrons, which produces photons and vice versa (the so-called *shower-like topology*). As opposed to muon tracks, the signature of showers in the detector appears as point-like bursts of light sources localised within a distance below the Molière radius [11]. The hadronic shower signature left in the detector is similar to that of EM showers, to a first approximation. The characteristic hadronic shower evolution and its corresponding Cherenkov light emission in water and ice are detailed in [44, 69]. As an example, Fig. 1.7 shows the display of two events reconstructed in ANTARES as shower-like (left) and track-like (right) topologies. A more detailed discussion on the signatures leaved by particles interacting in the water are summarized in Sec. 1.5.4.

1.5.3 Light Propagation

The attenuation of the Cherenkov light in water sets an upper limit to the distance between the optical sensors of the telescope. In order to properly describe the transparency of sea water as a function of wavelength, it is necessary to measure the parameters describing absorption and scattering, such as the absorption length $\lambda_{\text{abs}}(\lambda)$ and the scattering length $\lambda_{\text{s}}(\lambda)$. Each of these lengths represents

the path after which a beam of light of initial intensity I_0 and wavelength λ is reduced in intensity by a factor of $1/e$ through absorption or scattering according to:

$$I_{\text{abs, s}} = I_0 \cdot \exp\left(-\frac{x}{\lambda_{\text{abs, s}}}\right), \tag{1.14}$$

where x is the optical path traversed by the beam. The attenuation length is defined as $1/\lambda_{\text{att}}(\lambda) = 1/\lambda_{\text{abs}}(\lambda) + 1/\lambda_{\text{s}}(\lambda)$. In the literature, also the coefficients of absorption, $a = 1/\lambda_{\text{abs}}(\lambda)$, and scattering, $b = 1/\lambda_{\text{s}}(\lambda)$, are used to characterise the light transmission through matter. The sum of scattering and absorption coefficients is called *attenuation coefficient*, c.

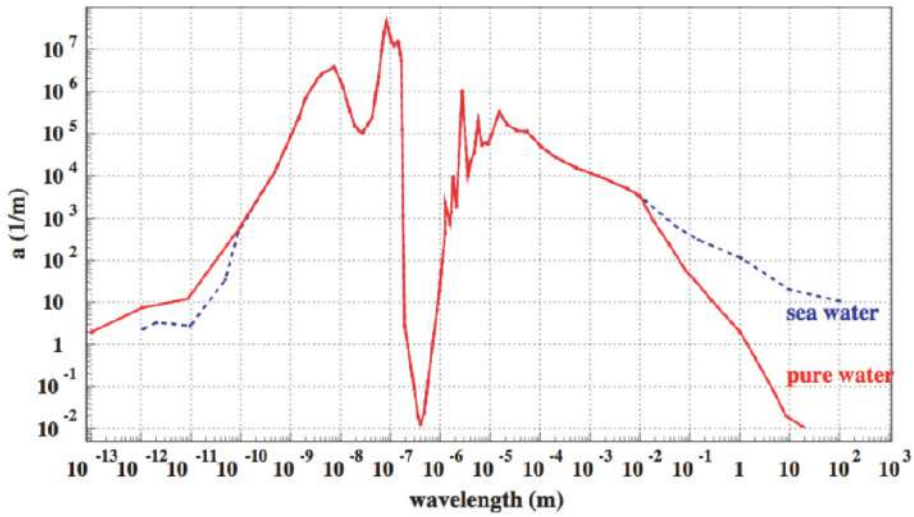

Figure 1.8: Light absorption coefficient a as a function of wavelength for pure water (solid red line) and sea water (dashed blue line) [70].

As shown in Fig. 1.8, water is transparent only to a narrow range of wavelengths (350 nm $\leq \lambda \leq$ 550 nm). In particular, λ_{abs} is about 100 m for deep polar ice [71], and it is about 70 m for clear ocean waters [70]. From these values one can get a first rough estimate of the number of optical sensors that are needed to instrument a km^3 of water, that turns out to be about 5000 [72]. For the deep Mediterranean sea water, the scattering length for a blue light of 473 nm measured by ANTARES is 265 m [73], whereas for ice, the measured scattering lenght for the same wavelength is about 25 m in average [74, 75]. These values mean that photons travel longer distances in water than in ice before scattering with the medium and changing its direction. In sea water, photons scatter 10 times less than in ice, favoring the median angular resolution of underwater neutrino telescopes like ANTARES or KM3Net over the ice based telescopes like IceCube.

1.5.4 Neutrino Signatures

In neutrino telescopes, different signatures can be distinguished based on: the type of interaction (NC, CC or Glashow resonance), the flavour of the neutrino involved (ν_e , ν_μ or ν_τ) and, the part of the interaction observed in the detector due to the decay of an outgoing lepton. Fig. 1.9 shows a summary of all possible signatures.

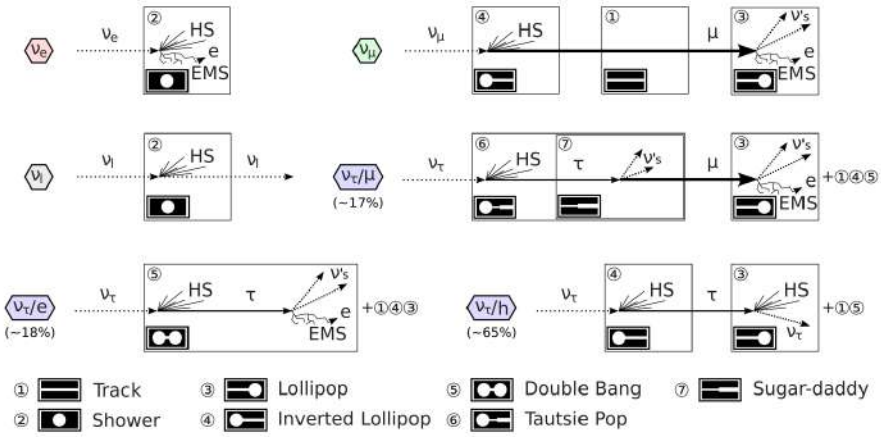

Figure 1.9: Types of events observed in neutrino telescopes depending on the type of interaction and incoming neutrino flavour. HS denotes hadronic shower and EMS electromagnetic shower. From [76].

A brief description of each signature is presented below [53, 77]:

- **Muon neutrinos interacting through CC,** produces an outgoing muon and an hadronic shower. The relativistic muon can travel up to several kilometers before decaying (τ_0 = 2.2 μs). The passage of the muon through the medium polarises the atoms and molecules, yielding Cherenkov radiation (see Sec. 1.5.1). The average angular separation between the neutrino and the outgoing muon, $\langle \alpha_{\nu\mu} \rangle$, is expressed as:

$$\langle \alpha_{\nu\mu} \rangle = \frac{0.6^\circ}{\sqrt{E_\nu / 1\text{TeV}}}, \tag{1.15}$$

  where E_ν is the energy of the incoming neutrino. For high-energy neutrinos (above 10 TeV), the median angular separation is $< 0.2^\circ$. The (almost) collinearity of the outgoing muon with the incoming neutrino allows the estimation of the direction of the original neutrino after reconstructing the muon track. The interaction can be expressed as:

$$\nu_\mu(\bar{\nu}_\mu) + N \rightarrow \mu^-(\mu^+) + X,$$

where N represents a nucleon and X is an hadronic shower localized at the interaction vertex.

- **Electron neutrinos through CC with nucleons.** The interaction of the neutrino produces an electron as a final state. From this interaction, two types of showers can be identified. First, an hadronic shower is produced from the *break-up* of the nucleon. Second, due to the interaction of the outgoing electron with matter through pair production and bremsstrahlung, an electromagnetic shower is produced. Since the production of both cascades occurs in the same interaction vertex, distinguish them is very complicated. The signature left at the detector is a *shower-like* event. The interaction can be expressed as:
$$\nu_e(\bar{\nu}_e) + N \rightarrow e^-(e^+) + X.$$

- **Neutrinos interacting through NC.** In NC interactions, the vast majority of the energy is transferred to the outgoing neutrino whereas a small fraction is transferred to the nucleus. This is the reason of not being possible to measure the total energy of the incoming neutrino. The remaining energy is seen as an hadronic cascade. The signature left in these interactions in the detector is so-called *cascade* or *shower-like* event. The interaction can be expressed as:
$$\nu_l(\bar{\nu}_l) + N \rightarrow \nu_l(\bar{\nu}_l) + X, \qquad (l = e, \mu, \tau).$$

- **Tau neutrinos through CC.** This neutrino interaction produces an outgoing τ lepton and an hadronic cascade. Due to the different decays of the τ particle, different topologies can be seen at the decay vertex. The τ can decay into pions and kaons (with a probability of about 65%), producing a hadronic cascade and, into an electron or a muon (with a probability of about 35%) [11]. When the τ lepton decays into hadrons or into an electron, a second cascade is observed. The short lifetime of the tau ($\sim 2.9 \times 10^{-13}$ s) makes it impossible to distinguish both cascades for energies under $\sim$2 PeV [78]. The interaction can be expressed as:
$$\nu_\tau(\bar{\nu}_\tau) + N \rightarrow \tau^-(\tau^+) + X.$$

- **Glashow resonance.** After the interaction of an electron antineutrino with an electron, a W^- boson is produced. Then, the $\sim 2/3$ of the times the W^- decays into hadrons, whereas the other $\sim 1/3$ of the times, it produces a $\bar{\nu}_l l^-$ pair. In 2020 IceCube reported the detection of a cascade of high-energy particles consistent with being created at the Glashow resonance [79].

1.6 Neutrino Telescopes

In 1960, Markov and Zheleznykh [80] proposed to use a large volume of sea water as neutrino detection medium to obtain a huge target mass in a cost effective way. The sea water works simultaneously as the target, the shield and the active

detection volume. The proposal foresaw the instrumentation of a large volume of water (as well as ice) with several optical sensors in order to detect the Cherenkov light emitted by the charged particles produced in the CC interaction of neutrinos with rock and water in the vicinity of the telescope.

The DUMAND (Deep Underwater Muon And Neutrino Detector) collaboration [81], conducted from 1976 until 1995 and located at $\sim$ 4800 m depth 30 km off-shore of Hawaii, was the first attempt to build an underwater neutrino telescope that stopped the operation due to technicall difficulties. This experiment set the precedents to high energy neutrino astronomy. In the following pages, some of the most relevant neutrino telescopes currently working and future projects are described.

ANTARES and KM3NeT

At the moment, the center of gravity of the research in underwater neutrino telescopes is the Mediterranean Sea. The presence of large abyssal planes, with depths ranging from 2500 to 4500 m and low deep-sea current favours this development. The ANTARES telescope was the first deep-sea underwater neutrino telescope, located at a depth of about 2500 m, 40 km offshore Toulon, France. The data taking period of ANTARES runs from 2007 until February 12, 2022, when it was switched off. A more detailed description of ANTARES is given in chapter 2.

KM3NeT is a research infrastructure comprising the ARCA and ORCA telescopes. The first is located about 80 km off-shore from the coast of Portopalo di Capo Passero, Sicily (Italy) at a depth of 3500 m. The second is located at about 10 km far from the ANTARES site. The ARCA detector will have a final instrumented volume of more than 1 km^3 and is designed for the investigation of high energy neutrino astrophysics and the search for the sources of cosmic neutrinos. The ORCA detector is optimised for the study of low energy neutrino oscillation physics and for the measurement of the neutrino mass ordering. A more detailed description of KM3NeT is given in chapter 4.

Apart from the mentioned above, both detectors have an extensive physics program including: nuclearities, monopoles, dark matter, non-standard interactions, multimessengers, among others.

Baikal GVD

A neutrino telescope has been built in the Lake Baikal, Russia, at a depth of $\sim$1800 m [82]. The first test detection units (e.g. NT-200 [83]) were deployed in the early nineties and, with these, it was possible to make a first search for high energy neutrinos [84]. Next generation cubic kilometer scale neutrino telescope Baikal-GVD (Gigaton Volume Detector) is currently under construction in Lake Baikal since 2015. The detector is specially designed to search for high energy neutrinos. The configuration of the telescope consists of functionally independent clusters of strings, which are connected to shore by individual electro-optical cables. Each cluster comprises 288 optical modules (OMs) arranged along 8 strings where seven peripheral strings are uniformly located at a 60 m distance around a

central one. The distances between the central strings of neighboring clusters are about 300 m. Fig. 1.10 shows a schematic view of the current configuration of the GVD detector. The latest results obatined from the colleted data are reported in [85].

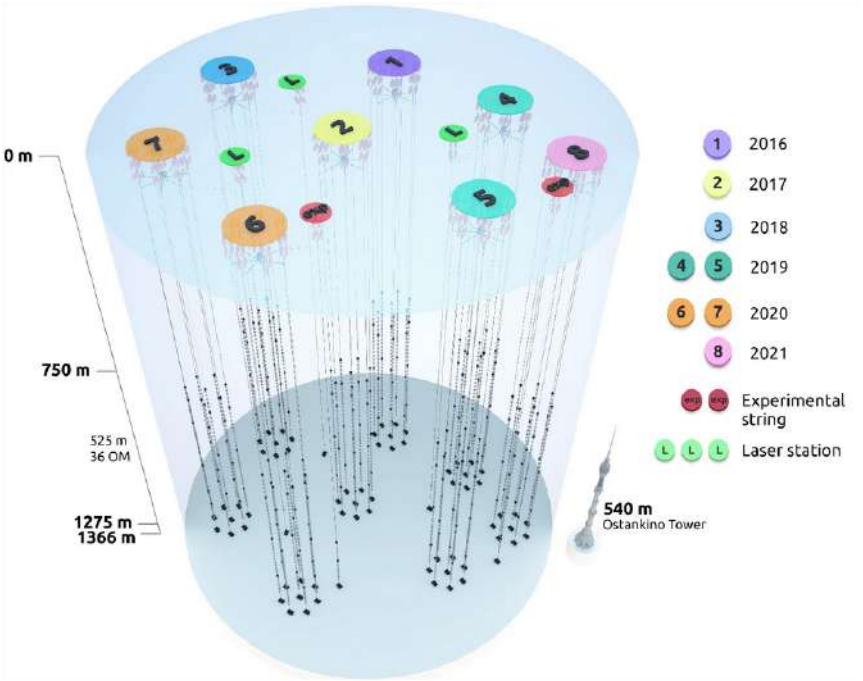

Figure 1.10: Schematic view of the Baikal-GVD detector. The yearly progression of the detector deployment is shown in the legend. From [86].

P-ONE

The Pacific Ocean Neutrino Experiment (P–ONE) is a new initiative with a vision towards constructing a multi-cubic kilometre neutrino telescope, to expand our observable window of the Universe to highest energies (TeV–PeV). P–ONE will be installed at the Cascadia Basin at a depth about ∼2600 m. The P–ONE *explorer*, comprising the 10 first strings and a total of 20 photo-sensors and 2 calibration modules per string, is planned to be deployed in 2023–2024. The remainder of the telescope array, comprising about 70 strings (Fig. 1.11), are planned for deployment between 2028-2030 [87].

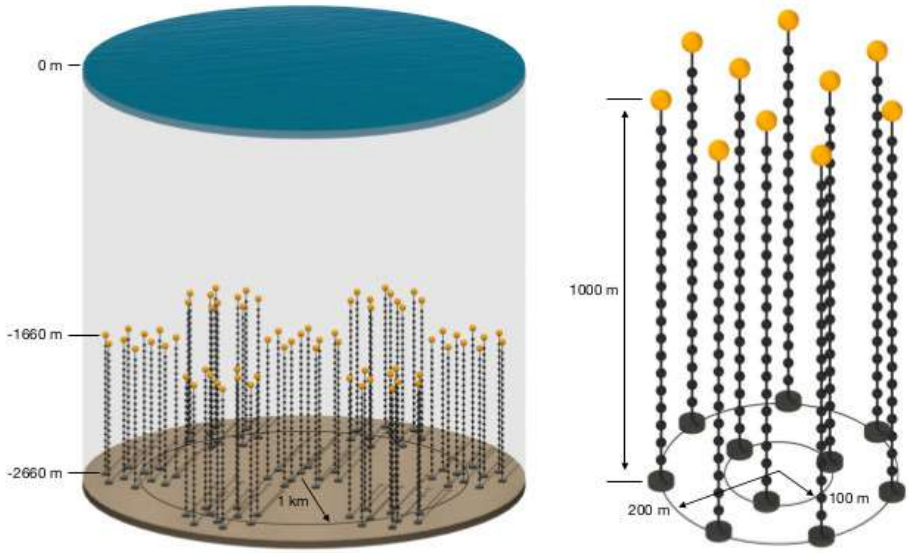

Figure 1.11: Design of the proposed final stage of instrumentation of the Pacific Ocean Neutrino Experiment consisting of seven segments optimized for energies above 50 TeV (left) and the design of an individual segment that is planned to be installed in 2023/24. From the P–ONE website.

AMANDA

The Antarctic Muon and Neutrino Detector Array (AMANDA) was the first-generation under-ice detector, designed to reach a relatively large telescope area and detection volume for a neutrino threshold not higher than 100 GeV. This relatively low threshold permits calibration of the novel instrument on the known flux of atmospheric neutrinos. Its architecture was optimized for reconstructing the Cherenkov light front radiated by up-going, neutrino-induced muons [88]. The AMANDA detector was operating since late nineties until 2010. Its full configuration comprised 677 optical modules arranged in 19 strings frozen between $\sim$1.5 km and $\sim$2 km deep in the ice sheet at the geographic South Pole. AMANDA achieved an angular resolution of about $1.5^\circ - 2.5^\circ$ for muon tracks [89]. The promising results obtained with AMANDA favoured the posterior development of a bigger under-ice neutrino telescope, IceCube (see next subsection) [90–92].

IceCube

IceCube (IC), the succesor of AMANDA, is currently the world largest neutrino telescope. It was deployed between the austral summer of 2004–2005 and has been taking data since February 2005 [93, 94]. The IceCube configuration can be splitted in three main parts: IceCube, DeepCore and IceTop (see Fig. 1.12).

The in-ice component of IceCube consists of 5160 digital optical modules (DOMs), each with a ten-inch photomultiplier tube and associated electronics. The DOMs are attached to vertical strings, frozen into 86 boreholes, and arrayed over a cubic kilometer from 1450 m to 2450 m depth. The strings are deployed on a hexagonal grid with 125 m spacing and hold 60 DOMs each. The vertical separation of the DOMs is 17 m. The full configuration of IceCube achieves a median angular resolution of about 0.6° for muon tracks [94].

Eight of these strings at the center of the array were deployed more compactly, with a horizontal separation of about 70 meters and a vertical DOM spacing of 7 meters. This denser configuration forms the DeepCore [95] subdetector, which lowers the neutrino energy threshold to about 10 GeV, creating the opportunity to study neutrino oscillations.

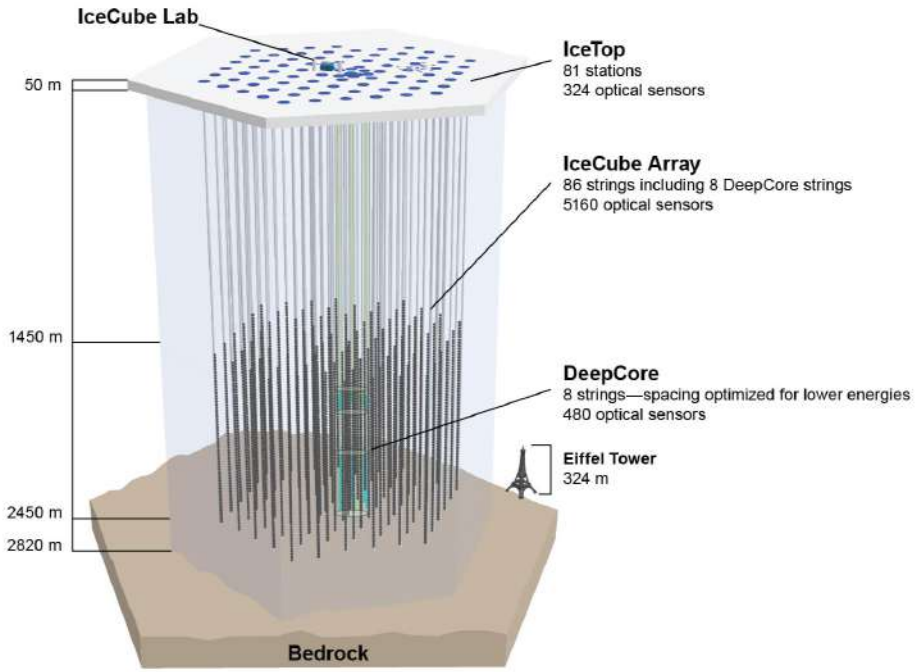

Figure 1.12: A schematic of the in-ice portion of IceCube, which includes 86 strings holding 5160 light sensors arranged in a three-dimensional hexagonal grid. Credit: IceCube Collaboration.

IceTop consists of 81 stations located on top of the same number of IceCube strings. Each station has two tanks, each equipped with two downward facing DOMs. IceTop, built as a veto and calibration detector for IceCube, also detects air showers from primary cosmic-rays in the 300 TeV to 1 EeV energy range. The surface array measures the cosmic-ray arrival directions in the Southern Hemisphere as well as the flux and composition of cosmic-rays [94, 96, 97].

Part II

Solar Atmospheric Neutrinos with the ANTARES Neutrino Telescope

2 The ANTARES Neutrino Telescope

"Measure what can be measured, and make measurable what cannot be measured."

Galileo Galilei

In this chapter the ANTARES neutrino telescope [98] is described. In section 2.1 the detector layout, their components, the data acquisition system and the calibration of the detector, needed for the accurate reconstruction of the events, are presented. A general description of the Monte Carlo (MC) strategy for the generation of events and their propagation through the medium is outlined in section 2.2. Finally, in section 2.3, the methods employed for the reconstruction of the events are explained.

2.1 Detector Description

ANTARES (acronym for Astronomy with a Neutrino Telescope and Abyss environmental RESearch) is the first operational undersea neutrino telescope [98]. It is located at a depth of 2475 m in the Mediterranean Sea at (45°45′ N, 6°10′ E), 40 km offshore from Toulon (France). The detector started taking data with the first lines in 2007 and was completed in May 2008. In February 12, 2022 the detector was switched off, and the dismantling of the infrastructure is foreseen by summer 2022.

The main physics goal of ANTARES is to perform neutrino astronomy, but the infrastructure also offers instrumentation for the sea and Earth science community [100, 101].

2.1.1 Detector Layout

The ANTARES full configuration consists on 12 vertical detection lines (also called *strings*) anchored to the ground, 450 m high and horizontaly spaced by 50-75 m, distributed on an octogonal layout. Each line holds 25 storeys, with the exception of line 12, equipped with 20 storeys plus acoustic detection devices. A storey is defined as an ensemble of: a mechanical structure, the Optical Module Frame (OMF) supporting three Optical Modules (OMs) and a titanium container, and the

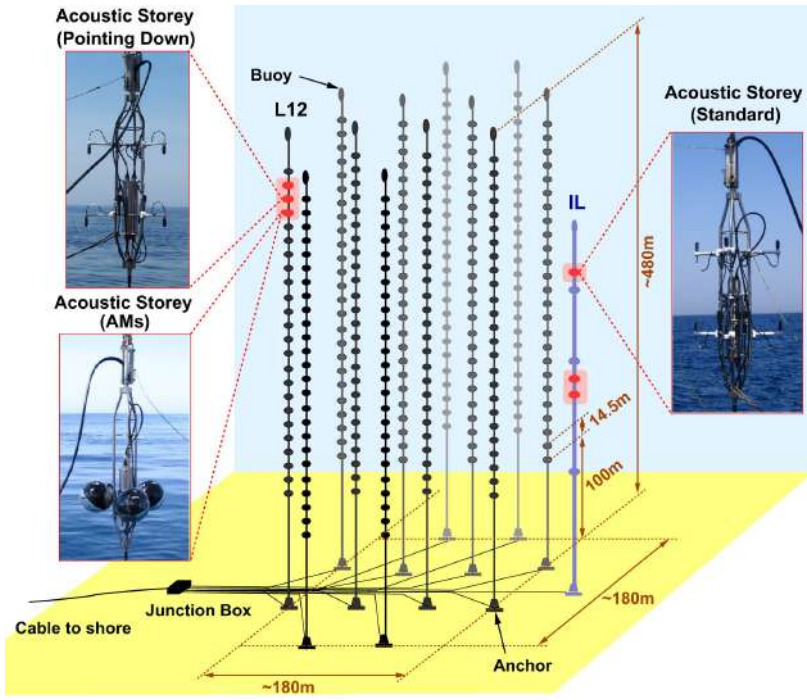

Figure 2.1: Schematic view of the ANTARES detector. From [99].

Local Control Module (LCM) housing the electronics. A system of buoys keep the lines vertical. A drawing of the detector layout is shown in figure 2.1.

Each storey hosts three optical modules, each containing a photomultiplier tube (PMT) of 10" (see section 2.1.2 for further details). The first storey is located $\sim$100 m above the sea-bed, and the distance between storeys in the same line is 14.5 m.

Each detection line is held vertically thanks to a buoy at the top of the lines and the buoyancy of the OMs. On the sea-bed, a Junction Box (JB) connects the lines to the shore station with the Main Electro-Optical Cable (MEOC), which provides power, transfers data to shore and distributes a clock signal responsible for the synchronisation of the different detector elements [98, 102].

2.1.2 Optical Module

The Optical Module (OM) [103] of a neutrino telescope is the main element for detecting events. The OMs have a diameter of 17", and are designed to optimise the light detection. They are made of components which withstand the hard conditions that are likely to occur during sea operations (corrosion, shocks, vibrations, high pressures, etc.), with a lifetime that surpass 10 years.

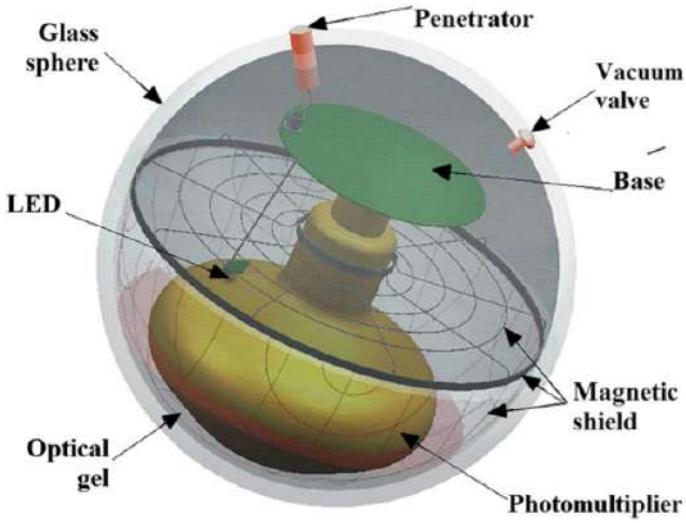

Figure 2.2: Schematic view of the ANTARES OM and their components. From [103].

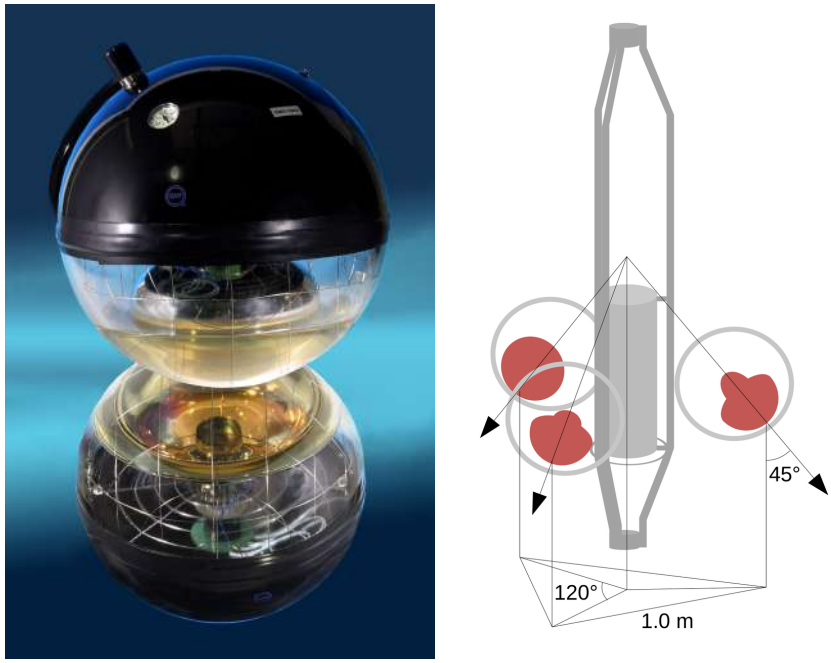

Figure 2.3: A photography of an ANATRES optical module positioned on a mirror (left) and an schematic drawing of an storey with 3 OMs pointing downwards. From [98, 104].

The OM main component is a large-area hemishperical PMT glued in a pressure resistant glass sphere with optical gel (see figures 2.2 and 2.3). Each ANTARES OM includes a 10" Hamamatsu R7081-20 PMT [105], with a photocathode area of 500 cm^2, a transit time spread (TTS) of 2.6 ns (FWHM) and a quantum efficiency of about 25% at a wavelength of 400 nm. Due to the size of the PMT, the magnetic field of the Earth modifies the trajectory of the electrons between the nodes inside the PMT, degrading the uniformity of the response. In order to avoid this undesirable effect, the PMTs are shielded with a μ-metal cage.

The reconstruction of the neutrino direction and energy is based on the detection of the incoming Cherenkov light yielded by relativistic charged particles in water, measuring the arrival time and its intensity. The OMs are also equipped with a flashing LED system for time calibration purposes (see Sec. 2.1.4).

2.1.3 Data Acquisition System and Triggers

The data acquisition system (DAQ) is responsible for the digitisation of the signals of the PMTs, and for the data transport, filtering and storage [106]. As described below, different trigger algorithms are applied depending on the data taking conditions.

DAQ

The ANTARES DAQ system follows the *all-data-to-shore* strategy, which ensures that all hits recorded by the PMTs are digitised and sent, without any selection, to the onshore station [106]. Once onshore, different trigger algorithms are adjusted according to the detector conditions, and applied to the data for selecting potential interesting events, which will be stored and processed by the reconstruction programs.

The DAQ system starts with the digitalisation of the PMT hits (the analog signal is transformed into a readable format for data analysis purposes). The dark current noise of the PMTs can be reduced by applying a threshold of 0.3 p.e.[1] in the integrated charge (L0 threshold). Every hit above threshold is "time-stamped" with a local clock and two time-to-voltage converters located in each Logical Control Modules (LCM). The data, temporarily stored in LCMs in arrays of hits within a time frame of 100 ms, is sent to the JB and then transferred offshore. This avoids traffic network overloads and possible data losses. The data streaming process is subdivided into so-called *runs* from 2 to 12 hours of duration, depending on the data taking setup.

Triggers

Once the raw data is on the onshore station, the Data Filter software applies a filtering process to the data. These programs apply a set of different algorithms

[1] Photo-electron (p.e.): electron emitted from an atom by interacting with a photon.

(triggers) based on different classification criteria: general purpose muon trigger, direction triger, muon triggers based on local coincidences, etc. [98, 107].

The main ANTARES triggers are summarize in the table below:

Trigger	Description
L0	Level-zero filter. Offshore threshold of 0.3 p.e. applied to reduce the effect of the dark current noise in the PMTs.
L1	Level-one filter. Coincidence of at least two L0 hits in the same storey within a 20 ns time window. Limits the accidental correlations of hits and reduces the background due to bioluminescence and ^{40}K decays.
3N	5 L1 hits in at least one of the 210 predefined directions within 20 ns time window from coincidence relation. Dominated by background atmospheric muons.
T3	2 L1 hits within a time window of 100 ns in adjacent storeys, or 200 ns for next-to-adjacent storeys.
2T3	2 T3 triggers with at least three (one line) or 4 L1 hits (whole detector) in 2 μs.
TQ	2 L1 triggers + 4 L0 hits in at least one of the 105 upward directions within 20 ns from coincidence relation.
K40	Coincidente between 2 L0 hits (same line) in 20 ns.

Table 2.1: Definition of the most relevant triggers used in ANTARES. Table based on content from [107].

2.1.4 Detector Calibration

In order to achieve an accurate event reconstruction, the arrival time, position and charge of the detected Cherenkov photons must be calibrated. A good time and position calibration is of paramount importance to guarantee the best angular resolution when reconstructing the direction of the event. On the other hand, a good charge calibration guarantee a good resolution on the energy reconstruction.

Position Calibration

As mention in Sec. 2.1.1, the ANTARES detector lines are anchored on the sea bed and maintained vertical by a buoy. Due to the flexible structure of the string needed for the deployment, the upper part of the strings can twist and rotate from their original position by the effect of the sea currents. Given that the efficency of the event reconstruction is very sensitive to the distance between OMs, the relative position of each OM is monitored with an accuracy better than $\sim$20 cm. The muon track reconstruction and the energy determination also requires the monitoring of the OM orientation, with a precision of few degrees.

The relative positioning of the detector is monitored combining two systems: an acoustic system giving the 3D position of five hydrophones along the line and

a set of tiltmetre-compasses giving the local tilt and orientation of each optical module storey. With this information, a global fit of the string shape leads to the 3D positioning of the detector within the requirements [108].

Each line is equipped with an acoustic transceiver fixed on its anchor and receiving hydrophones fixed on storeys 1, 8, 14, 19 and 25 [98]. The acoustic receivers are placed: one at the bottom of the storey, one at the top storey and the rest of the receivers are distributed in order to maximize the density of hydrophones in the top third part of the line, where the maximum curvature of the line shape is expected [108].

Charge Calibration

According to the working principle of PMTs, when a photon hits the photocathode, a photo-electron is emitted and accelerated through the HV field, starting an amplification process through secondary electron emission in the dynodes. Before deployment, the PMTs are calibrated in a dark room to measure the single-photo electron signal. In situ calibrations are also performed periodically for fine tunning the voltage in each PMT. For this purpose the light emitted by ^{40}K decays is used. In order reject background light emission due to the ^{40}K decays and the bioluminescence activity in the detector vicinity, a threshold of 0.3 p.e. is set.

Time Calibration

The time calibration process can be divided in two steps. A first time calibration is performed onshore, before the deployment of the detector. Then, in situ calibrations are done periodically in order to get every module synchronized with the master clock. This time calibration is crucial to achieve reconstructions with sub-degree precision.

The onshore time calibration is performed by illuminating simultaneously groups of OMs by short laser pulses. This calibration ensures the funtionality of each line and allows the measurement of the time delays due to the electronics [109].

After deployment, a master clock signal is sent from shore station to establish a common reference frame. The master clock information is used to check the stability and accuracy of the measurements as well as for measuring the in situ time delays after connecting the detector lines.

In situ time calibrations are performed periodically. These measurements allow to determine and correct the time offsets of all OMs through an optical beacon (OB) system [110].

The OB system comprises two subsystems [109]:

- **LED beacons:** Four LED OB are located along every line of the detector. This system, shown in Fig. 2.4 (left), monitors the relative time offsets among OMs of the same line (intra-line calibrations).
- **Laser beacons:** Two laser beacons (see Fig. 2.4, right) are located at the bottom of two central lines. Given that the laser can illuminate all detector lines

and that the time residuals do not depend on the position of the source, this system is used to calibrate the time offsets between different lines (inter-line calibration).

Figure 2.4: Picture of a LED optical beacon (left) and a LASER beacon (right). From [109].

The ^{40}K decays are used for intra-storey calibration, cross-checking within each storey the time offset provided by the onshore dark room and optical beacon calibrations.

An internal LED is also present in each optical module. This LED is used exclusively to monitor the stability of the PMT transit time.

Atmospheric muons [111] are used for intra and inter-line calibration, using an iterative method. From the high quality events of downward–going muons, a subset of hits (*probe hits*) is selected (they are not used to fit the muon track). The remaining hits (*reco hits*) are used for reconstructing the muon track. From the computed time residuals (defined as the difference between the expected and the measured arrival time of the Cherenkov photon) between the *probe hits* and the fitted track, a gaussian fit is performed in the time residual distribution of the probe hits, and the mean value is taken as the time correction, that will be applied to the hit times in the next iteration.

2.2 Monte Carlo Simulations

Monte Carlo (MC) simulations are extensively used in astroparticle and high-energy physics to assess the performance of a detector for the study of physics phenomena. These simulations have turned an essential tool in scientific research. Thanks to this tool, the response and performance of a detector can be evaluated.

The ANTARES MC simulation chain follows a *run-by-run* approach [102] in which physical events and the detector response are simulated accurately. Given that the environmental conditions in a deep-sea neutrino telescope vary with time (sea current, environmental background, etc.), the behaviour of the detector can be affected. In order to get a realistic set of simulated events, these effects are considered by: masking in the simulation the temporary or permanently non-operatinal

OMs, extracting directly from data the optical background in short segments of the data stream (*timeslices* $\approx$ 0.1 s), and measuring the OMs position and PMT efficiencies of individual OMs [102, 112].

MC simulations are also used to check the correct functioning of the apparatus, to optimise the selection cuts for rejecting background events and to evaluate the purity of the selected data sample.

The ANTARES simulation chain can be divided in three main steps:

- **Particle generation** (Sec. 2.2.1): neutrinos from all flavours, atmospheric muons and background light events are simulated in the vicinity of the detector within the relevant energy range and spatial distribution.
- **Particle propagation and light emission** (Sec. 2.2.2): particles are propagated through the detector and, Cherenkov photons are simulated and propagated to the optical modules.
- **Data acquisition** (Sec. 2.2.3): the response of the OMs and the data acquisition electronics are simulated. Filtering and triggering algorithms are applied. The background effects and the evolution of detector efficency with time is taken into account.

2.2.1 Particle Generation

In the Monte Carlo simulation three different regions are defined (see fig. 2.5):

- **Instrumented volume.** This volume is a cylinder where all the OMs are contained. A Cherenkov photon reaching this volume can produce a hit.
- **The *Can*.** The *Can* defines the active volume within which Cherenkov photon emission can lead to a signal in a PMT when reaches the instrumented volume. Outside this volume, only particle energy losses during propagation are considered. The *Can* surrounds the instrumented volume, and extends the volume by three light attenuation lengths.
- **World volume.** Region outside the *Can*. Cherenkov photons produced in this volume have low probability to reach a PMT. Therefore, in this volume only the energy loss of particles during propagation is taken into account.

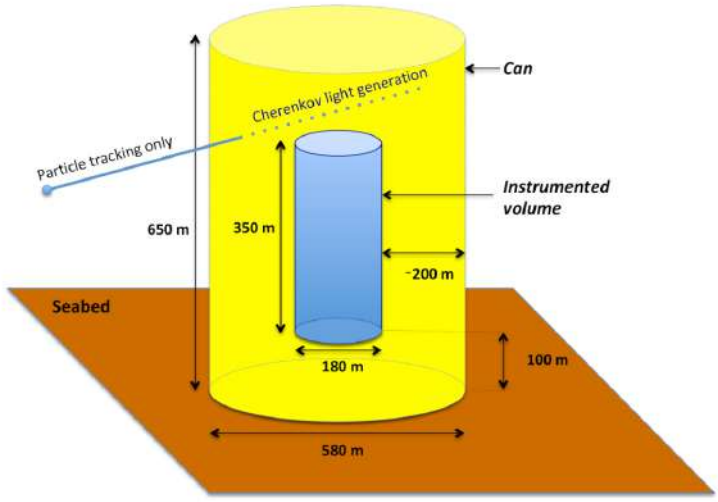

Figure 2.5: Schematic view of the ANTARES simulation volume: the instrumented volume (blue), the *Can* anchored (yellow) to the seabed (brown). From [112].

Neutrinos

The simulation of all neutrino interactions and flavours from the GeV up to PeV energies, is made through the dedicated package GENHEN (GENerator of High-Energy Neutrinos) [113]. In order to simulate all relevant processes, other simulation packages are used, like LEPTO [114] for deep-inelastic scattering at high energies which makes use of the CTEQ6-D parton distribution functions.

The neutrino generation follows a $dN/dE \propto E^{-\gamma}$ power law energy spectrum, where γ is the spectral index chosen by the user in order to have an adequate statistical significance across the considered energy range [112]. Later, these neutrinos can be re-weighted to reproduce any desired flux model.

Neutrino directions are generated isotropically within a generation volume (V_{gen}). This volume is a spatial region, whose size depends on the neutrino interaction type, flavour and energy, employed to generate the neutrino position and interaction vertex. Given that the dimensions of the volume are much less than the neutrino interaction length, every neutrino is considered as interacting within this volume and, secondary interactions are produced at the interaction vertex [112, 115].

Neutrinos traversing the Earth are not simulated. To account for this effect, the probability for a neutrino traversing the Earth, shown in Fig.2.6, is used as a

weight to each neutrino event, and depends on the interaction cross-section ($\sigma(E_\nu)$) and the density of the Earth matter ($\rho(\theta)$), following the equation:

$$P_{\text{Earth}}(E_\nu, \theta) = e^{-N_A \sigma(E_\nu) \rho(\theta)}, \tag{2.1}$$

where N_A is the Avogadro's number and θ is the zenith angle of the incoming neutrino.

In order to represent different neutrino fluxes, the generated neutrinos can be normalized with a generation weight w_2 [116] defined as:

$$w_2 = V_{gen} \cdot F \cdot I_\theta \cdot I_E \cdot E^\gamma \cdot \sigma_{E_\nu} \cdot \rho \cdot N_A \cdot P_{Earth}, \tag{2.2}$$

where

- V_{gen} $[m^3]$ is the generation volume,
- F $[s/year]$ is the number of seconds in a year,

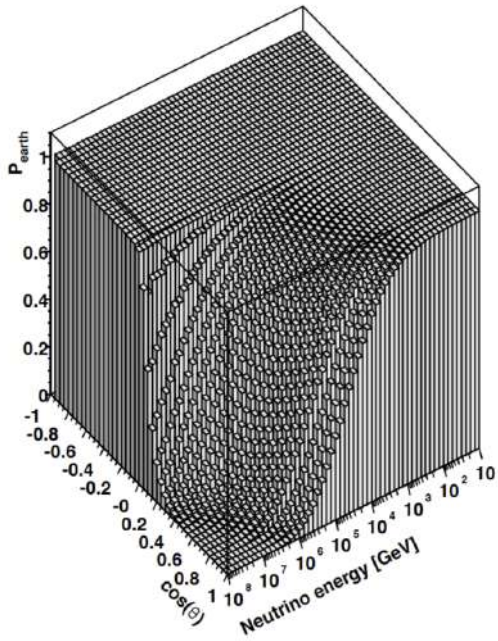

Figure 2.6: Neutrino-Earth interaction probability as a function of the neutrino energy and the cosine of the vertical incidence angle. $\cos(\theta_z) = 0$ corresponds to horizontal neutrinos and $\cos(\theta_z) = -1$ to upward-going neutrinos. From [115].

- I_θ $[sr]$ represents the angular space factor, which accounts for the range of the sky with neutrino zenith angle $\cos\theta_z$, and is defined as $I_\theta = 2\pi(\cos\theta_{max} - \cos\theta_{min})$,
- I_E represents the energy space factor, which takes into account the energy range of simulated neutrinos, and is defined as $I_E = \int_{E_{min}}^{E_{max}} E^{-\gamma} dE$,
- γ represents the spectral index of the neutrinos generated by the simulation,
- σ_{E_ν} $[m^2]$ respresents the total neutrino-nucleon cross-section,
- $\rho \cdot N_A$ $[m^{-3}]$ represents the total number of target nucleons per unit volume, where ρ is the target density,
- $P_{Earth}(E, \theta)$ is the probability for a neutrino with a given energy E and zentih θ_z to cross the Earth.

To obtain the number of neutrino events per year (for a given flux) generated as a function of the energy and zenith angle, we have to multiply the generation weight by the desired neutrino flux model:

$$\underbrace{\frac{dN(E_\nu, \theta_\nu)}{dt}}_{[\text{year}^{-1}]} = \underbrace{w_2}_{[\text{GeV}\cdot\text{m}^2\cdot\text{sr}\cdot\text{s}\cdot\text{year}^{-1}]} \cdot \underbrace{\phi(E_\nu, \theta_\nu)}_{[\text{GeV}^{-1}\cdot\text{m}^{-2}\cdot\text{sr}^{-1}\cdot\text{s}^{-1}]} , \tag{2.3}$$

In ANTARES the spectral index used goes from 1.1 up to 1.7 depending on the (anti-)neutrino flavour, interaction and energy range.

Atmospheric Muons

The vast majority of reconstructed events in the detector are due to atmospheric muons yield by the CR interactions with the upper atmosphere. Even though ANTARES gets advantage of the deep-sea water shielding effect, high energy muons can reach the vicinity of the detector constituting the main source of background. Even though only events reconstructed as upward-going are selected, a significant amount of misreconstructed atmospheric muons remains in the sample. Due to the almost constant and stable flux of atmospheric muons, these particles are useful to measure the evolution of the detector efficency with time, and are also used for time calibration purposes [111], as explained above.

In order to estimate accurately the final muon background contamination in the data sample, a full atmospheric muon simulation is done with the CORSIKA [117, 118] simulation package. This software allows for the generation of atmospheric showers, tracking all particles produced from the interaction point to the sea level. The simulation flexibility and the great amount of input parameters of CORSIKA comes at the cost of high computational time. All kinematics of the muon, such as the energy spectrum or the angular distribution, are described by CORSIKA. At sea level, muons from showers with energies larger than 500 GeV are transported to the detector using MUSIC [119], which is a 3-dimensional muon propagator

that accounts for the muon energy loss processes. The properties of the muons hitting the *Can* surface are registered for a posterior processing.

In addition to CORSIKA, another faster alternative for atmospheric muon simulation is used in ANTARES. This software is called MUPAGE [120], and is based on a set of parametric formulae which allows the fast production of a large number of Monte Carlo events at the *Can* surface, but lacks of the flexibility of CORSIKA in the definition of input parameters.

2.2.2 Particles and Light Propagation

The Cherenkov light induced by high-energy charged particles is simulated using a GEANT-based packaged, called KM3 [121]. Given the great number of photons yielded in these interactions, a full simulation of light emission and propagation is unaffordable. Instead, Cherenkov light is sampled from the so-called *photon tables* that store, depending on the event topology, positions, distances and orientations of the PMTs, the number of photons and their arrival time of PMT hits. These tables are previously generated from full photon simulation with GEANT [122].

2.2.3 DAQ Simulation

The final aim of the simulation chain is to transform the hits on the PMTs into a data stream with the same format and environmental conditions as real data. In order to achieve this goal, the optical background light emission (due to ^{40}K decays [104] and bioluminescence [123, 124] processes) has to be added to the total light produced by physics events. Moreover, the individual behaviour of the OMs can be affected by the environment, forcing an accurate reproduction of the data time evolution, which is achieved following the *run-by-run* strategy [112].

2.3 Event Reconstruction

Once the trigger algorithms have filtered the interesting events, the neutrino energy and direction have to be reconstructed from the hit information. In the following sections, the two main reconstruction algorithms for tracks used in ANTARES, called *AAFit* and *BBFit*, are described (see [125] for more details). The shower reconstruction algorithm is not treated here. The interested reader can check the reference [126] for a detailed description.

2.3.1 Direction Reconstruction

AAFit

The AAFit reconstruction strategy is a multistep fit based on a likelihood maximisation method [127]. The preliminary fits provide a starting point for the final likelihood maximisation.

1. **Hit selection:** Hits with charge higher than 3 p.e. and hits in local coincidence are selected. The local coincidence condition is defined as two or more hits on the same storey in a time window of 25 ns.
2. **Linear prefit:** The first fit is a linear fit through the positions of the hits. The hits are assumed to lie on the line of the muon track. The orientation of the PMT and the hit amplitude is used to estimate the distance of the muon track to each OM with a hit. This prefit gives an approximate reconstruction of the muon track, that serves as a starting point for the next steps.
3. **M-estimator:** After the prefit, the improvement in the accuracy on the angular resolution is achieved through an M-estimator fit. This fit is performed when at least 15 hits within a time window of $\pm$150 ns and at most 100 m away of the track are selected.
4. **Maximum likelihood:** The quality of the reconstructed tracks is measured following a maximum likelihood (ML) fit. The likelihood represents the probability of an event to belong to the given track, $P(\text{event} \mid \text{track})$, and is defined as follows:

$$\mathcal{L}(\vec{r},\vec{p}) \equiv P(\text{event} \mid \text{track}) = \prod_{i=1}^{N_{\text{hit}}} P\left(t_i|t_{\text{exp}},\vec{r},\vec{p}\right), \tag{2.4}$$

where the product runs over the number of hits, N_{hit}, and $P\left(t_i|t_{\text{exp}},\vec{r},\vec{p}\right)$ represents the probability of a hit with a measured arrival time t_i, to belong to the reconstructed track with the expected arrival time, t_{exp}, position, $\vec{r}$ and momentum, $\vec{p}$. This fit is repeated rotating and translating the initial prefit in order to find the global maximum. A final ML fit is performed in which the optical background is taken into account. Finally, the quality of the reconstruction is measured through the so-called Λ-parameter:

$$\Lambda = \frac{\log\mathcal{L}^{\max}}{N_{\text{hit}} - 5} + 0.1(N_{\text{comp}} - 1), \tag{2.5}$$

where $\mathcal{L}^{\max}$ is the maximum value of the likelihood, N_{hit} is the number of hits used in the reconstruction and N_{comp} is the number of iterations of the M-estimator and the maximum likelihood prefits. In addition, the angular error estimate of the track, β, can be derived from the errors on the azimuthal σ_ϕ, and zenith, angle σ_θ:

$$\beta = \sqrt{\sin^2(\theta_{rec})\sigma_\phi{}^2 + \sigma_\theta{}^2}. \tag{2.6}$$

Figure 2.7 shows that, for events reconstructed as upgoing, the Λ and β parameters can be used efficiently to distinguish misreconstructed atmospheric muons from neutrinos.

ANTARES achieves a muon track angular resolution better than 0.4° for neutrino energies above 10 TeV (Fig. 2.8).

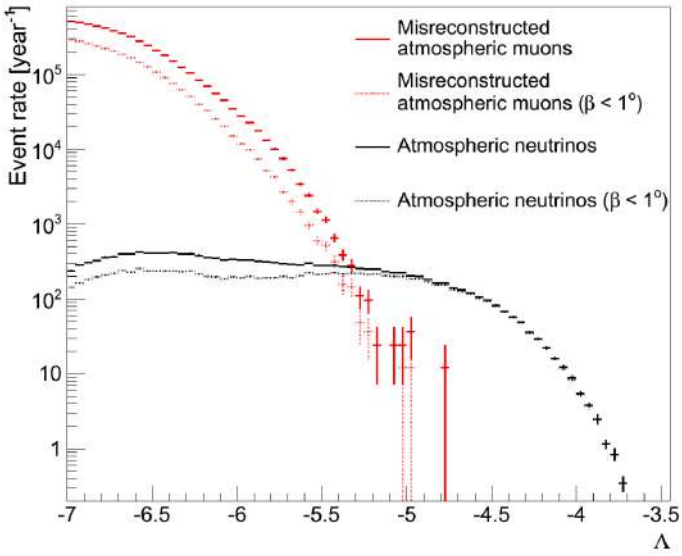

Figure 2.7: Λ-parameter distribution for events reconstructed as upgoing. Atmospheric neutrinos are shown in black, while misreconstructed atmospheric muons are in red. The effect of the β parameter selection is also shown. From [125].

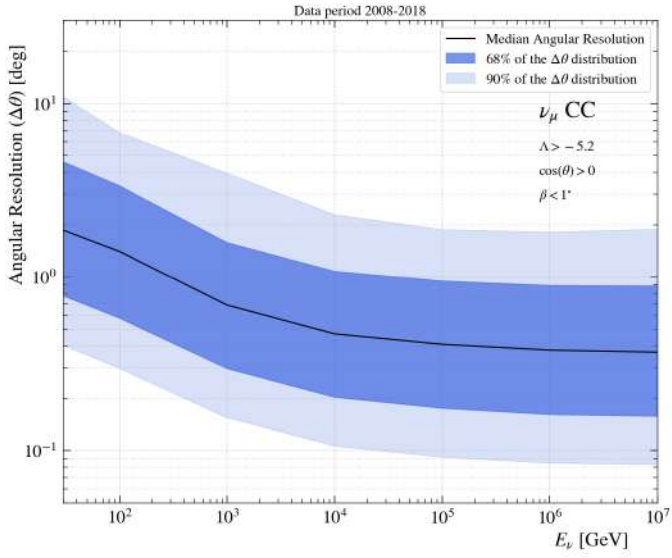

Figure 2.8: ANTARES median angular resolution for a muon track as function of the neutrino energy, for upward-goin events with $\Lambda > -5.2$, $\beta < 1^\circ$ parameters.

BBFit

The BBFit strategy provides a factor 10 of improvement in computational time in comparison with AAFit without losing robustness [127, 128]. Given its speed for the reconstruction, BBFit is used in online triggering follow-up observations among other multimessenger studies.

In order to achieve the reconstruction speed needed for real-time applications, BBFit considers only the time and position information of the hits, resulting in a simplified geometry. The approximations made are:

- Detector lines are considered to be completely vertical. Sea currents effects on the position of the lines are ignored.
- Each storey is considered as one single OM located directly on the detector line. Hence, signals within a time window of 20 ns coming from different OMs in the same storey are combined.
- The muon track is assumed to be a straight line, so multiple scattering are neglected.

As in the previous method, the reconstruction starts with a hit selection, whose objective is to select only the hits coming from the Cherenkov radiation and to avoid the hits from background optical photons. Only events with at least 5 hits within a 20 ns time window are selected for the subsequent fit. After the selection, photons are projected on the muon track in order to find the initial and last emission point. The fit procedure can be multi-line, if the selection occurs in different detection lines, or single-line if only one line is involved. The fit function is based on a χ^2 minimisation, function of the difference between the expected and the measured arrival time of the hits. A quality parameter, $\mathcal{Q}$, for selecting good reconstructed events can be defined using this minimisation:

$$\mathcal{Q} = \frac{\chi^2}{N_{\text{hit}} - N_{\text{par}}}, \tag{2.7}$$

where N_{hit} is the number of hits used in the reconstruction, and N_{par} is the number of fitted parameters. The median angular resolutions achieved by ANTARES, in the 20 GeV energy regime, is 3° for single-line and 0.8° for multi-line events [129].

2.3.2 Energy Reconstruction

The energy is the other essential parameter that needs to be determined to reconstruct the event. In ANTARES, several energy estimators can be used, but the dE/dx and the ANNenergy estimator are the most commonly used (see [130] for more details).

The dE/dx estimator is based on the total muon energy loss mechanism [11], which is parameterized as follows:

$$-\frac{dE_\mu}{dx} = a(E_\mu) + b(E_\mu)E_\mu, \tag{2.8}$$

where $-\frac{dE_\mu}{dx}$ represents the total muon energy loss per amount of matter traversed, $a(E_\mu)$ is the ionization energy loss, which dominates for muon energies below several hundreds of GeV, and $b(E_\mu)$ is the sum of the radiation contributions such as e^+e^- pair production, bremsstrahlung, and photonuclear contributions [11].

In order to determine the muon energy loss, the dE/dX estimator uses the total number of photons created by the muon. The total energy loss is approximated by ρ, which is defined as:

$$\frac{dE_\mu}{dx} \sim \rho = \frac{\sum_{i=1}^{N_{\text{hit}}} a_i}{L_\mu \epsilon}, \tag{2.9}$$

where N_{hit} is the number of hits used for the reconstruction of the track, L_μ is the muon path length in the detector, and ϵ is a correction factor for the detector efficiency, which is a function of the distances between the actives PMTs and the reconstructed muon track, and takes into account the angular acceptance of the OMs. The obtained value of ρ is converted to energy estimates through calibration tables created from MC simulations [125, 130].

On the other hand, the ANNenergy estimator [130] uses an Artificial Neural Network (ANN) to derive the dependence between a set of observables and the energy estimate. The ANNenergy parameter can be seen as a representation of the PDF describing the relation between the different observables and the energy estimation [125].

3 Solar Atmospheric Neutrino Searches with ANTARES

"Protons give an atom its identity, electrons its personality."

Bill Bryson

The Sun is the central body and the main energy source of our solar system. Due to its proximity to the Earth, the Sun is a perfect candidate for studying a variaty of processes (magnetohydrodynamic effects, plasma physics, dark matter searches, neutrino searches) from different perspectives. The structure of this chapter is as follows: in section 3.1, the strcuture of Sun as well as their main processes for energy production are described. Section 3.2 and 3.3 describes the study of solar neutrinos and its historical importance in the neutrino oscillation problem. Finally, section 3.4 describes the solar atmospheric neutrino search performed with the ANTARES neutrino telescope, and its results are highlighted.

3.1 The Sun

The Sun is our nearest star, but otherwise it represents a fairly typical star in our galaxy, classified as G2-Vspectral type, with a radius of $r_\odot \approx 700\,000$ km, a mass of $M_\odot \approx 2 \times 10^{30}$ kg, a luminosity of $L_\odot \approx 3.8 \times 10^{26}$ W, and an age $t_\odot \approx 4.6 \times 10^9$ years. The distance from the Sun to the Earth is called an Astronomical Unit (AU) and amounts to $\sim$150 $\times 10^6$ km. The Sun lies in a spiral arm of our galaxy, the Milky Way, at a distance of 8.5 kiloparsecs from the Galactic Center.

The basic structure of the Sun is sketched in Fig. 3.1. The Sun and the solar system were formed together from an interstellar cloud of molecular hydrogen some 5 billion years ago. After gravitational contraction and subsequent collapse, the central object became the Sun, with a central temperature hot enough to ignite thermonuclear reactions, the ultimate source of energy for the entire solar system. The chemical composition of the Sun is of 92.1% hydrogen and 7.8% helium by number (or 27.4% He by mass), and 0.1% of heavier elements (or 1.9% by mass, mostly C, N, O, Ne, Mg, Si, S, Fe). The central core, where hydrogen burns into helium, has a temperature of $\sim$15 million K (Fig. 3.1). The solar interior further consists of a radiative zone, where energy is transported mainly by radiative diffusion, a process where photons with hard X-ray (keV) energies get scattered, absorbed, and reemitted. The outer one-third of the solar interior is called the

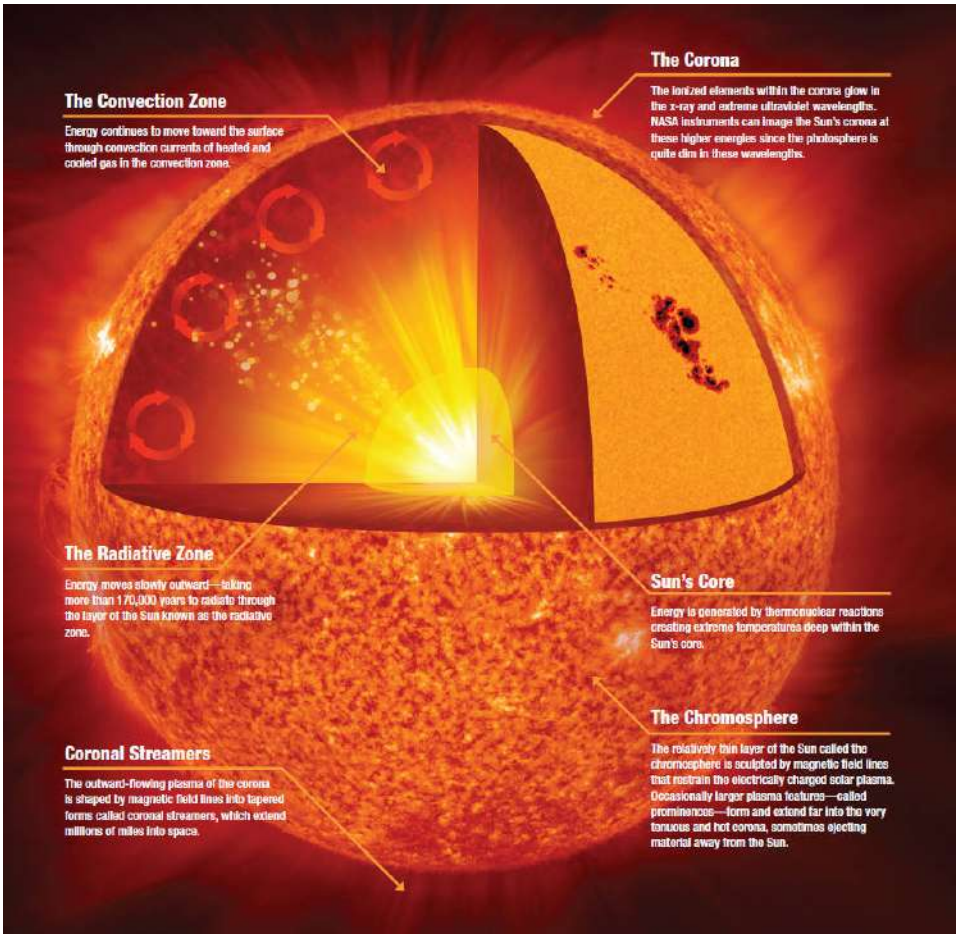

Figure 3.1: Image of the Sun with cut-away portion showing the solar interior. Credit: NASA/Jenny Mottar.

convective zone, where energy is transported mostly by convection. At the solar surface, photons leave the Sun in optical wavelengths, with an energy that is about a factor of 10^5 lower than the original hard X-ray photons generated in the nuclear core, after a random walk of $\sim 10^5 - 10^6$ years [131].

3.1.1 The Standard Solar Model

The Standard Solar Model (SSM) reproduces the thermodynamical profiles of the present Sun together with all the useful observables. This model results solving the stellar evolution equations from the contraction of the Sun up to the present age. This model is a reference in Astrophysics, because it is useful for establishing the chemical evolution of the galaxy through helium and oxygen evolution and

for validating the physics which relies stellar evolution to cosmology through the age of globular clusters [132].

The SSM satisfies the structural equations of stellar evolution applied to any star. These equations describe the hydrostatic equilibrium, the conservation of mass and energy and the transport of energy by photons in the radiative zone and by convective motions in the more external layers [132].

The solar structure can be splitted into different regions:

- **Solar Core and Radiative zone.** The solar core is the innermost part of the Sun. In this region, at a temperature about 15 million K, the hydrogen is fused into helium. The energy released in this process is transported, mainly, as high energy photons through the so-called *radiative zone* [133]. In this process, apart from photons, neutrinos are emitted as fusion products of the $p - p$ fusion chain [134].
- **Convenction zone.** The convection zone is the outtermost region of the solar interior, extending from about 200 000 km depth up to the visible surface and with a temperature of about 2 million K. In this region the energy is transported mainly by convective movements between the heated and cooled plasma [133].
- **Photosphere.** The photosphere [135] is the innermost part of the solar atmosphere and constitutes a thin layer of partially ionized plasma at the solar surface with a temperature $T = 6400$ K. It is defined as the range of heights from which photons directly escape the solar medium.
- **Chromosphere.** The chromosphere is the lowest part of the solar atmosphere, extending to an average height of $\sim$2000 km above the photosphere [136]. According to hydrostatic standard models assuming local thermal equilibrium, the temperature reaches a minimum of $T = 4300$ K at a height of $h \approx 500$ km above the photosphere and rises suddenly to $\sim$10 000 K in the upper chromosphere at $h \approx 2\,000$ km. However, these models neglect the magnetic field, the inhomogeneities, and dynamic processes among other effects [131].
- **Corona.** The solar corona is an extremely hot (10^6 K or about 0.1 keV), almost fully ionised plasma which extends from a few thousand km above the photosphere to where it freely expands into the Solar System as solar wind [133, 137, 138].

3.2 Solar Neutrinos

Neutrinos in the Sun are produced by several reactions, each giving rise to a characteristic energy distribution, or spectrum. Figure 3.2 illustrates the contributions of different reactions to the solar neutrino spectrum. All neutrinos produced in these cycles are created in the electron flavour. Observation of these neutrinos can offer insights into both the Sun, and into neutrino properties.

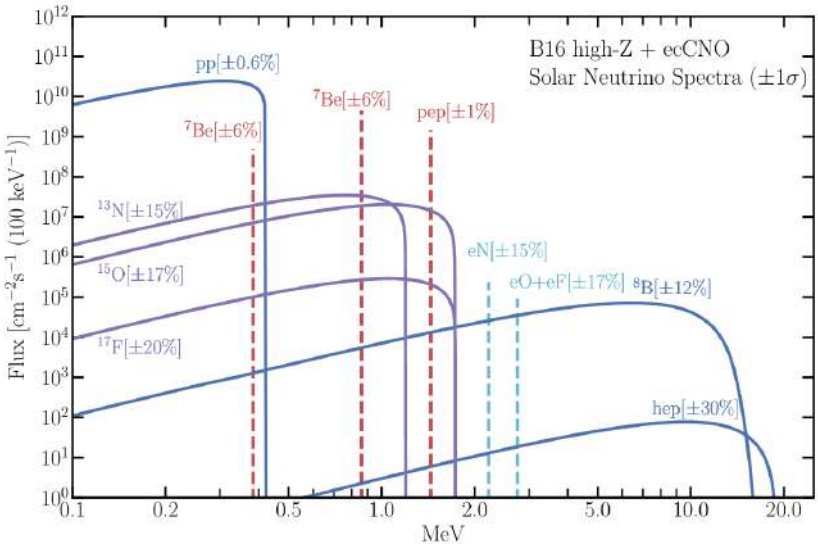

Figure 3.2: Spectrum of neutrino fluxes from different nuclear reactions. From [139].

The idea of B. Pontecorvo of using the nuclear reaction $^{37}Cl \rightarrow {}^{37}Ar$ to capture neutrinos developed in the successful Homestake experiment with the first observation of solar neutrinos [55]. This experiment found a deficit on the neutrino flux, detecting only 1/3 of the expected signal. Similar experiments (GALLEX [140], GNO [141] and SAGE [142]) aiming at the same objective were performed, each of which showed a deficit in the observed neutrino flux.

An independent research performed, around a similar time, by the water Cherenkov experiment Kamiokande confirmed the deficit in the solar neutrino flux [143, 144]. This effect was known as the *solar neutrino problem*. Among the different proposed solutions, the favoured one was the neutrino oscillation. Due to the pattern of fluxes across these experiments, a new generation of projects arose with the main goal of solving the solar neutrino problem. Sudbury Neutrino Observatory (SNO) was built to resolve the solar neutrino problem [145, 146]. Based on heavy water (D_2O), this experiment allowed the NC and CC neutrino interactions for their detection. This allowed the SNO collaboration to detect both the pure electron flavour (via CC) and the total flux (via NC) of solar neutrinos, thus demonstrating that the measured total solar flux agrees with solar model calculations [147, 148], and that the deficit is due to the change of neutrino flavour [139].

3.3 Solar Atmospheric Neutrinos

Cosmic-rays (CRs) entering the solar atmosphere undergo hadronic interactions and produce secondary particles, such as charged pions and kaons. These secondary particles can then decay into neutrinos, the so-called Solar Atmospheric

Neutrinos (SAνs). The process is similar to the production of Earth Atmospheric Neutrinos (EAνs) [149]. Nonetheless, there are differences between the neutrino production in solar and terrestrial air showers. First, since the region of the solar atmosphere where the neutrino production occurs is less dense and further extended that its terrestrial analogue, the high-energy hadrons decay before being absorbed (longer decay lenghts). This reduces the suppression of the high-energy neutrino flux observed in the atmosphere of the Earth. Second, due to the extension and density of the solar core respect to the Earth, more high-energy neutrinos interact and are lost when propagating through it. Finally, since the path lenghts in the atmosphere of the Sun are long enough, high-energy muons decay and produce a substantial contribution to the flux of solar atmospheric neutrinos. On the other hand, the terrestrial air showers are stopped abruptly in the crust of the Earth [150, 151].

Solar magnetic fields also affect the SAν contribution from CR interactions. At low energies, CRs reaching the solar atmosphere can modify their trajectory, not penetrate enough into the solar atmosphere or even been mirrored. At higher energies (>200 GeV) the particles are rigid enough that the magnetic effects can be neglected. These effects were modeled by Seckel, Stanev and Gaisser (SSG1991) [152].

The resulting flux of neutrinos from CR interactions with the solar atmosphere is called the *conventional* flux and has an approximate flavour ratio of $\{\nu_e : \nu_\mu : \nu_\tau\} = \{1 : 2 : 0\}$ at production. However, after propagation to the Earth, the flavour ratio of the neutrino flux is $\{1 : 1 : 1\}$ [33, 153]. Apart from the conventional neutrino flux, there is a contribution to the neutrino flux called the *prompt* flux. This is induced by decays of charmed mesons such as D^0 and $D^\pm$. Due to the higher masses and shorter lifetimes of these mesons, the prompt flux is mainly important at higher energies, where the conventional flux falls off faster with energy due to energy losses of the long-lived pions and kaons [33].

SAνs have been studied over the years [33, 152–155]. D. Seckle [152] and G. Ingelman [154] give three main motivations to study SAνs. First, the detection of SAνs can give indirect information about the primary cosmic-ray composition, the propagation of charged particles in the solar medium and, consequently, help the scientific community to understand the density and chemical structure of the Sun. Second, these neutrinos could be used as a *standard neutrino flux* for detector calibration [154]. Third, SAνs represent an unavoidable background source for solar DM indirect searches [33, 151]. Even though the sensitivity of current experiments has not been able yet to determine the intensity of their flux, the detection of SAνs would allow for the characterisation of this potential background. The new generation of neutrino telescopes is a promising oportunity for SAν detection [152].

3.4 Search for SAνs with ANTARES

In this analysis, two different CR models are tested: the *Hillas-Gaisser 3-generation model (H3a)* [156] and the *Gaisser-Stanev-Tilav 4-generation model (GST4)* [157]. In the *H3a* model, three different populations of CRs are assumed, one extragalactic component that starts to contribute to the spectrum at the ankle and two galactic components below the ankle. The *GST4* model assumes four populations, two of galactic origin and two extragalactic, the fourth one consisting of purely protons included to make the CR composition less heavy at the highest energies.

The Sun is modeled using the Standard Solar Model (SSM) for the interior of the Sun, and the *Ser+Stein* [158] and the *Grevesse & Sauval* (refered as *Ser+GS98*) solar density profiles models [159] for the region close to the solar surface. These density profile models consist of different magnetohydrodynamic simulations assuming different chemical compositions for the Sun.

These models for the CR as well as for the composition of the Sun are included within the *WimpSim 5.0* simulation package [160, 161]. Within the simulation, solar magnetic fields are not taken into account, and neutrino oscillations parameters from world best-fit values [162] and normal mass ordering parameters [11] are assumed to be:

- $\theta_{12} = 33.56^\circ$, $\theta_{13} = 8.46^\circ$, $\theta_{23} = 416^\circ$,
- $\delta = 261^\circ$,
- $\Delta m^2_{21} = 7.5 \times 10^{-5}$ eV^2 and $\Delta m^2_{31} = 2.524 \times 10^{-3}$ eV^2.

In addition, the spatial distribution of the incoming neutrinos are simulated following three different shapes for the Sun (see figure 3.3):

1. **Point-like**, i.e. SAνs are emitted from a single point in the sky.
2. **Filled disk shape**, neutrinos are produced uniformly from a disk source of 0.27° radius (the diameter of the Sun seen from the Earth is of about 0.53°).
3. **Ring-shaped**, the outcoming neutrinos are yielded only on the surface of the Sun (inner radius of 0.26° and outer radius of 0.27°).

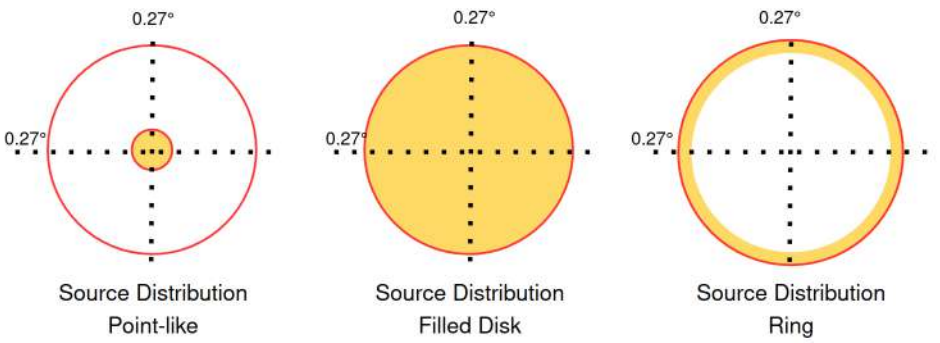

Figure 3.3: Sun shapes used for simulating the source of neutrinos. The red circle shows the solar extension as seen from the Earth. The coloured surface indicates the extension of the Sun in each scenario.

The signal consists of ν_μ CC simulated events, weighted by the SAν energy spectra. Fig. 3.4 shows the signal spectra corresponding to the four tested models, alongside the Honda atmospheric neutrino flux [163]. The Honda flux dominates for neutrino energies below ∼40 GeV, while the SAν flux prevails for $E_\nu \gtrsim 40$ GeV. Despite the fact that the SAν and conventional atmospheric neutrino fluxes are comparable, the difference between the solar solid angle (for the signal) and the *all-sky* solid angle (for the background) reduces the conventional atmospheric neutrino rate at the detector by a factor $\Omega_\odot/4\pi \simeq 5.4 \times 10^{-6}$. Finally, the considered *reference scenario*[1] in this analysis includes the *H3a* CR model with the *Ser+Stein* solar density profile, and considers the Sun as a *point source*. The results obtained with this refenrece scenario will be compared with the results obtained with other assumptions on what the Solar models are concerned.

The dataset used for the analysis consists of 3022 days of lifetime of data recorded by the ANTARES detector from 2008 to 2018 (both years included). The event selection criteria employed in this analysis (described in Sec. 3.4.1) is based on the minimization of an scale factor, C_{90} (see Sec. 3.4.2), for which the computation of the sensitivity to SAνs signal from ν_μ and $\bar{\nu}_\mu$ CC interactions is needed. The reconstruction algorithm used for this analysis is AAFit (see section 2.3.1).

[1] In this thesis the *reference model/scenario* and *baseline model/scenario* are used interchangeably to refer to the main model used in the analysis.

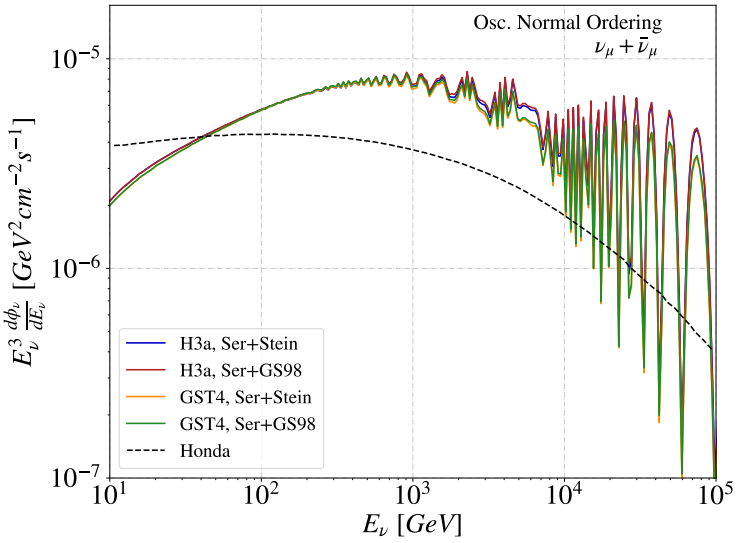

Figure 3.4: Muon neutrino energy fluxes ($\times E^3$), from the four different models tested in this work, after neutrino propagation, at the Earth position (color lines). Normal ordering and neutrino oscillations parameters from the world best-fit values are assumed. The Honda flux for Earth atmospheric muon neutrinos is shown for comparison (black dashed line) [163]. Fluxes are integrated over the solar solid angle $\Omega_\odot \simeq 6.8 \times 10^{-5}$ sr.

3.4.1 Event Selection

Pre-selection cuts

The SAνs analysis is performed with *runs* and events which pass the standard ANTARES quality cuts, which exclude runs taken in bad detector environmental conditions or clear missreconstructed events. Then, the reconstructed parameters of each event (energy, direction, quality of reconstructions, number of hits, etc.) are used to optimize the signal and background separation. The Monte Carlo and data comparison plots and the analysis cuts described below, are obtained by analysing only 10% of the total recorded statistics, folllowing the ANTARES data blinding rules.

The variables of interest in this analysis are (see Sec. 2.3 for further details):

- **Quality cuts.** Fig. 3.5 (top) shows how atmospheric muons dominate for lower values of the the quality reconstruction parameter Λ. A value of $\Lambda > -5.2$ is applied in order to reduce the atmospheric muon contamination without reducing the number of neutrinos. Muon contamination can be further reduced if the error estimate on the angular reconstruction (β) is constrained. To achieve that, a preliminary cut at $\beta < 1.5^\circ$ is set. Fig. 3.6

shows the event distribution as function of β parameter before (top) and after (bottom) applying the $\Lambda > -5.2$ cut.

- **Direction cut.** Atmospheric muons dominate the downward-going contribution. Particles reconstructed as upward-going are chosen with $\cos(\theta) > 0$, where θ is the reconstructed zenith angle. This cut reduces drasticaly the muon contamination in our sample. However, some of the atmospheric muon background remains in the sample misreconstructed as upward-going. Fig. 3.7 shows how the muon contribution is reduced as the event is reconstructed more vertically ($\cos(\theta) = 1$) before (top) and after (bottom) applying the $\Lambda > -5.2$ cut.
- **Muon track length cut.** High energy muons leave long tracks in the detector vicinity. In order to reject low energy muons, a cut in the reconstructed track length ($\mu_{\text{track length}}$) is imposed.

After a first data exploration, the *pre-selection* cuts chosen that allow a correct visualization and variable inspection are: $\Lambda > -6$, $\beta < 1.5^\circ$, $\cos(\theta) > -0.1$ and $\mu_{\text{track length}} > 380$ m. These cuts work as an initial event filter that will allow an *a posteriori* fine tuning of the selection parameters in order to minimize the C_{90} parameter.

The final set of pre-selected values for the event selection parameters are the following: $\Lambda \in [-5.2, -5.0, -4.8]$ and $\beta \in [1.0^\circ, 0.9^\circ, 0.8^\circ]$, with a fixed value of $\cos(\theta) > 0$ to select upward-going events and a cut on the muon track lenght of $\mu_{\text{track length}} > 380$ m. Among the three pre-selected values of Λ and β, the final ones will be chosen through the optimization of the scale factor C_{90}, for which both, the expected number of signal events and the detector sensitivity to the SAν signal are needed, as described in Sec. 3.4.2 and 3.4.3.

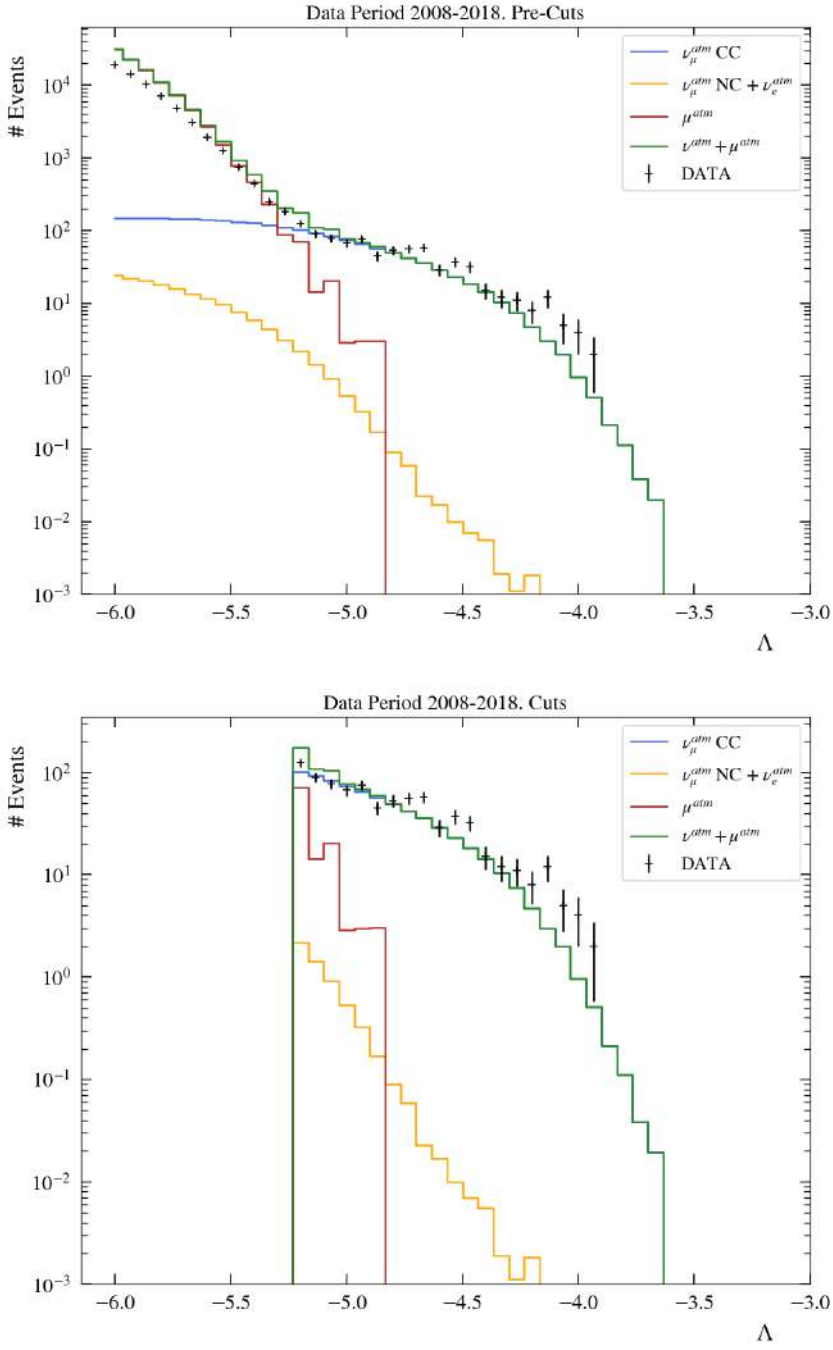

Figure 3.5: Data/Monte Carlo event distribution as function of the Λ parameter of the ANTARES data for the period 2008–2018. Atmopsheric neutrinos are plotted: ν_μ CC (blue), ν_e CC and ν NC (yellow). Atmospheric muons (red) and the sum of all contributions (green) is shown alongside the data (black dots). Cuts applied: $\beta < 1.5°$, $\cos(\theta) > -0.1$ and $\Lambda > -6$ (top), $\Lambda > -5.2$ (bottom).

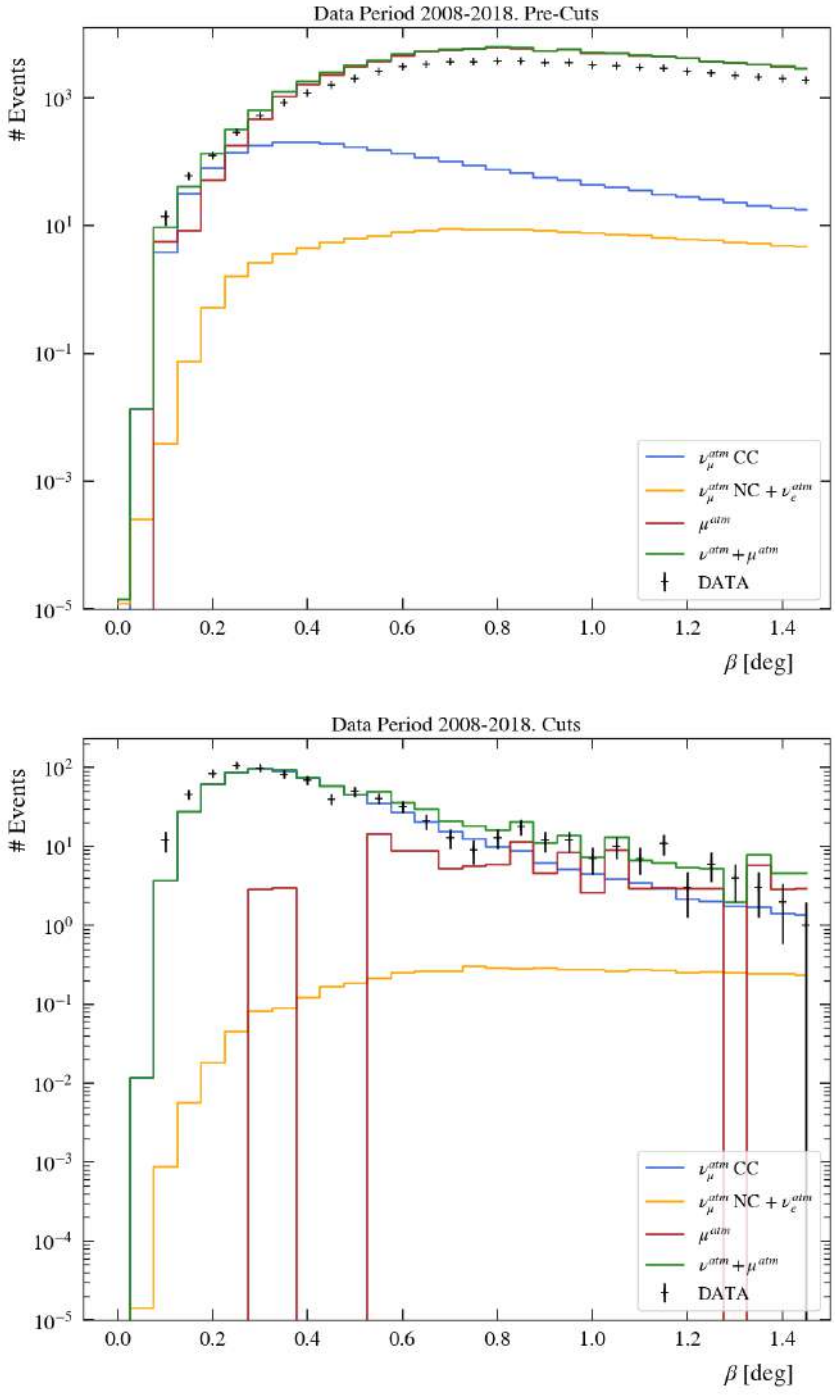

Figure 3.6: Data/Monte Carlo event distribution as function of the β parameter of the ANTARES data for the period 2008–2018. Atmopsheric neutrinos are plotted: ν_μ CC (blue), ν_e CC and ν NC (yellow). Atmospheric muons (red) and the sum of all contributions (green) is shown alongside the data (black dots). Cuts applied: $\beta < 1.5°$, $\cos(\theta) > -0.1$ and $\Lambda > -6$ (top), $\Lambda > -5.2$ (bottom).

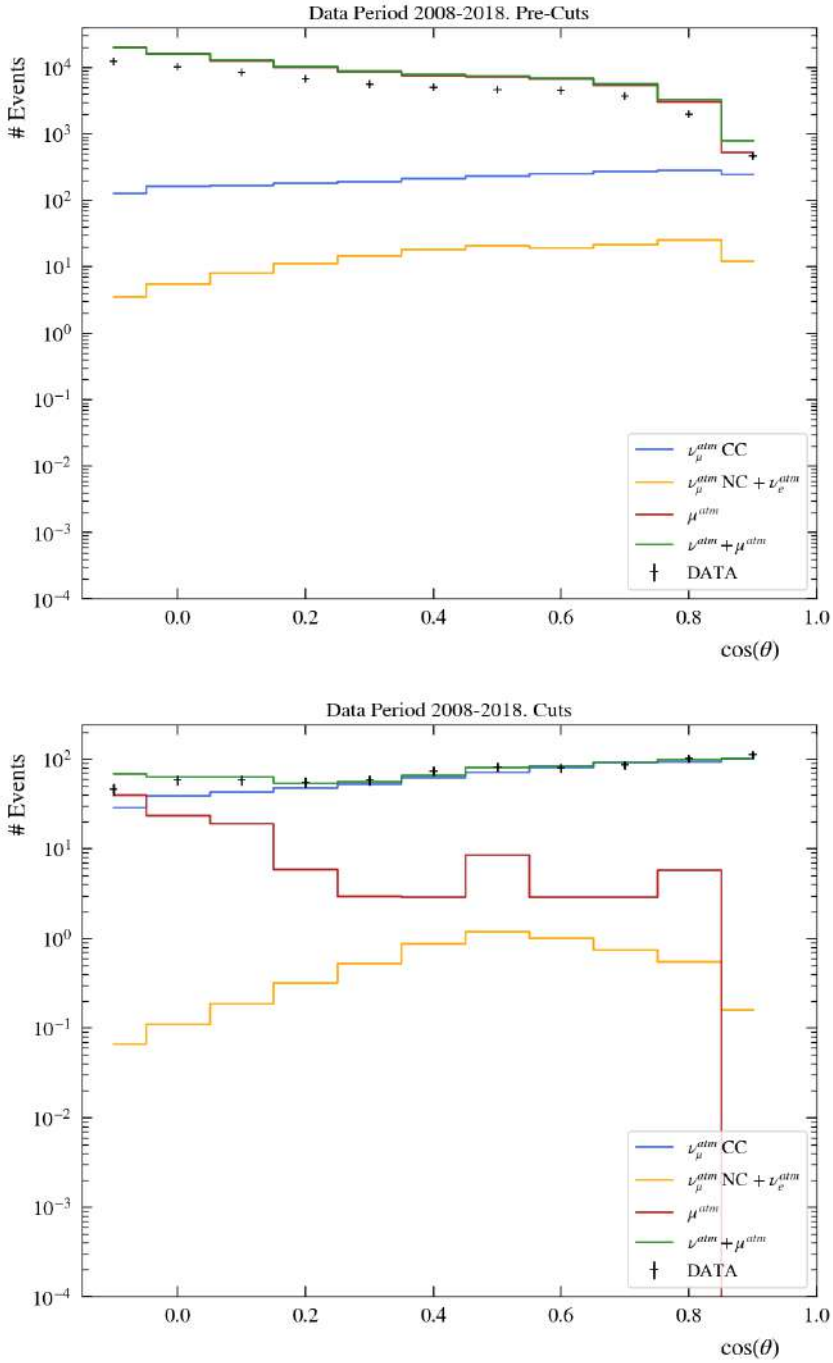

Figure 3.7: Data/Monte Carlo event distribution as function of the $\cos(\theta)$ parameter of the ANTARES data for the period 2008–2018. Atmopsheric neutrinos are plotted: ν_μ CC (blue), ν_e CC and ν NC (yellow). Atmospheric muons (red) and the sum of all contributions (green) is shown alongside the data (black dots). Cuts applied: $\beta < 1.5°$, $\cos(\theta) > -0.1$ and $\Lambda > -6$ (top), $\Lambda > -5.2$ (bottom).

3.4.2 Analysis

The main goal of the analysis is to search for an excess of SAνs over the expected background. In case of null observation, an upper limit in the SAν flux will be computed. In this study, the final values of the selection cuts are such that minimize the scale factor C_{90}. As described below, this needs the computation of the sensitivity of the ANTARES detector to a specific SAνs flux model. The analysis is based in the maximisation of an extended likelihood function. But before, some other quantities involved in the calculations have to be defined.

Effective Area

The effective area, expressed in m^2, is the equivalent surface of the detector to a given energy flux. This is a parameter that can only be determined through simulations. For a neutrino telescope such as ANTARES, the effective area to a specific neutrino flux is:

$$A_{\text{eff}}(E_\nu, \theta_\nu, \phi_\nu) = \frac{N_{\text{sel}}(E_\nu, \theta_\nu, \phi_\nu)}{N_{\text{gen}}(E_\nu, \theta_\nu, \phi_\nu)} \cdot V_{\text{gen}} \cdot \rho N_{\text{A}} \cdot \sigma(E_\nu) \cdot P_{Earth}(\theta_\nu, \phi_\nu), \tag{3.1}$$

where N_{sel} is the number of simulated events that are selected after reconstruction, triggering and quality selection, N_{gen} is the number of events generated in the simulations for a specific energy, zenith and azimuth angles, V_{gen} is the generation volume, ρN_{A} is the matter density times the Avogadro's number, $\sigma(E_\nu)$ is the neutrino cross-section at that energy, and P_{Earth} is the probability of absorption for a neutrino crossing the Earth (Eq. 2.1). In practice, this is done using a weight created with the simulation that encloses most of these parameters (see Eq. 2.2 and Sec. 2.2.1 for a more detailed description):

$$w_2 = V_{gen} \cdot F \cdot I_\theta \cdot I_E \cdot E^\gamma \cdot \sigma(E_\nu) \cdot \rho \cdot N_A \cdot P_{Earth}. \tag{3.2}$$

After some algebra, the final expression for the effective area for an energy bin $[E_m, E_M]$ becomes:

$$A_{\text{eff}}(E_\nu) = \frac{N_{\text{sel}}(E_\nu)}{k(E_M^{1-\gamma} - E_m^{1-\gamma})} \cdot \frac{w_2(1-\gamma)}{F \cdot I_\theta \cdot E^\gamma}, \tag{3.3}$$

where k is the full number of generated events, E_m and E_M represent the energy of the lower and upper bound of the bin, respectively. Since the events we are interested in come from the direction of the Sun, the Sun tracking effect is taken into account by weighting the selected events N_{sel} by the probability of this event to arrive from the solar path. Fig. 3.8 shows the solar path, in zenithal and azimuthal

coordinates, as seen from the ANTARES site. The blue curve represents the fraction of time (normalized to unity) that the Sun is in the i-th angular bin ($\theta_{\text{zenith},i}$, $\phi_{\text{azimuth},i}$). The horizon is at $\theta_{\text{zenith}} = 90^\circ$, and is represented by the dot-dashed line.

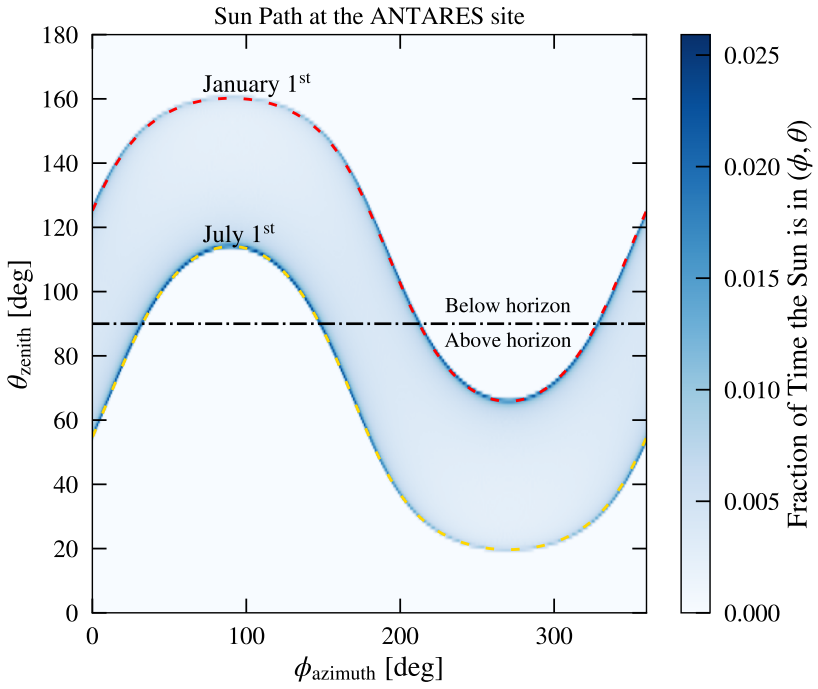

Figure 3.8: Solar path for the 2008 – 2018 period as seen from the ANTARES site. The red (yellow) dashed line shows the solar path on January (July) 1st , as a reference.

Fig. 3.9 shows the effect on the effective area for different combinations of the quality parameters Λ and β. The effect of variying the β parameter is negligible, however, the Λ parameter has a visible effect at high neutrino energies, because more events are selected when loosening the cut in Λ.

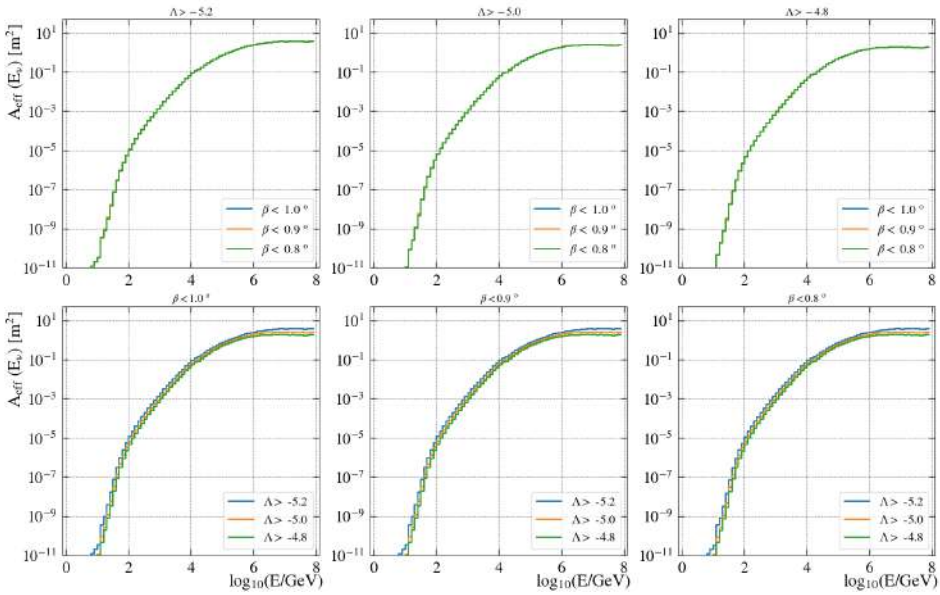

Figure 3.9: ANTARES upward-going ν_μ effective area comparison for different cuts on the quality parameters Λ and β as a function of the neutrino energy. Top plots show the effect of different β values for a fixed Λ, bottom plots show the effect of different Λ values for fixed β.

Likelihood function

The extended maximum likelihood (EML) [164] differs from the standard maximum likelihood (SML) in the normalization of the probability density function (PDF). The normalization in the EML can vary, while in the SML is fixed (usually to unity). Let us consider an experiment with a generic variable or set of variables x, consisting on a set of measurements, $\vec{x} = \{x_1, \ldots, x_N\}$, where x_i is a registered event of the experiment. Then, for SML, the likelihood function is maximized for a number N of measurements $\vec{x}$ as:

$$\mathcal{L} = \prod_{i=1}^{N} p\left(x_i; a_1, \ldots, a_m\right). \tag{3.4}$$

The aim of this process is to maximize $\mathcal{L}$ by variying the set of unknow parameters $a_1, \ldots, a_m$ where $p\left(x_i; a_1, \ldots, a_m\right)$ is the PDF of the sampling variable x. Given that the measurement is trusted to yield a result, the PDF has to be normalized to unity:

$$\int p\left(x_i; a_1, \ldots, a_m\right) dx = 1. \tag{3.5}$$

In the case of the EML, the probability density is replaced by a PDF with an unconstrained normalization:

$$\int P\left(x_i; a_1, \ldots, a_m\right) dx = \mathcal{N}\left(a_1, \ldots, a_m\right). \tag{3.6}$$

The interpretation of this is that $P\left(x_i; a_1, \ldots, a_m\right)$ not only describes the expected shape of the x distribution, but also its size. Events occur at random in the range of x, governed by Poisson statistics, and $P(x)\delta x$ gives the number of events expected in the interval x to $x + \delta x$. Then, $\mathcal{N}$ is the total number of events expected over the whole range of observations, which might differ from the observed number of events, N, due to the fluctuations of Poisson statistics [164].

Nonetheless, the effect on the likelihood function by replacing the normalized $p\left(x\right)$ by the unnormalized $P\left(x\right)$ is not obvious as the maximisation process will tend to make the normalisation large. To remedy this, the likelihood for a particular set of data $\{x_1, \ldots, x_N\}$ must containt the information that the event observed at x_i cannot be observed anywhere else [164, 165]. To achieve this, the range of parameters x_i is divided into narrow bins of width Δx, so small that the probability of a bin containing more than one event is negligible. The probability of detecting 0 (Eq. 3.7) or 1 (Eq. 3.8) event in a bin is governed by Poisson statistics:

$$P_0(x) = e^{-\Delta x \cdot P(x)}, \tag{3.7}$$

$$P_1(x) = \Delta x \cdot P(x) \cdot e^{-\Delta x \cdot P(x)}. \tag{3.8}$$

The extended likelihood $\mathcal{L}$ for the complete range of x then is the product of all individual probabilities:

$$\mathcal{L} = \prod_i^N \Delta x \cdot P(x_i) \prod_j^{N_{\text{bins}}} e^{-\Delta x \cdot P(x)}, \tag{3.9}$$

where the first i–product iterates over all bins containing an event, and the j–product over all bins, being N_{bins} the number of intervals of x. Then, in the limit $\Delta x \to dx$, the first term becomes the probability density to find an event between $x + dx$, with the form $\prod_i P(x_i) d^N x$, which is analogous to Eq. 3.5. The second term becomes:

$$e^{-\sum_j \Delta x \cdot P(x_j)} \to e^{-\int P(x) dx} = e^{-\mathcal{N}}. \tag{3.10}$$

Thus, the extended likelihood is given by:

$$\mathcal{L} = \left[\prod_{i=1}^N P(x_i)\right] e^{-\mathcal{N}}, \tag{3.11}$$

$$\ln \mathcal{L} = \sum_{i=1}^{N} \ln P(x_i) - \mathcal{N}. \tag{3.12}$$

The increment of the normalization $\mathcal{N}$ also increases the $\mathcal{L}$ through the first term, but will decrease it through the second. The normalization factor can be splitted in the expected number of signal and background events $\mathcal{N} = n_s + n_b$. The probability distribution can also be splitted into a signal and background contribution $P(x) = n_s\mathcal{S}(x) + n_b\mathcal{B}(x)$. Including these changes in Eq. 3.12 results in:

$$\ln \mathcal{L} = \sum_{i=1}^{N} \ln \left[n_s\mathcal{S}(x_i;\vec{a}) + n_b\mathcal{B}(x_i;\vec{a}) \right] - \left[n_s + n_b \right]. \tag{3.13}$$

The PDFs that represent the behaviour of the signal ($\mathcal{S}$) and the background ($\mathcal{B}$) are so-called *ingredients*. In this analysis, both PDFs are built using the information of the direction of the particles ($\Psi_\odot$[2]), its energy estimator (N_{hits}) and its error estimate on the reconstructed angle (β). So, the final form of the likelihood function for this analysis is shown in Eq. 3.14, where n_s is the parameter to fit.

$$\ln \mathcal{L}(n_s) = \sum_{i=1}^{N} \ln \left[n_s\mathcal{S}(\Psi_{\odot,i}, \beta_i, N_{\text{hits},i}) + n_b\mathcal{B}(\Psi_{\odot,i}, \beta_i, N_{\text{hits},i}) \right] - \left[n_s + n_b \right]. \tag{3.14}$$

Ingredients

The *ingredients* are histograms that describe the statistical behaviour of signal and background [165]. These PDFs are built from MC simulation weighted by the SAν energy spectra for the signal, and from scrambled data[3] for background. The main ingredient in this analysis is the angular distance of the reconstructed event to the Sun ($\Psi_\odot$), which is also refered to as the *Point Spread Function* (PSF). The PSF is defined as the probability density of $\Psi_\odot$ per solid angle Ω:

$$P(\Psi) = \frac{dP}{d\Omega} = \frac{d\Psi}{d\Omega}\frac{dP}{d\Psi} = \frac{1}{2\pi\sin(\Psi)}\frac{dP}{d\Psi}. \tag{3.15}$$

Apart from the PSF, other PDFs based on the energy estimator and the error estimate on the reconstructed angle are built. In this analysis, independence between these PDFs is assumed, leaving the PDF for signal and background as a product between a 1-dimensional and 2-dimensional PDFs: $P(\Psi_\odot) \cdot P(\beta, N_{\text{hits}})$. Even though this independence is not necessarily true, this is done to avoid numerical zeros or *holes* in the PDF, that can ruin the minimization. These distributions depend on the quality parameters (Λ, β, ...), as well as on the theoretical flux

[2] Ψ and $\Psi_\odot$ are used interchangeably throughout the text.

[3] The *data scrambling* is a technique used to *blind* the data and avoid any kind of bias when doing an analysis. In ANTARES the azimuthal angle is randomized between 0 and 2π.

model and shape of the source. Thus, each PDF needs to be recomputed for each set of quality cuts and model considered in the optimization process. Fig. 3.10 shows PSFs for the different sets of signal models tested and for the background, before (top) and after (bottom) normalizing per solid angle, assuming the Sun as a point-like source. As illustrated in Fig. 3.10, the signal is concentrated around the Sun. The spread of the signal is due to the finite angular resolution of the detector (PSF). The background is distributed uniformly at all distances to the Sun. Fig. 3.11 shows the one-dimensional PDF of the β and N_{hits} ingredients for one of the signal models (blue line) and for the background (red line).

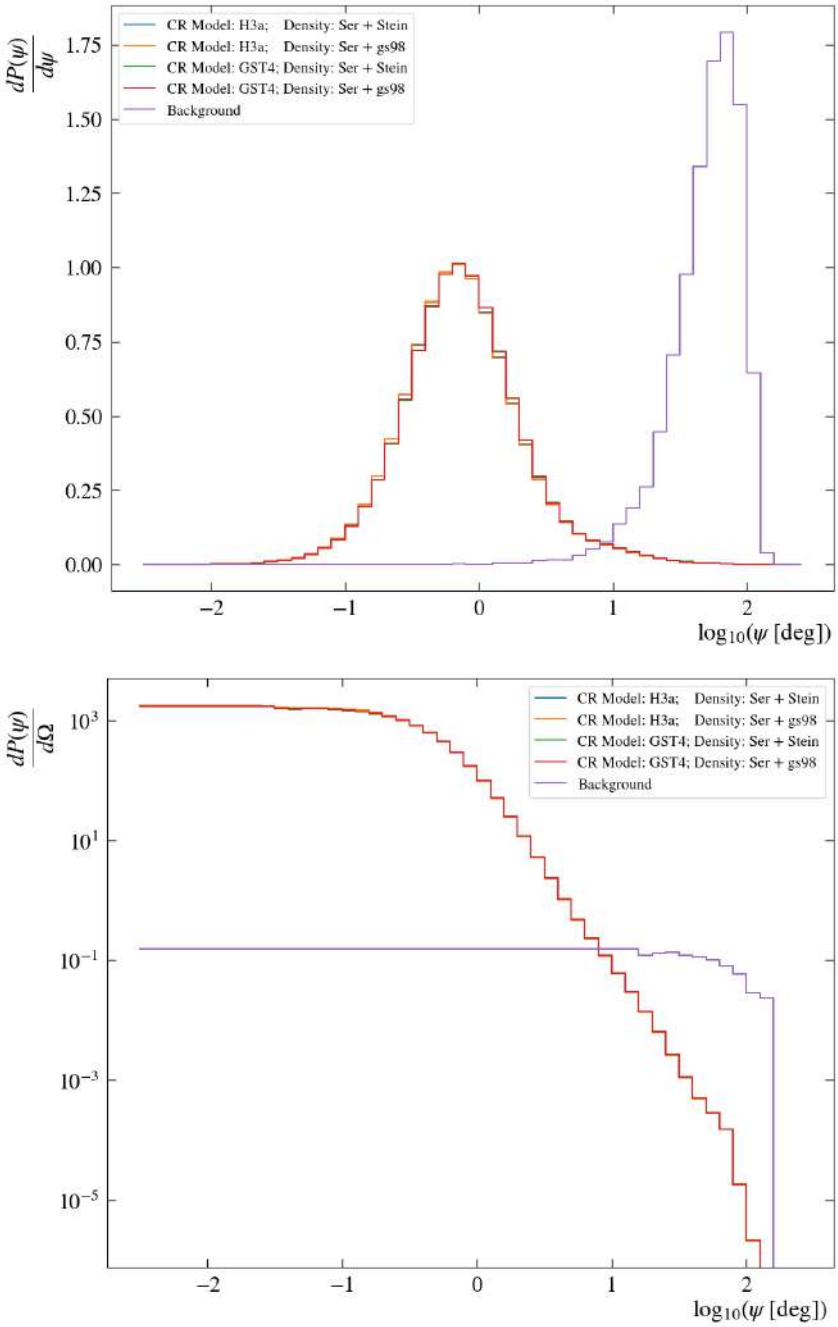

Figure 3.10: PSFs extracted from MC for signal and from scrambled data for background. The distribution of $\Psi_{\odot}$ is shown as the logarithm to allow the visualization of the spread and the differences of the distributions. The PSF of the four tested models are shown together with the background, before (top) and after (bottom) normalizing per solid angle. Cuts on quality parameters: $\Lambda > -5.2$, $\beta < 1^{\circ}$ and $\cos(\theta) > 0$.

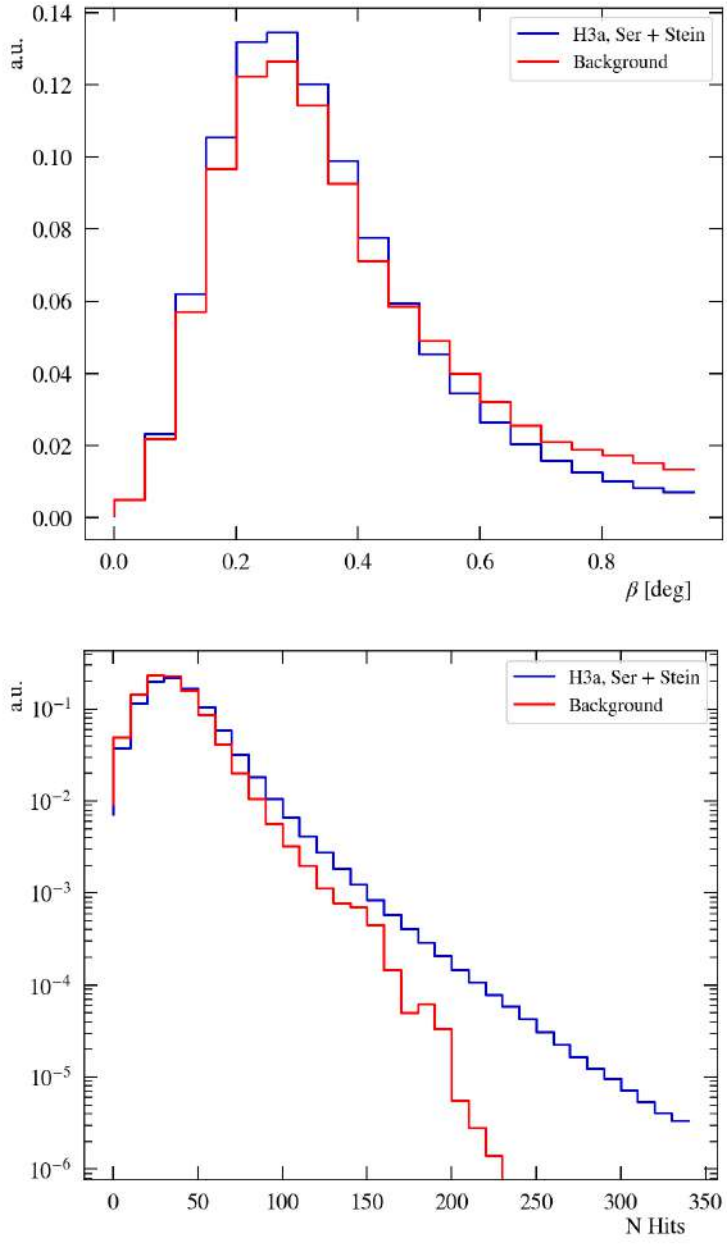

Figure 3.11: PDFs of the β (top) and N_{hits} (bottom) ingredients for one of the signal models (blue) and for the background (red). Cuts on quality parameters: $\Lambda > -5.2$, $\beta < 1^\circ$ and $\cos(\theta) > 0$.

Sensitivity

The sensitivity of the detector is defined as the 90% CL median upper limit, which is computed, before unblinding the data, by comparing the background test statistic (TS) distribution (from scrambled data) to the signal plus background TS distributions. The measured upper limit is computed from the observed TS after unblinding the data. If the observed TS is below the median of the TS background distribution, the upper limit is set equal to the sensitivity.

If no signal is observed, a limit on the neutrino flux is computed from the limit on the number of signal events, $n_{\text{sig}}^{90\%\text{CL}}$, according to the following expression:

$$\frac{d\Phi_{\nu_\mu}^{90\%\text{CL}}(E)}{dE} = \frac{n_{\text{sig}}^{90\%\text{ CL}}}{\bar{n}_{\text{sig}}^{\text{theor}}} \frac{d\Phi_{\nu_\mu}^{\text{theor}}(E)}{dE} = C_{90} \cdot \frac{d\Phi_{\nu_\mu}^{\text{theor}}(E)}{dE} \tag{3.16}$$

The first term in the Eq. 3.16 corresponds to the flux sensitivity/upper limit. The second and third terms represent the theoretical flux model multiplied by a scale factor, C_{90}, defined as the ratio between $n_{\text{sig}}^{90\%\text{CL}}$ and the expected number of detected signal events $\bar{n}_{\text{sig}}^{\text{theor}}$, computed in the following way:

$$\bar{n}_{\text{sig}}^{\text{theor}} = T \int \sum_{l \in \nu_\mu, \bar{\nu}_\mu} \left(\frac{d\Phi_l^{\text{theor}}(E)}{dE} A_{\text{eff}}^l(E) \right) dE, \tag{3.17}$$

where T is the livetime of data taking, A_{eff}^l is the ANTARES effective area for this analysis (see figure 3.15), and $\frac{d\Phi_l^{\text{theor}}(E)}{dE}$ is the theoretical flux model (Fig. 3.4). The superscript l indicates if the particle is a neutrino or an antineutrino.

Pseudo Experiments

In order to minimize the scale factor C_{90}, the sensitivity of our detector to the SAν signal has to be computed. To achieve this, a set of Pseudo Experiments (PEX) is performed. In these PEX, a known and fixed number of signal (n_{inj}) and background events are injected. The characteristics of these events are sampled from their corresponding ingredient PDF (see previous subsection). The expected background is estimated using the whole scrambled data sample. This estimation is justified given that the number of signal events is expected to be very small compared to the number of background events in the data sample. Once the sensitivity is obtained with the simulation and the C_{90} is minimized, the quality cuts are fixed and the analysis is applied to the non-scrambled data, in a process called *unblinding*.

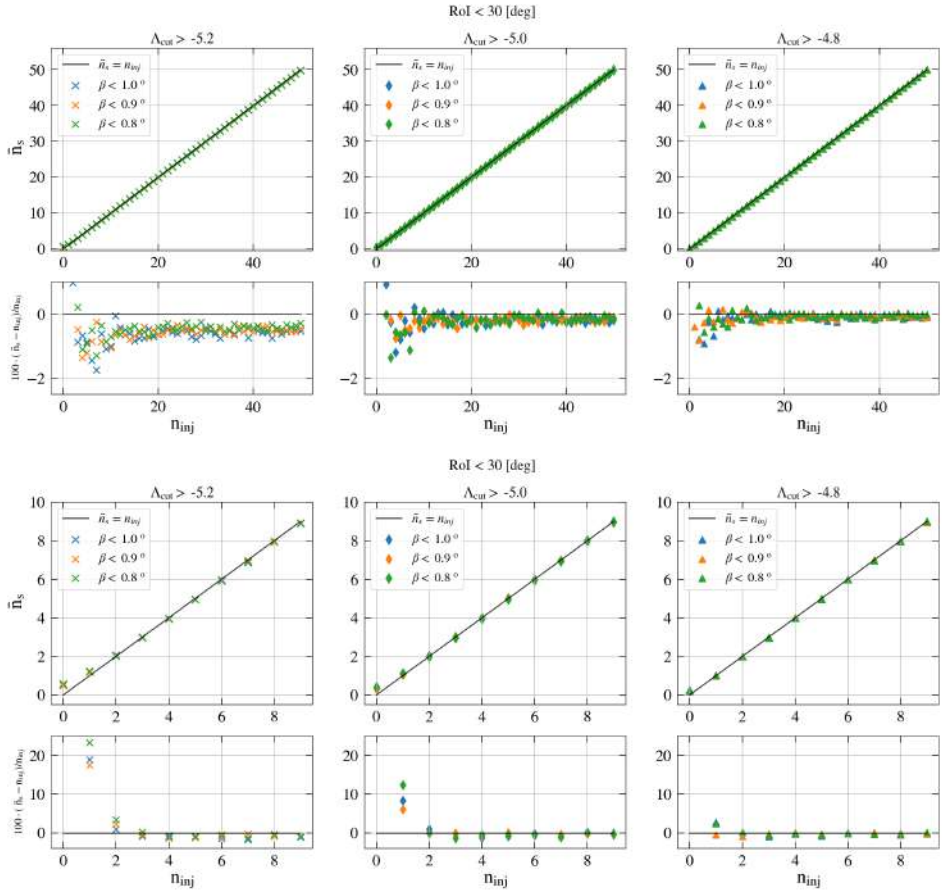

Figure 3.12: Mean value of the fitted number of signal events ($\bar{n}_s$) as a function of the number of injected signal events (n_{inj}), for the combination of Λ and β parameters. Top, full range of number injected signals. Bottom, zoom-in up to 9 injected signal events.

The total number of PEX performed is 10^4 for each combination of Λ and β parameters, and number of injected signal ($n_{\text{inj}} = 0, 1, \ldots, 10$). The likelihood function (Eq. 3.14) is optimized using the `ROOT` package `TMinuit` [166]. The optimization process runs over all reconstructed events inside a Region of Interest (RoI) of 30° around the Sun. Due to the small extension of the source, it is possible to constrain the search to this RoI, preserving a good number of reconstructed events without missing information, and speeding up the maximization process. The outcome of the maximization is the number of signal events ($\hat{n}_s$) that maximizes the likelihood for each pseudo experiment. For each set of PEX, the outcome of the fitting is different, and a distribution of $\hat{n}_s$ is obtained. Fig. 3.12 shows the mean value of these distributions as a function of the number of injected signal, for events passing the Λ and β cuts and reconstructed inside the RoI. The bottom plots of each

figure show the relative error between the fitted and the injected number of signal events.

Test Statistic

A hypothesis test is used to determine whether a signal has been detected or not. The hypothesis of being a signal within the data (H_1 or alternative hypothesis) is compared with the background-only hypothesis (H_0 or null hypothesis), which is built without injecting a signal ($n_{\text{inj}} = 0$), according to the likelihood ratio criteria [167, 168]. The likelihood for both hypotheses are built from the PEX, and a test statistic (TS) is computed from their ratio (Eq. 3.18).

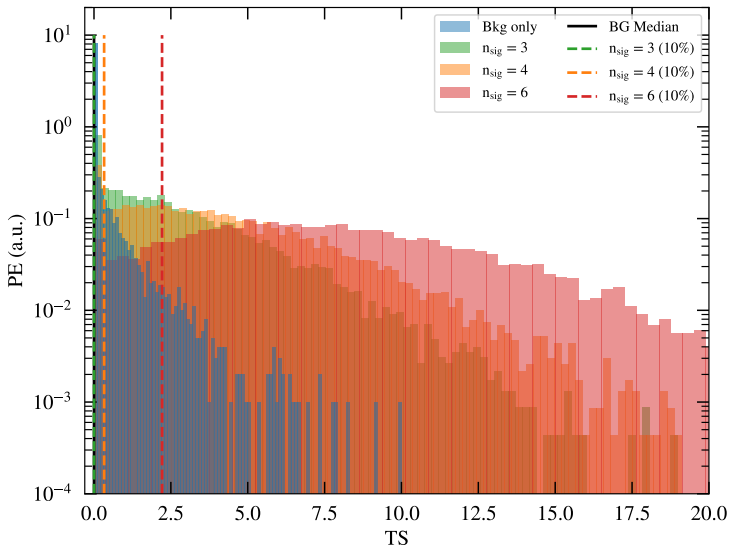

Figure 3.13: Example of TS distributions for different number of injected signals. The vertical dashed lines indicate the TS value for which the integral from zero to this TS value gives the 10% of the total distribution. The vertical solid black line on the left represents the median of the TS for the background-only distribution.

$$\text{TS} = \log_{10}\left(\frac{\mathcal{L}_{H_1}(\hat{n}_s)}{\mathcal{L}_{H_0}(0)}\right). \tag{3.18}$$

A TS value close to 0 means that both hypotheses are very similar. On the other hand, the larger TS the easier it will be to distinguish the two hypotheses. For each set of Λ and β parameters, a distribution of TS with 10^4 entries (Fig. 3.13) is built for each number of injected signals ($n_{\text{inj}} = 0, 1, \ldots, 10$). From these distributions we will compute the sensitivity of our detector (Fig. 3.14). To account for the statistical fluctuations on the building process of the Pseudo Experiments, the TS distributions are smeared by a Poisson function, returning the TS distributions as

a function of the Poissonian mean μ, in which is also included the 15% systematic uncertainty (see Sec. 3.4.2) that comes from the determination of the neutrino track direction:

$$P\left(\mathrm{TS}(\mu)\right) = \sum_{n_{\mathrm{inj}}=0}^{N} P\left(\mathrm{TS}(n_{\mathrm{inj}})\right) \cdot \mathrm{Poisson}\left(n_{\mathrm{inj}}, \mu\right), \tag{3.19}$$

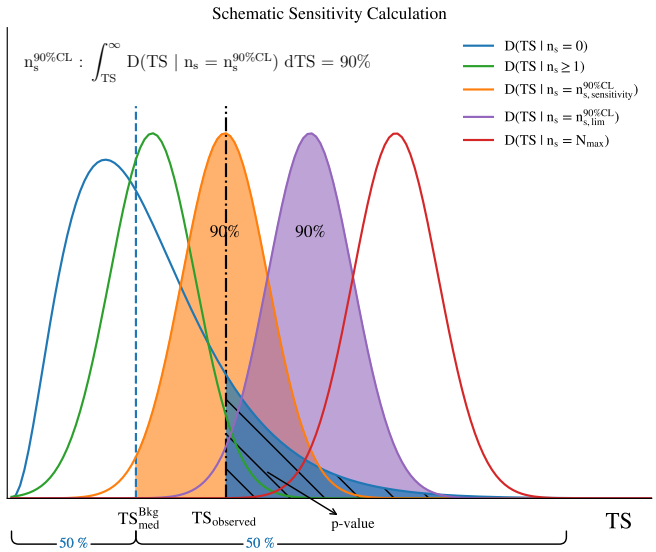

Figure 3.14: Schematic of the sensitivity and upper limit calculation. The blue curve represents the TS distribution for zero number of injected signal (background-only hypothesis), whereas the colored curves identify the TS distributions for different number of signal (n_s) events injected on the PEX (signal hypothesis). The sensitivity is represented by the orange curve, which has the 90% of the distribution over the median TS of the background. The upper limit is represented by the purple curve, which 90% distribution is over the measured TS after unblinding. Green and red curves represent other TS distributions as examples.

As illustrated in Fig. 3.13, the details of the TS distributions are hardly visible. To improve the visualization of the differences between TS distributions, each TS distribution is transformed as follows:

$$Q = \log_{10}(\mathrm{TS} + C), \tag{3.20}$$

where C is a constant that shifts the same amount every TS distribution and avoids the argument of the $\log_{10}$ function to be zero.

A final value of the test statistc ($TS_{observed}$) is obtained after evaluating the unblinded data by the likelihood, and its significance allows to evaluate the relevance of the obtained $TS_{observed}$. The significance is the probability of obtaining a test statistic value equal or higher than the measured one, but if there is no signal present in the dataset, this is also called the p-value. The p-value indicates how likely pure background can produce a scenario where $TS \geq TS_{observed}$ [169]. In addition, if no signal is observed, an upper limit is established (Fig. 3.14).

Summarizing, the sensitivity is computed as follows:

1. Compute the TS distributions.
2. Retrieve the TS value corresponding to the median of the background-only TS distribution ($TS_{med}^{bkg\text{-}only}$).
3. Find the value n_s for which 90% of its TS distribution is over the $TS_{med}^{bkg\text{-}only}$ (this is 90% CL).
4. The obtained n_s is the sensitivity, defined as the minimum number of signal events needed to be able to distinguish signal from background with a 90% CL.

The upper limit is computed following the same procedure listed above, but using the $TS_{observed}$ from the unblinded data.

Systematics

The main source of systematic uncertainties comes from the determination of the neutrino track direction. The track reconstruction relies on the time resolution of the detector, which in turn depends on the photomultiplier time spread, on the calibration and on possible space misalignment of the detector lines. The effect of systematic uncertainties was estimated in a previous analysis [168] to a total of 15%. A Gaussian smearing of 15% is applied to the signal PDFs to account for detector systematics (see Sec. 3.4.2) [170]. Other source of systematics comes from the different models used for the CR and solar density profile, as well as for the source shape. The *GST4* cosmic-ray model and the *Ser+GS98* solar density profile, which are already included within the `solar_crnu` package, have been tested in combination with the models used in the reference scenario (see Fig. 3.4), and the results are within a 2% difference with respect to the values from the reference model shown in Tab. 3.1. The solar shape selected has a systematic uncertainty in the upper limit about 3–9% with respect to point-like shape used as a refenrece.

3.4.3 Results and Discussion

As mentioned in the previous section, in the reference scenario the *H3a* CR model and the *Ser+Stein* solar density profile are considered. Normal mass ordering and neutrino oscillations from world best-fit values are assumed [33, 162]. Tab. 3.1 shows the sensitivities for the different set of quality parameters (Λ and β) and the different shapes considered for the Sun. The expected number of signal events

from the reference model, the scale factor (C_{90}), and the total number of events are shown for each set of cuts. In red are shown the values that minimize the C_{90} scale factor. Finally, the analysis is optimized for ν_μ CC interactions arriving at the detector. The quality parameters that minimize the factor C_{90} are: $\Lambda > -5.2$, $\beta < 1^\circ$ and $\cos(\theta) > 0$, with a total number of reconstructed events of 7071, for a total lifetime of 3022 days.

The total number of events as well as $\bar{n}_{\text{sig}}^{\text{theor}}$ changes with the selection cuts. The first is reduced because as the values of the parameters are more restrictive, less reconstructed events are selected. The second changes as a consecuence of the first. As shown in Eq. 3.3, the effective area is proportional to the number of events passing the cuts. The ANTARES effective area for the parameters that minimize the C_{90} is shown in Fig. 3.15.

Λ	β [deg]	$\bar{n}_{\text{sig}}^{\text{theor}}$	n_{90}^{Point}	n_{90}^{Ring}	n_{90}^{Disk}	$C_{90} = \frac{n_{90}^{\text{Point}}}{\bar{n}_{\text{sig}}^{\text{theor}}}$	Total events
	1.0	0.37	2.70	3.45	2.80	7.38	7071
-5.2	0.9	0.37	2.90	3.35	2.45	7.92	6880
	0.8	0.36	2.70	3.10	2.15	7.50	6619
	1.0	0.24	2.35	2.60	2.40	9.96	4573
-5.0	0.9	0.24	2.25	2.55	2.25	9.53	4521
	0.8	0.23	2.20	2.75	2.20	9.40	4423
	1.0	0.18	2.00	2.10	2.00	10.93	2753
-4.8	0.9	0.18	1.95	2.15	1.95	10.66	2731
	0.8	0.18	1.95	1.95	2.00	10.77	2689

Table 3.1: Summary of the results obtained on the search for Solar Atmospheric neutrinos with 3022 days of lifetime (2008–2018) with the ANTARES detector. For each cut in Λ and β, the following information is given: number of expected signal events from theoretical model ($\bar{n}_{\text{sig}}^{\text{theor}}$), obtained sensitivity (n_{90}) for the three solar model shapes, scale factor C_{90}, and total number of events passing the cuts in the data sample. The cut on $\cos(\theta) > 0$ is also applied in all cases.

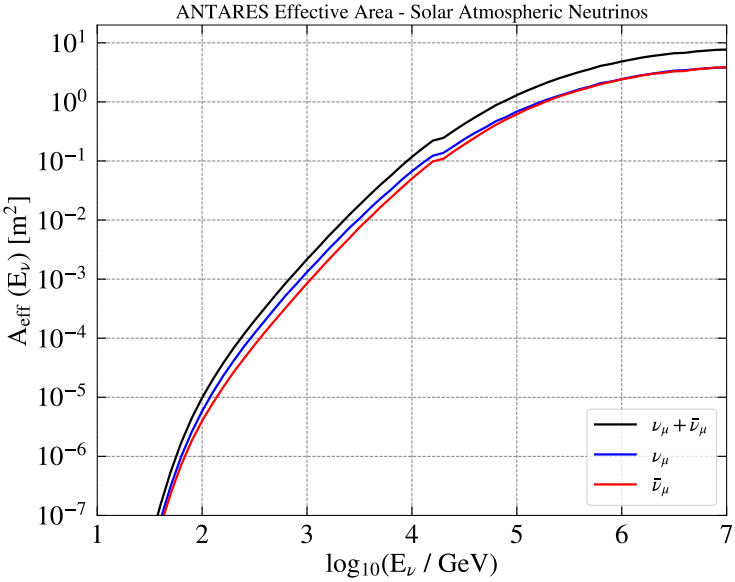

Figure 3.15: ANTARES effective area to SAνs, for ν_μ (blue), $\bar{\nu}_\mu$ (red), and the sum of both, arriving from the Sun direction. Cuts on the quality parameters that minimize the C_{90}: $\Lambda > -5.2$, $\beta < 1^\circ$ and $\cos(\theta) > 0$.

In the 3022 days of lifetime analyzed in this work, the number of events passing the final selection cuts ($\Lambda > -5.2$, $\beta < 1.0^\circ$ and $\cos(\theta) > 0$) in the RoI is $n = 461$, the number of expected background events is $\bar{n}^{MC}_{bkg} = 470$ and the expected SAν signal from the *reference model* amounts to $\bar{n}^{theor}_{sig} \approx 0.37$. Therefore, no excess of SAν signal over the expected background is observed in the 11 years of analized data.

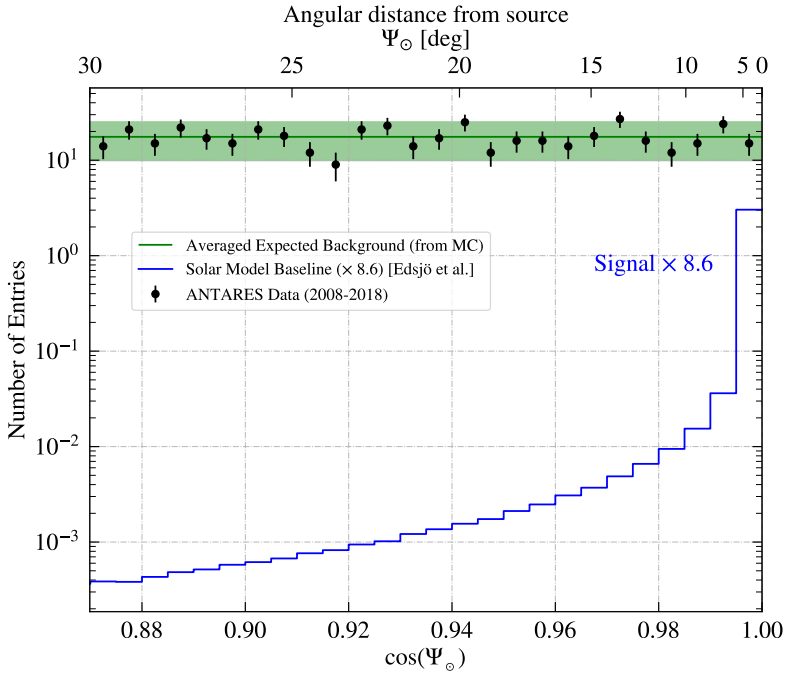

Figure 3.16: Event distribution as a function of the reconstructed angular separation $\Psi_\odot$ around the Sun. The expected signal, in blue, is scaled up by a factor 8.6. The expected background (green line) is shown with a 2σ band along the data (black dots).

Model	Sun Shape	$n_{\text{sig, sens}}^{90\%\text{ CL}}$	$n_{\text{sig, up-lim}}^{90\%\text{ CL}}$	*p-val*
H3a-Ser+Stein [156, 158]	Point-like	2.70	3.15	0.41
	Filled Disk	2.80	3.25	0.43
	Ring-shaped	3.45	3.45	0.50

Table 3.2: Sensitivities and 90% CL upper-limits for the reference Solar Atmospheric neutrino model, and for three different Sun shapes considered. The last column shows the *p-values* corresponding to the quoted upper limits.

The 90% CL upper limit obtained after analysing the unblided data is $n_{\text{sig, up-lim}}^{90\%\text{ CL}} = 3.15$, corresponding to a flux scale factor of $C_{90} = 8.6$. The value of this scale factor indicates the possibility of excluding at 90% CL the tested model. A value smaller than one will directly constrain the model. In this study the flux that can be constrained is 8.6 times larger than the one of the reference model. Figure 3.16 shows the distribution of the events within the RoI of 30° around the Sun, for the expected signal (blue histogram) and background (green line), alongside the observed data (black dots). The signal is magnified by a factor 8.6 for comparison.

Table 3.2 shows the sensitivities and upper limits for the three Sun shapes considered, as well as the corresponding *p-values*. Figure 3.17 presents the sensitivity (dotted red line) and the 90% CL upper limit (solid red line) on the SAν flux for the ANTARES detector over 11 years of data taking. The theoretical flux model (solid blue line) and latest upper limit results obtained by the IceCube collaboration (solid black line) [171] are shown for comparison.

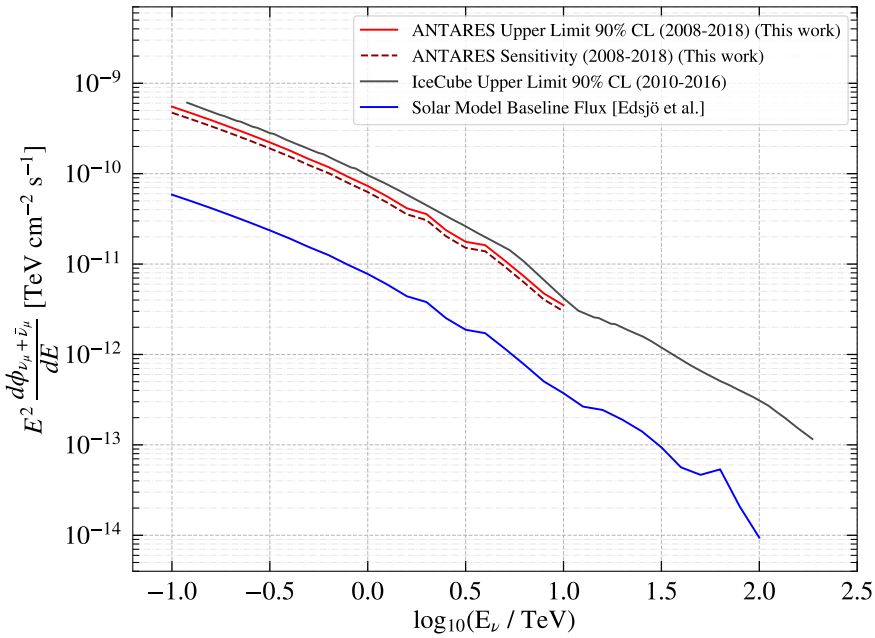

Figure 3.17: ANTARES upper limit (solid red) and sensitivity (dashed red) for 11 years of data, assuming the Sun as a point-like source for the reference model *H3a-Ser+Stein* (solid blue line). For comparison, the current 6 years IceCube upper limit [171] is also shown (solid black line). The ANTARES limit and sensitivity lines expand in the energy range which contains 90% of the expected number of events. Results published in [172].

After analysing 11 years of ANTARES data, corresponding to 3022 days of total lifetime, with an unbinned likelihood method, using three different sun shapes, no signal evidence of SAν is observed. As a result, a 90% CL upper limit on the energy flux of 7×10^{-11} [TeV cm^{-2} s^{-1}] at 1 TeV is established (corresponding to a *p-value* = 0.41).

Part III

Dark Matter Searches in the Sun with the KM3NeT-ORCA Neutrino Telescope

4 The KM3NeT Neutrino Telescope

"Scientists have become the bearers of the torch of discovery in our quest for knowledge."

Stephen Hawkings

The KM3NeT detector is a new generation of undersea neutrino telescopes which draws from all that has been learned from previous experiments, such as ANTARES (see chapter 2). KM3NeT, with an increased instrumented volume located in two different sites, has an ambitious physics plan which includes point-like, dark matter, nuclearities, magnetic monopoles, multimessenger, mass ordering, neutrino oscillation, among others.

In this chapter, the KM3NeT neutrino telescope is presented. Section 4.1 makes a general description of the layout and the different configurations of the detector. Additionally, this section outlines the main components for light detection of KM3NeT, the trigger algorithms, the data acquisition system as well as the calibration of the detector. The simulation of the event generation, light propagation and the detector response using Monte Carlo techniques, is described in section 4.2. Section 4.3 presents the methods used in KM3NeT for the reconstruction and identification of the events that reach the detector.

4.1 Detector Description

The KM3NeT (acronym for KiloMetre cube Neutrino Telescope) detector is an undersea neutrino telescope, currently under deployment, located in the Mediterranean Sea [173]. The infrastructure consists on two different detectors placed at different deep-sea sites: Toulon (France) and Capo Passero (Italy). A futurible third installation site is projected to be placed in Pylos (Greece) (see Fig. 4.1 for reference).

The whole project is divided in phases in order to maximize the access to regional funds, the availability of human resources and the synergistic opportunities for the Earth and sea science community. During **Phase-1**, technical designs, software tools and assembly and deployment sites were set up. The deployment of the first detection lines was accomplished. The **Phase-2** main objective is to complete the

construction of ARCA and ORCA configurations. At the time of writing there are already deployed 9 lines of ARCA and 10 lines of ORCA. The first results with ARCA and ORCA were presented at the ICRC21 conference [174, 175].

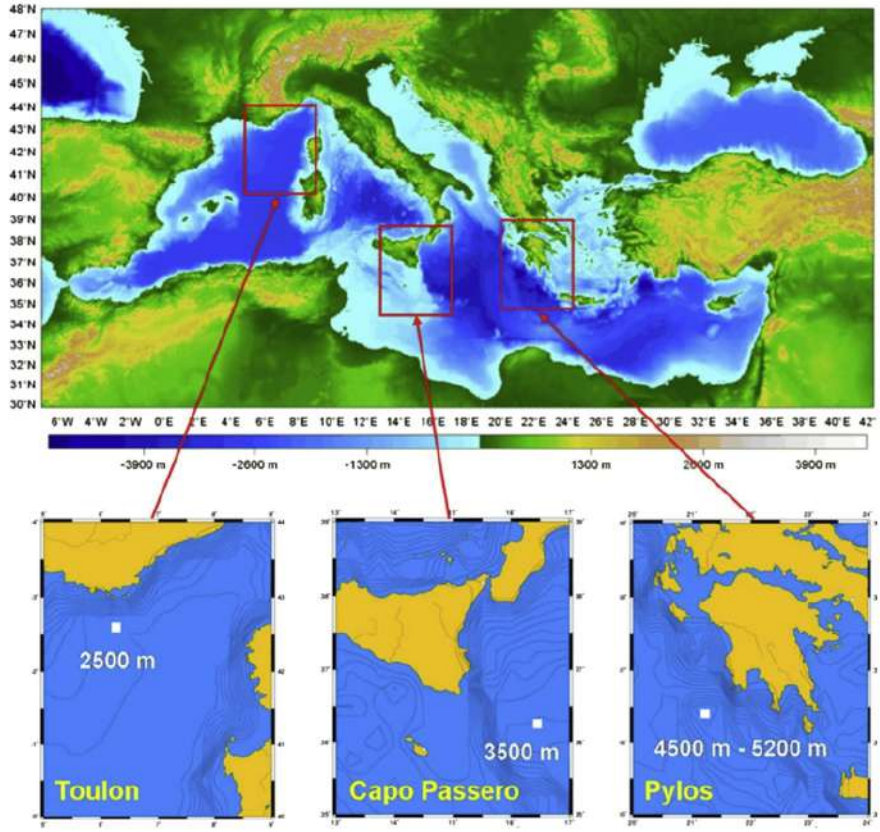

Figure 4.1: KM3NeT installation sites in the Mediterranean Sea. From [176].

A building block comprises 115 strings or detection units [177] (DUs) [1]. The modular concept of strings allows the construction of building blocks with different spacings between lines and between digital optical modules (DOMs), enabling targeting different neutrino energy regimes. Each string consists of 18 DOMs (see section 4.1.2) and each DOM embodies 31 photo-multiplier tubes (PMTs). Each building block constitutes a three-dimensional array of photo-sensors used to detect the Cherenkov light yielded by relativistic particles emerging from neutrino interactions. Figure 4.2 shows an artistic illustration of the KM3NeT detector.

[1] In the text the terms *string*, *DU* or *line* are used interchangeably.

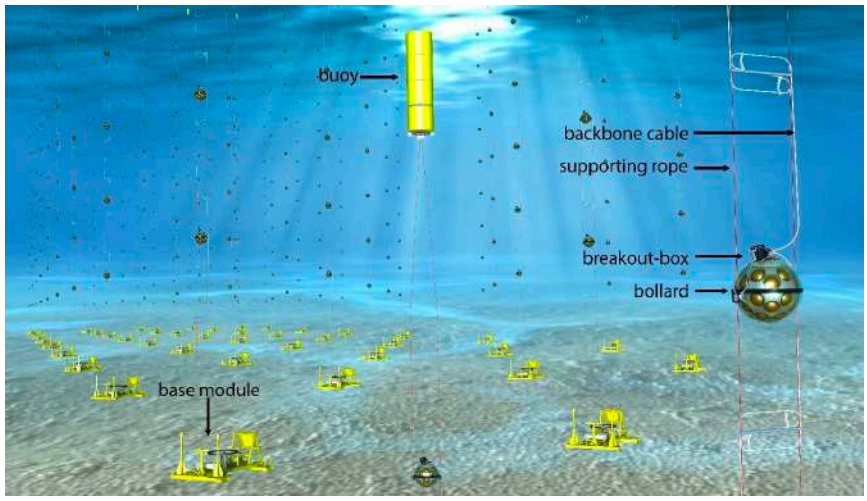

Figure 4.2: Artist impression of the finalised KM3NeT underwater neutrino telescope, with an optical module held in a (double-rope) string in the right-hand-side foreground. The white tube along the ropes is the oil-filled backbone with copper wire and optical fibres inside. The yellow cylinder in the centre of the image is the top buoy, which is above each string. From [178].

4.1.1 Detector Topology and Layout

In its final configuration, the KM3NeT neutrino telescope will be composed of two detector sub-arrays with the following configurations [173]:

- **ARCA** stands for *Astroparticle Research with Cosmics in the Abyss*. The ARCA site is located offshore of Sicily, Italy, at (36°16′ N, 16 °06′ E). At 3500 m depth, starting about 80 m from the sea floor, the ARCA detection units are 700 m high, separated horizontally by about 95 m, with 18 DOMs spaced 36 m in vertical direction. The full ARCA infrastructure will consist on 2 building blocks of 115 strings each, with the aforementioned configuration. With an instrumented volume of $\sim$1 km^3, ARCA was designed mainly for detection of high-energy cosmic neutrinos and neutrino astronomy (GeV to TeV energy range).
- **ORCA** stands for *Oscillation Research with Cosmics in the Abyss*. The ORCA site is located offshore of Toulon, France, at (42°41′ N, 6°02′ E). At 2450 m depth, starting about 40 m from the sea floor, the ORCA detection units are 200 m high, separated horizontally by about 20 m, with 18 DOMs spaced 9 m in vertical direction. The ORCA full configuration will consist on 1 building block of 115 strings with the aforementioned configuration. With an instrumented volume of $\sim$5 x 10^{-3} km^3, ORCA was designed mainly for studying neutrino properties at a lower energy range than ARCA (few GeVs).

A size comparison between ARCA and ORCA configuration is shown in figure 4.3.

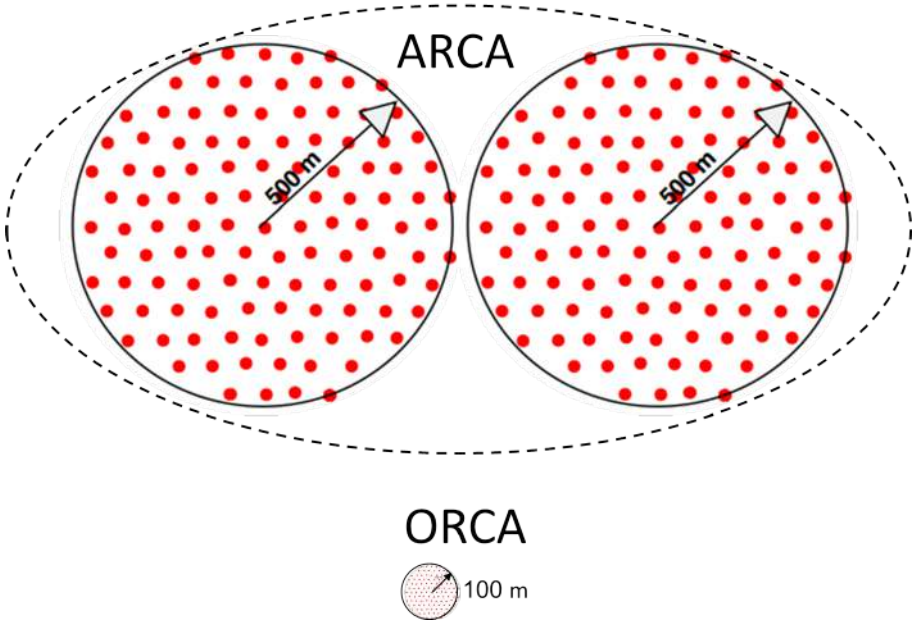

Figure 4.3: Comparison between the size of the horizontal footprints of the two building blocks of ARCA (top) and the unique building block of ORCA (bottom) detectors. The red dots represent the position of the detection units. Credits to the KM3NeT collaboration.

4.1.2 Digital Optical Module

The DOM [179], shown in figure 4.4, is a glass sphere of ∼43 cm (17") diameter. Instead of being equiped with a single large PMT as in the traditional optical module design for large-volume neutrino telescopes, each KM3NeT DOM consists of two separated hemispheres housing 31 small PMTs of 3" diameter [176] and their readout electronics. The multi-PMT design provides a large photocathode area, good separation between single-photon and multiple-photon hits, and information on the photon direction [180]. This configuration also allows measuring the number of photons by counting the number of PMTs registering a photon hit and, by comparing the hit coincidences between the different neighbour PMTs, the background from uncorrelated photons can be reduced.

The 31 PMTs, arranged in five rings of six PMTs each plus one at the bottom pointing vertically downwards, are distributed in the two hemispheres: 12 in the upper and 19 in the lower hemisphere. The PMTs are spaced at 60° in azimuth and the successive rings are staggered by 30°, achieving an almost isotropical angular coverage.

The PMTs used are the Hamamatsu R12199-02, with a maximum quantum efficiency of ∼30% and a transint time spread lower than 5 ns, allowing great accuracy in the photon arrival timing at about 400 nm wavelength [181].

Each DOM also houses instrumentation for monitoring purposes such as: a piezo-sensor for acoustic positioning, temperature and humidity sensors, a tiltmeter and a compass for orientation, and an LED in the upper hemisphere for the inter-DOM time calibration (Fig. 4.4, right).

Figure 4.4: A KM3NeT Digital Optical Module (left) and its components (right). From [182].

4.1.3 Triggers and Data Acquisition System

The KM3NeT Trigger and Data Acquisition System (TriDAS) [183, 184] is the infrastructure in charge of the readout, aggregation and filtering of all the detector data. Both systems have been inherited and adapted from the ones developed for the operation of ANTARES.

The readout process is based on the *all-data-to-shore* philosophy, just like in the ANTARES detector (see Sec. 2.1.3), in which all PMT signals passing the 0.3 p.e. threshold are digitised and sent to the onshore station to be processed in real time. The filtering process of physical events is done on the onshore station via trigger algorithms (see Tab. 2.1).

4.1.4 Detector Calibration

The detector calibration [185] is a crucial step for the accurate reconstruction of events. For this purpose, the DOM position, the arrival time of the photons and their energy, in the form of collected charge at the PMTs, have to be well known. An initial charge/time calibration, before deployment, is performed in a dark-room, but *in situ* calibrations are also needed due to the changes in voltage of the DOMs and the connection of lines or displacement of the DUs due to the sea currents.

Position Calibration

The uppermost part of the strings can move up to 15 m from the vertical by the sea currents. This displacement changes the relative position between DOMs. In order to have an accurate event reconstruction, the exact position of each DOM has to be monitored with high precision. To achieve this, KM3NeT uses an Acoustic Positioning System (APS) [186], which involves acoustic transmitters and receivers placed at the base of each detection unit at a well known position, and an acoustic receiver within each DOM. Onshore, a farm of PCs measures the Time of Flight (ToF) of the acoustic signals and determines the DOM position in coordinate system referenced geographically. Also, a Tiltmeter-Compass System (TCS) measures the pitch, yaw and roll of each DOM and determines its orientation.

The APS, in conjunction with a TCS, pressure, current and sound velocity data, measures the DOMs position with an accuracy of about 10 cm.

Charge Calibration

The PMT works by amplifying the emission of secondary electrons off dynodes through photoelectric effect. A photon hitting the photocathode area of a PMT produces an electron. This electron is then accelerated by an electric field between dynodes. After each acceleration step, in the dynodes, the number of electrons grows. The charge generated by the photon signal is digitised by an Analog-to-Voltage Converter (AVC) into a value related to the number of produced photoelectrons.

In order to know the number of photoelectrons arriving at each PMT, onshore calibrations must be done [53, 65, 187]. This calibrations are performed in a dark-room where the AVC values are measured for different number of photons hitting the PMTs. The threshold is pre-established at a level of 0.3 p.e. to remove noise hits.

Time Calibration

Neutrino telescopes need to be synchronized at nanosecond precision to reach a neutrino event reconstruction with an angular precision better than 1° [177, 180]. In addition, to be able to correlate events detection with other experiments, it is also necessary to monitor the absolute timing of an event with respect to the Coordinated Universal Time (UTC).

The signal processing and transfer, time synchronization, and the instruments control is performed by identical Control Logic Boards (CLBs) [188] placed at each DOM and at the base. LED nanobeacons [189] and lasers are in charge of the *in-situ* time synchronisation [190] between different parts of the detector and PMTs. Part of the information recorded on a PMT consists of the start time (time at which the pulse passes beyond the 0.3 p.e. threshold) and the Time over Threshold (ToT, time the pulse remains above this threshold). These quantities are used for tuning the high voltage of the PMTs when single photons are detected.

To achieve the foreseen precision, different time offsets have to be determined:

- **Intra-DOM:** The time offset between different PMTs in the same DOM depends on the PMT transit time, which is measured to spread up to 5 ns. Coincidences between signals in different PMTs produced by single decays of ^{40}K are exploited for calibrating the DOMs.
- **Inter-DOM:** Time offsets between DOMs primarily depends on the cable lengths. Nanobeacons installed in each DOM provide light detection from one DOM to the neighbour DOMs. This Inter-DOM time calibration is cross-checked by the signal produced by vertical muons. The measured time offsets are in agreement within 2 ns.
- **Inter-DU:** The time calibration between detection lines is based on the measurement of the Round-Trip-Time (RTT) delay of the laser signal between the master clock (reference clock) and the DU base [180].

4.2 Monte Carlo Simulations

The simulation tools used by KM3NeT have been inherited and adapted from the ANTARES experiment [191] to be usable for km^3-scale detectors. These tools, however, were never intended to be used for such a large detector arrays. Especially, implementing support for new optical module design options requires a lot of low-level changes to their code and is thus error-prone. Additionally, most of the ANTARES tools are Fortran-based and have become hard to maintain on newer computer system architectures over time [192]. In order to solve these problems and to provide means to cross-check results produced with the existing software, a new set of KM3NeT Monte Carlo tools has been developed within a modular software framework [193]. These tools include a GEANT4-based muon propagator, a photon propagation tool including a full light scattering simulation and a new optical module acceptance and readout simulator. Together with pre-existing event generators, they form a completely alternative Monte Carlo simulation chain for KM3NeT (figure 4.5).

4.2.1 Event generation

In order to simulate the interaction of neutrinos and atmospheric muons in sea water, the detector geometry is defined and divided in three different volumes (see Sec. 2.2.1 for more details):

- **Instrumented volume.** This volume consists of a cylinder containing the detection units of the detector. The size of this volume matches the real radius and height of the detectors.
- **The *Can*.** This volume is defined as a second cylinder surrounding the instrumented volume, where the Cherenkov ligh propagation is simulated. The size of this volume exceeds the instrumented volume by 3 times the light absortion length in water ($\sim$70 m), but this quantity can be defined by the user.

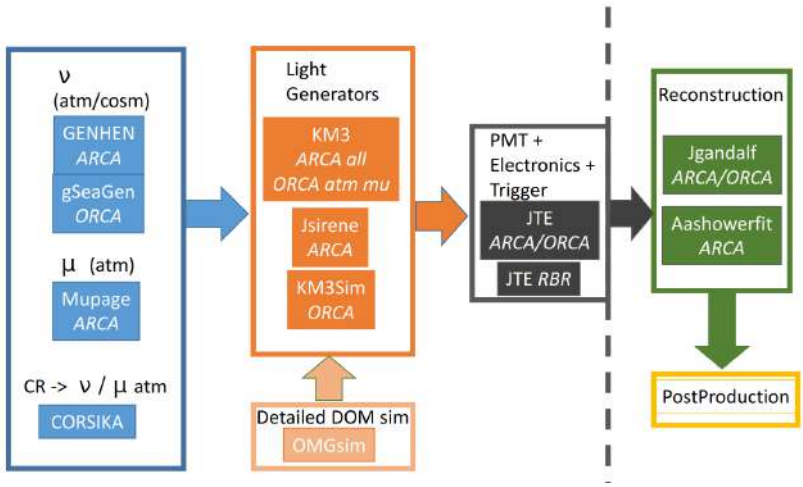

Figure 4.5: Representation of the simulation chain used in the KM3NeT experiment. The procedure is split in four steps, from left to right in the figure: event generation (section 4.2.1), light production (section 4.2.2), detector response (section 4.2.3), event reconstruction (section 4.3). Credits to the KM3NeT collaboration.

- **World volume.** Is the volume outside the *Can* where only muon energy losses are considered (no Cherenkov light is produced in this volume).

Neutrinos

In KM3NeT, neutrinos are generated using GENHEN [113] and gSeaGen [194].

The GENHEN code is used to generate the neutrino-induced muon flux at the detector. This program includes a complete simulation of incident neutrinos, their interactions in the medium and of the resulting secondary particles up to neutrino energies of 10^8 GeV. Produced muons are propagated to the detector and their energy loss is calculated in the process [72].

The gSeaGen code is a GENIE-based application developed to efficiently generate samples of high number of events, induced by neutrino interactions, detectable in a neutrino telescope. The gSeaGen code is able to generate events induced by all neutrino flavours, considering topological differences between track-type and shower-like events. Neutrino interactions are simulated taking into account the density and the composition of the media surrounding the detector [194].

Just like in ANTARES, the generation of neutrinos follows a $dN/dE \propto E^{-\gamma}$ power law spectrum. The neutrino directions are generated isotropically within a generation volume (see Sec. 2.2.1 for more details).

Atmospheric Muons

The generation of atmospheric muons is performed using the MUPAGE [120] and CORSIKA [117, 118] packages. The procedure to generate atmospheric muons follows the same steps used in ANTARES (see Sec. 2.2.1 for more information).

4.2.2 Light Production and Propagation

The light production in KM3NeT is performed through different programs, as described in [44, 195]:

- **OMGSim [196]:** is a complete and detailed GEANT4 simulation of the DOM, oriented to the study of its response in sea water, focusing on the characterisation of the radioactive backgrounds, providing a reliable model for the in-situ calibration of the detector.
- **KM3 [115]:** is the standard ANTARES simulation package for the generation and propagation of Cherenkov light by muons and electromagnetic showeres in sea water, that makes use of tabulated results from GEANT3.21. The code has been modified to take into account the KM3NeT DOM and PMT characteristics.
- **JSirene [197]:** is part of the custom KM3NeT software suite Jpp; it is a fast Cherenkov light simulator exploiting tabulated probability density functions for the arrival times of photons from muons [198, 199], tau particles and electromagnetic showers. In addition to the light induced by a particle in the minimum ionising regime, the simulation of delta rays and Brehmsstralung radiation is implemented in native code.
- **KM3Sim:** is part of the HOURS software package [200] and simulates the response of the water-based Cherenkov detector. It propagates all particles emerging from a neutrino interaction using tools oofered by the GEANT4 simulation package [122], generates Cherenkov photon emission, tracks the photons in sea water taking into account photon absorption and scattering, and simulates the photon detection taking into account the KM3NeT DOM and PMT characteristics (PMT photocathode area, quantum efficiency, angular acceptance, and transmission of light in the optical module glass and in the optical gel).

4.2.3 Detector Response

Once the emitted photons reach the DOMs, the hits have to be converted to an equivalent signal that is readable by the DAQ system. At this stage, the procedure is divided in three parts: **a)** the Monte Carlo hit conversion in a DAQ signal, **b)** the simulation of the optical background, and **c)** the application of data filtering and triggering algorithms to the simulated data. This part of the detector simulation is implemented via a set of classes and applications part of the ROOT-based KM3NeT software suite, *Jpp* (see [195, 201] for more details).

In case of one or more photoelectrons occurring within the ToT of the first hit, the hits are merged in a single pulse whose amplitude is parameterised according to the characterisation of the PMT response from laboratory measurements. If the final amplitude is above the discrimination threshold (0.3 p.e.), the corresponding hit time and ToT data are generated. Here, the hit time accounts for the transit time distribution. When atmospheric muons or neutrino interactions are simulated, the optical background is added according to fixed rates of single hits and coincidences. At this last stage, a *run-by-run* simulation can optionally be performed. In this, the summary slice data from a run file is randomly sampled to simulate a realistic data taking condition for every triggered input event. The individual PMT counting rates are used to simulate the optical background, and channels are disabled according to the high-rate-veto flags in the sampled data. Non-functional PMTs are disabled according to the detector description file. Once all the hits in an event have been simulated, the corresponding data are processed by the same clustering and triggering algorithms applied to the real data [195].

4.3 Event Reconstruction

Once the events have been filtered and triggered, the last step in the simulation chain starts. The event reconstruction is a multistage process which uses the hits information (charge, photon arrival time, PMT position and orientation) to unveil the characteristics of its parent neutrino. In this section, only the algorithm for the reconstruction of the *tracks* is treated in detail (see also [127, 202]). For a detailed description of the *shower* reconstruction see Ref. [44].

In this section, the description of the KM3NeT event reconstruction algorithms will focus in ORCA, even though the same algorithms and techniques are used in ARCA.

4.3.1 Track Reconstruction

Muons with energies above 100 GeV can traverse the whole detector and have track directions almost colinear with their parent neutrino. Muon tracks can be characterised by 5 independent parameters: **1)** the position of the muon, $\vec{p}$, at a fixed time t_0; **2-3)** the direction of the track, that can be parametrised as a function of the azimuthal (ϕ) and zenithal angles (θ); **4)** the arrival time (t_0); **5)** the position of the hits along the trajectory.

The reconstruction of the track turns to be more complex given that the hits from the optical background (hits caused by ^{40}K and bioluminescence) are added to the hits from the signal. Therefore, before starting the reconstruction, hits have to be selected. *Scores* are given to hits that fulfills different coincidence pattern criteria. These scores represent the probability that a pattern can be randomly generated by the background. Hits with higher scores are selected, and those separated by less than 20 ns are merged (see [72] for more in-depth explanation).

As in the ANTARES muon track reconstruction algorithm (see Sec. 2.3), a linear prefit is performed over the positions of the hits to estimate a starting point for the muon track. The hits are assumed to occur on points that are along the track of the muon. This linear prefit is sensitive to the outliers from optical background hits and strongly scattered photons [72, 202]. In order to exclude these, a cluster of causally related hits is selected from the data. For events with eight hits or less, the solution with the largest number of hits is selected, unless a solution exists which yields a χ^2 smaller by (typically) three standard deviations or more when one hit less is used. For events with more than eight hits the fit is applied to all hits. Possible outliers are subsequently removed as long as their contribution to the total χ^2 is larger than (typically) three standard deviations. The process is repeated until reach a set of 12 best fitted test directions is reached, which provides at least one suitable start value for the subsequent fit stage [202].

The core of the reconstruction is the JGandalf algorithm. Starting from the prefit result, the five parameters that needs to be determined through the maximisation of a likelihood function are the muon direction and its position at a given initial time:

$$\mathcal{L} = \prod_{i=1}^{N_{\text{hits}}} \left[\frac{\partial P(\rho_i, \phi_i, \theta_i, t_{\text{res}})}{\partial t} \right]. \tag{4.1}$$

The maximisation runs over the number of selected hits in the PMTs. The PDF, P, is a function of the minimum distance of the muon to the i-th PMT (ρ_i), the orientation of the PMT (ϕ_i, θ_i) and the time residual of the hit (t_{res}). The maximisation of the likelihood function (Eq. 4.1) gives the reconstructed vertex and the direction of the muon trajectory [65, 202]. The median angular resolution for the KM3NeT-ORCA detector is shown in Fig. 4.6 for different classes of neutrino events.

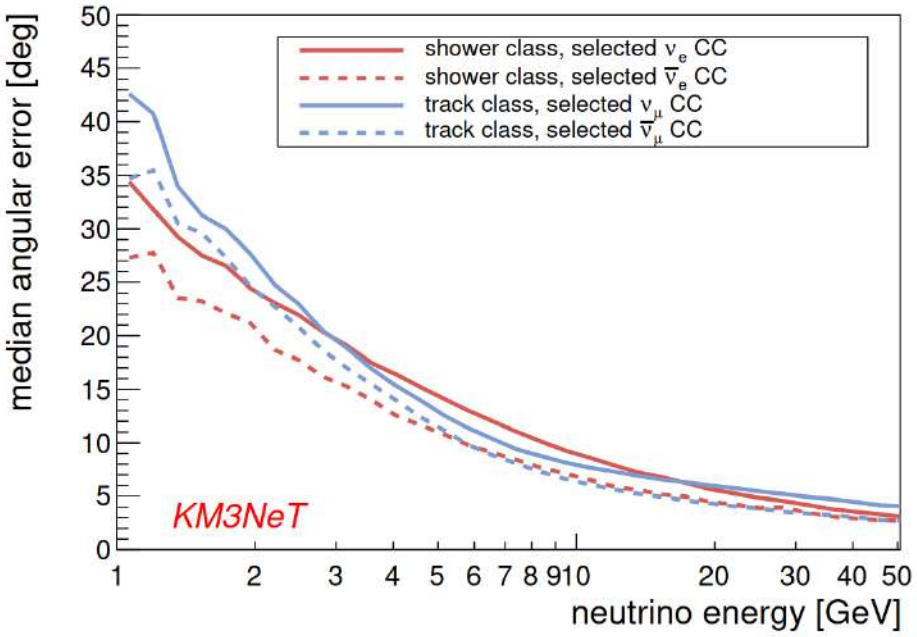

Figure 4.6: ORCA median angular resolution as function of the neutrino energy in the range of 1–50 GeV for different classes of neutrino events. From [195].

4.3.2 Energy Reconstruction

The estimation of the neutrino energy for muons comprises two steps. The first step consist in the estimation of the muon energy by reconstructing the length of the muon track and the interaction vertex. The estimation of the neutrino energy depends on the muon track length and the number of hits used in the reconstruction. By computing the distance between the first and last DOM hitted along the muon path, the muon track length can be calculated. The integration of the PDF (P) over a time window (δt) gives the number of hits N_{hits} used in the reconstruction. The relation between the number of hits and the energy of the interacting neutrino is obtained by fitting the median distribution of E_ν as a function of N_{hits} [72]. The light yield by shower signatures is proportional to the energy of the shower. Short tracks with large number of hits is an indicator of an energetic hadronic shower and hence, the energy of the neutrino is scaled up accordingly [44, 65, 203]. Figure 4.7 shows the MC energy *vs.* the reconstructed energy for $\nu_\mu(\bar{\nu}_\mu)$ and $\nu_e(\bar{\nu}_e)$ CC channels, clasiffied as *tracks* and *showers* respectively. At $E_\nu = 10$ GeV, the median energy resolution for ν_e CC events is about 25% whereas for ν_μ CC interactions is $\sim$30% since the outgoing muon deposits only a fraction of its energy before leaving the detector vicinity (Fig. 4.8).

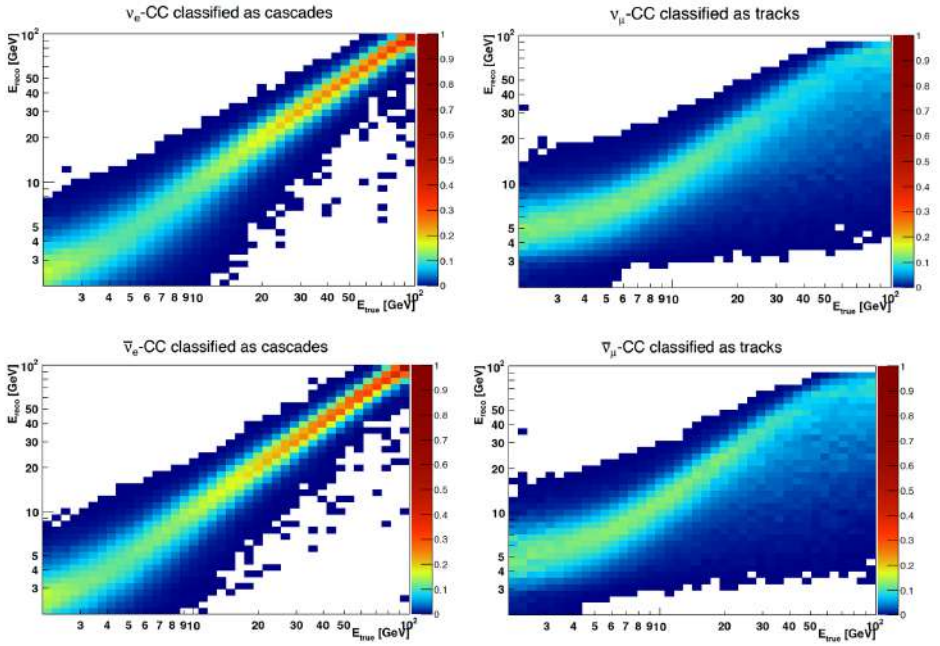

Figure 4.7: True neutrino energy *vs.* reconstructed neutrino energy for up-going ν_e (top) and $(\bar{\nu}_e)$ (bottom) CC classified as shower-like events (left) and ν_μ (top) and $(\bar{\nu}_\mu)$ (bottom) CC classified as track-like events (right). From [204].

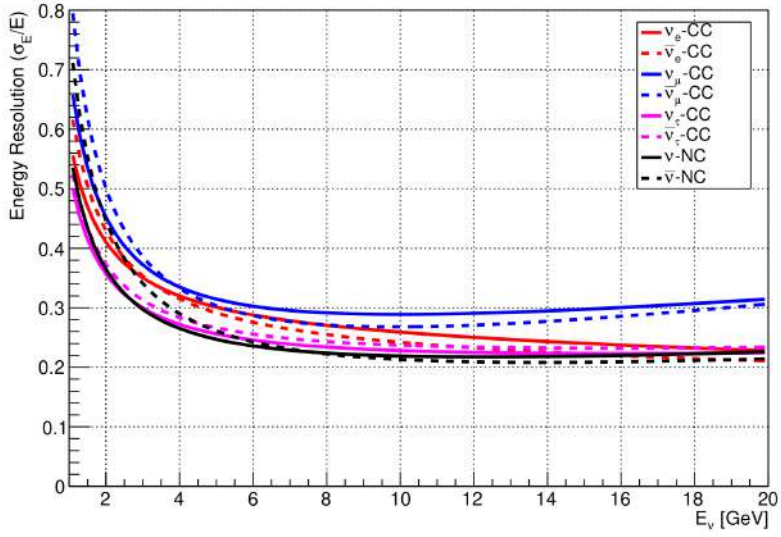

Figure 4.8: Energy resolution of ORCA as a function of neutrino energy E_ν for different neutrino interaction channels separated by flavour. From [65].

4.3.3 Particle Identification

At the detector, two different event topologies can be identified depending on the Cherenkov light yield after the neutrino interaction: track-like and shower-like events. Track-like events are produced in ν_μ CC and ν_τ CC (with muonic τ decays) interactions. The shower-like topology is produced by ν_e CC, ν_τ interactions with non-muonic τ decay, as well as NC interacctions of all flavours [65].

The event classification is performed using a machine learning classifier known as Random Decision Forest (RDF) [205] which has been developed within the collaboration [206]. A RDF is an ensamble of binary decision trees fed and trained with features characterising different classes. The output of the RDF is the class which received the majority of the votes.

In ORCA, the Particle IDentification chain (PID) is fed and trained with the reconstruction information of ν_μ CC for track-like topologies, and with ν_e CC and all NC events for shower-like topologies. The PID consists in a set of three consecutive RDF employed to filter out the background and the physics with the following output parameters:

- **Muon score:** represents the probability for an event of being an atmospheric muon *vs.* a neutrino.
- **Noise score:** represents the probability of an event of being pure noise *vs.* a neutrino.
- **Track score:** represents the probability of a neutrino event of being track-like *vs.* shower-like.

The values of the scores range between 0 and 1, with higher values representing higher probability of being an atmospheric muon, pure noise and track-like, respectively. Fig. 4.9 shows a schematic representation of the classification chain.

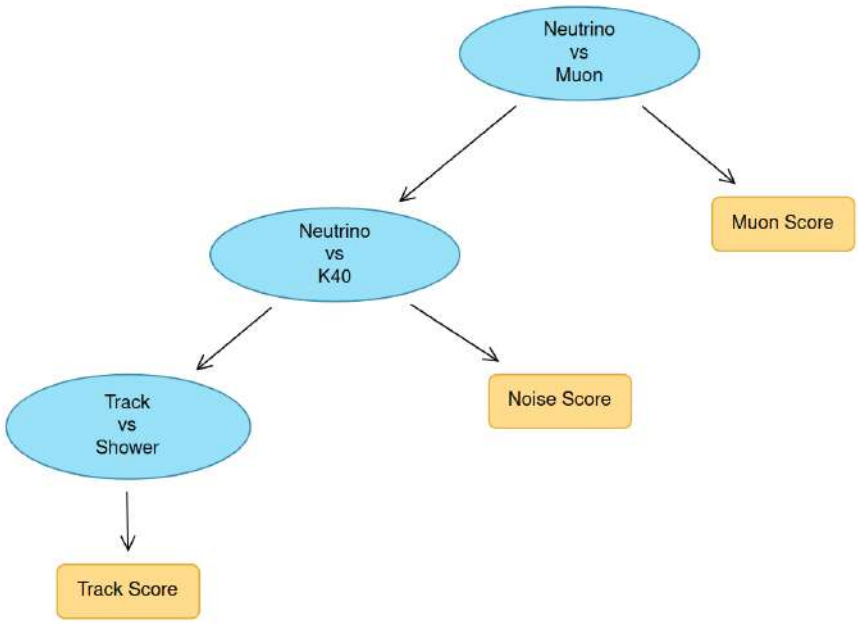

Figure 4.9: Schematic representation of the classification process. Each stage returns a value between 0 and 1, indicating the probability of a given event being classified as an atmospheric muon, a random noise event or as a track-like event.

The classifier performance of the event type classifier for neutrinos as *tracks* or *showers* is shown in figure 4.10.

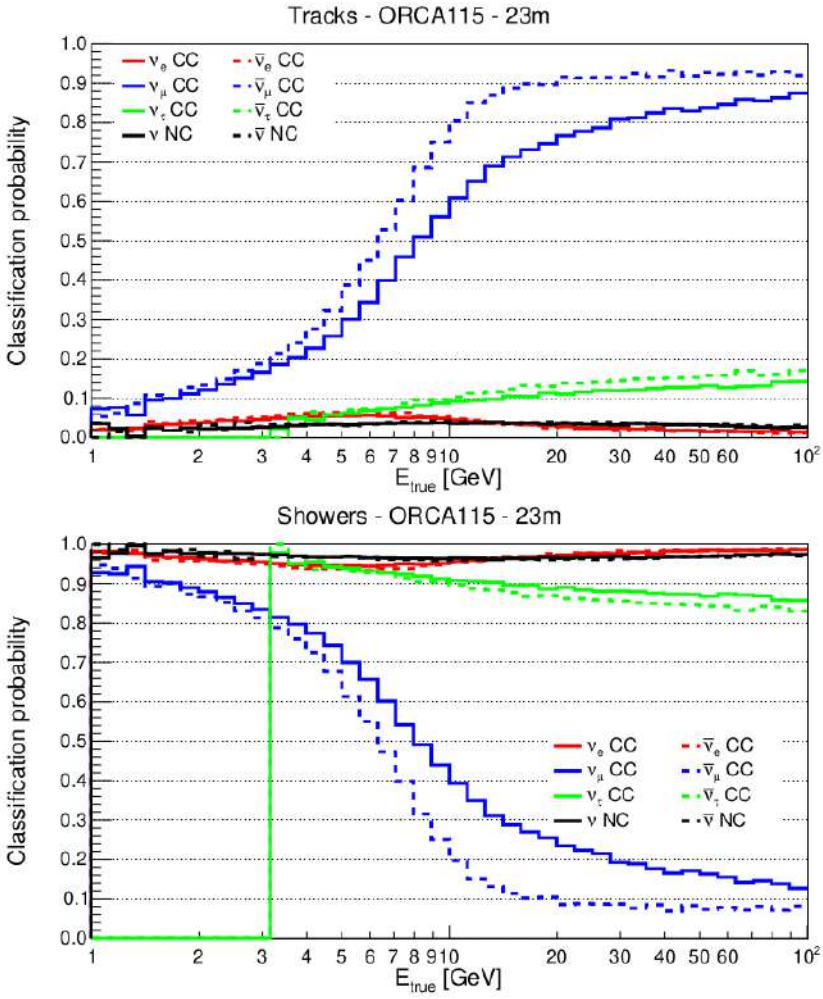

Figure 4.10: Classification probabilities for track (top) and shower-like (bottom) events for different interaction channels, as a function of the neutrino energy. The classification algorithm is based on a RDF classifier. From [65].

5 Indirect Searches for Dark Matter in the Sun

"What's the matter? What's the dark matter? Does it matter?"

Wes Nisker

The Universe is dominated by two invisible ingredients. The first one accounts for most of the energy of the Universe, and is called *dark energy*. Regarding the second one, many theories have been proposed to explain it, known as *dark matter*, that accounts for most of the mass of the Universe. The analysis described in this chapter focuses on the indirect search for dark matter with neutrino telescopes In Sec. 5.1, the basic concepts of dark matter (DM) and its properties are described. Some of the most important evidences for the existence of DM are presented in Sec. 5.1.1. In Sec. 5.1.2 and 5.1.3, dark matter candidates and different experimental strategies applied on the search for these elusive particles are presented. The second part of the chapter is devoted to the specific search for DM in the Sun with ORCA. In Sec. 5.2.2 the selection criteria applied to identify the signal over the background are described. The details of the analysis and the results are presented in Sec. 5.2.3 and 5.2.4, respectively.

5.1 Dark Matter

Despite the enormous efforts made by the scientific community, dark matter remains one of the biggest open problems in cosmology, astroparticle and particle physics. The nature of dark matter is yet unknown, and a large ammount of models and candidates can be found in the literature [207, 208]. However, in the past decades scientists have made significant progress to understand the properties of these particles, mostly by learning *what is not dark matter* [209]:

- Dark matter carries no color or electric charges and is no baryonic.
- Dark matter is not composed of *ordinary matter* (Standard Model particles).
- Dark matter does not emit nor absorb light (no electromagnetic interaction).
- Dark matter should be mostly non-relativistic (cold/warm dark matter).
- Dark matter particles do have mass, so they interact gravitationally. Its gravitational effect is ubiquitous in various aspects of the structure of the Universe.

According to the Big Bang Nucleosynthesis (BBN) [210], the ΛCDM model [11, 211] and the latest results from the Planck experiment [212], only about 4% of the energy–matter content of the Universe can be explained by *ordinary matter*. The remaining 96% is made of by a mix of dark matter (∼27%) and dark energy (∼69%), which was introduced to explain the observed accelerated expansion of the Universe at the present era [11, 213].

5.1.1 Evidence

The existence of dark matter is strongly evidenced by several astronomical phenomena. Without the presence of dark matter, a number of diverse astrophysical and cosmological events could not be explained and hence, as a common response to these, the cold non-baryonic dark matter arose. Among the evidences supporting the existence of dark matter are included: the galaxy rotation curves, the gravitational lensing effect, the galaxy red-shift surveys and the cosmic microwave background anisotropy. In this section, a brief overview of the most relevant evidences for the existence of DM is given [209].

Rotation Curve of Spiral Galaxies

In the 1970s, Ford and Rubin [214] discovered that rotation curves of galaxies are flat in the periphery of galaxies. The velocities of objects (stars or gas) orbiting the centers of galaxies, rather than decreasing as a function of the distance from the galactic centers as is expected by Kepler's law ($v(r) \propto 1/\sqrt{r}$), remain constant out to very large radius ($v(r) \approx$ constant). Similar observations of flat rotation curves have now been found for all galaxies studied, including our Milky Way. The simplest explanation is that galaxies contain far more mass than can be explained by the bright stellar objects residing in galactic disks [215–217]. This mass provides the force to speed up the orbits. To explain the data, galaxies must have enormous *dark halos* (neither absorbs nor emits light) made of unknown dark matter.

Fig. 5.1 illustrates the velocity profile of galaxy NGC 6503 as a function of radial distance from the galactic center. The baryonic matter which accounts for the gas and disk cannot alone explain the galactic rotation curve. However, adding a dark matter halo allows for a good fit to data [218].

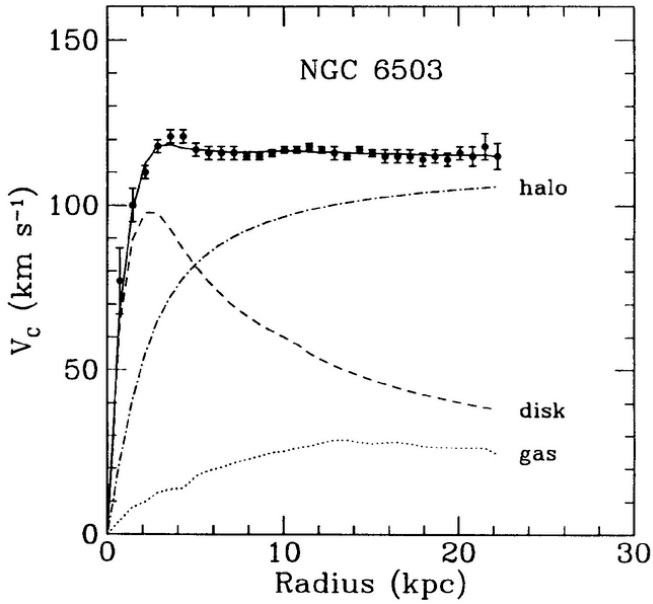

Figure 5.1: The rotation curve of galaxy NGC 6503 (data from [218]). The dark matter halo contribution is shown by the dashed-dotted line. From [219].

Gravitational Lensing

The phenomenon of light bending around a massive object is called *Gravitational Lensing* and was predicted by general relativity [220]. This phenomenon is a geometric effect sensitive to all types of matter, independent of any astrophysical assumptions. The gravitational lensing effect distorts background images in two ways: the *convergence* magnifies the background object by increasing its size and the *shear* stretches the image of an object tangentially around the foreground mass.

Fig. 5.2 shows the use of the gravitational lensing effect to reveal galaxies located behind nearest galaxy or galaxy cluster. In the probe of dark matter, the roles of the foreground and background matter distributions are switched. The appearance of lensing images of background galaxies reveals the existence of a foreground mass distribution which is otherwise invisible. The foreground mass distribution is generally referred to as the lensing mass [209].

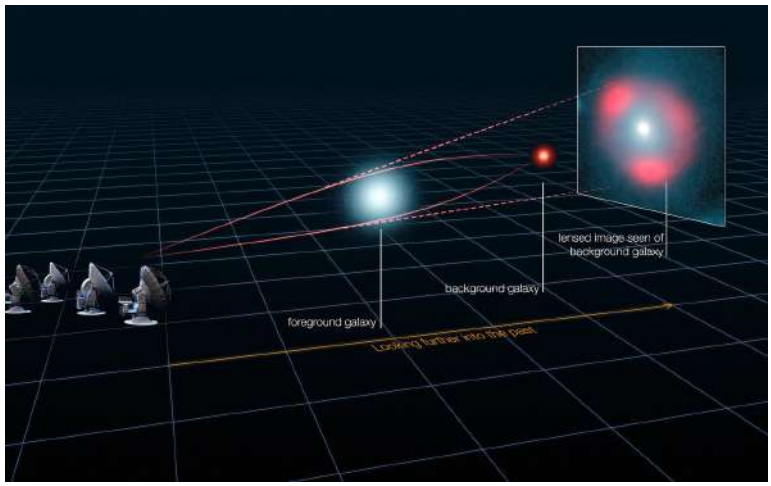

Figure 5.2: Schematic of the gravitational lensing effect. Credit to: ALMA (ESO/NRAO/NAOJ), L. Calçada (ESO), Y. Hezaveh et al.

The observation of the lensing effects without any apparent of luminous mass responsible for these lensing, indicates the presence of a huge amount of dark matter (see Fig. 5.3).

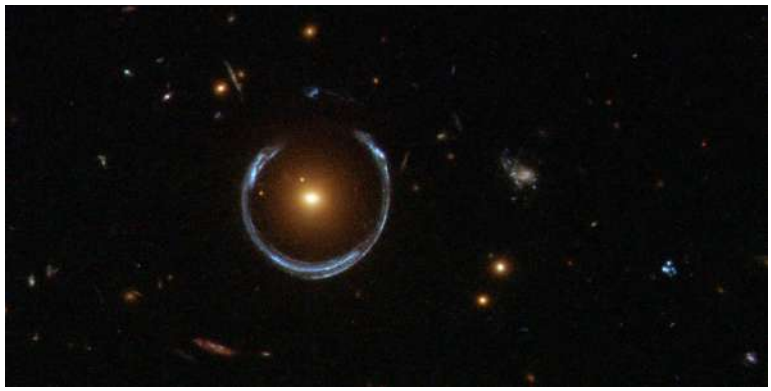

Figure 5.3: The gravity of a luminous red galaxy (LRG) has gravitationally distorted the light from a much more distant blue galaxy. More typically, such light bending results in two discernible images of the distant galaxy, but here the lens alignment is so precise that the background galaxy is distorted into a horseshoe – a nearly complete ring. Credit: ESA/Hubble & NASA.

The gravitational lensing effect and its manifestation in observational astronomy can be broadly classified into three categories, namely, strong lensing, weak lensing, and microlensing. In the case of strong lensing, multiple images or Einstein's rings are produced for a distant object in the background, while the weak lensing

causes distorted or deshaped images of a background object. In case of gravitational microlensing, the brightness of the object in the background of the gravitating mass appears to have increased to the observer in the foreground [221]. For a more detailed description about gravitational lensing effect, see [209, 222].

Bullet Cluster

As explained in [221], the weak and strong gravitational lensing phenomena have been put to use for discovering one of the most prolific evidences of dark matter in the *bullet cluster* or, more formally, in the cluster 1E0657-56. The bullet cluster (Fig. 5.4) was created as a result of one of the most energetic events to have happened in our Universe after the Big Bang, whereby two giant galaxy clusters collided at a distance of around 4 billion light years from the Earth at the constellation Carina. As a result of the collision, the smaller cluster passed through the larger one.

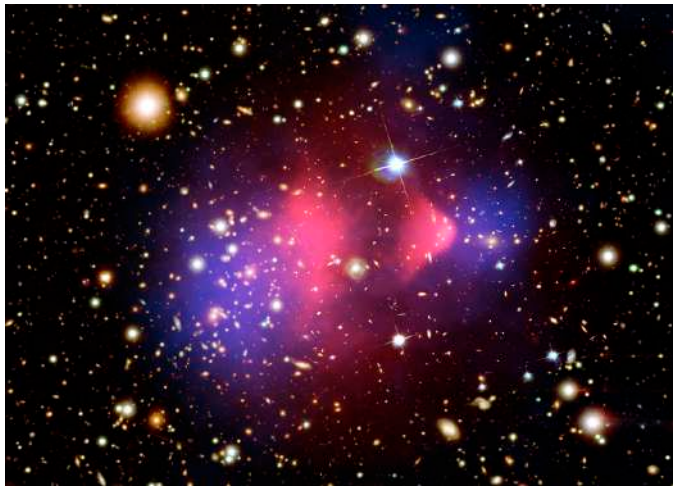

Figure 5.4: The gravitational lensing map (blue), overlayed over the optical and X-ray (pink) data of the Bullet cluster [223, 224]. Credit to: X-ray: NASA/CXC/CfA/M.Markevitch et al.; Optical: NASA/STScI; Magellan/U.Arizona/D.Clowe et al.; Lensing Map: NASA/STScI; ESO WFI; Magellan/U.Arizona/D.Clowe et al.

The X-ray analyses reveal the baryonic mass distribution of the two colliding clusters, while the weak and strong lensing reconstruct the dark matter components in them. The analysis shows that after the collision of the two clusters, when the smaller one passed through the core of the larger, the baryonic mass distribution of the smaller cluster suffered distortion in shape due to the immensity of the collision. As a result of the collision, the cluster took the shape of a bullet (and hence the name). The analysis also reveals that the impact was so great that it caused the baryonic matter (*ordinary matter*) in each colliding cluster to displace from its respective dark matter halo, while the dark matter halos themselves passed through

each other rather unperturbed and undistorted. Thus, the phenomenon of the *bullet cluster* not only gives an observational evidence of the existence of dark matter, but also indicates that the dark matter is almost collisionless. Moreover, it is very hard to explain by some alternatives to models of dark matter as the Modified Newtonian Dynamics (MOND) theory. Similar results were also obtained for the cluster MACS J0025.4-1222 [225].

N-body Simulations

To understand the large scale formation and structure of the Universe, the gravitational instability on cosmological scales and galaxy evolution, numerical N-body simulations are one of the most used approaches. Over recent years, the computational resources have allowed to create high resolution simulations that recreate the evolution of the Universe since the Cosmic Microwave Background (CMB) epoch. Cosmological evolution is simulated with linear gravitational clustering on large scales ($\geq$ 100 Mpc) and non-linear theory on small scales (between 10 kpc and 1 Mpc). On small scales, specific initial conditions are created to evolve the dark matter particles, with the consideration that the dynamics can be enhanced by introducing effects of gas dynamics, chemical processing, radiative transfers and other astrophysical phenomena.

There is a large variety of numerical codes that use the N-body theory and several applications including gas dynamics modelled by Smoothed Particle Hydrodynamics (SPH). These codes have proved being a realistic approach according to observations [226].

The hierarchically formation process of the Universe, in which galaxies are formed before clusters (the so-called *bottom-up scenario*), is supported by the measurement of the age of the stars in galaxies. The stars age ranges from 10 to 14 billion year old while many clusters are still in formation. Cold dark matter is needed to work as a compactor, allowing the matter to collapse and form structures.

The consistency of cold dark matter model of structure formation with the large-scale structures (Fig. 5.5) observed by galaxy surveys is comfirmed by N-body computer simulations, in which billions of dark matter particles are included [227]. The construction of the ΛCDM[1] model was constructed due to these studies (*e.g.* 2dF Galaxy Redshift Survey, Lyman-alpha forest and Sloan Digital Sky Survey).

[1] The ΛCDM model assumes that the Universe is made up of cold dark matter and dark energy (Λ).

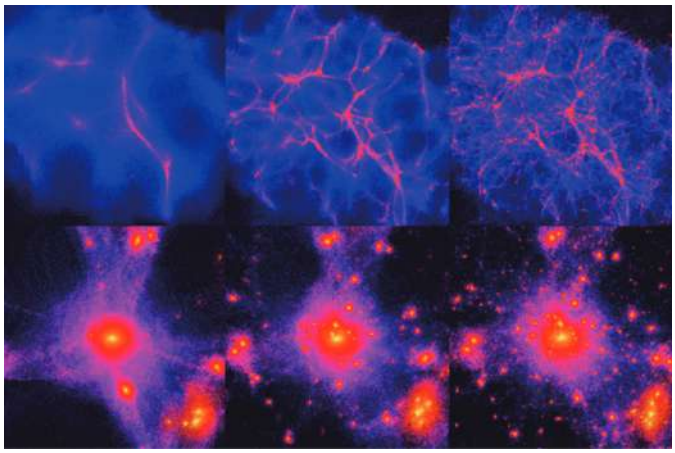

Figure 5.5: Numerical simulations of the large structure of the Universe. The upper panel is the cold dark matter model, the lower panel is the hot dark matter model. From [209].

The cold dark matter model explains successfully the structure formation of the Universe at large-scales but, fails at the scales related to the formation of galaxies (small-scales). Some of the problems of the cold dark matter model can be alleviated by the inclusion of the warm dark matter (WDM) component [209].

5.1.2 Candidates

All of the evidence for dark matter noted above is based on its gravitational interactions. Given the universality of gravity, this evidence does little to pinpoint what dark matter is. At the same time, the identity of dark matter has far-reaching implications: in astrophysics, the properties of dark matter determine how structure forms and impact the past and future evolution of the Universe; and in particle physics, dark matter is the leading empirical evidence for new particles. The identification of dark matter is therefore of central importance in both fields and ties together studies of the Universe at both the largest and smallest observable length scales [208].

According to their physical properties, dark matter candidates can be classified by: their velocity at the time of its decoupling, their production mechanism and, their particle type [209].

Kinematics

The CMB anisotropy spectrum is affected by the dark matter kinematic properties [228], playing an important role in the structure formation of the Universe. According to kinematic properties at the time of decoupling, dark matter can be divided in three categories[229].

- **Hot Dark Matter (HDM).** The composition of HDM [230] is made up of light particles, with masses of the order of eV or less ($m_{\mathrm{HDM}} \leq 1$ eV). The HDM model is disfavoured due to the relativistic nature of HDM, since highly relativistic particles generate high pressure and, as a consequence, inhibit the formation of galaxies by destroying the small-scale structure of the Universe (as demonstrated by N-body simulations), which is in contraposition with the observed scale structure.
- **Cold Dark Matter (CDM).** The CDM [231, 232] is made up of particles with masses in the GeV to TeV range, and are non-relativistic at decoupling. There is a plethora of CDM candidates, such as WIMPs (weakly interacting massive particles), WIMPZILLAs, etc. Due to the non-relativistic nature of CDM, the pressure and the diffusion distance of these particles is expected to be very low, favouring the formation of small-scale structres, as demonstrated by N-body simulations [233]. Even though CDM faces various problems, it is nowadays the favoured dark matter model.
- **Warm Dark Matter (WDM).** The WMD [234, 235] consist of particles in or above the keV mass range ($m_{\mathrm{WDM}} \geq 1$ keV) and hence, lies something in between the CDM and HDM. WDM is relativistic at decoupling, but non-relativistic at the radiation-to-matter dominance transition. Some of the possible WDM candidates are photinos, sterile neutrinos or light gravitinos.

Production Mechanism

Attending to the production mechanisms (as relics of the early Universe), dark matter can be classified as thermal or non-thermal. For a more in-depth discussion, see [236, 237].

- **Thermal relics.** Thermal relic particles are defined as particles which, due to annihilation, creation or scattering processes, are in thermal equilibrium in the early Universe. The expansion of the Universe drops the cosmic temperature as well as the particle density and the particle annihilation rate. The annihilation process becomes ineffective when the annihilation rate drops below the expansion rate and hence, particles freeze in to decouple from the cosmic heat bath (either if the particle is relativistic or non-relativistic). Dark matter is then formed by the resultant freeze out. This mechanism gives rises to the so-called *WIMP miracle* [238]. The WIMP miracle makes two assumptions in cosmological and particle physics. On the one hand, it assumes that the Universe is dominated by radiation before the freeze out. On the other hand, the model requires that the annihilation of dark matter into standard model particles is of order of the weak interaction cross-section. The WIMP miracle is the most accepted model, forming the theoretical basis of most of dark matter search experiments.
- **Non-thermal relics.** These are particles that have been produced non-thermally and never have been in thermal equilibrium with other particles [239]. As a consequence, their energy distributions are different from a normal thermal distribution. The non-thermal production is motivated by experimental

and theoretical considerations. The WIMP miracle assumptions are not satisfied. While the radiation dominance is established in the BBN period to the matter-radiation equality (temperature range of 1 MeV to 1 eV), the radiation dominance has not been probed. In addition, various large regions of the WIMP parameter space [240] have been ruled out by various indirect and direct WIMP searches [241, 242]. So new possibilities should be considered.

Particle Type

The results published by the Planck [212, 243] and WMAP [244] collaborations reveal that most of the dark matter must be non-baryonic, stable, and electrical and color neutral. Thus, the dark matter candidates are likely to interact weakly with ordinary matter [221].

Among the plethora of models and DM candidates reported in the literature [11, 208], some of the most popular are reviewed below:

- **WIMPs.** The WIMP paradigm has been a preferred framework chiefly because it often arises in beyond the Standard Model scenarios that address the hierarchy problem whilst also providing a simple mechanism to explain the observed relic abundance. This model includes different kind of dark matter candidates, from supersymmetric particles like the neutralino, to non-supersymmetric candidates such as little Higgs or universal extra dimensions [245, 246].
- **Axions and axion-like particles.** Quantum chromodynamics (QCD) effects produce an effective periodic potential in which the axion field moves. The oscillations of the axion field about the minimum of the effective potential, the so-called misalignment mechanism, generate a cosmological population of cold axions with an abundance depending on the mass of the axion [247, 248].
- **Dark photons.** The dark photon is a hypothetical hidden sector [249, 250] particle, proposed as a force carrier similar to the photon of electromagnetism but potentially connected to dark matter. The dark photon can interact with the Standard Model fermions.
- **Sterile neutrinos.** These hypothetical particles interact only gravitationally. The term *sterile* is used to distinguish it from the neutrino of the Standard Model [251].

5.1.3 Dark Matter Searches

There are three main strategies used by the scientific community to search for dark matter (see Fig. 5.6): production at colliders, direct detection via scattering with target nuclei, and indirect searches through the detection of signals from annihilation products.

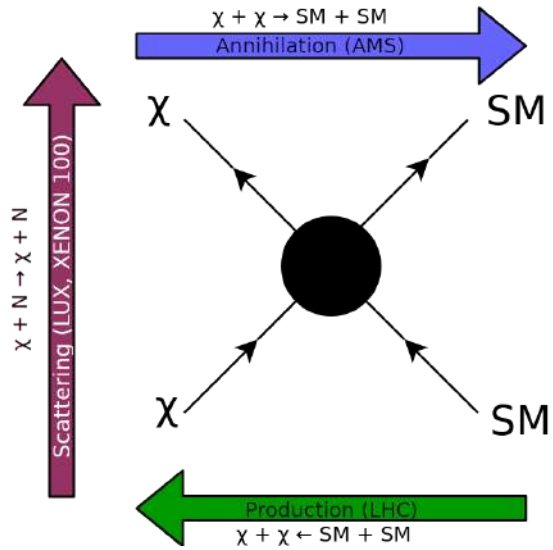

Figure 5.6: Diagram of dark matter detection mechanisms. χ represents the dark matter particle, SM stands for Standard Model particles, and N for the nucleus.

Collider Searches

Collider searches aim to detect signals from DM particles produced when colliding SM particles (e.g. protons in the case of the LHC) in controlled laboratory conditions. The presence of DM particles can be inferred using transverse momentum conservation. The net momentum in the plane perpendicular to the colliding beams before collision is zero, and must also be so after the collision has taken place. An imbalance in this plane, obtained as the negative vector sum of the transverse momenta of all detected particles, is the main signature for direct production of DM at colliders (see Fig. 5.7). This quantity is termed *missing transverse momentum* or *missing transverse energy* [252, 253].

Collider searches are only able to ascertain the WIMP stability on the timescale required for these particles to exit the detector. Examples of dark matter searches at the LHC can be found in Ref. [254–256].

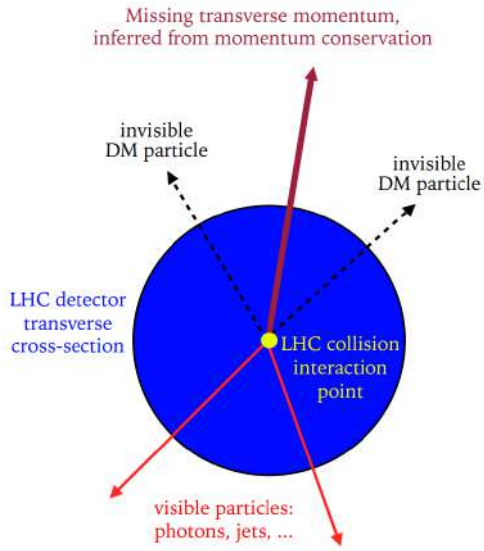

Figure 5.7: Schematic illustration of missing transverse momentum from DM production inferred from the recoil of visible particles, in a general purpose LHC detector. From [252].

Direct Searches

According to cosmological models of structure formation, the galaxy is immersed in a dark matter halo which bounds the luminous matter. The dark matter halo surrounding the Milky Way seems not being co-rotating with the solar system. Consequently, a flux of dark matter particles distributed in the halo would be passing through the Earth, the so-called dark matter *wind* [257]. Occasionally, dark matter particles could interact with ordinary matter, taking out a nucleus and signaling its encounter with a dark matter particle.

Since DM is electrically neutral, in most scenarios it will not interact with the atomic electrons but will instead scatter off, elastically, the atomic nucleus. The momentum transfer gives rise to a nuclear recoil which might be detectable. The expected rate of WIMPs scattering target nucleus depends on the local dark matter density, the WIMP velocity distribution, and the mass of the WIMP as well as the mass of the detector target nucleus.

Due to the circular motion of the Earth around the Sun, the velocity of the WIMP-nucleon changes with time. The different mean incident WIMP velocity in Summer and in Winter leads to a harder or softer WIMP spectrum [258] (see Fig. 5.8). Consequently, the number of DM signal events observed in a detector will be modulated over the year [11, 259].

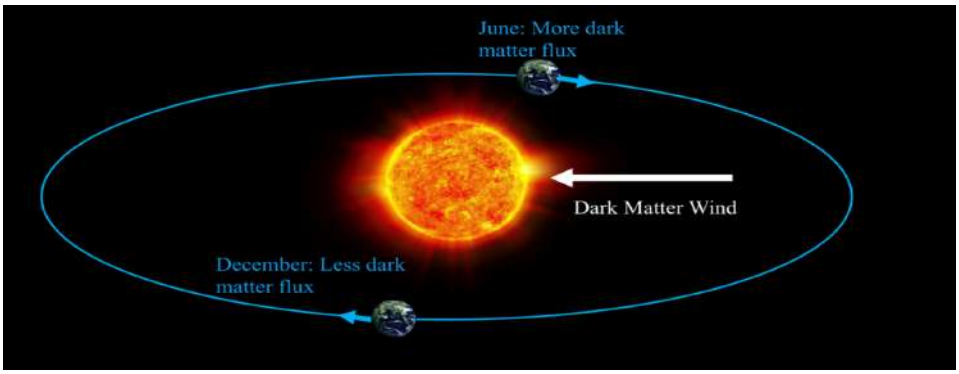

Figure 5.8: Illustration of the expected annual modulation in the dark matter collision rate. The flux of DM particles at the Earth will be higher in June than in December, because the Earth is travelling into the dark matter wind, whereas in December, the Earth is travelling away from the wind. From [260].

Since the interaction of WIMPs with baryonic matter is a priori unknown, the cross-section is parametrized as a contribution of two terms: one for spin-independent (SI) and another for spin-dependent (SD) couplings. At small momentum transfers (q) all partial waves of the nucleons add up and the WIMP scatters coherently off the entire nucleus. For higher q, the de Broglie wavelength $\lambda = h/q$ of the WIMP is reduced and only part of the nucleus participates in the interaction. This loss of coherence is only relevant for heavy targets such as Xe, I or W.

The spin-independent (SI) cross-section is given by:

$$\sigma_{\mathrm{SI}} = \sigma_n \frac{\mu^2}{\mu_n^2} \frac{(f_p Z + f_n (A - Z))^2}{f_n^2} = \sigma_n \frac{\mu^2}{\mu_n^2} A^2, \tag{5.1}$$

where μ is the WIMP-nucleus reduced mass, μ_n is the reduced mass of the WIMP-nucleon system, σ_n is the WIMP-nucleon cross-section, f_p and f_n are factors describing the WIMP coupling strength to protons and neutrons, respectively. Z and A are the atomic and mass number of the target, respectively. The second expression assumes $f_p = f_n$ which leads to an A^2 dependence of the cross-section, implying that heavier target nuclei are expected to produce higher event rates. On the contrary, the expected recoil energy will be smaller, hindering the detection.

The differential spin-dependent (SD) cross-section, where the WIMP is assumed to be a fermion coupling to unpaired nuclear spins J, has the following expression [261]:

$$\frac{d\sigma_{\mathrm{SD}}}{d|\vec{q}|^2} = \frac{8 G_F^2}{\pi v^2} \left[a_p \langle S_p \rangle + a_n \langle S_n \rangle \right]^2 \frac{J+1}{J} \frac{S(|\vec{q}|)}{S(0)}, \tag{5.2}$$

with momentum trasfer $|\vec{q}|$. $\langle S_p \rangle$ and $\langle S_n \rangle$ are the expectation values of the total spin operator for protons and neutrons in the target nucleus, which have to be calculated. G_F is the Fermi constant, and v is the WIMP velocity relative to the Earth. There is no dependence on A from coherence effects, instead the cross-section depends on the total nuclear spin J of the target nucleus as well as its spin-structure function $S(|\vec{q}|)$. While heavy nuclei are typically more sensitive to SI-interactions, the situation is different for SD-scattering, as only the spin structure of the nucleus is relevant: nuclei without unpaired spins are "blind", while the nuclear spin-structure of the light nucleus make them an excellent target to probe SD-interactions. Neutrons and protons typically contribute differently to the total spin of the target. For this reason, SD-results are commonly quoted assuming that WIMPs couple either only to neutrons (coupling strength $a_p = 0$) or to protons ($a_n = 0$) [11, 258].

Due to the dependence on the material and mass of the detector, different experimental techniques and approaches are used today on the quest for dark matter searches. Some of them are listed below [11]:

- **Solid-state cryogenic detectors:** Some of the current experiments are SuperCDMS at Soudan [262], EDELWEISS (Ge) at the Laboratoire Souterrain de Modane (LSM) [263] and CRESST ($CaWO_3$) at the Laboratori Nazionali del Gran Sasso (LNGS) [264]. These experiments are optimized for low-mass DM searches, and can probe masses down to ~ 0.2 GeV.
- **Noble liquids:** Liquid Argon (LAr) and liquid Xenon (LXe) are employed in dark matter experiments because of the high atomic number of the target. At present the best constraints on DM-nucleus interactions come from experiments using Xenon: the LUX experiment which was operated at SURF [265], PandaX-II at CJPL [266] and XENON1T at LNGS [267]. These experiments probe particle masses down to about 6 GeV (when using both light and charge signals) and the SI DM-nucleon cross-section down to 4.1×10^{-47} cm^2 (at 30 GeV). LAr experiments use the powerful pulse shape discrimination (PSD) that allows for distinguishing between electron recoils (ER) and nuclear recoils (NR) events, at the expense of higher energy thresholds than in LXe.
- **Directional detectors:** Detectors capable of measuring the direction of the recoiling nucleus would unequivocally confirm the Galactic origin of a signal and could probe the region below the neutrino floor [2] [268–270]. Because nuclear recoils have a range which is about 10 times smaller than the one of Compton recoils of the same energy, gaseous detectors have an excellent intrinsic background rejection if they can measure the range of events precisely. Several directional detectors are presently in operation: DRIFT in the Boulby Mine [271], DMTPC at the Waste Isolation Pivot Plant [272], MIMAC at LSM [273] and NEWAGE in the Kamioka laboratory [274]. A 1 m^3 detector has a typical mass of a few 100 g, depending on the target gas and its

[2] Neutrino floor: *"A theoretical lower limit on WIMP-like dark matter models that are discoverable in direct detection experiments. It is commonly interpreted as the point at which dark matter signals become hidden underneath a remarkably similar-looking background from neutrinos."*

operating pressure, and can measure the direction of an incoming nuclear recoil above a few tens of keV.

Indirect Searches

Dark matter particles that populate our Universe in galactic and extragalactic scales may self-annihilate and produce a flux of gamma-rays, cosmic-rays, neutrinos or anti-matter. Indirect searches for dark matter look for these occasional signatures [275]. The flux originated from dark matter annihilation can be parametrized as follows:

$$\frac{d\Phi}{d\Omega dE} = \frac{\langle\sigma v\rangle}{8\pi m_\chi^2} \times \frac{dN}{dE} \times \int_{l.o.s} \rho^2(l,\Omega) dl. \tag{5.3}$$

The differential flux in energy and solid angle Ω is proportional to the thermally averaged annihilation cross-section $\langle\sigma v\rangle$, to the number of particles of interest produced in the annihilation (dN/dE), and to the number density squared of dark matter particles (ρ/m_χ). The dark matter density ρ is integrated over the line of sight (l.o.s.) from the observer to the source, the so-called J-factor which accounts for the "shape" of the dark matter halo.

Indirect detection is, therefore, sensitive to the dark matter density distribution, to the annihilation cross-section, and to the dark matter mass. These are complementary information to collider and direct detection searches. For example, if a signal is seen in direct detection and the mass and scattering cross-section are inferred with a certain precision, this information could be used by indirect detection experiments to determine the dark matter density profile. One of the most popular dark matter density profiles is the so-called NFW [276]:

$$\rho_{\rm NFW}(r) = \frac{\rho_\odot}{\left(\frac{r}{r_s}\right)\left[1+\left(\frac{r}{r_s}\right)\right]^2}, \tag{5.4}$$

where r is the distance from the center of the halo and r_s a scale radius ($\sim$20 kpc for the Milky Way). $\rho_\odot$ is the dark matter density at the position of the Sun. Another option is the Einasto [277] profile, which has the following form:

$$\rho_{\rm Ein}(r) = \rho_\odot \exp\left\{-\left(\frac{2}{a}\right)\left[\left(\frac{r}{r_s}\right)^a - 1\right]\right\}, \tag{5.5}$$

where a is an extra shape parameter which takes the value $a \sim 0.2$ for the Milky Way. The third most common density profile is the Burket profile [278]:

$$\rho_{\rm Burk}(r) = \frac{\rho_\odot}{\left(1+\frac{r}{r_s}\right)\left(1+\frac{r^2}{r_s^2}\right)}, \tag{5.6}$$

which exhibits constant density for radii much smaller than the scale radius r_s (a value of $r_s \approx 6$ kpc is assumed for the Milky Way). The most favorable targets for indirect searches are generally those that are relatively nearby, have high dark matter densities, and low backgrounds [279].

The total spectrum of particles emitted in the source per annihilation/decay can be written as the sum of the spectra produced for all possible final states f,

$$\frac{dN}{dE} = \sum_f B_f \frac{dN_f}{dE}, \tag{5.7}$$

where B_f is the branching ratio to final state f and dN_f/dE is the spectrum of a certain particle produced for the final state f. The branching ratios to different final states are model-dependent. Indirect searches often take a model-independent approach and instead express results in terms of sensitivity to annihilation or decay to a particular final state. The final state can be any SM particle which is kinematically accessible. In particular, in the case of neutrino-based indirect searches like ANTARES or KM3NeT, the W^+W^-, $\mu^+\mu^-$, and $\tau^+\tau^-$ are considered *hard* channels whereas $b\bar{b}$ and $t\bar{t}$ are *soft* channels [279]. The terms *hard* and *soft* refer to the amount of particles yielded in the high and low energy spectra, respectively.

In general, indirect dark matter searches can be performed in different final states channels (see Ref. [11, 279] for a complete review):

- **Gamma-Rays:** Searches for gamma-ray emission from DM annihilation have focused on targets chosen taking into account a variety of considerations, primarily intended to maximize signal to noise. Nearby dwarf spheroidal galaxies contain very small amounts of gas, and do not host any significant astrophysical background at gamma-ray or X-ray frequencies, and are thus an optimal target choice for DM searches. A second target is the inner region of the Milky Way: while nearby and potentially hosting a large density of DM, the Galactic center region is however very bright at almost any wavelength, making the extraction of a signal highly challenging; nearby clusters of galaxies are also known to host significant astrophysical emission, but are potentially ideally suited to constrain DM decay. A great variety of experiments are searching (or will search) for dark matter through gamma-ray detection: FermiLAT [280], HESS [281], MAGIC [282], VERITAS [283], HAWC [284] or CTA [285].
- **Cosmic-Rays:** Stable charged particles produced by decays of products of, or directly from DM annihilation or decay, populate the cosmic radiation and are a prime target for indirect DM searches. To maximize signal to noise, searches focus on relatively rare particle species, such as positrons, antiprotons and antinuclei. While in certain models the production of particles and antiparticles is not symmetric [286], generally DM annihilation or decay produces as many particles as antiparticles in the final state. Charged particles produced by DM propagate and lose energy prior to reach the detector. Experiments such as PAMELA [287] and AMS [288] follow this approach.

- **Neutrinos:** DM can be captured in celestial bodies in significant amounts, depending on the DM-nucleon scattering cross section, the DM mass, and the DM flux incident on the celestial body of interest. DM annihilation in celestial bodies can result in the production of particles that can escape the body, such as the neutrino. Neutrinos, like gamma-rays, preserve spectral information and point back to the source, making them a useful astroparticle for indirect searches. Detection of astrophysical neutrinos generally involves instrumenting a large volume of water or ice and detecting the Cherenkov light produced in the detector medium as the products of neutrino interactions pass through it. Large volumes are needed to amass sufficient statistics for neutrino-based dark matter searches. The major contributions to these searches are being carried out by IceCube/DeepCore [289–291], ANTARES/KM3NeT [170, 292–295], BAIKAL-GVD [296, 297] and SuperKamiokande [298, 299].

5.2 Indirect Search for Dark Matter in the Sun with ORCA

As described in Sec. 4.1, ORCA has a ∼few GeV low energy threshold which allows for studies on oscillations with atmospheric neutrinos. ORCA will contribute, among others, to two fundamental questions: the neutrino mass ordering (NMO) and the nature of dark matter, with important advantages with respect to other experiments. The measurement of the neutrino oscillation parameters, the detection of neutrinos from supernova (SN) explosions, the search for point-like sources of cosmic neutrinos and the measurement of the diffuse neutrino cosmic flux are also among the topics covered in the ORCA physics program. Regarding dark matter, the Sun and the Galactic Center are among the preferred sources where to look for, taking advantage of their large masses and proximity or excellent visibility from the detector location on Northen Hemisphere [173].

5.2.1 Dark Matter in the Sun

Due to its popularity among the scientific community, the WIMP dark matter particle is the scenario assumed in this analysis. As mentioned in Sec. 5.1.2, WIMP particles tend to accumulate in massive bodies, such as the Sun. The proximity of the Sun to the Earth makes it an ideal candidate to perform indirect dark matter searches. Moreover, the Sun is a source with an expected low neutrino astrophysical background.

In order to generate the neutrino spectrum needed for the analysis, the WimpSim [160] package is used. This package relies on other simulation codes to perform different tasks: DarkSusy [300], Pythia [301] and Nusigma [302]. The WimpSim simulation chain can be summarized as follows:

1. **Model selection.** Before starting the simulation, different parameters and models have to be selected. DarkSUSY provides several elegible models needed for the simulation.
   - Select the dark matter model. The model chosen for this analysis is the Minimal Supersymmetric Standard Model (this is the default model in DarkSUSY).
   - Fix the value of the local dark matter density: $\rho_{\odot} = 0.3$ GeV/cm^3 (DarkSUSY).
   - Define the halo profile model. In this work, the NFW [276] profile and a Maxwellian velocity distribution with mean value of 270 km/s are chosen.
   - Select the solar density profile model. The Standard Solar Model (SSM) is chosen (default model).
   - The neutrino oscillation and mass parameters have to be inputed in WimpSim. The values chosen are the world best-fit values [11]:
     - $\theta_{12} = 33.56^{\circ}$, $\theta_{13} = 8.46^{\circ}$, $\theta_{23} = 416^{\circ}$,
     - $\delta = 261^{\circ}$,
     - $\Delta m^2_{21} = 7.5 \times 10^{-5}$ eV^2 and $\Delta m^2_{31} = 2.524 \times 10^{-3}$ eV^2.
2. **WIMP–WIMP annihilation.** WIMPs that are captured in the Sun, annihilate and produce high energy quarks, leptons and bosons. Then, these particles decay and hadronize and eventually produce final state neutrinos. These processes are simulated through Pythia [301].
3. **Neutrino interaction.** Final estate neutrinos may interact with the solar medium through charged or neutral channel interactions. If a non-τ CC interaction takes place, the neutrino is "destroyed". Instead, if a τ particle is produced, the neutrino would regenerate and be taken into account until the end of the simulation. If a NC interaction takes place, the neutrino lose energy and continue propagating. These interactions are taken care of by Nusigma [302] and Pythia.
4. **Neutrino propagation.** Once neutrinos leave the solar medium, they are propagated and oscillated until they reach the Earth. These processes are simulated by WimpSim.

In this analysis, the chosen range of WIMP masses goes from 15 to 100 GeV, and only three annihilation channels ($\tau^+\tau^-$, $b\bar{b}$, W^+W^-) have been considered, assuming a 100% branching ratio for each channel. For a more detailed description of the simulation codes and their parameters, see [160, 161, 300–302].

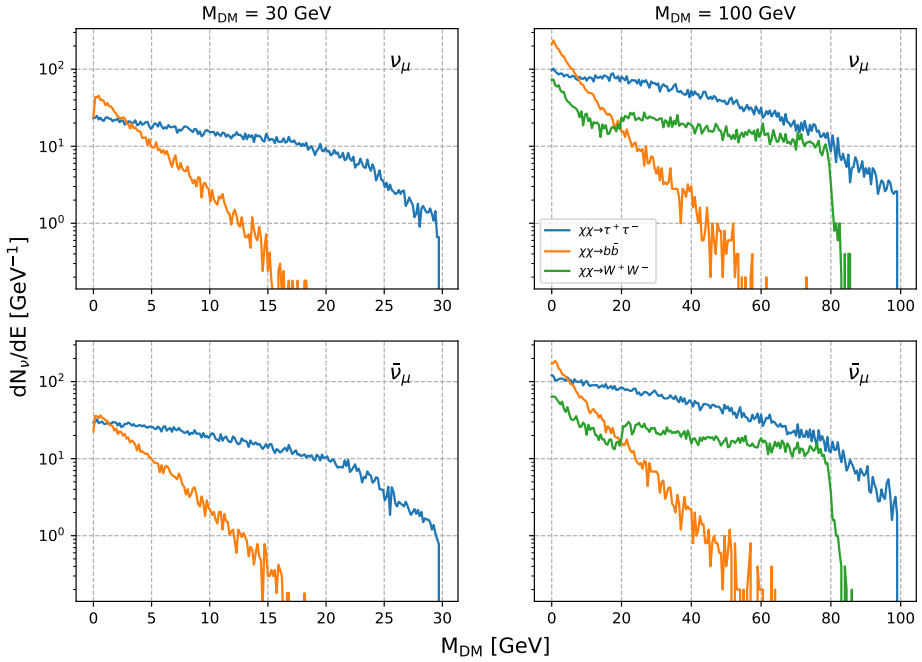

Figure 5.9: Neutrino (top) and antineutrino (bottom) yield from DM annihilation, at Earth, from the $\tau^+\tau^-$ (blue), $b\bar{b}$ (orange) and W^+W^- (green) annihilation channels, as a function of the neutrino energy for two WIMP masses (M_{DM}). The W^+W^- channel is only accessible for WIMP masses above the W mass ($\sim$80.4 GeV).

Fig. 5.9 illustrates the neutrino and antineutrino spectra from DM annihilation in the Sun, after propagation to Earth, and as a function of the DM mass. The colour lines correspond to the three channels.

5.2.2 Event Selection

The detector configuration considered in this analysis is the so called *full ORCA configuration*, consisting on 115 DUs, horizontally spaced by 23 m and with 9 m vertical spacing between DOMs.

This analysis is focused in the ν_μ signature. Therefore, in order to reduce the atmospheric muon and noise contamination in the data sample and to optimize the selection of *track-like* events, a set of cuts has to be defined. The selection criteria is detailed below:

- **Zenith cut:** the atmospheric muon contribution comes from downward–going events so, a cut selecting only upward–going events ($\theta_{\text{zenith}} > 90°$) reduces significantly the amount of atmospheric muons in the sample.

- **Muon track:** in the final sample only an atmospheric muon contamination below 5% is allowed by choosing a cut of `muon_score` < 0.05.
- **Noise cut:** to reject events from pure-noise contamination, a cut on the `noise_score` < 0.1 is imposed.
- **Angular error estimate (β):** only events with an error in the angular reconstruction below 1° are taken into account.
- **Track cut:** track events are selected with high values of the `track_score` parameter. In contrast to the previous parameters that are fixed for the analysis, the `track_score` parameter is not, and values ranging from 0.7 to 0.95 are explored in order to achieve the best discovery potential (see Sec. 5.2.3).

θ_{zenith}	β	`Noise_score`	`Muon_score`	`Track_score`
$> 90^\circ$	$< 1^\circ$	< 0.1	< 0.05	[0.7, 0.95]

Table 5.1: List of selection cuts applied on the search for DM in the Sun with ORCA.

Assuming the Honda flux [32] for atmospheric muons and neutrinos, the expected number of events passing the selection cuts for one year of ORCA full configuration is shown in Tab. 5.2.

Component	Events	%
ν NC + $\nu_{e,\tau}$ CC	512	3.3
ν_μ CC	14865	96.7
Atm. μ	0	0
Total	15377	100

Table 5.2: Monte Carlo number of expected events for one year of ORCA 115 DUs 23 m, after cuts on `track_score` > 0.7, `noise_score` > 0.1, `muon_score` > 0.05, $\beta < 1^\circ$ and $\theta_{\text{zenith}} > 90^\circ$.

The purity on the track selection achieved, for a `track_score` > 0.7, is about 96.7% with a negligible contribution from atmospheric muons.

5.2.3 Analysis

The goal of this analysis is to establish the discovery potential of the ORCA detector to a WIMP signal from the Sun. In order to achieve this, an unbinned likelihood method is used in which the *signal + background* hypothesis is compared to the *background-only* hypothesis, retrieving the number of signal events that maximizes the likelihood, for each annihilation channel and selection cut. Once the optimum selection cuts are defined, the final number of signal events is obtained and a neutrino flux computed. After that, this flux is used to calculate a limit on the WIMP-proton interaction cross-section.

Effective Area and Acceptance

As described in Sec. 3.4.2, the effective area is the equivalent surface of the detector to a certain energy flux. This is a parameter that can only be determined through simulations. The effective area does not depend on the model of the neutrino flux, but on the neutrino energy, azimuthal and zenithal angles as well as on the number of detected events, which relies on the parameter cuts applied to the MC sample.

The effective area is computed in the following way:

$$A_{\text{eff}}(E_\nu) = \frac{N_{\text{sel}}(E_\nu)}{k(E_M^{1-\gamma} - E_m^{1-\gamma})} \cdot \frac{w_2(1-\gamma)}{F \cdot I_\theta \cdot E^\gamma}, \tag{5.8}$$

where N_{sel} is the number of simulated events that are selected after reconstruction, triggering and quality selection, k is the full number of generated events, E_m and E_M represent the energy of the lower and upper bounds of the energy bin, respectively, w_2 is the generation weight (see Eq. 3.2), γ is the spectral index defined in Sec. 2.2.1, F is the number of seconds in one year and I_θ is the angular space factor (defined in Sec. 2.2.1).

Fig. 5.10 shows the effective area of the ORCA detector (full configuration), for the upward–going ν_μ and $\bar{\nu}_\mu$ CC channel and different `track_score` cuts (see Table 5.1).

The expected number of events to be detected (n_{ev}), for a given neutrino flux Φ_ν (units of $[\text{m}^{-2}\text{s}^{-1}]$) after a data taking period T (lifetime, in [s]) [76, 165, 169] is given by:

$$n_{\text{ev}} = \underbrace{A_{cc}(M_\chi^l)}_{\text{m}^2} \cdot \underbrace{\Phi_\nu}_{\text{events}/(\text{m}^2\ \text{s})} \cdot \underbrace{T}_{\text{s}} \tag{5.9}$$

where $A_{cc}(M_\chi^l)$ is the detector acceptance (in units of $[\text{m}^2]$), where the superscript l indicates the annihilation channel ($\tau^+\tau^-$, $b\bar{b}$, ...). The acceptance can be understood as a weighted average of the effective area of the detector with the neutrino spectra $dN_{\nu_\mu(\bar{\nu}_\mu)}/dE_{\nu_\mu(\bar{\nu}_\mu)}$ (see Fig. 5.9) yielded by the WIMP annihilation:

$$A_{cc}(M_\chi^l) = \langle A_{\text{eff}}(M_\chi)\rangle = \frac{\int_0^{M_\chi} \left(A_{\text{eff}}^{\nu_\mu}(E_{\nu_\mu}) \frac{dN_{\nu_\mu}}{dE_{\nu_\mu}} dE_{\nu_\mu} + A_{\text{eff}}^{\bar{\nu}_\mu}(E_{\bar{\nu}_\mu}) \frac{dN_{\bar{\nu}_\mu}}{dE_{\bar{\nu}_\mu}} dE_{\bar{\nu}_\mu} \right)}{\int_0^{M_\chi} \left(\frac{dN_{\nu_\mu}}{dE_{\nu_\mu}} dE_{\nu_\mu} + \frac{dN_{\bar{\nu}_\mu}}{dE_{\bar{\nu}_\mu}} dE_{\bar{\nu}_\mu} \right)}, \tag{5.10}$$

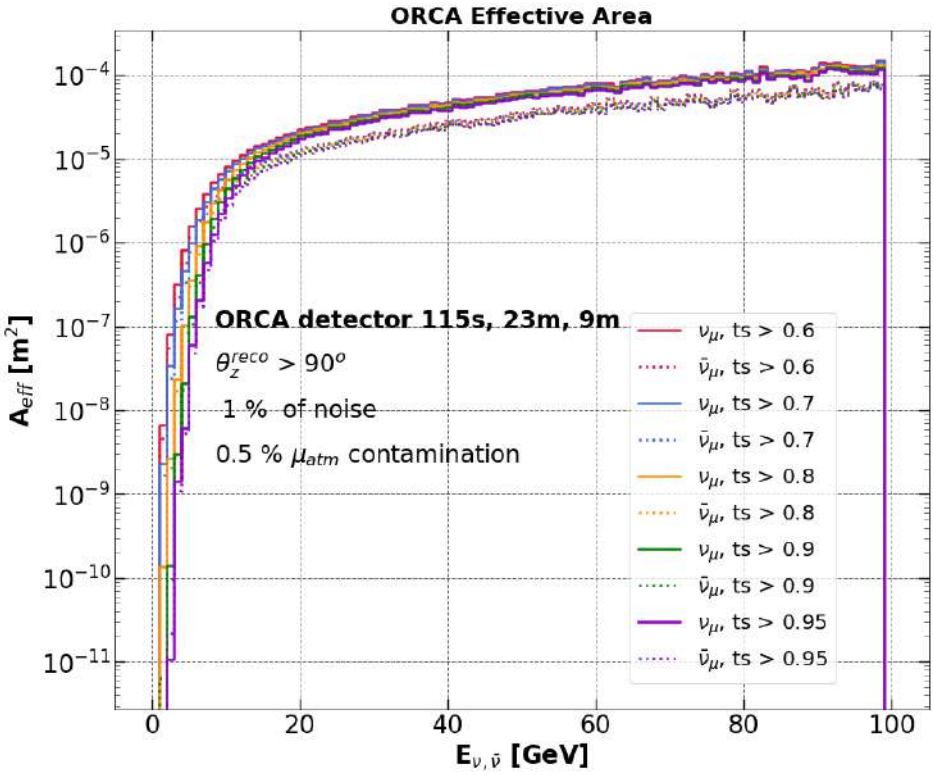

Figure 5.10: Effective area for the 115 DU and 23 m ORCA configuration for upward-going ν_μ (solid line) and $\bar{\nu}_\mu$ (dotted line) for different values of `track_score` (color code in the legend).

where the effective area has been averaged for neutrinos and antineutrinos. The denominator on the previous equation is the total number of events (neutrinos + antineutrinos) predicted by the model (figure 5.9).

The acceptance (Fig. 5.11) not only depends on the neutrino effective area, but also on the upper-bound WIMP mass (M_χ)[3] and on the considered annihilation channel ($\tau^+\tau^-$, $b\bar{b}$, W^+W^-), given that different channels and WIMP masses yield different neutrino spectra.

[3]The mass of the WIMP in this text will be shown interchangeably as M_{DM}, M_χ or M_{WIMP}.

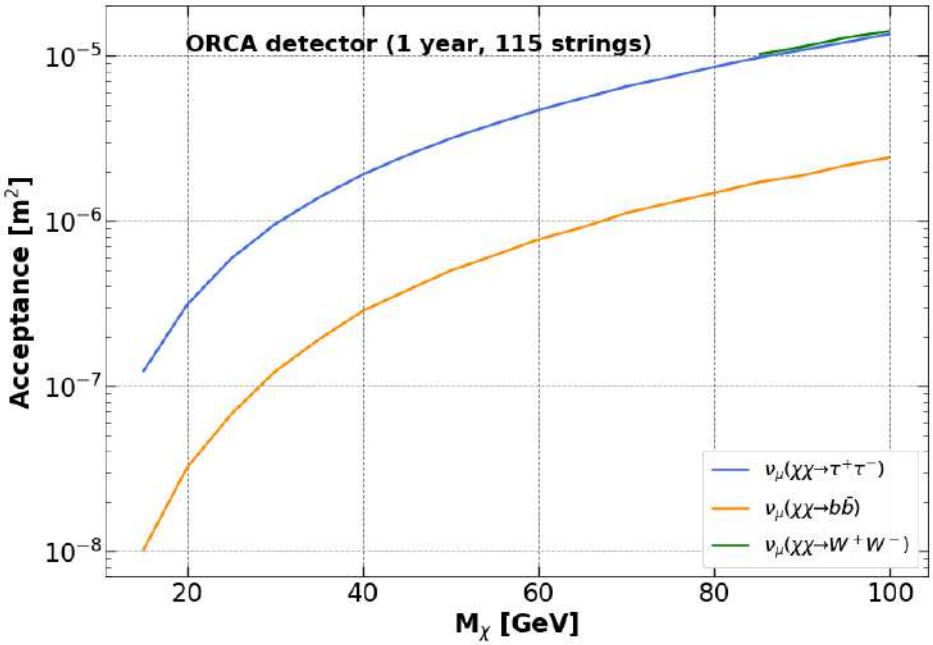

Figure 5.11: Acceptance of the ORCA detector for the $\tau^+\tau^-$ (blue), $b\bar{b}$ (orange) and W^+W^- (green) annihilation channels, for upward-going ($\nu_\mu + \bar{\nu}_\mu$) with `track_score` > 0.7.

Likelihood Ingredients

The expression of the Likelihood function used in this analysis is similar to the one applied in the SAνs with ANTARES (Eq. 3.14):

$$\ln \mathcal{L}(n_s) = \sum_{i=1}^{N} \ln \left[n_s \mathcal{S}(\Psi_{\odot,i}, \beta_i, N_{\text{hits},i}) + n_b \mathcal{B}(\Psi_{\odot,i}, \beta_i, N_{\text{hits},i}) \right] - \left[n_s + n_b \right]. \quad (5.11)$$

As described in Sec. 3.4.2, the *ingredients* are histograms that describe the statistical behaviour of the signal ($\mathcal{S}$) and the background ($\mathcal{B}$). Then, these ingredients work as PDFs. In this analysis, both PDFs are built using the information of the direction of the particles[4] ($\Psi_\odot$), the energy estimator (N_{hits}) and the error estimate on the reconstructed angle (β). The total number expected events, N, can be splitted in the expected number of signal and background events $N = n_\text{s} + n_\text{b}$. The parameter to fit is n_s.

For the signal, the ingredients are built from MC simulations weighted by the DM-neutrino energy spectra (for each annihilation channel). Instead of doing a follow

[4] Ψ and $\Psi_\odot$ are used interchangeably throughout the text.

up of the Sun along its path and comparing its position at a certain time with the MC sample (which has a high computational cost), all signal events from the MC sample are assumed to arrive from the Sun. The PSF is built by comparing the reconstructed direction with the *true* direction (the one generated at Monte Carlo level).

For the background, the MC sample is weighted with the HONDA flux [32]. The background is distributed uniformly at all distances to the Sun. The PSF of the background is built from a comparison of a MC scrambled direction with the reconstructed direction in the following way:

$$\cos(\Psi) = \vec{v}(1, \theta_{\mathrm{MC}}, \phi_{\mathrm{MC}}) \cdot \vec{u}(1, \theta_{\mathrm{reco}}, \phi_{\mathrm{reco}}), \tag{5.12}$$

where Ψ is the angular difference between the *true* direction, $\vec{v}(1, \theta_{\mathrm{MC}}, \phi_{\mathrm{MC}})$, and the reconstructed direction, $\vec{u}(1, \theta_{\mathrm{reco}}, \phi_{\mathrm{reco}})$. These directions are unitary vectors in spherical coordinates.

In addition to the PSF distributions, two more parameteres are included in the PDFs: the reconstruction quality parameter β and the number of hits (N_{hits}) considered in the track reconstruction, used as an energy estimator. As in the SAν analysis (Sec. 3.4.2), instead of considering the PDFs for the signal and background as a 3-dimensional PDFs ($P(\Psi_{\odot}, \beta, N_{\mathrm{hits}})$), they are considered as the joint distribution of a 1-dimensional and a 2-dimensional PDFs: $P(\Psi_{\odot}) \cdot P(\beta, N_{\mathrm{hits}})$.

Fig. 5.12 shows an example of the PSF for the signal ingredient of the three annihilation channels: $\tau^+\tau^-$ (blue), $b\bar{b}$ (orange) and W^+W^- (green) for a WIMP mass of 85 GeV, alongside the background PSF (red). The top plots represent the distributions of the $\log_{10}(\Psi_{\odot})$, while the distributions of $\Psi_{\odot}$ per solid angle are shown at the bottom.

Fig. 5.13 illustrates the two-dimensional PDF ingredient for the signal (top) and for the background (bottom). These PDFs are normalized to unity. The colorbar on the right shows the probability, in logarithmic scale, for a signal (top) and background (bottom) event, to be reconstructed with a certain β and N_{hit}. Lighter colors represent higher probabilities.

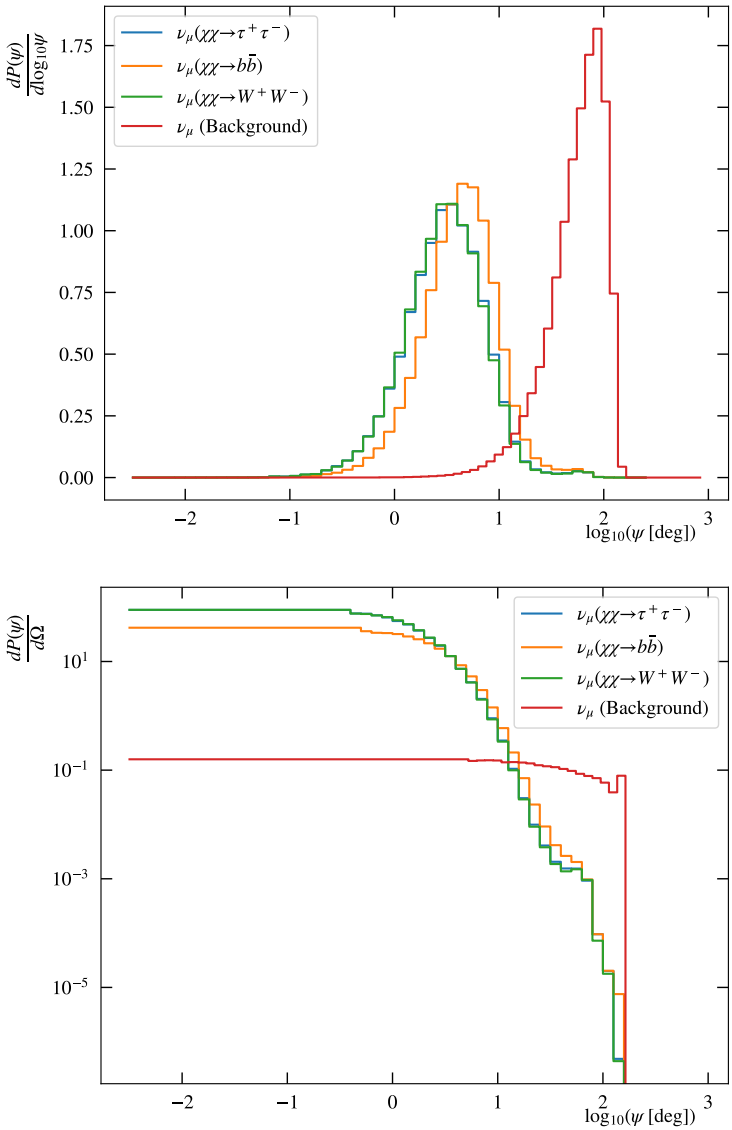

Figure 5.12: PSF for $\nu_\mu + \bar{\nu}_\mu$ built from MC simulations for a WIMP mass of 85 GeV. The distribution of $\log_{10}(\Psi_\odot)$ is shown on the top panel, while the $\Psi_\odot$ per solid angle is shown at the bottom. The PSF of the three annihilation channels, $\tau^+\tau^-$, $b\bar{b}$ and W^+W^-, is shown together with the background.

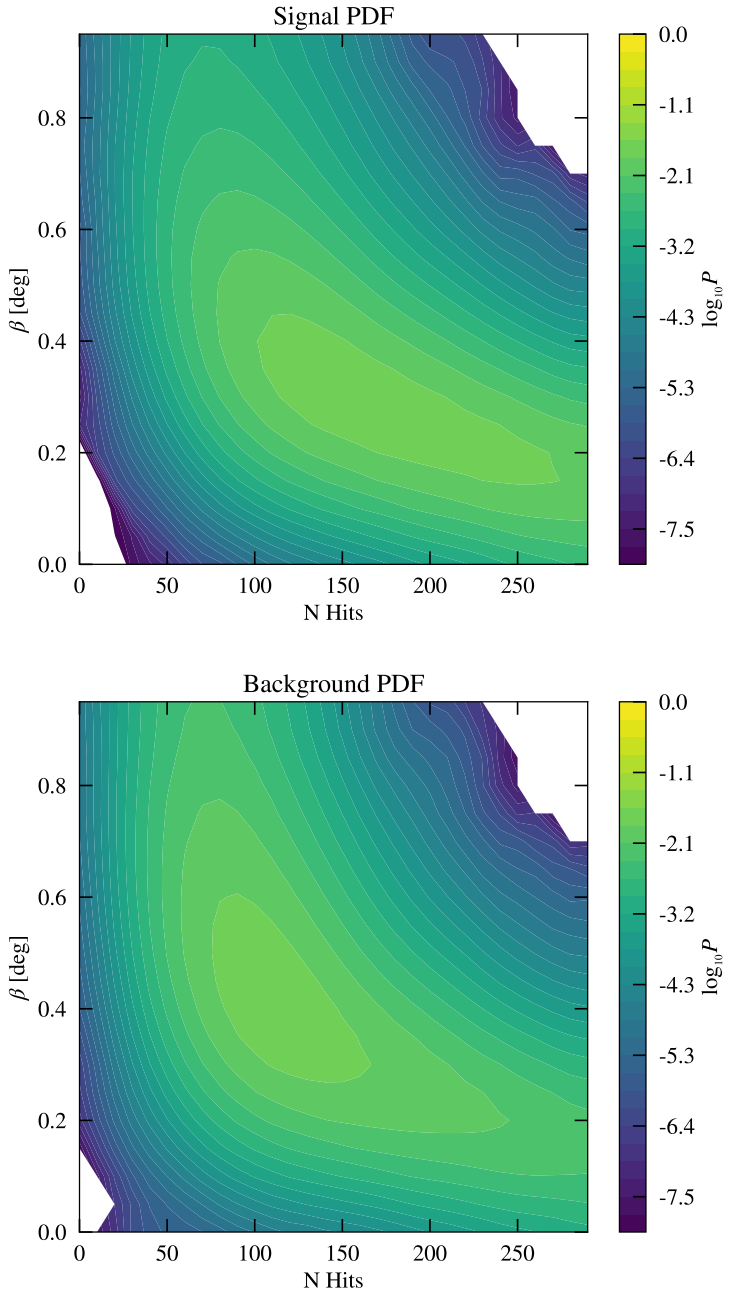

Figure 5.13: Two-dimensional PDFs of $\nu_\mu + \bar{\nu}_\mu$ for the signal (top) and background (bottom). The signal PDF shown is for the $\tau^+\tau^-$ annihilation channel and a WIMP mass of 85 GeV. See text for more details.

Pseudo Experiments

The *Pseudo Experiments* (PEXs), as explained in Sec. 3.4.2, are a series of simulations in which a large number of skymaps are populated with different number of signal and background events. The features (distance to the source, β parameter and number of hits) of these events are sampled from the ingredient PDFs. Once the skymaps are generated, the optimization method searches for a number of signal events ($\hat{n}_s$) that maximize the likelihood function (Eq. 5.11). In order to optimize the search for DM toward the Sun, 10^4 PEXs have been performed for different values of the `track_score` parameter, for different number of injected signal events (n_{inj}), annihilation channels and WIMP masses.

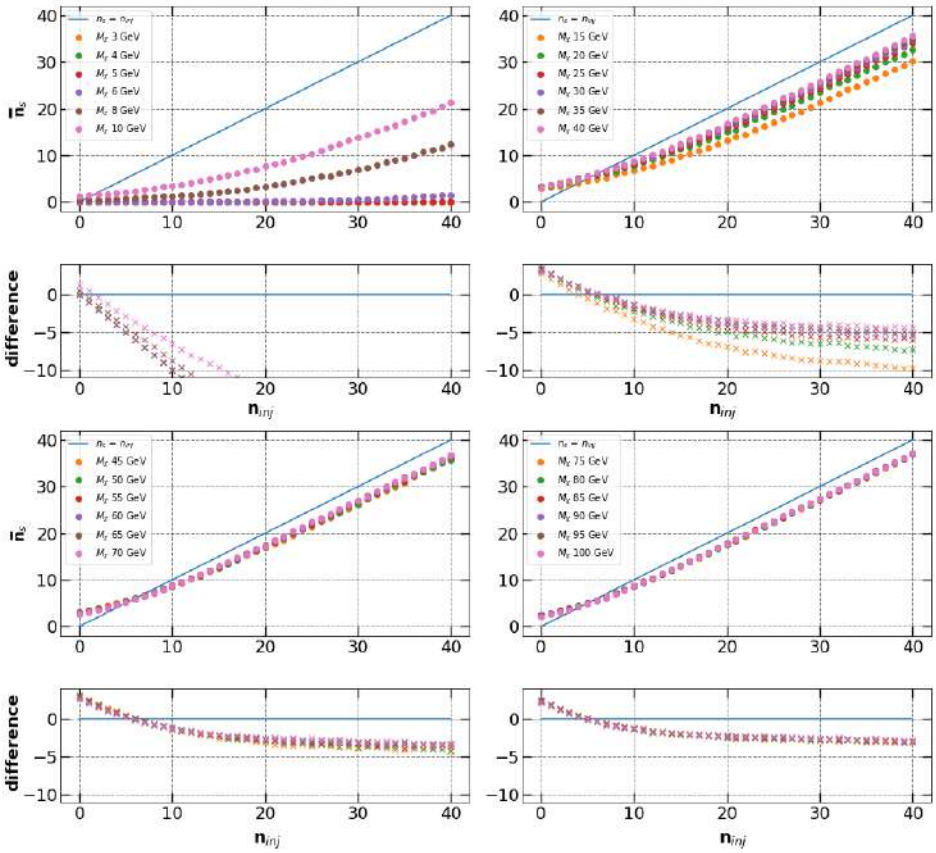

Figure 5.14: Average value of the fitted number of signal events ($\bar{n}_s$) as a function of the number of injected signal for the whole range of WIMP masses considered and the $\tau^+\tau^-$ annihilation channel. Bottom plots show the difference between the averaged fitted value and the expected value as $\bar{n}_s - n_{\text{inj}}$. Selected quality cuts: $\theta_{\text{zenith}} > 90°$, `track_score` > 0.7 and $\beta < 1°$.

As an example, Fig. 5.14 shows the average value of the $\hat{n}_s$ distribution for the full range of WIMP masses and for the $\tau^+\tau^-$ annihilation channel, as a function of the number of injected signals (n_{inj}). The blue line on the top plots represents the best-case scenario where $\bar{n}_s = n_{\text{inj}}$, and is shown for reference. A general underestimation on the fit parameter is found. The difference with the best-case scenario (shown in the bottom plots of each panel) is greater for low WIMP masses, and is reduced as the mass of the WIMP rises. This underestimation can be explained by the similarities on the PSF of the signal and the background for this range of WIMP masses, hindering the optimization process of the likelihood.

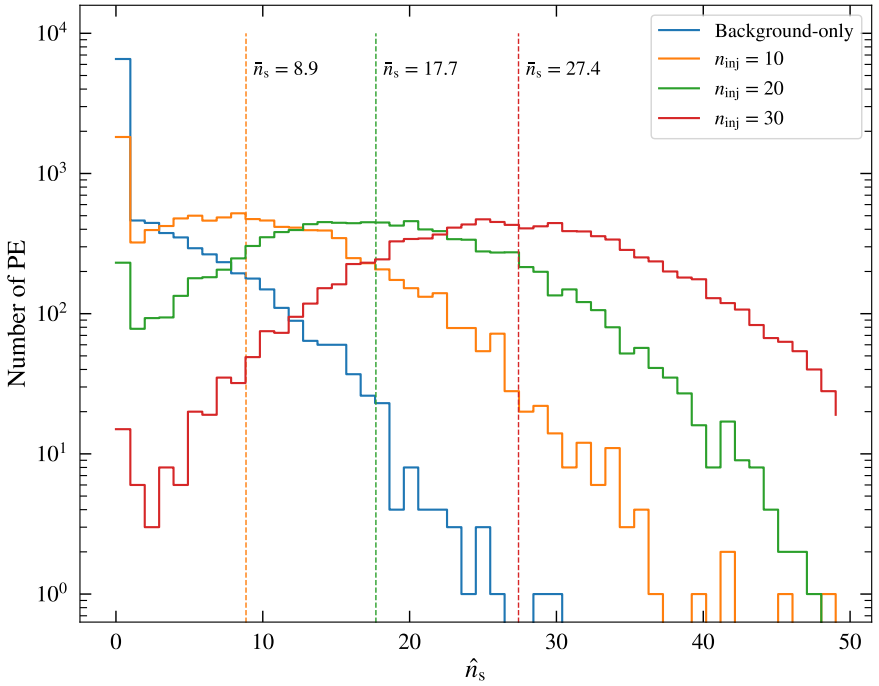

Figure 5.15: Distribution of $\hat{n}_s$ for different number of injected signal events (n_{inj}) for the W^+W^- channel and a WIMP mass of 100 GeV. Vertical dashed lines show the mean value of each distribution (y–axis on figure 5.14).

Figure 5.15 shows an example of the distributions of the $\hat{n}_s$ values which optimize the Likelihood function (Eq. 5.11) for each Pseudo Experiment. The distributions correspond to the W^+W^- annihilation channel and a WIMP mass of 100 GeV. The coloured distributions refer to the background-only case (blue) and, to a number of injected (n_{inj}) signal events equal to 10, 20 and 30 (orange, green and red, respectively). The vertical dashed-lines represent the mean ($\bar{n}_s$) of each distribution (y–axis in figure 5.14).

Test Statistic

To determine the significance of the presence of a signal among the overwhelming background, we use an hypothesis test. The hypothesis of having a signal in the dataset (H_1) is compared with the background-only hypothesis (H_0), which assumes a null presence of signal in the data, following the likelihood ratio ordering [167, 168]. The likelihoods of both hypotheses are built from PEXs and, a test statistic (TS) is computed from their ratio:

$$\mathrm{TS} = \log_{10}\left(\frac{\mathcal{L}_{H_1}(\hat{n}_s)}{\mathcal{L}_{H_0}(0)}\right). \tag{5.13}$$

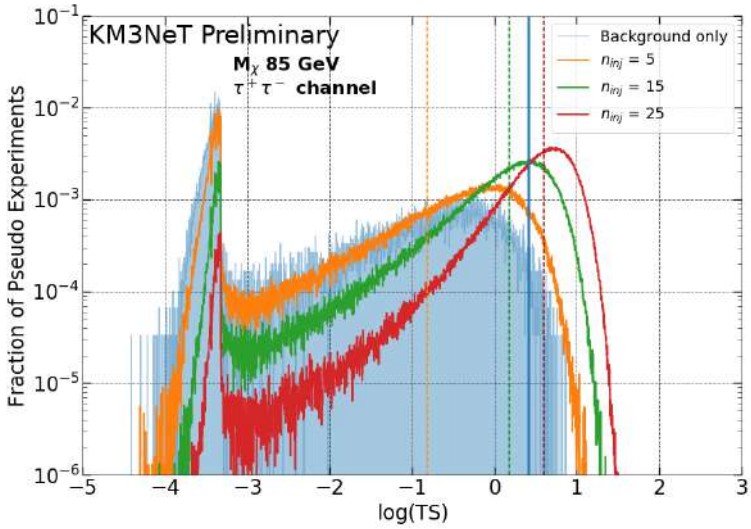

Figure 5.16: Normalized (to unity) distribution of the test statistic for a WIMP mass of 85 GeV, for the $\tau^+\tau^-$ annihilation channel, `track_score` > 0.7 and different number of injected signal events n_{inj} (coloured empty histograms). The blued filled histogram corresponds to the background–only case ($n_{\mathrm{inj}} = 0$). The solid blue vertical line corresponds to the 95% area of the background–only distribution. The dashed coloured vertical lines indicate the median values of the respective coloured empty histograms, corresponding to log(TS) distributions for different n_{inj} values.

In order to obtain continuos values on the number of signal events, and to account for the statistical fluctuations, the TS distributions are smeared with a Poissonian distribution. After the smearing, the resulting TS distributions are function of the Poissonian mean μ, in which is also included the 10% systematic uncertainty [203]

that comes from the determination of the neutrino track direction.

$$P\left(\mathrm{TS}(\mu)\right) = \sum_{n_{\mathrm{inj}}=0}^{N} P\left(\mathrm{TS}(n_{\mathrm{inj}})\right) \cdot \mathrm{Poisson}\left(n_{\mathrm{inj}}, \mu\right). \tag{5.14}$$

Fig. 5.16 shows an example of the smeared TS distributions (in log scale) for the background–only case (blue distribution), together with the distributions corresponding to different signal hypotheses (*i.e.*, differerent number of signal injected events), for the $\tau^+\tau^-$ annihilation channel and a WIMP mass of 85 GeV. In order to improve the visualization of the distributions, the TS distributions are transformed as follows:

$$Q = \log_{10}(TS + C), \tag{5.15}$$

where C is a constant factor that shifts every TS distribution the same amount to avoid a zero value in the argument of the $\log_{10}$ function. In figure 5.16 is also shown the percentile 95 of the background distribution as a vertical blue solid line, together with the median of the different signal hypothesis, reresented as vertical coloured dashed lines.

Discovery Potential

The discovery potential is defined as the minimum number of signal events needed to claim a *discovery* within the data sample with a confidence level greater than 95%. In other words [303], the discovery potential is the minimum number of events needed to reject the null hypothesis (*i.e.*, the background–only hypothesis) with a 95% CL (or a significance of $\alpha = 0.05$) with a 50% of probability to accept the alternative hypothesis (*i.e.*, there is a signal within the dataset) when the alternative hypothesis is actually true (this is also known as the power of the test, $1 - \beta$, where β in this context is the probability to accept the null hypothesis when it is actually false). Fig. 5.17 illustrates an schematic view of hypothesis testing.

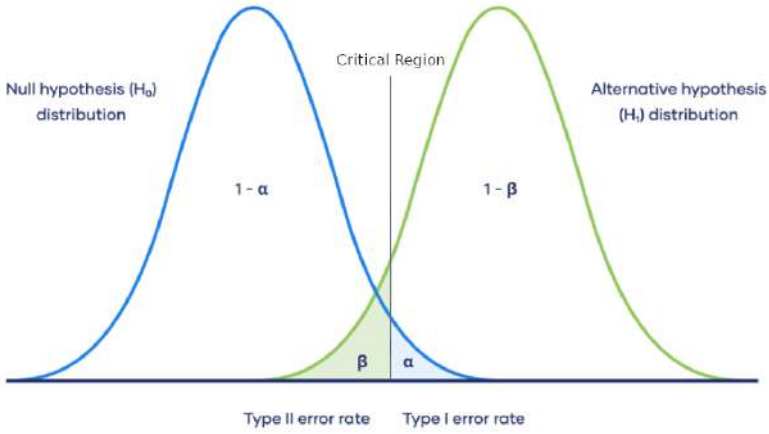

Figure 5.17: Schematic of the hypotheses test. The blue distribution on the left represents the null hypothesis (background–only hypothesis, *i.e.*, there is no signal in the data sample). The green distribution on the right is the alternative hypothesis (there is a signal in the data sample). The shaded region in blue is the significance (α), or the type–I error, interpreted as the probability to reject the null hypothesis when it is true. The green shaded region is the type–II error (β), interpreted as the probability to accept the null hypothesis when it is false. The $1-\alpha$ is the confidence level (CL), and the $1-\beta$ is the power of the test, interpreted as the probability to reject the null hypothesis when it is actually false. The vertical black line represents the *critical value/region*, the value against the null hypothesis is contrasted in order to reject or accept it.

The computation of the discovery potential is summarized as follows:

1. Build the TS distributions for the different hypotheses from the PEXs, including the background–only hypohtesis.
2. Compute the TS value for the percentile 95 of the background–only distribution ($\mathrm{TS}^{\mathrm{Bkg}}_{95\%}$). This is equal to set a 5% significance ($\alpha = 0.05$).
3. Find the TS distribution for the signal hypothesis whose median value (set the power of the test to 50%) is equal to the percentile 95 of the background ($\mathrm{TS}^{\mathrm{Sig}}_{50\%} \geq \mathrm{TS}^{\mathrm{Bkg}}_{95\%}$).
4. The corresponding μ (see Eq. 5.14) is the minimum number of signal events needed to claim a discovery with a 95% CL ($\alpha = 0.05$), in 50% of the experiments ($1-\beta = 0.5$), and is noted as μ_{95}.

Fig. 5.18 shows the number of events needed to claim a discovery (following the criteria explained above), as a function of the WIMP mass for the three considered channels, for different values on the `track_score` cut.

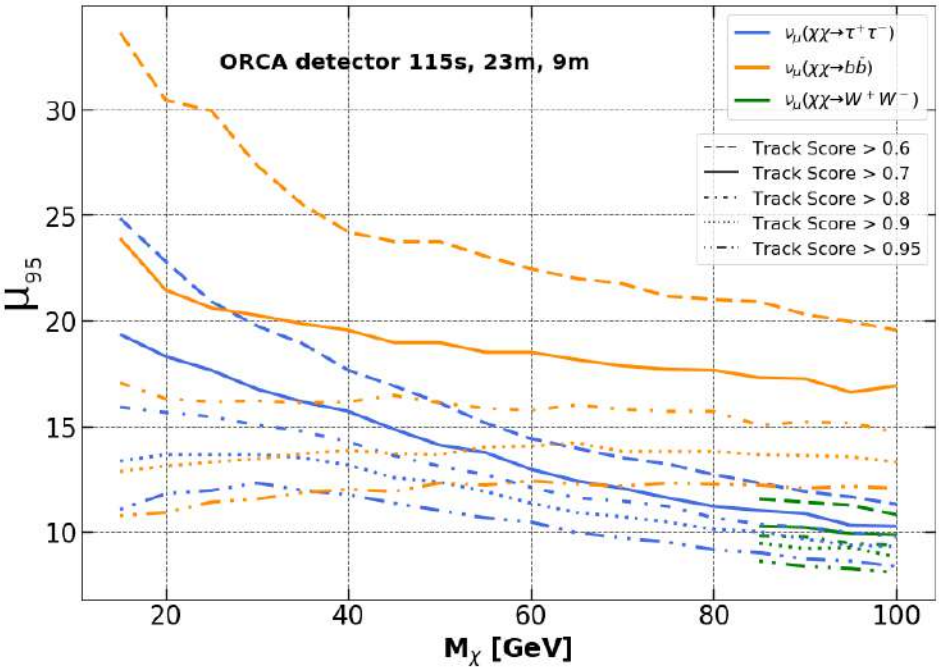

Figure 5.18: Minimum number of signal events needed to claim a discovery with a 95% CL as a function of the WIMP mass. Different values of the `track_score` are shown with different lines (see legend). The three annihilation channels considered are plotted together for comparison.

Once the minimum number of events needed to claim a discovery has been obtained, the calculation of the *discovery flux* for a given data period (T) is trivial. Recalling Eq. 5.9 and rearranging the terms, the discovery flux for each channel as a function of the WIMP mass can be obtained as

$$\Phi^{95\%CL}_{\nu+\bar{\nu}}(M_\chi) = \frac{\mu_{95}}{A_{cc}(M_\chi)\cdot T}. \tag{5.16}$$

The result is shown in Fig. 5.19 for 1 year of the full ORCA configuration.

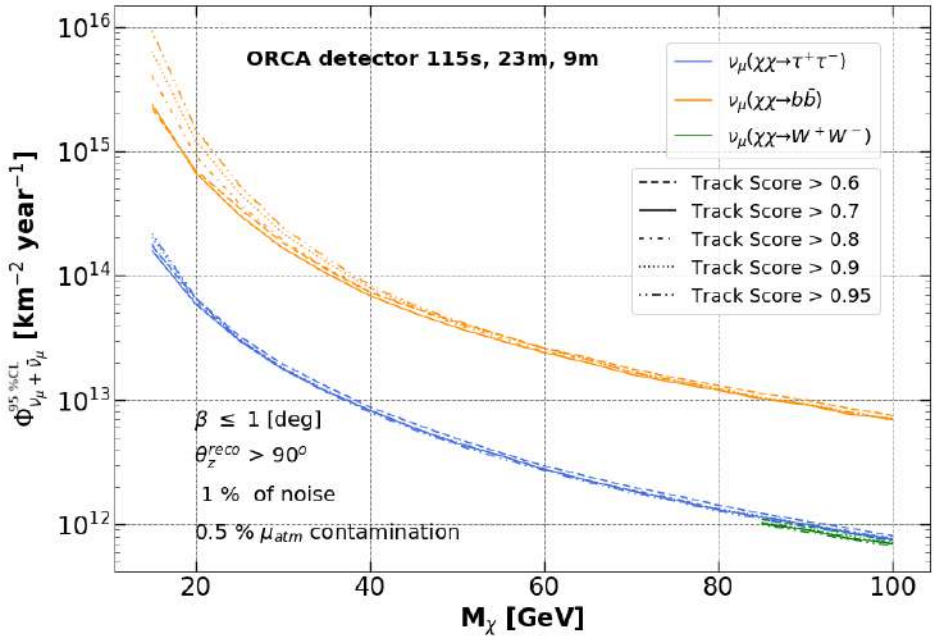

Figure 5.19: Discovery flux for 1 year of data for the full configuration of the ORCA detector. The three annihilation channels and different values of the `track_score` parameter are shown together for comparison as a function of the WIMP mass.

5.2.4 Results and Discussion

Once the discovery flux has been computed, it can be transformed into a limit in the WIMP–nucleon interaction cross-section through the DarkSUSY [300] package. Assuming that there is equilibrium between the annihilation (Γ_A) and capture (C_C) processes inside the Sun, we have the following relation:

$$\Gamma_A = \frac{1}{2} C_C. \tag{5.17}$$

The neutrino flux is related to the annihilation rate by the following expression:

$$\Gamma_A = \frac{2\pi D_\odot^2}{N^f_{\nu+\bar{\nu}}(M_\chi)} \cdot \Phi^f_{\nu+\bar{\nu}} = \eta_f^{-1}(M_\chi)\Phi^f_{\nu+\bar{\nu}}, \tag{5.18}$$

where $D_\odot$ is the mean distance between the detector and the Sun (1 AU), and $N^f_{\nu+\bar{\nu}}(M_\chi)$ is the total number of expected neutrinos from a given annihilation channel, f.

The annihilation rate can be related to the interaction cross-section ($\sigma_{\mathrm{SD,SI}}$) through:

$$\Gamma_A = \Lambda^{-1}_{\mathrm{SD,SI}}(M_\chi) \cdot \sigma_{\mathrm{SD,SI}}, \tag{5.19}$$

where $\Lambda^{-1}_{SD,SI}(M_\chi)$ is a factor related to the capture probability (see [304] for a detailed description). Finally, the flux and the interaction cross-section are related by:

$$\sigma_{\mathrm{SD,\,SI}} = \frac{\Lambda_{\mathrm{SD,SI}}(M_\chi)}{\eta_f(M_\chi)} \cdot \Phi^f_{\nu+\bar{\nu}} = \kappa^f_{\mathrm{SD,\,SI}} \cdot \Phi^f_{\nu+\bar{\nu}}, \tag{5.20}$$

where $\kappa^f_{\mathrm{SD,\,SI}}$ is the conversion factor computed by DarkSUSY, for each annihilation channel (f).

θ_{zenith}	β	`Noise_score`	`Muon_score`	`Track_score`
$> 90°$	$< 1°$	< 0.1	< 0.05	0.7

Table 5.3: Final list of parameters and cuts that optimize the discovery potential on the search for DM in the Sun with the full ORCA detector.

Table 5.3 shows the cuts which optimize the discovery potential on the flux of neutrinos from DM annihilation in the Sun (see Fig. 5.19). Figure 5.20 shows the WIMP–nucleon SD (top) and SI (bottom) interaction cross-section for the three annihilation channels for 5 years of simulated data of the full ORCA configuration (red lines). In addition, best limits from other experiments are shown as a reference.

As shown in figure 5.20, the ORCA detector is potentially competitive in the search for DM in the Sun, surpassing the previous results from the ANTARES and SK searches, and being close to the IceCube results. In order to properly compare with other running experiments, an extension to higher WIMP masses is needed.

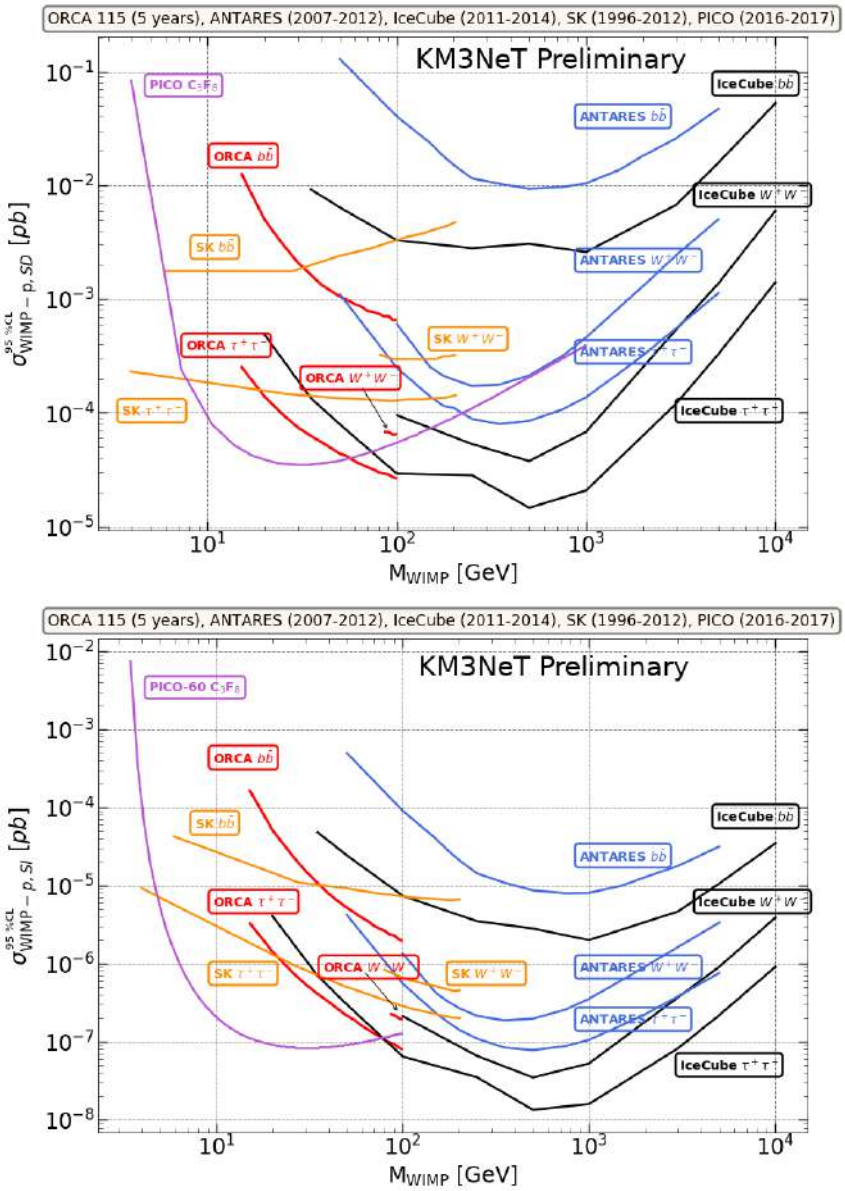

Figure 5.20: WIMP-proton SD (top) and SI (bottom) scattering cross-sections sensitivity at 95% CL as a function of WIMP mass for the three annihilation channels. Comparative between 5 years of ORCA simulated data, 5 years of ANTARES data [305], IceCube 3 years of data [306], Super Kamiokande 16 years [307] and PICO-60 C_3F_8 [308] 1 year. Results published in [295].

Summary

"An expert is a person who has made all the mistakes that can be made in a very narrow field."

Niels Bohr

Solar Atmospheric neutrinos (SAνs) produced by the interaction of cosmic-rays with the solar atmosphere have been source of study over the last decade [33, 152–155]. The comprehension of these neutrinos is important at different levels. First, the detection of SAνs can give indirect information about the primary cosmic-ray composition, the propagation of charged particles in the solar medium and, consequently, help the scientific community to understand the density and chemical structure of the Sun. Second, these neutrinos could be used as a *standard neutrino flux* for detector calibration [154]. Third, SAνs represent an unavoidable background source for solar DM indirect searches [33, 151]. On the other hand, despite the enormous efforts made by the scientific community, dark matter remains one of the biggest open problems in cosmology, astroparticle and particle physics. The nature of dark matter is yet unknown, and a large ammount of models and candidates can be found in the literature [207, 208]. However, in the past decades scientists have made significant progress to understand the properties of these particles, mostly by learning *what is not dark matter* [209]. The existence of dark matter is strongly evidenced by several astronomical phenomena. Without the presence of dark matter, a number of diverse astrophysical and cosmological events could not be explained and hence, as a common response to these, the cold non-baryonic dark matter arose. Among the evidences supporting the existence of dark matter are included: the galaxy rotation curves, the gravitational lensing effect, the galaxy red-shift surveys and the cosmic microwave background anisotropy.

The detection of a SAν signal or the discovery of neutrinos produced in dark matter annihilations would entail reaching a milestone in the astroparticle physics community. The potential of the ANTARES and ORCA neutrino telescopes to search for SAνs and neutrinos from dark matter annihilations, respectively, have been studied in this thesis.

Objectives

This thesis has two main research goals that are summarized as follows:

- Search for SAνs with 11 years of ANTARES. The data collected by ANTARES during the period 2008–2018 have been analysed and limits on the SAνs flux have been established.
- Sensitivity to DM towards the Sun with ORCA: The discovery potential of the full ORCA detector to a neutrino signal from DM annihilation in the Sun has been studied.

Methodology

ANTARES (Ch. 2) is the first operational undersea neutrino telescope [98]. It is located at a depth of 2475 m in the Mediterranean Sea at (45°45′ N, 6°10′ E), 40 km offshore from Toulon (France). The detector started taking data with the first lines in 2007 and was completed in May 2008. In February 12, 2022 the detector was switched off, and the dismantling of the infrastructure is foreseen by summer 2022, after more than 15 years of successful operation. The ANTARES full configuration consists of 12 vertical detection lines (also called *strings*) anchored to the ground, 450 m high and horizontaly spaced by 50-75 m, distributed on an octogonal layout. Each line holds 25 storeys, with the exception of line 12, equipped with 20 storeys plus acoustic detection devices.

The ORCA detector (Sec. 4.1.1) is located offshore of Toulon, France, at (42°41′ N, 6°02′ E). At 2450 m depth, starting about 40 m from the sea floor, the ORCA detection units are 200 m high, separated horizontally by about 20 m, with 18 DOMs spaced 9 m in vertical direction. The ORCA full configuration will consist on 1 building block of 115 strings with the aforementioned configuration.

The method summarized here is applied to the two analyses mentioned above. In order to look for a statistical excess of neutrinos from any kind of source over the expected background, a complete simulation of the detector and its response is needed. Every physical event and the detector response are simulated accurately following a *run-by-run* approach. This simulation takes into account the environmental conditions at a deep-sea site (sea current, environmental background, etc.), the temporary or permanently non-operational OMs and monitoring the OMs position and PMT efficiencies of individual OMs [102, 112, 195].

The simulation chain is divied in three main steps:

- **Particle generation**: neutrinos and anti-neutrinos of all flavours, atmospheric muons and background light events are simulated in the vicinity of the detector within a given energy range and spatial distribution.
- **Particle propagation and light emission**: particles are propagated through the detector and Cherenkov photons are simulated and propagated to the optical modules.
- **Data acquisition**: the response of the OMs and the data acquisition electronics are simulated. Filtering and triggering algorithms are applied. The background effects and the evolution of detector efficency with time is taken into account.

Once the trigger algorithms have filtered the interesting events, the neutrino energy and direction have to be reconstructed from the hit information. Depending on the Cherenkov signatures of the outgoing lepton from the ν_μ and ν_e CC and NC interactions, two distinct event topologies are observed at the detector: *track-like* and *shower-like* events. ν_μ CC and ν_τ CC interactions with muonic τ decays mostly account for the *track-like* topology, since the outgoing muon appears as a track within the detector. The *shower-like* topology corresponds to events from ν_e CC, ν_τ CC interactions with non-muonic τ decays and NC interactions of all flavours.

The expected background for both neutrino telescopes comes from: atmospheric neutrinos and muons, bioluminescence processes and light emission by ^{40}K decays. These background sources are simulated using a variaty of software packages: GENHEN [113], MUPAGE [120], CORSIKA [117, 118] and gSeaGen [194], among others.

The signal events are simulated using the WimpSim simulation package [160, 161]. For the SAν search with ANTARES, the signal reference model consists on a combination of the *H3a* cosmic–ray model [156], in which three different populations of cosmic–rays are assumed (one extragalactic component that starts to contribute to the spectrum at the *ankle* and two galactic components below the *ankle*), the *Ser+Stein* [158] solar density profile and the Sun is considered as a point source. For the analysis on the discovery potential of the full ORCA to DM in the Sun, the signal component consists on a neutrino energy spectra coming from three different dark matter annihilation channels ($\tau^+\tau^-$, $b\bar{b}$ and W^+W^-).

Prior to start the analyses, a series of preprocessing steps are needed. In these steps, the data is visualized and a set of pre-selection cuts are applied in order to achieve a sample as clean as possible from atmospheric muons and background noise. For ANTARES, the selected pre-cuts are (Sec. 3.4.1): $\Lambda > -6$, $\beta < 1.5^\circ$ and $\theta_{\text{zenith}} > 90^\circ$ (events reconstructed as upward–going). For ORCA, the preselection cuts are (Sec. 5.2.2): $\theta_{\text{zenith}} > 90^\circ$, $\beta < 1^\circ$, `noise_score` < 0.1, `muon_score` < 0.05 and `track_score` > $[0.7, 0.95]$.

In these analyses, the method to estimate the sensitivity and discovery potential of the detectors to a neutrino flux is an hypotheses test based in an unbinned maximum likelihood estimation approach [167, 168]. The likelihood is described by the following expression:

$$\ln \mathcal{L}(n_s) = \sum_{i=1}^{N} \ln \left[n_s \mathcal{S}(\Psi_{\odot,i}, \beta_i, N_{\text{hits},i}) + n_b \mathcal{B}(\Psi_{\odot,i}, \beta_i, N_{\text{hits},i}) \right] - \left[n_s + n_b \right], \quad (21)$$

where $\mathcal{S}$ and $\mathcal{B}$ are PDFs which describe the statistical behaviour of signal and background components. These PDFs are built using the information of the direction of the particles ($\Psi_\odot$), the energy estimator (N_{hits}) and the error estimate on the reconstructed angle (β). The total number of expected events, N, can be splitted in the expected number of signal and background events $N = n_{\text{s}} + n_{\text{b}}$. The fit

parameter in the Likelihood is n_s. The fitted value maximizing the likelihood is noted as $\hat{n}_s$.

To determine the significance of the presence of a signal among the overwhelming background, we use an hypothesis test. The hypothesis of having a signal in the dataset (H_1) is compared with the background-only hypothesis (H_0), which assumes a null presence of signal in the data, following the likelihood ratio ordering [167, 168]. The likelihoods of both hypotheses are built from Pseudo Experiments and, a test statistic (TS) is computed from their ratio:

$$\mathrm{TS} = \log_{10}\left(\frac{\mathcal{L}_{H_1}(\hat{n}_s)}{\mathcal{L}_{H_0}(0)}\right). \tag{22}$$

The value of the TS indicates the similarity between the two hypotheses. A TS close to 0 means that both hypotheses are quite similar, whereas the greater the TS value the different the hypotheses are, and the easiest will be to distinguish them. This TS is later used to compute the sensitivity and/or discovery potential of the detector for a given neutrino signal.

Results

The results of the two physics analyses are reported in the following subsections. First, the ANTARES results in the search for SAνs is presented. Then, the discovery potential to DM signals towards the Sun for 5 years of the full ORCA configuration is summarized.

Solar Atmospheric Neutrino Searches with ANTARES

After analysing 11 years of ANTARES data, corresponding to 3022 days of lifetime, the number of events passing the final selection cuts ($\Lambda > -5.2$, $\beta < 1.0^\circ$ and $\theta_{\mathrm{zenith}} > 90^\circ$ in a region of interest (RoI) of 30°around the Sun is $n = 461$, the number of expected background events is 470 and the expected SAν signal from the *reference model* amounts to ≈ 0.37. Therefore, no excess of SAν signal over the expected background is observed in the data. Figure 21 shows the distribution of the events within the RoI around the Sun, for the expected signal (blue histogram) and background (green line), alongside the observed data (black dots). The signal is magnified by a factor 8.6 for comparison.

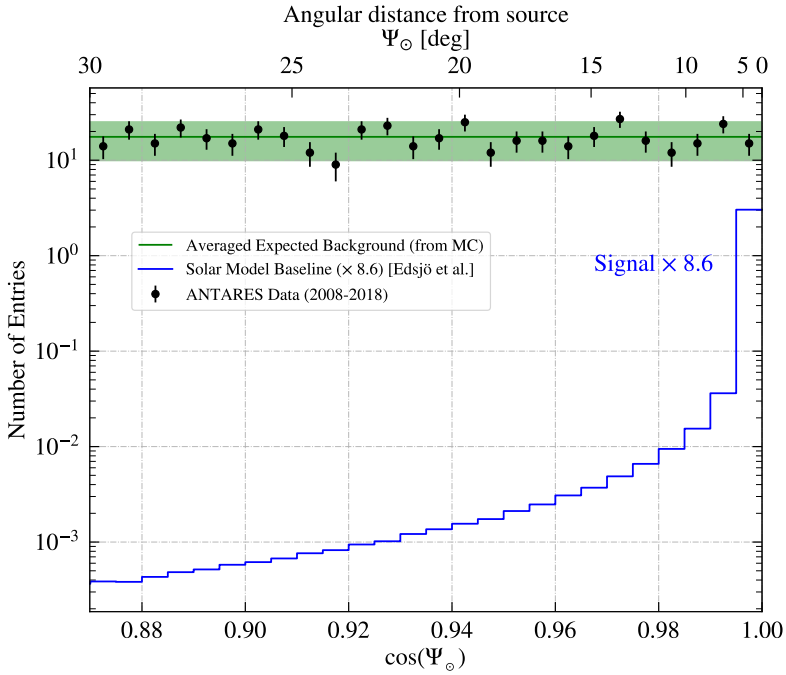

Figure 21: ANTARES search for SAνs. Event distribution as a function of the reconstructed angular separation $\Psi_\odot$ from the Sun. The expected signal, in blue, is scaled up by a factor 8.6. The expected background (green line) is shown with a 2σ band along the data (black dots).

The analysis of the 2008–2018 data taking period of ANTARES data, with an unbinned likelihood method, gives no evidence of a SAν signal.

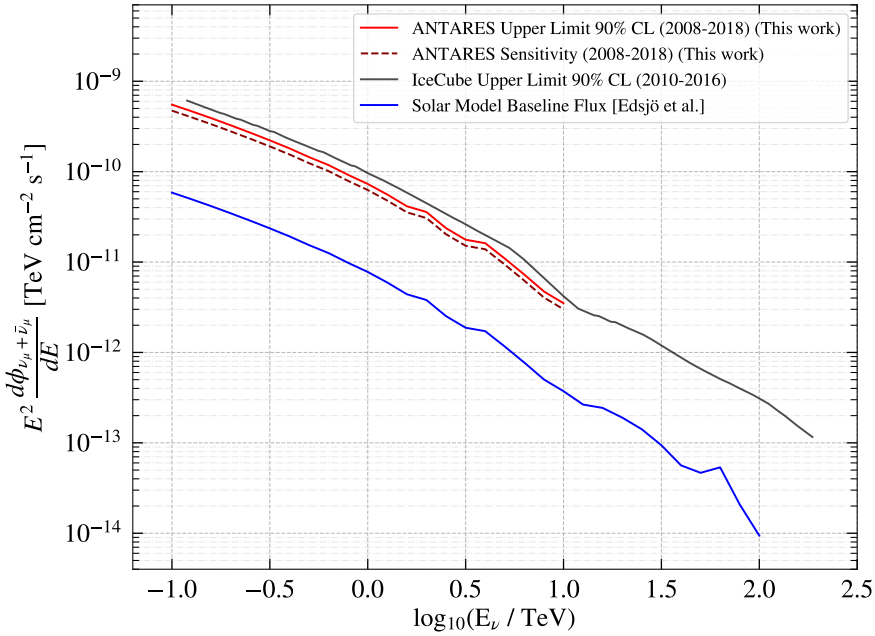

Figure 22: ANTARES upper limit (solid red) and sensitivity (dashed red) on the search for SAνs, for 11 years of data, assuming the Sun as a point-like source for the reference model *H3a-Ser+Stein* (solid blue line). For comparison, the current 6 years IceCube upper limit [171] is also shown (solid black line). The ANTARES limit and sensitivity lines expand in the energy range which contains 90% of the expected number of events. Results published in [172].

Figure 22 presents the sensitivity (dotted red line) and the 90% CL upper limit (solid red line) on the SAν flux for the ANTARES detector over 11 years of data taking (this thesis). The theoretical flux model (solid blue line) and latest upper limit results obtained by the IceCube collaboration (solid black line) [171] are shown for comparison. As a result, a 90% CL upper limit on the energy flux of 7×10^{-11} [TeV cm^{-2} s^{-1}] at 1 TeV is established (corresponding to a *p-value* = 0.41).

Indirect Searches for Dark Matter in the Sun with ORCA

The discovery potential of the full ORCA neutrino telescope, for 5 years of data taking, to neutrinos from DM annihilations in the Sun has been studied. WIMP masses in the 15 to 100 GeV energy range and three annihilation channels ($\tau^+\tau^-$, $b\bar{b}$, W^+W^-) have been tested.

After performing the Pseudo Experiments and computing the minimum number of events needed to claim a discovery, the discovery flux for a given data taking

period is computed (figure 23) for three annihilation channels and different values of the `track_score` cut[5] as a function of the WIMP mass.

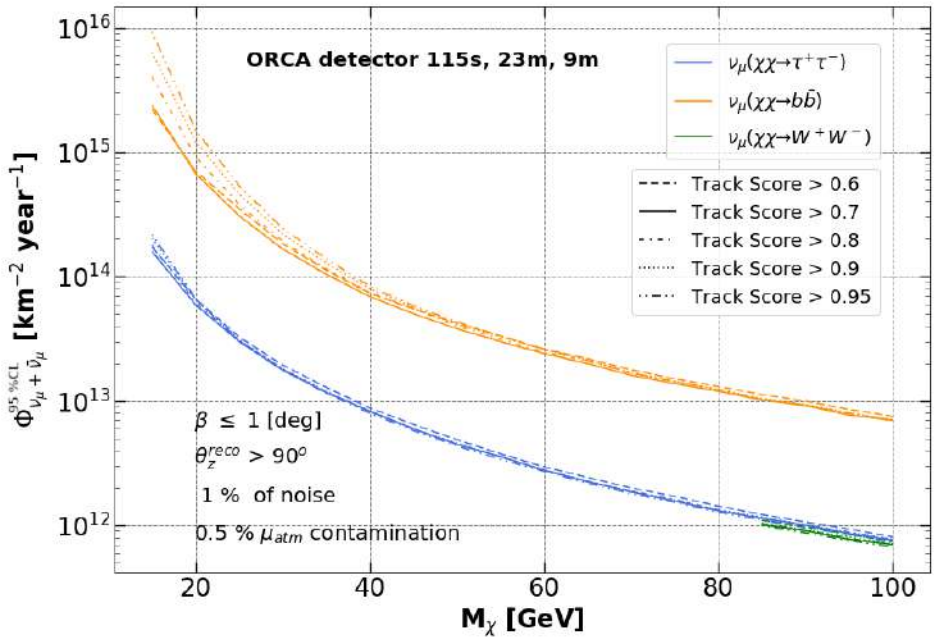

Figure 23: Discovery neutrino flux from DM annihilation in the Sun for 1 year of data for the full configuration of the ORCA detector. The three annihilation channels and different values of the `track_score` parameter are shown together for comparison as a function of the WIMP mass.

Once the discovery flux has been computed, it can be transformed into a limit in the WIMP–nucleon interaction cross-section through the DarkSUSY [300] package using the following equation:

$$\sigma_{\mathrm{SD,\,SI}} = \kappa^{f}_{\mathrm{SD,\,SI}} \cdot \Phi^{f}_{\nu+\bar{\nu}}, \tag{23}$$

where $\kappa^{f}_{\mathrm{SD,\,SI}}$ is the conversion factor computed by DarkSUSY, for each annihilation channel (f).

Table 4 shows the cuts which optimize the discovery potential on the flux of neutrinos from DM annihilation in the Sun (see Fig. 23). Figure 24 shows the WIMP–nucleon spin–dependent (top) and spin–independent (bottom) interaction cross-section for the three annihilation channels for 5 years of simulated data of the full ORCA configuration (red lines). In addition, best limits from other experiments are shown as reference.

[5]The `track_score` parameter is the output parameter of a boost decision tree that classify events in the *track-like* or *shower-like* topology. Values close to 1 means the event is classified as more *track-like*.

θ_{zenith}	β	`Noise_score`	`Muon_score`	`Track_score`
$> 90°$	$< 1°$	< 0.1	< 0.05	0.7

Table 4: Final list of parameters and cuts that optimize the discovery potential on the search for DM in the Sun with the full ORCA detector.

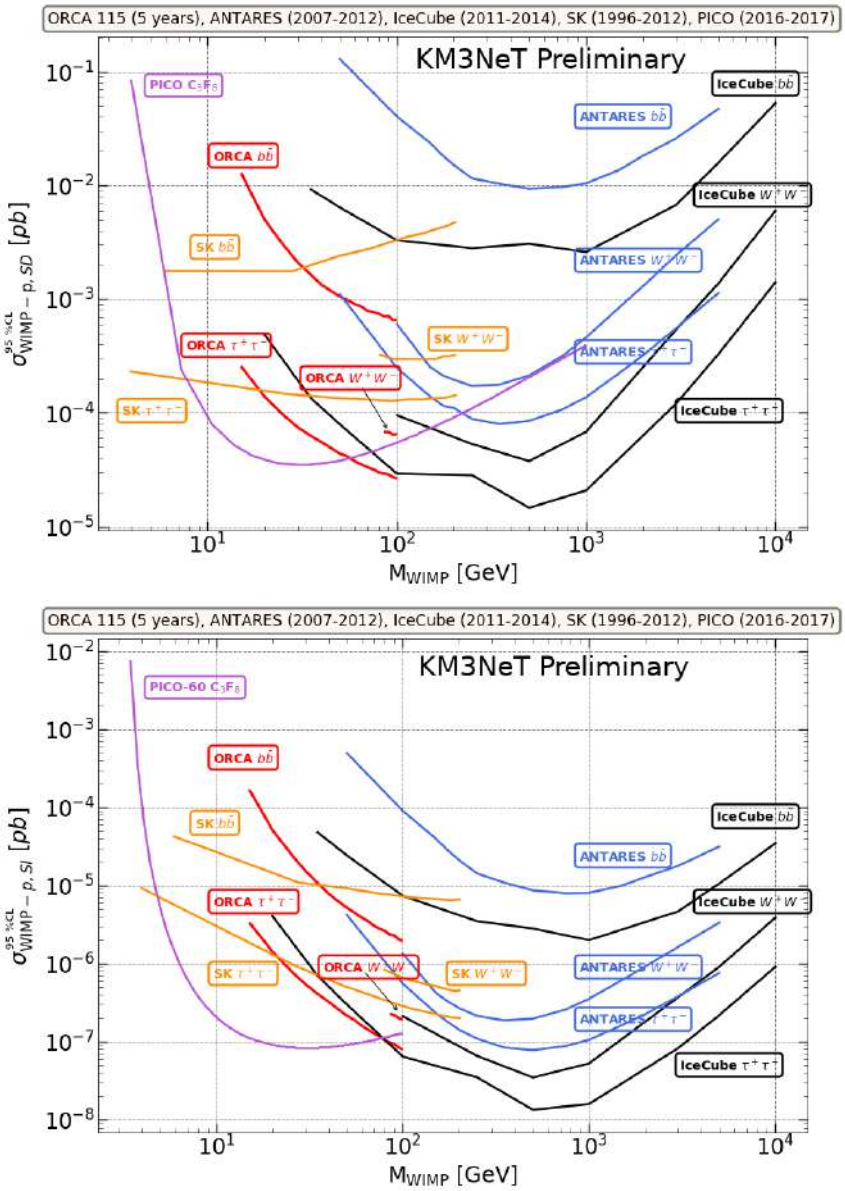

Figure 24: WIMP-proton SD (top) and SI (bottom) scattering cross-sections discovery potential at 95% CL as a function of WIMP mass for the three annihilation channels. Comparative between 5 years of ORCA simulated data, 5 years of ANTARES data [305], Ice Cube 3 years of data [306], Super Kamiokande 16 years [307] and PICO-60 C_3F_8 [308] 1 year. Results published in [295].

As shown in figure 24, the ORCA detector is potentially competitive in the search for DM in the Sun, surpassing the previous results from the ANTARES and SK

searches, and being close to the IceCube results. In order to properly compare with other running experiments, an extension to higher WIMP masses is needed.

Outlook

The results of the ANTARES search to SAν opens up the path to perform this search with the under-construction KM3NeT detector. This detector has a larger instrumented volume, promissing a better performance and greater detection capabilities.

It has been shown that ORCA is a well suited infrastructure to perform indirect dark matter searches towards the Sun. At the time of writing this document, an analysis of the ORCA-6 line configuration is being carried out.

ANTARES was switched off on February 12, 2022, and the decommissioning of the infrastructure is foreseen by summer 2022. On the other hand, the ARCA and ORCA detectors reached the 6 and 10 line configuration on 2021, respectively.

Resumen

"Un experto es una persona que ha cometido todos los errores posibles en un campo del conocimiento muy concreto."

Niels Bohr

Los neutrinos atmosféricos solares (SAνs, del inglés Solar Atmospheric Neutrinos) producidos por la interacción de rayos cósmicos con la atmósfera solar, han sido objeto de estudio durante la última década [33, 152–155]. Comprender la naturaleza de estos neutrinos es importante a diferentes niveles. En primer lugar, la detección de estos SAνs nos puede brindar información, indirectamente, sobre la composición de los rayos cósmicos primarios, la forma de propagarse que tienen las partículas cargadas en el medio solar y, consecuentemente, ayudar a comprender la densidad y la composición química del Sol. En segundo lugar, este tipo de neutrinos se podrían utilizar como un *flujo estándar* para calibrar detectores [154]. En tercer lugar, los SAνs representan una fuente ineludible de fondo para la búsqueda indirecta de materia oscura (DM, del inglés Dark Matter) en el Sol [33, 151]. Por otro lado, a pesar del enorme esfuerzo que se ha hecho por parte de la comunidad científica, la materia oscura sigue siendo uno de los mayores problemas que siguen sin resolver en el campo de la cosmología, las astropartículas y la física de partículas. La naturaleza de la materia oscura permanece aún desconocida, y se puede encontrar en la literatura gran cantidad de modelos, teorías y candidatos intentando explicarla [207, 208]. Sin embargo, en las últimas dos décadas se han realizado significantes progresos que han permitido entender algunas de sus propiedades, principalmente a partir de aprender *qué no es la materia oscura* [209]. Existen una serie de fuertes evidencias de carácter astronómico que apoyan la existencia de materia oscura. La materia oscura fría y no bariónica surge como respuesta común a una diversa cantidad de fenómenos astrofísicos y cosmológicos que no podrían ser explicados por teorías cosmológicas que no incluyesen esta componente de materia. Las observaciones incluyen las curvas de rotación de galaxias, el efecto de lente gravitacional o la anisotropía del fondo de cósmico de microondas, entre otras.

Detectar una señal de SAνs o descubrir neutrinos producidos por la aniquilación de materia oscura, supondría alcanzar una piedra angular en la física de astropartículas. En esta tesis se ha estudiado el potencial que tienen los detectores ANTARES y ORCA para realizar búsquedas de SAνs y neutrinos producidos por aniquilaciones de materia oscura, respectivamente.

Objetivos

Los objetivos de esta tesis son dos, y están resumidos como sigue:

- Búsqueda de SAνs usando 11 años de datos de ANTARES. Los datos recopilados por ANTARES durante el periodo 2008–2018 se han analizado, y se han establecido límites en el flujo de SAνs.
- Estudio de la sensibilidad del detector ORCA a la materia oscura solar: Se ha estudiado el potencial de descubrimiento que posee la configuración completa del detector ORCA a señales de neutrinos provenientes de la aniquilación de partículas de materia oscura acumuladas en el Sol.

Método

ANTARES (Cap. 2) es el primer telescopio de neutrinos submarino funcional [98]. Se encuentra localizado en a una profundida de 2475 m en el mar Mediterráneo (45°45′ N, 6°10′ E), a 40 km de la costa de Toulon (Francia). El detector comenzó a tomar datos con sus primeras líneas en 2007, siendo 2008 la fecha en la que sería completado. El 12 de Febrero de 2022, se desconectó el detector y su desmantelamiento se prevé para el verano de ese mismo año. La configuración completa de ANTARES consiste en 12 líneas verticales ancladas en el fondo marino, con 450 m de altura y un espaciado horizontal de 50-75 m, distribuidos formando una estructura octogonal. Cada línea tiene unos 25 *storeys*, a excepción de la línea 12, que está equipada con 20 *storeys* además de dispositivos de detección acústica.

El detector ORCA (Sec. 4.1.1) se encuentra localizado en la costa de Toulon (Francia) (42°41′ N, 6°02′ E), a una profunidad de 2450 m, y comenzando a una altura de 40 m sobre el fondo marino. Las líneas de detección de ORCA poseen una altura de 200 m, separadas horizontalmente unos 20 m y con 18 DOMs separados verticalmente 9 m. La configuración completa de ORCA consiste en un bloque de 115 líneas con la configuración antes mencionada.

El método que se resume aquí se ha aplicado a ambos estudios. Para ser capaz de detectar un exceso de neutrinos de cualquier tipo sobre el ruido de fondo, en primer lugar es necesario disponer de una simulación completa y precisa de la física y de la respuesta del detector. Siguiendo un procedimiento *run-by-run*, se han simulado todos los procesos físicos y la respuesta del detector de forma precisa. Esta simulación tiene en cuenta las condiciones ambientales a las que se encuentra el detector en el fondo del mar (corrientes marinas, ruido ambiental, etc.), los módulos opticos (OMs, del inglés Optical Modules) que están temporal o permanentemente fuera de servicio y monitorea la posición de estos OMs y la eficiencia de los tubos fotomultiplicadores (PMTs, del inglés photomultiplier tube) de cada módulo óptico [102, 112].

El proceso de simulación se puede dividir en tres etapas principales:

- **Generación de partículas**: se simulan todos los sabores de nuetrinos, los muones atmosféricos y la luz de fondo (ruido) en las cercanías del detector.

- **Propagación de partículas y emisión de luz**: se propagan las partículas hacia el detector, y se simulan y propagan los fotones Cherenkov hacia los módulos ópticos.
- **Adquisición de datos**: se simula la respuesta de los módulos ópticos así como la electrónica y el proceso de adquisición de datos. En esta etapa se tienen en cuenta los efectos ambientales, la generación de ruído de fondo así como el efecto del tiempo sobre la eficiencia del detector, y se aplican algoritmos de filtrado de eventos.

Una vez se han filtrado los eventos de interés, la energía y dirección de los neutrinos se reconstruye usando la información de los *hits*. En el detector se pueden catalogar dos topologías de eventos diferentes en función de cómo se produce la radiación Cherenkov: *trazas* y *cascadas*. La topología de *traza* se debe mayoritariamente a interacciones de corriente cargada (CC, del inglés Charged Current) de los ν_μ y ν_τ cuya partícula τ decae posteriormente a un μ. La topología de *cascada* se corresponde a interacciones de ν_e CC, ν_τ CC sin decaimiento muónico, e interacciones de corriente neutra (NC, del inglés Neutral Current) de todos los sabores de nuetrinos.

El fondo esperado para ambos telescopios de neutrinos proviene de: neutrinos y muones atmosféricos, procesos de bioluminiscencia y emisión de luz por el decaimiento del ^{40}K. Esta fuente de fondo se simula utilizando un conjunto dfe software variado: ese background sources are simulated using a variaty of software packages: GENHEN [113], MUPAGE [120], CORSIKA [117, 118] and gSeaGen [194], entre otros.

La señal esperada se simula usando el programa WimpSim [160, 161]. Para la búsqueda de SAν con ANTARES, la señal del modelo de referencia consiste en la combinación del modelo de rayos cósmicos *H3a* [156], en el cual se asumen tres poblaciones diferentes de reayos cósmicos (una de componente extragaláctica que comienza a contribuir al espectro en el *codo*, y dos de componente galáctico que contribuyen por debajo del *codo*), el modelo de densidad solar *Ser+Stein* [158] y considera que el Sol es una fuente puntual. Para el análisis del potencial de descubrimiento de ORCA a una señal de materia oscura proveniente del Sol, la señal consiste en tres espectros de neutrinos proveniente de tres canales de aniquilación diferentes ($\tau^+\tau^-$, $b\bar{b}$ and W^+W^-).

Antes de comenzar los análisis, se necesita prepocesar la información. Para ello, se visualizan los datos y se aplican una serie de cortes de preselección con el objetivo de obtener una muestra lo más limpia posible de muones atmosféricos y de ruido de fondo. Para ANTARES, los cortes de selección son (Sec. 3.4.1): $\Lambda > -6$, $\beta < 1.5^\circ$ y $\theta_{\text{zenith}} > 90^\circ$ (eventos reconstruídos como ascendentes). Para ORCA, los cortes de preselección son (Sec. 5.2.2): $\theta_{\text{zenith}} > 90^\circ$ (eventos reconstruídos como ascendentes), $\beta < 1^\circ$, `noise_score` < 0.1, `muon_score` < 0.05 y `track_score` > $[0.7, 0.95]$.

En estos análisis, para estimar la sensibilidad y el potencial de descubrimiento de los detectores a un determinado flujo de neutrinos, se ha utilizado un test de

hipótesis basado en una estimación de máxima verosimilitud [167, 168]. La función de verosimilitud empleada se define como sigue:

$$\ln \mathcal{L}(n_s) = \sum_{i=1}^{N} \ln \left[n_s \mathcal{S}(\Psi_{\odot,i}, \beta_i, N_{\text{hits},i}) + n_b \mathcal{B}(\Psi_{\odot,i}, \beta_i, N_{\text{hits},i}) \right] - \left[n_s + n_b \right], \quad (24)$$

donde $\mathcal{S}$ y $\mathcal{B}$ son funciones de densidad de probabilidad (PDFs, del inglés Probability Density Function) las cuales describen el comportamiento estadístico de la señal y del fondo. Estas PDFs se construyen usando la información de la dirección de las partículas ($\Psi_{\odot}$), el estimador de la energía (N_{hits}) y el error estimado en la resconstrucción angular (β). El número total de eventos esperados, N, se puede expresar como la suma del número de eventos esperados de señal de fondo $N = n_{\text{s}} + n_{\text{b}}$. El parámetro de ajuste es n_s. El valor que maximiza la función de verosimilitud se denota como $\hat{n}_s$.

Para determinar la significancia de la presencia de señal entre la abrumadora cantidad de ruido de fondo, se emplea un test de hipótesis. Se compara la hipótesis de existencia de señal en el conjunto de datos (H_1) con la hipótesis de existencia de sólo fondo (H_0). Esta comparativa sigue el criterio de orden *likelihood ratio ordering* [167, 168]. Las funciones de verosimilitud de ambas hipótesis se construyen a partir de Pseudo Experimentos, y el estadístico de contraste (TS, del inglés Test Statistic) se calcula a partir de su razón.

$$\text{TS} = \log_{10} \left(\frac{\mathcal{L}_{H_1}(\hat{n}_s)}{\mathcal{L}_{H_0}(0)} \right). \quad (25)$$

El valor del TS indica la similitud de ambas hipótesis. Un valor del TS cercano a 0 significa que ambas hipótesis son muy similares, mientras que cuanto mayor sea dicho valor, más diferencia existe entre ambas hipótesis y más fácilmente se podrá distinguir una de otra. Este TS se usa posteriormente para calcular la sensibilidad y/o el potencial de descubrimiento del detector para un cierto tipo de señal.

Resultados

En las siguientes subsecciones se resume el resultado de ambos análisis. En primer lugar se presentan los resultados de la búsqueda de SAνs con el detector ANTARES. Más adelante se muestra el potencial que tiene la configuración completa de ORCA, para 5 años de toma de datos, para descubrir neutrinos provenientes de la aniquilación de materia oscura en el Sol.

Búsqueda de Neutrinos Atmosféricos Solares con ANTARES

Tras analizar 11 años de datos de ANTARES, correspondientes a 3022 días de toma de datos, el número de eventos que pasan los cortes de selección finales ($\Lambda > -5.2$, $\beta < 1.0^{\circ}$ y $\theta_{\text{zenith}} > 90^{\circ}$) en una apertura de 30°alrededor del Sol es $n = 461$,

el número esperado de eventos de fondo es 470 y el número esperado de eventos de señal de SAν para el *modelo de referencia*[6] es $\approx$ 0.37. Por lo tanto, no se ha observado un exceso de eventos de señal de SAν sobre el fondo esperado en los 11 años de datos analizados. La figura 25 muestra la distribución de los eventos en el RoI alrededor del Sol, para la señal esperada (histograma azul) y el fondo esperado (línea verde), junto a los datos observados (puntos negros). La señal se ha aumentado 8.6 veces por razones comparativas.

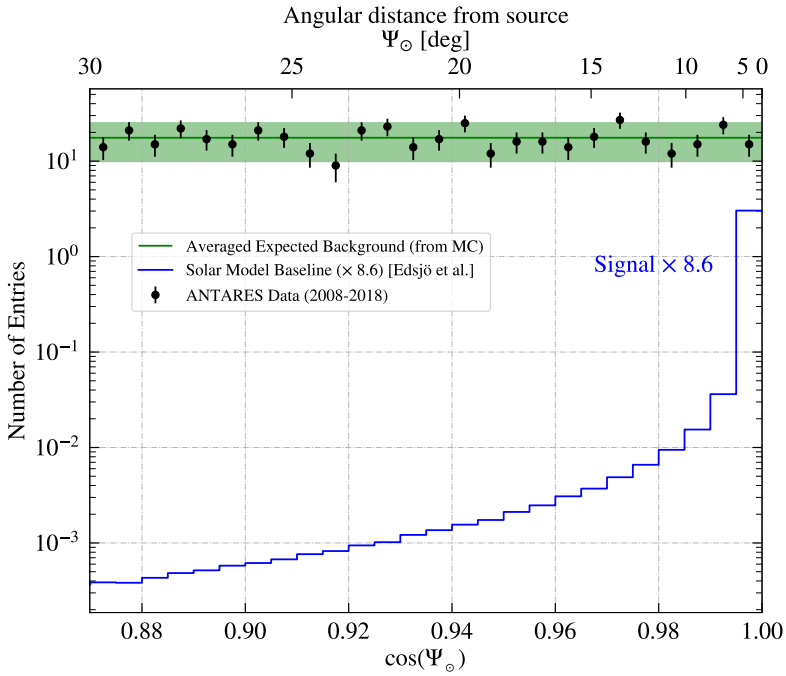

Figure 25: Búsqueda de neutrinos atmosféricos solares con ANTARES. Distribución de eventos como función de la distancia angular al Sol $\Psi_\odot$. La señal esperada, en azul, está escalada un factor 8.6. El fondo esperado (línea verde) se muestra, con una banda de 2σ, junto a los datos (puntos negros).

El análisis de los datos de ANTARES para el periodo 2008–2018 (3022 días de toma de datos), usando un método de máxima verosimilitud, no muestra evidencias de neutrinos atmosféricos solares. Por lo tanto, se ha establecido un límite en el flujo a estos neutrinos, a un nivel de confianza del 90%, cuyo valor es 7×10^{-11} [TeV cm^{-2} s^{-1}] para 1 TeV (se corresponde con un *p-val* = 0.41).

[6] El *modelo de referencia* se refiere al conjunto del modelo de rayos cósmicos *H3a* y el de densidar solar*Ser+Stein* empleados como modelo principal para probar la presencia de señal de SAν en el conjunto de datos de ANTARES.

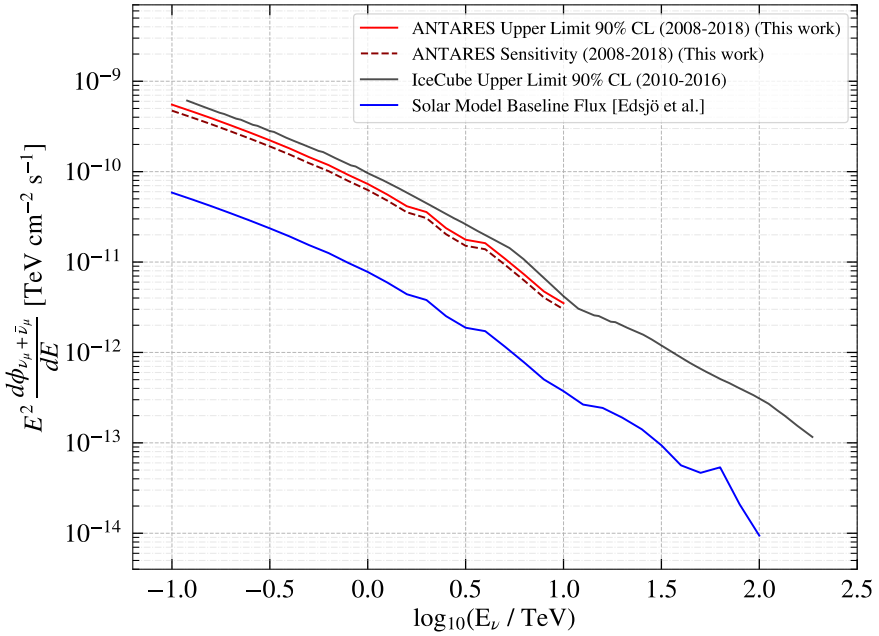

Figure 26: Límite (línea roja continua) y sensibilidad (línea roja punteada) de ANTARES al flujo de neutrinos atmosféricos solares para 11 años de datos, asumiendo que el Sol es una fuente puntual y usando el modelo de referencia *H3a-Ser+Stein* (línea azul continua). El límite actual de IceCube para 6 años de datos [171] (línea negra sólida) se muestra con motivos comparativos. El límite de ANTARES y su sensibilidad se expande en el rango de energía que contiene el 90% del número de eventos esperados. Este resultado está publicado en [172].

La figura 26 muestra la sensibilidad (línea roja punteada) y el límite al 90% (línea roja continua) en el flujo de SAν para 11 años de toma de datos de ANTARES. El flujo del modelo teórico (línea azul continua) y el último límite publciado por IceCube (línea negra contínua) [171] se muestran con motivos comparativos.

Búsqueda Indirecta de Materia Oscura en el Sol con ORCA

En este análisis se ha estudiado el potencial que tiene la configuración completa de ORCA, para 5 años de toma de datos, para realizar búsquedas de materia oscura en el Sol. Se han comprobado tres canales de aniquilación ($\tau^+\tau^-$, $b\bar{b}$, W^+W^-) para el rango de masas de WIMP de 15 a 100 GeV.

Tras realizar Pseudo Experimentos y calcular el mínimo número de eventos necesarios para anunciar ese descubrimiento (figura 27), se ha calculado el *discovery flux*, o flujo mínimo necesario para anunciar un descubrimiento al 95% de confianza, para tres canales de aniquilación y diferentes valores del parámetro de corte

`track_score`[7] como función de la masa del WIMP.

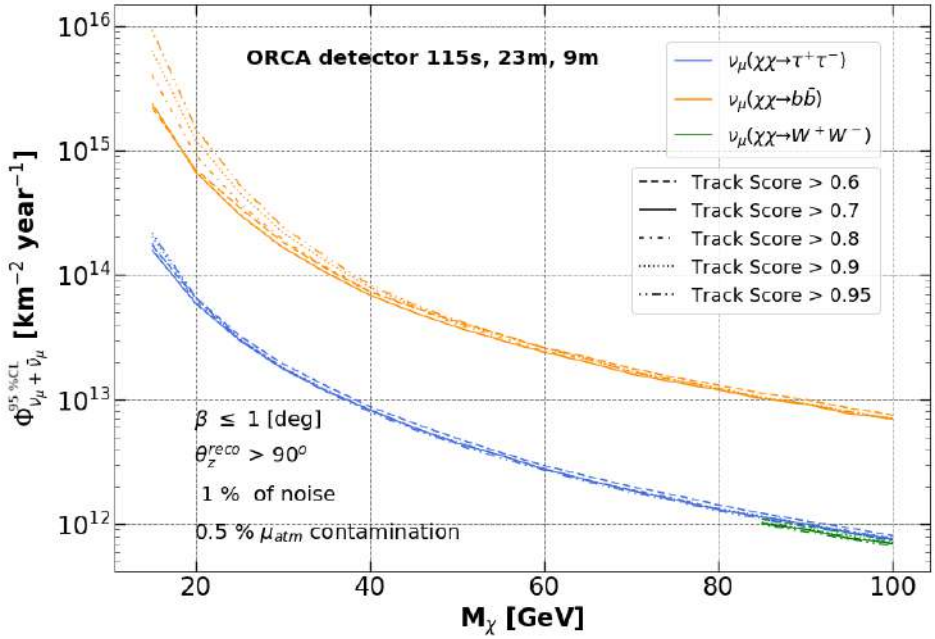

Figure 27: *Discovery flux* para un año de datos con la configuración completa de ORCA. Se muestran juntos, por comparación, los resultados para los tres canales de aniquilación y diferentes valores del parámetro `track_score` como función de la masa del WIMP.

Una vez que se ha calculado el *discovery flux*, podemos transformalo en un límite en la sección eficaz de interacción WIMP–nucleón usando el programa DarkSUSY [300] usando la siguiente ecuación:

$$\sigma_{\mathrm{SD,\,SI}} = \kappa^f_{\mathrm{SD,\,SI}} \cdot \Phi^f_{\nu+\bar{\nu}}, \tag{26}$$

donde $\kappa^f_{\mathrm{SD,\,SI}}$ es el factor de conversión calculado con DarkSUSY, para cada canal de aniquilación (f).

En la tabla 5 se presentan los cortes finales que optimizan el potencial de descubrimiento para un flujo de neutrinos producidos por la aniquilación de materia oscura en el Sol (Fig. 27). En la figura 28 se muestra el límite en la sección eficaz de interacción WIMP–nucleón SD (superior) and SI (inferior) para los tres canales de aniquilación y 5 años de datos simulados para la configuración completa de

[7] El parámetro de corte `track_score` es un parámetro de clasificación que se obtiene como salida de un árbol de decisión. Este árbol de decisión clasifica los sucesos como *traza* o como *cascada*. Valores cercanos a 1 significa que el suceso se clasifica, con mayor probabilidad, como *traza*.

ORCA (líneas rojas). Además, como referencia, se muestran los mejores límites obtenidos por otros experimentos.

θ_{zenith}	β	`Noise_score`	`Muon_score`	`Track_score`
$> 90°$	$< 1°$	< 0.1	< 0.05	0.7

Table 5: Lista final de parámetros de corta que optimizan el potencial de descubrimiento en la búsqueda de materia oscura en el Sol, para la configuración completa de ORCA.

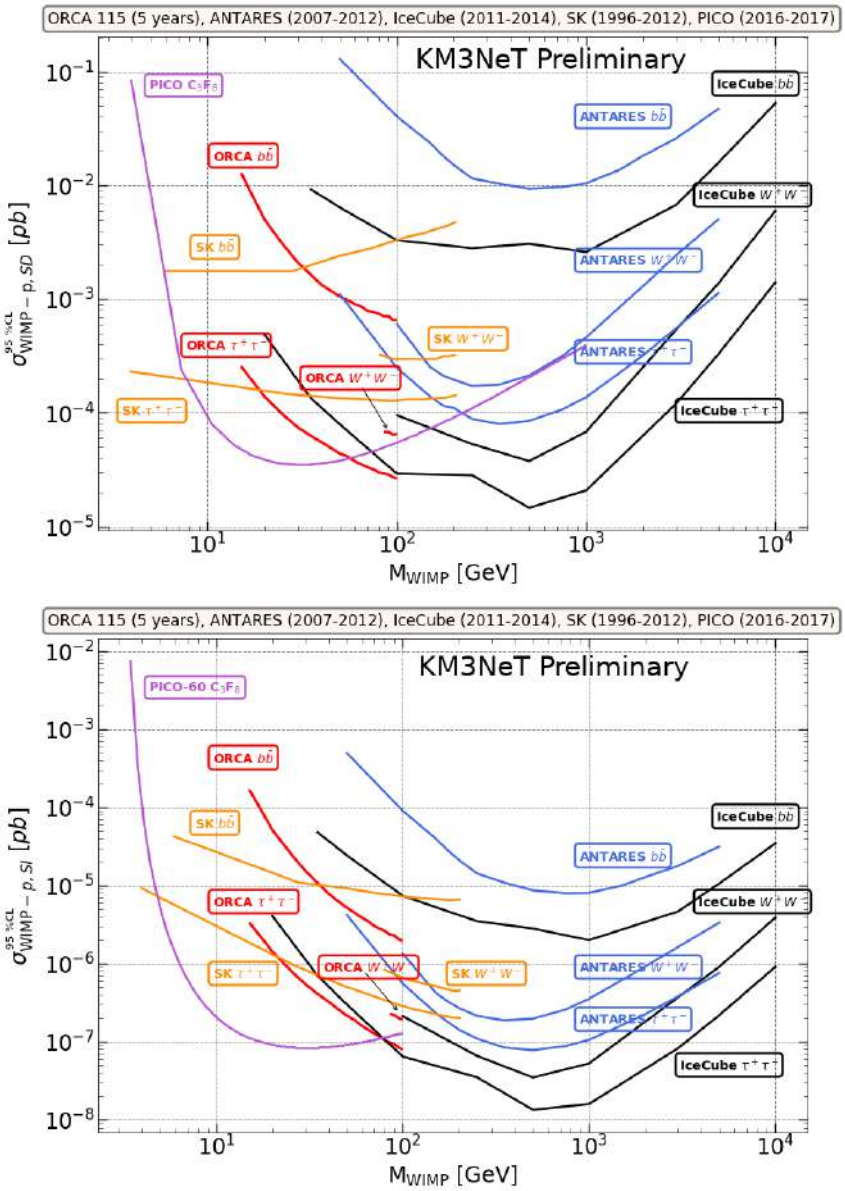

Figure 28: Sección eficaz de interacción WIMP-protón SD (superior) and SI (inferior) al 95% de confianza como función de la masa de WIMP para los tres canales de aniquilación. Se comparan los 5 años de datos simulados de ORCA con los 5 años de datos ANTARES [305], los 3 años de datos IceCube [306], 16 años de datos de Super Kamiokande [307] and y 1 año de datos de PICO-60 C_3F_8 [308]. Estos resultados están publicados en [295].

Como se muestra en la figura 28, el detector ORCA es potencialmente competitivo

en la búsqueda de materia oscura en el Sol, sobrepasando los resultados previos de ANTARES y SK, y estando muy cerca de los resultados de IceCube. Para poder comprar debidamente con el resto de experimentos, se necesita que el rango de masas de WIMP estudiado por ORCA se amplíe.

Perspectivas

Los resultados obtenidos de la búsqueda de SAνs con ANTARES abren paso a realizar este tipo de búsquedas con el detector KM3NeT (actualmente en construcción). Dicho detector posee un mayor volumen de instrumentación, lo que promete un mejor desempeño y mayores capacidades de detección.

Se ha mostrado que ORCA es una infraestructura bien provista para realizar búsquedas indirectas de materia oscura en el Sol. En este momento, se está realizando este mismo análisis para la configuración de ORCA con 6 líneas de detección.

ANTARES se desconectó el 12 de Febrero de 2022, y se ha previsto su desmantelamiento para el verano de este mismo año. Por otro lado, los detectores ARCA y ORCA han conseguido tener desplegadas 6 y 10 líneas de detección, respectivamente.

Main Publications

Journals

- **Search for Solar Atmospheric Neutrinos with the ANTARES Neutrino Telescope.**
  In journal review.

Proceedings

- **Dark Matter Searches from the Sun with the KM3NeT-ORCA detector.**
  PoS ICRC2019 (2020) 536.
- **Solar Atmospheric Neutrino searches with the ANTARES neutrino telescope.**
  PoS ICRC2021 (2021) 1122.
- **Indirect Dark Matter Searches with the ANTARES and KM3NeT Neutrino Telescopes.**
  PoS EPS-HEP2021 (2021) 174.

Bibliography

[1] J. Chadwick. *Intensitätsverteilung im magnetischen Spektrum der β-Strahlen von Radium B + C*. Verhandl. Dtsch. Phys. (1914). (Cited on pp: 4, 6).

[2] C. D. Ellis et al. "The average energy of disintegration of radium E". In: *Proceedings of the Royal Society of London. Series A, Containing Papers of a Mathematical and Physical Character*. Vol. 117. 776. The Royal Society, 1927. 109–123.
DOI: 10.1098/rspa.1927.0168. (Cited on p: 4).

[3] W. Pauli. "Pauli letter collection: letter to Lise Meitner". Typed copy. 1930 (Cited on p: 4).

[4] J. Chadwick. *Possible Existence of a Neutron*. Nature **129**, 312–312 (1932).
DOI: 10.1038/129312a0 (Cited on p: 4).

[5] E. Fermi. *Tentativo di una Teoria Dei Raggi β*. Il Nuovo Cimento **11**, 1–19 (1934).
DOI: 10.1007/bf02959820 (Cited on p: 4).

[6] F. Perrin. *Possibilité démission de particules neutres de masse intrinsèque nulle dans les radioactivités beta*. Comptes Rendues (1933). (Cited on p: 4).

[7] F. Reines et al. *Detection of the Free Antineutrino*. Phys. Rev. **117**, 159–173 (1960).
DOI: 10.1103/PhysRev.117.159 (Cited on p: 4).

[8] *The Nobel Prize in Physics 1995*. URL: https://www.nobelprize.org/prizes/physics/1995/summary/ (Cited on p: 4).

[9] F. Reines. *The neutrino: from poltergeist to particle*. Rev. Mod. Phys. **68**, 317–327 (1996).
DOI: 10.1103/RevModPhys.68.317 (Cited on pp: 4, 11).

[10] C. Giunti et al. *Fundamentals of Neutrino Physics and Astrophysics*. OXFORD UNIV PR, 2007. (Cited on p: 4).

[11] P. A. Zyla et al. *Review of Particle Physics*. Progress of Theoretical and Experimental Physics **2020**, 083C01 (2020).
DOI: 10.1093/ptep/ptaa104 (Cited on pp: 4–6, 16, 19, 42, 48, 92, 99, 101, 103, 105, 107).

[12] B. Pontecorvo. *Inverse beta processes and nonconservation of lepton charge*. Soviet Physics JETP (1957). (Cited on p: 5).

[13] B. Pontecorvo. *Neutrino Experiments and the Problem of Conservation of Leptonic Charge*. Zh. Eksp. Teor. Fiz. **53**, 1717–1725 (1967). (Cited on p: 6).

[14] V. Gribov et al. *Neutrino astronomy and lepton charge*. Phys. Lett. B **28**, 493–496 (1969).
DOI: 10.1016/0370-2693(69)90525-5 (Cited on p: 6).

[15] L. Wolfenstein. *Neutrino oscillations in matter*. Phys. Rev. D **17**, 2369–2374 (1978).
DOI: 10.1103/physrevd.17.2369 (Cited on p: 6).

[16] M. Doi et al. *Neutrinoless double-beta decay with Majoron emission*. Phys. Rev. D **37**, 2575–2589 (1988).
DOI: 10.1103/physrevd.37.2575 (Cited on p: 6).

[17] J. D. Vergados et al. *Neutrinoless double beta decay and neutrino mass*. Int. J. Mod. Phys. E **25**, 1630007 (2016).
DOI: 10.1142/s0218301316300071 (Cited on p: 6).

[18] S. M. Bilenky et al. *Neutrinoless double-beta decay: A probe of physics beyond the Standard Model*. Int. J. Mod. Phys. A **30**, 1530001 (2015).
DOI: 10.1142/s0217751x1530001x (Cited on p: 6).

[19] S. Bilenky. *Neutrinos: Majorana or Dirac?* (2020). (Cited on p: 6).

[20] R. Davis et al. *Search for Neutrinos from the Sun*. Phys. Rev. Lett. **20**, 1205–1209 (1968).
DOI: 10.1103/physrevlett.20.1205 (Cited on p: 6).

[21] Y. Fukuda et al. *Evidence for Oscillation of Atmospheric Neutrinos*. Phys. Rev.Lett. **81**, 1562–1567 (1998).
DOI: 10.1103/physrevlett.81.1562 (Cited on p: 6).

[22] Q. R. Ahmad et al. *Measurements of the Rate of $\nu_e + d \rightarrow p + p + e^+$ Interactions produced by ^8B Solar Neutrinos at the Sudbury Neutrino Observatory*. Phys. Rev. Lett. **87**, 071301 (2001).
DOI: 10.1103/physrevlett.87.071301 (Cited on pp: 6, 11).

[23] M. G. Aartsen et al. *Evidence for High-Energy Extraterrestrial Neutrinos at the IceCube Detector*. Science **342**, (2013).
DOI: 10.1126/science.1242856 (Cited on p: 6).

[24] A. Albert et al. *All-flavor Search for a Diffuse Flux of Cosmic Neutrinos with Nine Years of ANTARES Data*. Astrophys. J. **853**, L7 (2018).
DOI: 10.3847/2041-8213/aaa4f6 (Cited on p: 6).

[25] A. Albert et al. *Joint Constraints on Galactic Diffuse Neutrino Emission from the ANTARES and IceCube Neutrino Telescopes*. Astrophys. J. **868**, L20 (2018).
DOI: 10.3847/2041-8213/aaeecf (Cited on p: 6).

[26] A. Albert et al. *Constraining the contribution of Gamma-Ray Bursts to the high-energy diffuse neutrino flux with 10 yr of ANTARES data*. Mon. Notices Royal

Astron. Soc. **500**, 5614–5628 (2020).
DOI: 10.1093/mnras/staa3503 (Cited on p: 6).

[27] G. Giacomelli. *The CNGS Neutrino Beam*. J. Phys. Conf. Ser. (2007).
DOI: 10.1088/1742-6596/116/1/012004 (Cited on p: 6).

[28] K. Abe et al. *The T2K Neutrino Flux Prediction*. Phys. Rev. D (2013).
DOI: 10.1103/PhysRevD.87.012001 (Cited on p: 6).

[29] S. E. Kopp. *Accelerator Neutrino Beams*. Phys. Rept. (2007).
DOI: 10.1016/j.physrep.2006.11.004 (Cited on p: 6).

[30] T. K. Gaisser. *Atmospheric Neutrinos*. (2019). (Cited on p: 6).

[31] A. Mirizzi et al. *Supernova neutrinos: production, oscillations and detection*. Riv. del Nuovo Cim. **39**, 1–112 (2016).
DOI: 10.1393/ncr/i2016-10120-8 (Cited on p: 7).

[32] M. Honda et al. *Atmospheric neutrino flux calculation using the NRLMSISE-00 atmospheric model*. Phys. Rev. D **92**, 023004 (2015).
DOI: 10.1103/physrevd.92.023004 (Cited on pp: 7, 9, 109, 113).

[33] J. Edsjö et al. *Neutrinos from cosmic ray interactions in the Sun*. J. Cosmol. Astropart. Phys. **2017**, 033–033 (2017).
DOI: 10.1088/1475-7516/2017/06/033 (Cited on pp: 7, 47, 67, 125, 135).

[34] U. F. Katz et al. *High-energy neutrino astrophysics: Status and perspectives*. Progress in Particle and Nuclear Physics **67**, 651–704 (2012).
DOI: 10.1016/j.ppnp.2011.12.001 (Cited on p: 7).

[35] H. J. Voelk et al. *Maximum energy of cosmic-ray particles accelerated by supernova remnant shocks in stellar wind cavities*. Astrophys. J. **333**, L65 (1988).
DOI: 10.1086/185289 (Cited on p: 8).

[36] A. De Angelis et al. *Introduction to Particle and Astroparticle Physics*. Springer Milan, 2015.
DOI: 10.1007/978-88-470-2688-9. (Cited on p: 8).

[37] Adam Burrows et al. *Neutrinos from SN 1987A*. Astrophys. J. **318**, L63 (1987).
DOI: 10.1086/184938 (Cited on p: 8).

[38] P. L. Biermann. *The origin of cosmic rays*. Nucl. phys., B Proc. suppl. **43**, 221–228 (1995).
DOI: 10.1016/0920-5632(95)00478-r (Cited on p: 8).

[39] K. Koyama et al. *Evidence for shock acceleration of high-energy electrons in the supernova remnant SN1006*. Nature **378**, 255–258 (1995).
DOI: 10.1038/378255a0 (Cited on p: 8).

[40] T. Tanimori et al. *Discovery of TeV Gamma Rays from SN 1006: Further Evidence for the Supernova Remnant Origin of Cosmic Rays*. Astrophys. J. **497**, L25–L28 (1998).
DOI: 10.1086/311267 (Cited on p: 8).

[41] M. G. Baring. "Cosmic ray origin, acceleration and propagation". In: *AIP Conference Proceedings*. AIP, 2000.
DOI: 10.1063/1.1291474. (Cited on p: 8).

[42] F. Aharonian et al. *Evidence for TeV gamma ray emission from Cassiopeia A*. Astron. Astrophys. **370**, 112–120 (2001).
DOI: 10.1051/0004-6361:20010243 (Cited on p: 8).

[43] T. K. Gaisser. *Cosmic rays and particle physics*. Cambridge England New York: Cambridge University Press, 1990. (Cited on p: 8).

[44] J. Hofestädt. *Measuring the neutrino mass hierarchy with the future KM3NeT/ORCA detector*. PhD thesis. 2017 (Cited on pp: 9, 15, 16, 83, 84, 86).

[45] J. G. Learned et al. *High-Energy Neutrino Astrophysics*. Annu. Rev. Nucl. Part. Sci. **50**, 679–749 (2000).
DOI: 10.1146/annurev.nucl.50.1.679 (Cited on p: 9).

[46] H. Netzer. *Revisiting the Unified Model of Active Galactic Nuclei*. Annu. Rev. Astron. Astrophys. **53**, 365–408 (2015).
DOI: 10.1146/annurev-astro-082214-122302 (Cited on p: 10).

[47] B. Carroll. *An introduction to modern astrophysics*. San Francisco: Pearson Addison-Wesley, 2007. (Cited on p: 10).

[48] C. M. Urry et al. *Unified Schemes for Radio-Loud Active Galactic Nuclei*. Publ. Astron. Soc. Pac. **107**, 803 (1995).
DOI: 10.1086/133630 (Cited on p: 10).

[49] M. Böttcher et al. *Leptonic and HadronicModeling of Fermi-Detected Blazars*. Astrophys. J. **768**, 54 (2013).
DOI: 10.1088/0004-637x/768/1/54 (Cited on p: 10).

[50] A. A. Abdo et al. *The Spectral Energy Distribution of Fermi bright blazars*. Astrophys. J. **716**, 30–70 (2010).
DOI: 10.1088/0004-637x/716/1/30 (Cited on p: 10).

[51] J. H. Fan et al. *The Spectral Energy Distributions of FermiBlazars*. Astrophys. J., Suppl. Ser. **226**, 20 (2016).
DOI: 10.3847/0067-0049/226/2/20 (Cited on p: 10).

[52] E. Angelakis et al. *F-GAMMA: Multi-frequency radio monitoring ofFermi-blazars*. Astron. Astrophys. **626**, A60 (2019).
DOI: 10.1051/0004-6361/201834363 (Cited on p: 10).

[53] J. Barrios-Martí. *Search for cosmic sources in neutrino telescopes and time calibration in the ANTARES neutrino telescope*. PhD thesis. 2018 (Cited on pp: 10, 18, 80).

[54] K. McFarland. *Neutrino Interactions*. (2008). (Cited on p: 10).

[55] B. T. Cleveland et al. *Measurement of the Solar Electron Neutrino Flux with the Homestake Chlorine Detector*. Astrophys. J. **496**, 505–526 (1998). DOI: 10.1086/305343 (Cited on pp: 11, 46).

[56] D. Casper. "The nuance neutrino physics simulation, and the future". In: *Nuclear Physics B - Proceedings Supplements*. Vol. 112. 1-3. Elsevier BV, 2002. 161–170. DOI: 10.1016/s0920-5632(02)01756-5. (Cited on p: 12).

[57] J. L. Hewett et al. *Fundamental Physics at the Intensity Frontier*. (2012). DOI: https://doi.org/10.2172/1042577 (Cited on p: 12).

[58] J. Alvarez-Muñiz et al. *Practical and accurate calculations of Askaryan radiation*. Phys. Rev. D **84**, 103003 (2011). DOI: 10.1103/PhysRevD.84.103003 (Cited on p: 13).

[59] C. Deaconu et al. *A search for ultrahigh-energy neutrinos associated with astrophysical sources using the third flight of ANITA*. J. Cosmol. Astropart. Phys. **04**, 017 (2021). DOI: 10.1088/1475-7516/2021/04/017 (Cited on p: 13).

[60] R. Lahmann et al. *Acoustic neutrino detection investigations within ANTARES and prospects for KM3NeT*. EPJ Web of Conferences **116**, 03004 (2016). DOI: 10.1051/epjconf/201611603004 (Cited on p: 13).

[61] J. V. Jelley. *Cerenkov radiation and its applications*. Br. J. Appl. Phys. **6**, 227–232 (1955). DOI: 10.1088/0508-3443/6/7/301 (Cited on p: 13).

[62] P. A. Cerenkov. *Visible Emission of Clean Liquids by Action of γ Radiation*. Doklady Akad. Nauk SSSR (1934). (Cited on p: 13).

[63] P. A. Cerenkov. *Visible Radiation Produced by Electrons Moving in a Medium with Velocities Exceeding that of Light*. Phys. Rev. **52**, 378–379 (1937). DOI: 10.1103/physrev.52.378 (Cited on p: 13).

[64] V. Kulikovskiy. *Neutrino Astrophysics with the ANTARES Telescope*. Springer International Publishing, 2015. DOI: 10.1007/978-3-319-20412-3. (Cited on p: 14).

[65] N. R. Khan-Chowdhury. *Search for Neutrino Non-Standard Interactions with ANTARES and KM3NeT-ORCA*. PhD thesis. 2021 (Cited on pp: 15, 80, 85–88, 90).

[66] R. Kopp et al. *Energy loss of muons in the energy range 1-10000 GeV*. en. (1985). DOI: 10.5170/CERN-1985-003 (Cited on p: 15).

[67] K. Mitsui. *Muon energy-loss distribution and its applications to muon energy determination*. Phys. Rev. D **45**, 3051–3060 (1992). DOI: 10.1103/physrevd.45.3051 (Cited on p: 15).

[68] F. Versari. *Measurement of the atmospheric electron and muon neutrino flux with the ANTARES neutrino telescope*. PhD thesis. 2021 (Cited on p: 16).

[69] C. H. Wiebusch. *The Detection of Faint Light in Deep Underwater NeutrinoTelescopes*. PhD thesis. 1995 (Cited on p: 16).

[70] C. Mobley. *Light and water : radiative transfer in natural waters*. San Diego: Academic Press, 1994. (Cited on p: 17).

[71] M. Ackermann et al. *Optical properties of deep glacial ice at the South Pole*. J. Geophys. Res. **111**, (2006).
DOI: 10.1029/2005jd006687 (Cited on p: 17).

[72] A. Trovato. *Development of reconstruction algorithms for large volume neutrino telescopes and their application to the KM3NeT detector*. PhD thesis. 2013 (Cited on pp: 17, 82, 84–86).

[73] J. A. Aguilar et al. *Transmission of light in deep sea water at the site of the Antares neutrino telescope*. Astropart. Phys. **23**, 131–155 (2005).
DOI: 10.1016/j.astropartphys.2004.11.006 (Cited on p: 17).

[74] M. Ackermann et al. *Optical properties of deep glacial ice at the South Pole*. J. Geophys. Res. **111**, (2006).
DOI: 10.1029/2005jd006687 (Cited on p: 17).

[75] J. Lundberg et al. *Light tracking through ice and waterScattering and absorption in heterogeneous media with Photonics*. Nucl. Instrum. Meth. A **581**, 619–631 (2007).
DOI: 10.1016/j.nima.2007.07.143 (Cited on p: 17).

[76] A. Sánchez-Losa. *Search for high energy cosmic muon neutrinos from variable gamma-ray sources and time calibration of the optical modules of the ANTARES telescope*. PhD thesis. 2015 (Cited on pp: 18, 110).

[77] T. Chiarusi et al. *High-energy astrophysics with neutrino telescopes*. Eur. Phys. J. C **65**, 649–701 (2010).
DOI: 10.1140/epjc/s10052-009-1230-9 (Cited on p: 18).

[78] T. DeYoung et al. *Astrophysical tau neutrino detection in kilometer-scale Cherenkov detectors via muonic tau decay*. Astropart. Phys. **27**, 238–243 (2007).
DOI: 10.1016/j.astropartphys.2006.11.003 (Cited on p: 19).

[79] M. G. Aartsen et al. *Detection of a particle shower at the Glashow resonance with IceCube*. Nature **591**, [Erratum: Nature 592, E11 (2021)], 220–224 (2021).
DOI: 10.1038/s41586-021-03256-1 (Cited on p: 19).

[80] M. A. Markov et al. *On high energy neutrino physics in cosmic rays*. Nucl. Phys. **27**, 385–394 (1961).
DOI: 10.1016/0029-5582(61)90331-5 (Cited on p: 19).

[81] A. Roberts. *The birth of high-energy neutrino astronomy: A personal history of the DUMAND project*. Rev. Mod. Phys. **64**, 259–312 (1992).
DOI: 10.1103/revmodphys.64.259 (Cited on p: 20).

[82] I. A Belolaptikov et al. *The Baikal underwater neutrino telescope: Design, performance, and first results*. Astropart. Phys. **7**, 263–282 (1997).
DOI: 10.1016/s0927-6505(97)00022-4 (Cited on p: 20).

[83] V. Aynutdinov et al. *The Baikal Neutrino Telescope: From NT200 to NT200+*. Czechoslovak Journal of Physics **56**, A349–A360 (2006).
DOI: 10.1007/s10582-006-0168-5 (Cited on p: 20).

[84] V. Aynutdinov et al. *Search for a diffuse flux of high-energy extraterrestrial neutrinos with the NT200 neutrino telescope*. Astropart. Phys. **25**, 140–150 (2006).
DOI: 10.1016/j.astropartphys.2005.12.005 (Cited on p: 20).

[85] I. Belolaptikov et al. "Neutrino Telescope in Lake Baikal: Present and Nearest Future". In: *Proceedings of 37th International Cosmic Ray Conference - PoS(ICRC2021)*. Vol. ICRC2021. Sissa Medialab, 2021. 002.
DOI: 10.22323/1.395.0002. (Cited on p: 21).

[86] V. A. Allakhverdyan et al. *Measuring muon tracks in Baikal-GVD using a fast reconstruction algorithm*. Eur. Phys. J. C **81**, (2021).
DOI: 10.1140/epjc/s10052-021-09825-y (Cited on p: 21).

[87] M. Agostini et al. *The Pacific Ocean Neutrino Experiment*. Nat. Astron. **4**, 913–915 (2020).
DOI: 10.1038/s41550-020-1182-4 (Cited on p: 21).

[88] E. C. Andrés et al. *The AMANDA neutrino telescope*. Nucl. phys., B Proc. suppl. **77**, 474–485 (1999).
DOI: 10.1016/s0920-5632(99)00469-7 (Cited on p: 22).

[89] R. Abbasi et al. *Search for point sources of high energy neutrinos with final data from AMANDA-II*. Phys. Rev. D **79**, 062001 (2009).
DOI: 10.1103/physrevd.79.062001 (Cited on p: 22).

[90] J. Ahrens et al. *Muon track reconstruction and data selection techniques in AMANDA*. Nucl. Instrum. Methods Phys. Res. B **524**, 169–194 (2004).
DOI: 10.1016/j.nima.2004.01.065 (Cited on p: 22).

[91] M. Ackermann et al. *Search for Ultra-High-Energy Neutrinos with AMANDA-II*. Astrophys. J. **675**, 1014–1024 (2008).
DOI: 10.1086/527046 (Cited on p: 22).

[92] A. Achterberg et al. *Limits on the High-Energy Gamma and Neutrino Fluxes from the SGR 1806-20 Giant Flare of 27 December 2004 with the AMANDA-II Detector*. Phys. Rev. Lett. **97**, 221101 (2006).
DOI: 10.1103/physrevlett.97.221101 (Cited on p: 22).

[93] A. Karle. "IceCube". In: *Proceedings of the 31st ICRC, Lodz, Poland, July 2009*. 2010. (Cited on p: 22).

[94] M. G. Aartsen et al. *Search for neutrinos from dark matter self-annihilations in the center of the Milky Way with 3 years of IceCube/DeepCore*. Eur. Phys. J. C **77**, (2017).
DOI: 10.1140/epjc/s10052-017-5213-y (Cited on pp: 22, 23).

[95] R. Abbasi et al. *The design and performance of IceCube DeepCore*. Astropart. Phys. **35**, 615–624 (2012).
DOI: 10.1016/j.astropartphys.2012.01.004 (Cited on p: 23).

[96] M. G. Aartsen et al. *First Observation of PeV-Energy Neutrinos with IceCube*. Phys. Rev. Lett. **111**, 021103 (2013).
DOI: 10.1103/physrevlett.111.021103 (Cited on p: 23).

[97] M. G. Aartsen et al. *Evidence for High-Energy Extraterrestrial Neutrinos at the IceCube Detector*. Science **342**, (2013).
DOI: 10.1126/science.1242856 (Cited on p: 23).

[98] M. Ageron et al. *ANTARES: The First Undersea Neutrino Telescope*. Nucl. Instrum. Meth. A **656**, 11–38 (2011).
DOI: https://doi.org/10.1016/j.nima.2011.06.103 (Cited on pp: 27–29, 31, 32, 126, 136).

[99] J. A. Aguilar et al. *AMADEUS The acoustic neutrino detection test system of the ANTARES deep-sea neutrino telescope*. Nucl. Instrum. Meth. A **626-627**, 128–143 (2011).
DOI: 10.1016/j.nima.2010.09.053 (Cited on p: 28).

[100] Y. Tapilatu et al. *Isolation of alkane-degrading bacteria from deep-sea Mediterranean sediments*. Lett. Appl. Microbiol. **50**, 234–236 (2010).
DOI: 10.1111/j.1472-765x.2009.02766.x (Cited on p: 27).

[101] A. A. Badr et al. *Luminous bacteria in the deep-sea waters near the ANTARES underwater neutrino telescope (Mediterranean Sea)*. Chem. Ecol. **26**, 57–72 (2010).
DOI: 10.1080/02757540903513766 (Cited on p: 27).

[102] L. A. Fusco et al. *The Run-by-Run Monte Carlo simulation for the ANTARES experiment*. EPJ Web of Conferences **116**, 02002 (2016).
DOI: 10.1051/epjconf/201611602002 (Cited on pp: 28, 33, 34, 126, 136).

[103] P. Amram et al. *The ANTARES optical module*. Nucl. Instrum. Meth. A **484**, 369–383 (2002).
DOI: https://doi.org/10.1016/S0168-9002(01)02026-5 (Cited on pp: 28, 29).

[104] A. Albert et al. *Long-term monitoring of the ANTARES optical module efficiencies using ^{40}K decays in sea water*. Eur. Phys. J. C **78**, 669 (2018).
DOI: 10.1140/epjc/s10052-018-6132-2 (Cited on pp: 29, 38).

[105] J. A. Aguilar et al. *Study of large hemispherical photomultiplier tubes for the ANTARES neutrino telescope*. Nucl. Instrum. Meth. A **555**, 132–141 (2005).
DOI: 10.1016/j.nima.2005.09.035 (Cited on p: 30).

[106] J. A. Aguilar et al. *The data acquisition system for the ANTARES neutrino telescope*. Nucl. Instrum. Meth. A **570**, 107–116 (2007).
DOI: https://doi.org/10.1016/j.nima.2006.09.098 (Cited on p: 30).

[107] M. de Jong. *The ANTARES Trigger Software*. ANTARES internal note, ANTARES-Soft/2005-005 (2005). (2005) (Cited on p: 31).

[108] M. Ardid and. *Positioning system of the ANTARES neutrino telescope*. Nucl. Instrum. Meth. A **602**, 174–176 (2009).
DOI: https://doi.org/10.1016/j.nima.2008.12.033 (Cited on p: 32).

[109] J. A. Aguilar et al. *Time calibration of the ANTARES neutrino telescope*. Astropart. Phys. **34**, 539–549 (2011).
DOI: 10.1016/j.astropartphys.2010.12.004 (Cited on pp: 32, 33).

[110] M. Ageron et al. *The ANTARES optical beacon system*. Nucl. Instrum. Meth. A **578**, 498–509 (2007).
DOI: https://doi.org/10.1016/j.nima.2007.05.325 (Cited on p: 32).

[111] S. Adrián-Martínez et al. *Time calibration with atmospheric muon tracks in the ANTARES neutrino telescope*. Astropart. Phys. **78**, 43–51 (2016).
DOI: 10.1016/j.astropartphys.2016.02.001 (Cited on pp: 33, 37).

[112] A. Albert et al. *Monte Carlo simulations for the ANTARES underwater neutrino telescope*. J. Cosmol. Astropart. Phys. **2021**, 064–064 (2021).
DOI: 10.1088/1475-7516/2021/01/064 (Cited on pp: 34, 35, 38, 126, 136).

[113] G. de Bonis. *GENHEN release v7r1*. ANTARES internal note, ANTARES-Soft/2014-001. (2014) (Cited on pp: 35, 82, 127, 137).

[114] G. Ingelman et al. *LEPTO 6.5 A Monte Carlo generator for deep inelastic lepton-nucleon scattering*. Comput. Phys. Commun. **101**, 108–134 (1997).
DOI: 10.1016/S0010-4655(96)00157-9 (Cited on p: 35).

[115] D. J. L. Bailey. *Monte Carlo tools and analysis methods for understanding the ANTARES experiment and predicting its sensitivity to Dark Matter*. PhD thesis. 2002 (Cited on pp: 35, 36, 83).

[116] J. Brunner. *Updated tag list for the new ANTARES event format*. ANTARES internal note, ANTARES-Soft/1999-003. (1999) (Cited on p: 36).

[117] D. Heck et al. *CORSIKA: A Monte Carlo code to simulate extensive air showers*. en. Tech. rep. 1998, 98.
DOI: 10.5445/IR/270043064 (Cited on pp: 37, 83, 127, 137).

[118] A. A. Alves et al. "CORSIKA 8". In: *EPJ Web of Conferences*. Ed. by C. Biscarat et al. Vol. 251. EDP Sciences, 2021. 03038.
DOI: 10.1051/epjconf/202125103038. (Cited on pp: 37, 83, 127, 137).

[119] P. Antonioli et al. *A three-dimensional code for muon propagation through the rock: MUSIC*. Astropart. Phys. **7**, 357–368 (1997).
DOI: 10.1016/S0927-6505(97)00035-2 (Cited on p: 37).

[120] G. Carminati et al. *Atmospheric MUons from PArametric formulas: a fast GEnerator for neutrino telescopes (MUPAGE)*. Comput. Phys. Commun. **179**, 915–923 (2008).
DOI: 10.1016/j.cpc.2008.07.014 (Cited on pp: 38, 83, 127, 137).

[121] S. Navas et al. *KM3 user guide and reference manual.* KM3NeT internal note, KM3NeT-SIM/2015-001. (2015) (Cited on p: 38).

[122] S. Agostinelli et al. *Geant4 - a simulation toolkit*. Nucl. Instrum. Meth. A **506**, 250–303 (2003).
DOI: https://doi.org/10.1016/S0168-9002(03)01368-8 (Cited on pp: 38, 83).

[123] H. van Haren et al. *Acoustic and optical variations during rapid downward motion episodes in the deep north-western Mediterranean Sea*. Deep Sea Research Part I: Oceanographic Research Papers **58**, 875–884 (2011).
DOI: 10.1016/j.dsr.2011.06.006 (Cited on p: 38).

[124] C. Tamburini et al. *Deep-Sea Bioluminescence Blooms after Dense Water Formation at the Ocean Surface*. PLoS ONE **8**, e67523 (2013).
DOI: https://doi.org/10.1371/journal.pone.0067523 (Cited on p: 38).

[125] E. L. Visser. *Neutrinos from the Milky Way*. PhD thesis. Netherlands: Universitet Leiden, 2015 (Cited on pp: 38, 40, 42).

[126] A. Albert et al. *An algorithm for the reconstruction of high-energy neutrino-induced particle showers and its application to the ANTARES neutrino telescope*. Eur. Phys. J. C **77**, 419 (2017).
DOI: 10.1140/epjc/s10052-017-4979-2 (Cited on p: 38).

[127] A. J. Heijboer. *Track Reconstruction and Point Source Searches with Antares*. PhD thesis. Institute for High Energy Physics (IHEF), 2004 (Cited on pp: 38, 41, 84).

[128] J. A. Aguilar et al. *A fast algorithm for muon track reconstruction and its application to the ANTARES neutrino telescope*. Astropart. Phys. **34**, 11 (2011).
DOI: 10.1016/j.astropartphys.2011.01.003 (Cited on p: 41).

[129] S. Adrián-Martnez et al. *Searches for Point-like and Extended Neutrino Sources Close to the Galactic Center Using the ANTARES Neutrino Telescope*. Astrophys. J. **786**, L5 (2014).
DOI: 10.1088/2041-8205/786/1/L5 (Cited on p: 41).

[130] J. Schnabel et al. *Muon energy reconstruction in the ANTARES detector*. Nucl. Instrum. Meth. A **725**, 106–109 (2013).
DOI: 10.1016/j.nima.2012.12.109 (Cited on pp: 41, 42).

[131] M. J. Aschwanden. "Chapter 11 - The Sun". In: *Encyclopedia of the Solar System (Third Edition)*. Ed. by Tilman Spohn et al. Third Edition. Boston: Elsevier, 2014. 235–259.
DOI: https://doi.org/10.1016/B978-0-12-415845-0.00011-6. (Cited on pp: 44, 45).

[132] S. Turck-Chièze. *The Standard Solar Model and beyond*. J. Phys. Conf. Ser. **665**, 012078 (2016).
DOI: 10.1088/1742-6596/665/1/012078 (Cited on p: 45).

[133] H. M. Antia et al. *Lectures on Solar Physics*. Ed. by H. M. Antia et al. Springer Berlin Heidelberg, 2003.
DOI: 10.1007/3-540-36963-5. (Cited on p: 45).

[134] W. C. Haxton et al. *Solar Neutrinos: Status and Prospects*. Annu. Rev. Astron. Astrophys. **51**, 21–61 (2013).
DOI: 10.1146/annurev-astro-081811-125539 (Cited on p: 45).

[135] N. Grevesse et al. *The composition of the solar photosphere*. Adv. Space Res. **30**, 3–11 (2002).
DOI: 10.1016/s0273-1177(02)00170-9 (Cited on p: 45).

[136] C Fröhlich. "Solar Composition and its Evolution – from Core to Corona". In: *Proceedings of an ISSI Workshop 26-30 January 1998, Bern, Switzerland*. Dordrecht: Springer Netherlands Imprint Springer, 1998. (Cited on p: 45).

[137] C. A. Prieto. *Chemical composition of the solar surface*. J. Astrophys. Astron **41**, (2020).
DOI: 10.1007/s12036-020-09666-3 (Cited on p: 45).

[138] M. Aschwanden. *Physics of the Solar Corona*. Springer Science & Business Media, 2006. (Cited on p: 45).

[139] Gabriel D. Orebi Gann et al. *The Future of Solar Neutrinos*. Annu. Rev. Nucl. Part. Sci. **71**, 491–528 (2021).
DOI: 10.1146/annurev-nucl-011921-061243 (Cited on p: 46).

[140] P. Anselmann et al. *Solar neutrinos observed by GALLEX at Gran Sasso*. Phys. Lett. B **285**, 376–389 (1992).
DOI: 10.1016/0370-2693(92)91521-a (Cited on p: 46).

[141] M. Altmann et al. *Complete results for five years of GNO solar neutrino observations*. Phys. Lett. B **616**, 174–190 (2005).
DOI: 10.1016/j.physletb.2005.04.068 (Cited on p: 46).

[142] J. N. Abdurashitov et al. *Measurement of the solar neutrino capture rate with gallium metal. III. Results for the 20022007 data-taking period*. Phys. Rev. C **80**, 015807 (2009).
DOI: 10.1103/physrevc.80.015807 (Cited on p: 46).

[143] K. S. Hirata et al. *Observation of B-8 solar neutrinos in the Kamiokande-II detector*. Phys. Rev. Lett. **63**, 16–19 (1989).
DOI: 10.1103/physrevlett.63.16 (Cited on p: 46).

[144] Y. Fukuda et al. *Solar Neutrino Data Covering Solar Cycle 22*. Phys. Rev. Lett. **77**, 1683–1686 (1996).
DOI: 10.1103/physrevlett.77.1683 (Cited on p: 46).

[145] Herbert H. C. *Direct Approach to Resolve the Solar-Neutrino Problem*. Phys. Rev. Lett. **55**, 1534–1536 (1985).
DOI: 10.1103/physrevlett.55.1534 (Cited on p: 46).

[146] J. Boger et al. *The Sudbury Neutrino Observatory*. Nucl. Instrum. Methods. Phys. Res. B **449**, 172–207 (2000).
DOI: 10.1016/s0168-9002(99)01469-2 (Cited on p: 46).

[147] Q. R. Ahmad et al. *Measurement of the Rate of $\nu_e + d/top + p + e^-$ Interactions Produced by B-8 Solar Neutrinos at the Sudbury Neutrino Observatory*. Phys. Rev. Lett. **87**, 071301 (2001).
DOI: 10.1103/physrevlett.87.071301 (Cited on p: 46).

[148] S. N. Ahmed et al. *Measurement of the Total Active B-8 Solar Neutrino Flux at the Sudbury Neutrino Observatory with Enhanced Neutral Current Sensitivity*. Phys. Rev. Lett. **92**, 181301 (2004).
DOI: 10.1103/physrevlett.92.181301 (Cited on p: 46).

[149] T. K. Gaisser et al. *Flux of Atmospheric Neutrinos*. Annu. Rev. Nucl. Part. Sci. **52**, 153–199 (2002).
DOI: 10.1146/annurev.nucl.52.050102.090645 (Cited on p: 47).

[150] K. C. Y. Ng et al. *Solar atmospheric neutrinos: A new neutrino floor for dark matter searches*. Phys. Rev.D **96**, 103006 (2017).
DOI: 10.1103/physrevd.96.103006 (Cited on p: 47).

[151] C. A. Argüelles et al. *Solar atmospheric neutrinos and the sensitivity floor for solar dark matter annihilation searches*. J. Cosmol. Astropart. Phys. **2017**, 024–024 (2017).
DOI: 10.1088/1475-7516/2017/07/024 (Cited on pp: 47, 125, 135).

[152] D. Seckel et al. *Signatures of cosmic-ray interactions on the solar surface*. Astrophys. J. **382**, 652 (1991).
DOI: 10.1086/170753 (Cited on pp: 47, 125, 135).

[153] C. Hettlage. *The sun as a high energy neutrino source*. Astropart. Phys. **13**, 45–50 (2000).
DOI: 10.1016/s0927-6505(99)00120-6 (Cited on pp: 47, 125, 135).

[154] G. Ingelman et al. *High Energy Neutrino Production by Cosmic Ray Interactions in the Sun*. Phys. Rev. D **54**, 4385–4392 (1996).
DOI: 10.1103/PhysRevD.54.4385 (Cited on pp: 47, 125, 135).

[155] G. L. Fogli et al. *Oscillations of solar atmosphere neutrinos*. Phys. Rev. D **74**, 093004 (2006).
DOI: 10.1103/physrevd.74.093004 (Cited on pp: 47, 125, 135).

[156] T. K. Gaisser. *Spectrum of cosmic-ray nucleons, kaon production, and the atmospheric muon charge ratio*. Astropart. Phys. **35**, 801–806 (2012).
DOI: 10.1016/j.astropartphys.2012.02.010 (Cited on pp: 48, 70, 127, 137).

[157] T. K. Gaisser et al. *Cosmic ray energy spectrum from measurements of air showers*. Front Phys-beijing **8**, 748–758 (2013).
DOI: 10.1007/s11467-013-0319-7 (Cited on p: 48).

[158] A. M. Serenelli et al. *New Solar Composition: The Problem with Solar Models Revisited*. Astrophys. J. **705**, L123–L127 (2009).
DOI: 10.1088/0004-637x/705/2/l123 (Cited on pp: 48, 70, 127, 137).

[159] N. Grevesse et al. *Standard solar composition*. Space Sci. Rev. **85**, 161–174 (1998).
DOI: 10.1023/a:1005161325181 (Cited on p: 48).

[160] J. Edsjö et al. *WIMPSIM 5.0: WimpAnn, med_dec, solar_crnu and WimpEvent*. 2019 (Cited on pp: 48, 106, 107, 127, 137).

[161] M. Blennow et al. *Neutrinos from WIMP annihilations obtained using a full three-flavor Monte Carlo approach*. J. Cosmol. Astropart. Phys. **2008**, 021 (2008).
DOI: 10.1088/1475-7516/2008/01/021 (Cited on pp: 48, 107, 127, 137).

[162] I. Esteban et al. *Updated fit to three neutrino mixing: exploring the accelerator-reactor complementarity*. J. High Energy Phys. **2017**, (2016).
DOI: 10.1007/jhep01(2017)087 (Cited on pp: 48, 67).

[163] M. Honda et al. *Calculation of atmospheric neutrino flux using the interaction model calibrated with atmospheric muon data*. Physical Review D **75**, 043006 (2007).
DOI: 10.1103/physrevd.75.043006 (Cited on pp: 49, 50).

[164] R. Barlow. *Extended maximum likelihood*. Nucl. Instrum. Meth. A **297**, 496–506 (1990).
DOI: https://doi.org/10.1016/0168-9002(90)91334-8 (Cited on pp: 57, 58).

[165] C. Tonnis. *Indirect search for dark matter in the Sun and the Galactic Centre with the ANTARES neutrino telescope*. PhD thesis. 2017 (Cited on pp: 58, 59, 110).

[166] F. James et al. *Minuit - a system for function minimization and analysis of the parameter errors and correlations*. Comput. Phys. Commun. **10**, 343–367 (1975).
DOI: 10.1016/0010-4655(75)90039-9 (Cited on p: 64).

[167] J. Neyman. *Outline of a Theory of Statistical Estimation Based on the Classical Theory of Probability*. Phil. Trans. R. S. of London, Ser. A **236**, 333–380 (1937).
DOI: https://doi.org/10.1098/rsta.1937.0005 (Cited on pp: 65, 118, 127, 128, 138).

[168] A. Albert et al. *First all-flavor neutrino pointlike source search with the ANTARES neutrino telescope*. Phys. Rev. D **96**, 082001 (2017).
DOI: 10.1103/PhysRevD.96.082001 (Cited on pp: 65, 67, 118, 127, 128, 138).

[169] A. Nuñez-Castiñeyra. *From cosmological simulations to Dark Matter detection*. PhD thesis. 2020 (Cited on pp: 67, 110).

[170] A. Albert et al. *Search for dark matter towards the Galactic Centre with 11 years of ANTARES data*. Phys. Lett. B **805**, 135439 (2020).
DOI: 10.1016/j.physletb.2020.135439 (Cited on pp: 67, 106).

[171] M. G. Aartsen et al. *Searches for neutrinos from cosmic-ray interactions in the Sun using seven years of IceCube data*. J. Cosmol. Astropart. Phys. **2021**, 025–025 (2021).
DOI: 10.1088/1475-7516/2021/02/025 (Cited on pp: 71, 130, 140).

[172] A. Albert et al. *Search for solar atmospheric neutrinos with the ANTARES neutrino telescope*. (2022). (Cited on pp: 71, 130, 140).

[173] S. Adrián-Martínez et al. *Letter of intent for KM3NeT 2.0*. J. Phys. G: Nucl. Part. Phys. **43**, 084001 (2016).
DOI: 10.1088/0954-3899/43/8/084001 (Cited on pp: 75, 77, 106).

[174] A. Sinopoulou et al. "Atmospheric neutrinos with the first detection units of KM3NeT-ARCA". In: *Proceedings of 37th International Cosmic Ray Conference - PoS(ICRC2021)*. Sissa Medialab, 2021.
DOI: 10.22323/1.395.1134. (Cited on p: 76).

[175] L. Nauta et al. "First neutrino oscillation measurement in KM3NeT/ORCA". In: *Proceedings of 37th International Cosmic Ray Conference - PoS(ICRC2021)*. Sissa Medialab, 2021.
DOI: 10.22323/1.395.1123. (Cited on p: 76).

[176] A. Margiotta and. *The KM3NeT deep-sea neutrino telescope*. Nucl. Instrum. Meth. A **766**, 83–87 (2014).
DOI: 10.1016/j.nima.2014.05.090 (Cited on pp: 76, 78).

[177] S. Adrián-Martínez et al. *The prototype detection unit of the KM3NeT detector: KM3NeT Collaboration*. Eur. Phys. J. C **76**, 54 (2016).
DOI: 10.1140/epjc/s10052-015-3868-9 (Cited on pp: 76, 80).

[178] S. Aiello et al. *Deep-sea deployment of the KM3NeT neutrino telescope detection units by self-unrolling*. J. Instrum. **15**, P11027–P11027 (2020).
DOI: 10.1088/1748-0221/15/11/p11027 (Cited on p: 77).

[179] R. Bruijn et al. "The KM3NeT Multi-PMT Digital Optical Module". In: *Proceedings of The 34th International Cosmic Ray Conference PoS(ICRC2015)*. The 34th International Cosmic Ray Conference. The Hague, The Netherlands: Sissa Medialab, 2016. 1157.
DOI: 10.22323/1.236.1157. (Cited on p: 78).

[180] I. Di Palma. "KM3NeT Time Calibration". In: *EPJ Web of Conferences*. Ed. by C. Spiering. Vol. 207. EDP Sciences, 2019. 07001.
DOI: 10.1051/epjconf/201920707001. (Cited on pp: 78, 80, 81).

[181] S. Aiello et al. *Characterisation of the Hamamatsu photomultipliers for the KM3NeT Neutrino Telescope*. J. Instrum. **13**, P05035–P05035 (2018).
DOI: 10.1088/1748-0221/13/05/P05035 (Cited on p: 78).

[182] KM3NeT Collaboration. *KM3NeT Website*. URL: https://www.km3net.org/ (Cited on p: 79).

[183] T. Chiarusi et al. *The Trigger and Data Acquisition System for the KM3NeT-Italy neutrino telescope*. J. Phys. Conf. Ser. **898**, 032042 (2017). DOI: 10.1088/1742-6596/898/3/032042 (Cited on p: 79).

[184] T. Chiarusi et al. *KM3NeT: R&D and technical solutions for the next generation underwater neutrino telescope*. Nuclear Part. Phys. Proc. **273-275**, 2357–2359 (2016). DOI: 10.1016/j.nuclphysbps.2015.09.390 (Cited on p: 79).

[185] V. Van Elewyck et al. *The Calibration Units of the KM3NeT neutrino telescope*. EPJ Web of Conferences **116**, 06006 (2016). DOI: http://dx.doi.org/10.1051/epjconf/201611606006 (Cited on p: 79).

[186] S. Viola et al. "Acoustic positioning system for KM3NeT". In: *Proceedings of The 34th International Cosmic Ray Conference - PoS(ICRC2015)*. The 34th International Cosmic Ray Conference. The Hague, The Netherlands: Sissa Medialab, 2016. 1169. DOI: 10.22323/1.236.1169. (Cited on p: 80).

[187] KM3NeT Collaboration. *KM3NeT Technical Design Report for a Deep-Sea Research Infrastrcture in the Mediterranean Sea Incorporating a Very Large Volume Neutrino Telescope*. (2015). (Cited on p: 80).

[188] P. Musico. *The Central Logic Board for the KM3NeT detector: Design and production*. Nucl. Instrum. Meth. A **824**, 322–323 (2016). DOI: 10.1016/j.nima.2015.10.043 (Cited on p: 80).

[189] D. Real et al. *Nanobeacon: A time calibration device for KM3NeT*. EPJ Web of Conferences **207**, 07002 (2019). DOI: 10.1051/epjconf/201920707002 (Cited on p: 80).

[190] K. Melis. "In-Situ Calibration of KM3NeT". In: *Proceedings of 35th International Cosmic Ray Conference PoS(ICRC2017)*. Sissa Medialab, 2017. 7. DOI: https://doi.org/10.22323/1.301.1059. (Cited on p: 80).

[191] J. Brunner. *ANTARES Simulations*. ANTARES internal note, ANTARES-SOFT/2003-009. (2003) (Cited on p: 81).

[192] C. Kopper. *Development of Monte-Carlo tools for the KM3NeT neutrino telescope*. Nucl. Instrum. Meth. A **626-627**, S243–S245 (2011). DOI: 10.1016/j.nima.2010.06.251 (Cited on p: 81).

[193] C. Kopper et al. *A software framework for KM3NeT*. **602**, 107–110 (2009). DOI: 10.1016/j.nima.2008.12.047 (Cited on p: 81).

[194] S. Aiello et al. *gSeaGen: The KM3NeT GENIE-based code for neutrino telescopes*. Comput. Phys. Commun. **256**, 107477 (2020). DOI: 10.1016/j.cpc.2020.107477 (Cited on pp: 82, 127, 137).

[195] M. Lincetto. *Development of multi-messenger real-time analyses for the KM3NeT neutrinotelescope*. PhD thesis. Aix-Marseille Université, 2021 (Cited on pp: 83, 84, 86, 126).

[196] D. Dornic et al. "Detailed KM3NeT optical module simulation with Geant4 and supernova neutrino detection study". In: *Proceedings of The 35th International Cosmic Ray Conference - PoS(ICRC2017)*. Sissa Medialab, 2017. DOI: 10.22323/1.301.0983. (Cited on p: 83).

[197] M. de Jong. *JSirene : A program to simulate the detector response*. ANTARES internal note, ANTARES-SOFT/2012-004. (2012) (Cited on p: 83).

[198] M. de Jong. *The probability density function of the arrival time of light*. ANTARES internal note, ANTARES-SOFT/2010-002. (2010) (Cited on p: 83).

[199] M. de Jong. *Multi-dimensional interpolations in C++*. (2019). (Cited on p: 83).

[200] A. G. Tsirigotis et al. *HOU Reconstruction & Simulation (HOURS): A complete simulation and reconstruction package for very large volume underwater neutrino telescopes*. Nucl. Instrum. Meth. A **626-627**, S185–S187 (2011). DOI: 10.1016/j.nima.2010.06.258 (Cited on p: 83).

[201] M. de Jong. *The Jpp - JTools package*. (2011) (Cited on p: 83).

[202] K. Melis et al. "KM3NeT/ARCA Event Reconstruction Algorithms". In: *Proceedings of 35th International Cosmic Ray Conference - PoS(ICRC2017)*. 35th International Cosmic Ray Conference. Bexco, Busan, Korea: Sissa Medialab, 2017. 950. DOI: 10.22323/1.301.0950. (Cited on pp: 84, 85).

[203] S. Adrián-Martínez et al. *Intrinsic limits on resolutions in muon- and electron-neutrino charged-current events in the KM3NeT/ORCA detector*. J. High Energy Phys. **2017**, 8 (2017). DOI: 10.1007/JHEP05(2017)008 (Cited on pp: 86, 118).

[204] L. Quinn. *Determining the Neutrino Mass Hierarchy with KM3NeT/ORCA*. Theses. Aix Marseille Universitè, 2018 (Cited on p: 87).

[205] L. Breiman. *Random Forest*. Machine Learning **45**, 5–32 (2001). DOI: 10.1023/a:1010933404324 (Cited on p: 88).

[206] S. Hallmann. *Sensitivity to atmospheric tau-neutrino appearance and all-flavour search for neutrinos from the Fermi Bubbles with the deep-sea telescopes KM3NeT/ORCA and ANTARES*. PhD thesis. FAU Erlangen-Nuremberg, 2020 (Cited on p: 88).

[207] L. Bergström. *Dark matter candidates*. New J. Phys **11**, 105006 (2009). DOI: 10.1088/1367-2630/11/10/105006 (Cited on pp: 91, 125, 135).

[208] J. L. Feng. *Dark Matter Candidates from Particle Physics and Methods of Detection*. Annu. Rev. Astron. Astr. **48**, 495–545 (2010). DOI: 10.1146/annurev-astro-082708-101659 (Cited on pp: 91, 97, 99, 125, 135).

[209] B. L. Young. *A survey of dark matter and related topics in cosmology*. Front. Phys. **12**, (2016).
DOI: 10.1007/s11467-016-0583-4 (Cited on pp: 91–93, 95, 97, 125, 135).

[210] R. H. Cyburt et al. *Big bang nucleosynthesis: Present status*. Rev. Mod. Phys. **88**, 015004 (2016).
DOI: 10.1103/revmodphys.88.015004 (Cited on p: 92).

[211] L. Perivolaropoulos et al. *Challenges for CDM: An update*. (2021). (Cited on p: 92).

[212] N. Aghanim et al. *Planck 2018 results*. Astron. Astrophys. **641**, A6 (2020).
DOI: 10.1051/0004-6361/201833910 (Cited on pp: 92, 99).

[213] E. Oks. *Brief review of recent advances in understanding dark matter and dark energy*. New Astron. Rev. **93**, 101632 (2021).
DOI: 10.1016/j.newar.2021.101632 (Cited on p: 92).

[214] V. C. Rubin et al. *Rotation of the Andromeda Nebula from a Spectroscopic Survey of Emission Regions*. Astrophys. J. **159**, 379 (1970).
DOI: 10.1086/150317 (Cited on p: 92).

[215] H. W. Babcock. *Spectrographic Observations of the Rotation of the Andromeda Nebula*. Publ. Astron. Soc. Pac. **50**, 174 (1938).
DOI: 10.1086/124921 (Cited on p: 92).

[216] H. W. Babcock. *The rotation of the Andromeda Nebula*. Lick Observatory bulletin **19**, 41–51 (1939).
DOI: 10.5479/ads/bib/1939licob.19.41b (Cited on p: 92).

[217] K. C. Freeman. *On the Disks of Spiral and so Galaxies*. Astrophys. J. **160**, 811 (1970).
DOI: 10.1086/150474 (Cited on p: 92).

[218] K. Freese. *Review of Observational Evidence for Dark Matter in the Universe and in upcoming searches for Dark Stars*. EAS Publ. Ser. **36**, 113–126 (2009).
DOI: 10.1051/eas/0936016 (Cited on pp: 92, 93).

[219] A. G. Doroshkevich et al. *A solution to the problems of cusps and rotation curves in dark matter halos in the cosmological standard model*. Uspekhi Fizicheskih Nauk **182**, 3 (2012).
DOI: 10.3367/ufnr.0182.201201a.0003 (Cited on p: 93).

[220] A. Einstein. *Lens-Like Action of a Star by the Deviation of Light in the Gravitational Field*. Science **84**, 506–507 (1936).
DOI: 10.1126/science.84.2188.506 (Cited on p: 93).

[221] D. Majumdar. *Dark matter : an introduction*. Boca Raton, FL: CRC Press, Taylor and Francis, 2015. (Cited on pp: 95, 99).

[222] R. Massey et al. *The dark matter of gravitational lensing*. Rep. Prog. Phys. **73**, 086901 (2010).
DOI: 10.1088/0034-4885/73/8/086901 (Cited on p: 95).

[223] M. Markevitch. *Chandra observation of the most interesting cluster in the universe*. ESA Spec. Publ. **604**, 723 (2005). (Cited on p: 95).

[224] D. Clowe et al. *A Direct Empirical Proof of the Existence of Dark Matter*. Astrophys. J. **648**, L109–L113 (2006).
DOI: 10.1086/508162 (Cited on p: 95).

[225] M. Brada et al. *Revealing the Properties of Dark Matter in the Merging Cluster MACS J0025.4-1222*. Astrophys. J. **687**, 959–967 (2008).
DOI: 10.1086/591246 (Cited on p: 96).

[226] J. Chacón et al. *Dark matter with n-body numerical simulations*. Rev. Mex. de Fis. **17**, 241–254 (2020).
DOI: 10.31349/revmexfise.17.241 (Cited on p: 96).

[227] V. Springel et al. *Simulations of the formation, evolution and clustering of galaxies and quasars*. Nature **435**, 629–636 (2005).
DOI: 10.1038/nature03597 (Cited on p: 96).

[228] A. Challinor. *CMB anisotropy science: a review*. Proc. Int. Astron. Union **8**, 42–52 (2012).
DOI: 10.1017/s1743921312016663 (Cited on p: 97).

[229] J. Silk. *The big bang*. New York: W.H. Freeman, 1989. (Cited on p: 97).

[230] T. Hambye et al. *Dark matter as a heavy thermal hot relic*. Phys. Lett. B **807**, 135553 (2020).
DOI: https://doi.org/10.1016/j.physletb.2020.135553 (Cited on p: 98).

[231] D. H. Weinberg et al. *Cold dark matter: Controversies on small scales*. Proc. Natl. Acad. Sci **112**, 12249–12255 (2015).
DOI: 10.1073/pnas.1308716112 (Cited on p: 98).

[232] A. R. Liddle et al. *Cold dark matter models with a cosmological constant*. Mon. Notices Royal Astron. Soc. **282**, 281–290 (1996).
DOI: 10.1093/mnras/282.1.281 (Cited on p: 98).

[233] N. I. Libeskind et al. *Cold versus Warm Dark Matter Simulations of a Galaxy Group*. Publ. Astron. Soc. Aust. **30**, (2013).
DOI: 10.1017/pasa.2013.16 (Cited on p: 98).

[234] R. Kennedy et al. *Constraining the warm dark matter particle mass with Milky Way satellites*. Mon. Notices Royal Astron. Soc. **442**, 2487–2495 (2014).
DOI: 10.1093/mnras/stu719 (Cited on p: 98).

[235] O. Newton et al. *Constraints on the properties of warm dark matter using the satellite galaxies of the Milky Way*. J. Cosmol. Astropart. Phys. **2021**, 062 (2021).
DOI: 10.1088/1475-7516/2021/08/062 (Cited on p: 98).

[236] G. Gelmini et al. "DM production mechanisms". In: *Particle Dark Matter: Observations, Models and Searches*. Cambridge U. Press, 2010. Chap. 7 (Cited on p: 98).

[237] H. Baer et al. *Dark matter production in the early Universe: Beyond the thermal WIMP paradigm*. Phys. Rep. **555**, 1–60 (2015).
DOI: 10.1016/j.physrep.2014.10.002 (Cited on p: 98).

[238] N. Craig et al. *The fraternal WIMP miracle*. J. Cosmol. Astropart. Phys. **2015**, 054–054 (2015).
DOI: 10.1088/1475-7516/2015/10/054 (Cited on p: 98).

[239] G. L. Kane et al. *Dark matter production mechanisms with a nonthermal cosmological history: A classification*. Phys. Rev. D **93**, 063527 (2016).
DOI: 10.1103/physrevd.93.063527 (Cited on p: 98).

[240] B. S. Acharya et al. *Nonthermal WIMP miracle*. Phys. Rev. D **80**, 083529 (2009).
DOI: 10.1103/physrevd.80.083529 (Cited on p: 99).

[241] T. R. Slatyer et al. *CMB constraints on WIMP annihilation: Energy absorption during the recombination epoch*. Phys. Rev. D **80**, 043526 (2009).
DOI: 10.1103/physrevd.80.043526 (Cited on p: 99).

[242] S. Galli et al. *CMB constraints on dark matter models with large annihilation cross section*. Phys. Rev. D **80**, 023505 (2009).
DOI: 10.1103/physrevd.80.023505 (Cited on p: 99).

[243] P. A. R. Ade et al. *Planck2013 results. XVI. Cosmological parameters*. Astron. Astrophys. **571**, A16 (2014).
DOI: 10.1051/0004-6361/201321591 (Cited on p: 99).

[244] G. Hinshaw et al. *Nine year Wilkinson Microwave Anisotropy Probe (WMAP) observations: cosmological parameter results*. Astrophys. J. **208**, 19 (2013).
DOI: 10.1088/0067-0049/208/2/19 (Cited on p: 99).

[245] G. Arcadi et al. *The waning of the WIMP? A review of models, searches, and constraints*. Eur. Phys. J. C **78**, (2018).
DOI: 10.1140/epjc/s10052-018-5662-y (Cited on p: 99).

[246] F. S. Queiroz. *WIMP Theory Review*. (2017). (Cited on p: 99).

[247] F. Chadha-Day et al. *Axion Dark Matter: What is it and Why Now?* (2021). (Cited on p: 99).

[248] M. Gorghetto et al. *More axions from strings*. SciPost Phys. **10**, (2021).
DOI: 10.21468/scipostphys.10.2.050 (Cited on p: 99).

[249] P. Barnes et al. *Simple hidden sector dark matter*. Phys. Rev. D **102**, 075019 (2020).
DOI: 10.1103/physrevd.102.075019 (Cited on p: 99).

[250] T. Hambye et al. *Dark matter from dark photons: A taxonomy of dark matter production*. Phys. Rev. D **100**, 095018 (2019).
DOI: 10.1103/physrevd.100.095018 (Cited on p: 99).

[251] A. Boyarsky et al. *Sterile neutrino Dark Matter*. Prog. Part. Nucl. Phys. **104**, 1–45 (2019).
DOI: 10.1016/j.ppnp.2018.07.004 (Cited on p: 99).

[252] O. Buchmueller et al. *Search for dark matter at colliders*. Nat. Phys. **13**, 217–223 (2017).
DOI: 10.1038/nphys4054 (Cited on pp: 100, 101).

[253] A. Boveia et al. *Dark Matter Searches at Colliders*. Annu. Rev. Nucl. Part. **68**, 429–459 (2018).
DOI: 10.1146/annurev-nucl-101917-021008 (Cited on p: 100).

[254] P. J. Fox et al. *LEP shines light on dark matter*. Phys. Rev. D **84**, 014028 (2011).
DOI: 10.1103/physrevd.84.014028 (Cited on p: 100).

[255] J. Ellis et al. *Dark matter in the light of LEP*. Phys. Rev. D **245**, 251–257 (1990).
DOI: 10.1016/0370-2693(90)90143-t (Cited on p: 100).

[256] Yang Bai et al. *The Tevatron at the frontier of dark matter direct detection*. J. High. Energy. Phys. **2010**, (2010).
DOI: 10.1007/jhep12(2010)048 (Cited on p: 100).

[257] F. Froborg et al. *Annual modulation in direct dark matter searches*. J. Phys. G Nucl. Part. Phys. **47**, 094002 (2020).
DOI: 10.1088/1361-6471/ab8e93 (Cited on p: 101).

[258] M. Schumann. *Direct detection of WIMP dark matter: concepts and status*. J. Phys. G Nucl. Part. Phys. **46**, 103003 (2019).
DOI: 10.1088/1361-6471/ab2ea5 (Cited on pp: 101, 103).

[259] A. M. Green. *Astrophysical uncertainties on the local dark matter distribution and direct detection experiments*. J. Phys. G Nucl. Part. Phys. **44**, 084001 (2017).
DOI: 10.1088/1361-6471/aa7819 (Cited on p: 101).

[260] E. Shields. *Reaching for the Heavens under a Mountain: The Search for Dark Matter*. (2013). (Cited on p: 102).

[261] J. Engel et al. *Nuclear physics of Dark Matter detection*. Int. J. Mod. Phys. E **01**, 1–37 (1992).
DOI: 10.1142/s0218301392000023 (Cited on p: 102).

[262] R. Agnese et al. *Results from the Super Cryogenic Dark Matter Search Experiment at Soudan*. Phys. Rev. Lett. **120**, 061802 (2018).
DOI: 10.1103/physrevlett.120.061802 (Cited on p: 103).

[263] Q. Arnaud et al. *Optimizing EDELWEISS detectors for low-mass WIMP searches*. Phys. Rev. D **97**, 022003 (2018).
DOI: 10.1103/physrevd.97.022003 (Cited on p: 103).

[264] A. H. Abdelhameed et al. *First results from the CRESST-III low-mass dark matter program*. Phys. Rev. D **100**, 102002 (2019).
DOI: 10.1103/physrevd.100.102002 (Cited on p: 103).

[265] D. S. Akerib et al. *Results from a Search for Dark Matter in the Complete LUX Exposure*. Phys. Rev. Lett. **118**, 021303 (2017).
DOI: 10.1103/physrevlett.118.021303 (Cited on p: 103).

[266] X. Cui et al. *Dark Matter Results from 54-Ton-Day Exposure of PandaX-II Experiment*. Phys. Rev. Lett. **119**, 181302 (2017).
DOI: 10.1103/physrevlett.119.181302 (Cited on p: 103).

[267] E. Aprile et al. *Dark Matter Search Results from a One Ton-Year Exposure of XENON1T*. Phys. Rev. Lett. **121**, 111302 (2018).
DOI: 10.1103/physrevlett.121.111302 (Cited on p: 103).

[268] P. Grothaus et al. *Directional dark matter detection beyond the neutrino bound*. Phys. Rev. D **90**, 055018 (2014).
DOI: 10.1103/physrevd.90.055018 (Cited on p: 103).

[269] C. A. J. O'Hare et al. *Readout strategies for directional dark matter detection beyond the neutrino background*. Phys. Rev. D **92**, 063518 (2015).
DOI: 10.1103/physrevd.92.063518 (Cited on p: 103).

[270] C. A. J. O'Hare. *New Definition of the Neutrino Floor for Direct Dark Matter Searches*. Phys. Rev. Lett. **127**, 251802 (2021).
DOI: 10.1103/physrevlett.127.251802 (Cited on p: 103).

[271] J. B. R. Battat et al. *Low threshold results and limits from the DRIFT directional dark matter detector*. Astropart. Phys. **91**, 65–74 (2017).
DOI: 10.1016/j.astropartphys.2017.03.007 (Cited on p: 103).

[272] C. Deaconu et al. *Measurement of the directional sensitivity of Dark Matter Time Projection Chamber detectors*. Phys. Rev. D **95**, 122002 (2017).
DOI: 10.1103/physrevd.95.122002 (Cited on p: 103).

[273] Y. Tao et al. *Track length measurement of 19F+ ions with the MIMAC directional Dark Matter detector prototype*. Nucl. Instrum. Meth. A **985**, 164569 (2021).
DOI: 10.1016/j.nima.2020.164569 (Cited on p: 103).

[274] T.I. Hashimoto et al. "Development of a low-alpha-emitting μ-PIC for NEWAGE direction-sensitive dark-matter search". In: *AIP Conference Proceedings 1921, 070001 (2018)*. Author(s), 2018.
DOI: 10.1063/1.5019004. (Cited on p: 103).

[275] F. S. Queiroz. *Dark Matter Overview: Collider, Direct and Indirect Detection Searches*. (2016). (Cited on p: 104).

[276] J. F. Navarro et al. *A Universal Density Profile from Hierarchical Clustering*. Astrophys. J. **490**, 493–508 (1997).
DOI: 10.1086/304888 (Cited on pp: 104, 107).

[277] J. Einasto. *On the Construction of a Composite Model for the Galaxy and on the Determination of the System of Galactic Parameters*. Trudy Astrofizicheskogo Instituta Alma-Ata **5**, 87–100 (1965). (Cited on p: 104).

[278] A. Burkert. *The Structure of Dark Matter Halos in Dwarf Galaxies*. Astrophys. J. **447**, (1995).
DOI: 10.1086/309560 (Cited on p: 104).

[279] J. M. Gaskins. *A review of indirect searches for particle dark matter*. Contemp. Phys. **57**, 496–525 (2016).
DOI: 10.1080/00107514.2016.1175160 (Cited on p: 105).

[280] A. Albert et al. *Searching for dark matter annihilation in recently discovered Milky Way satellites with Fermi-LAT*. Astrophys. J. **834**, 110 (2017).
DOI: 10.3847/1538-4357/834/2/110 (Cited on p: 105).

[281] H. Abdallah et al. *Search for dark matter annihilation signals from unidentified Fermi-LAT objects with H.E.S.S*. Astrophys. J. (2021).
DOI: 10.3847/1538-4357/abff59 (Cited on p: 105).

[282] V. A. Acciari et al. *A search for dark matter in Triangulum II with the MAGIC telescopes*. Phys. Dark Universe **28**, 100529 (2020).
DOI: 10.1016/j.dark.2020.100529 (Cited on p: 105).

[283] R. G. Wagner. "Indirect Dark Matter Searches with VERITAS". In: *Proceedings of the 31st International Cosmic Ray Conference (ICRC), Lodz, Poland, July 2009*. 2009. (Cited on p: 105).

[284] T. Yapici et al. "Dark Matter Searches with HAWC". In: *Proceedings of 35th International Cosmic Ray Conference - PoS(ICRC2017)*. Sissa Medialab, 2017.
DOI: 10.22323/1.301.0891. (Cited on p: 105).

[285] A. Acharyya et al. *Sensitivity of the Cherenkov Telescope Array to a dark matter signal from the Galactic centre*. J. Cosmol. Astropart. Phys. **2021**, 057–057 (2021).
DOI: 10.1088/1475-7516/2021/01/057 (Cited on p: 105).

[286] Y. Zhao et al. *Indirect detection signatures for the origin of asymmetric dark matter*. J. High Energy Phys. **2014**, (2014).
DOI: 10.1007/jhep07(2014)017 (Cited on p: 105).

[287] M. Boezio et al. *PAMELA and indirect dark matter searches*. New J. Phys. **11**, 105023 (2009).
DOI: 10.1088/1367-2630/11/10/105023 (Cited on p: 105).

[288] W. Xu. "The Latest Results from AMS on the Searches for Dark Matter". In: *Proceedings, 28th International Symposium on Lepton Photon Interactions at High Energies (LP17) : Guangzhou (Guangdong), China, August 7-12, 2017*. WORLD SCIENTIFIC, 2020.
DOI: 10.1142/9789811207402_0014. (Cited on p: 105).

[289] N. Iovine et al. "Indirect search for dark matter in the Galactic Centre with IceCube". In: *Proceedings of the 37th International Cosmic Ray Conference (ICRC 2021)*. 2021. (Cited on p: 106).

[290] M. G. Aartsen et al. *All-flavour search for neutrinos from dark matter annihilations in the Milky Way with IceCube/DeepCore*. Eur. Phys. J. C **76**, (2016). DOI: 10.1140/epjc/s10052-016-4375-3 (Cited on p: 106).

[291] A. Bäckström et al. *Assessing the sensitivity of PINGU to effective dark matter-nucleon interactions*. J. Cosmol. Astropart. Phys. **2019**, 023–023 (2019). DOI: 10.1088/1475-7516/2019/05/023 (Cited on p: 106).

[292] J. D. Zornoza et al. "Results of dark matter searches with the ANTARES neutrino telescope". In: *Proceedings of Neutrino 2016 Conference, London (UK), July 2016*. Vol. 888. IOP Publishing, 2017. 012206. DOI: 10.1088/1742-6596/888/1/012206. (Cited on p: 106).

[293] A. Albert et al. *Combined search for neutrinos from dark matter self-annihilation in the Galactic Centre with ANTARES and IceCube*. Phys. Rev. D **102**, 082002 (2020). DOI: 10.1103/PhysRevD.102.082002 (Cited on p: 106).

[294] V. Bertin et al. *Recent results from the ANTARES deep sea neutrino telescope*. J. Phys.: Conf. Ser. **1342**, 012021 (2020). DOI: 10.1088/1742-6596/1342/1/012021 (Cited on p: 106).

[295] S. Navas et al. "Dark Matter Searches from the Sun with the KM3NeT-ORCA detector". In: *Proceedings of 36th International Cosmic Ray Conference PoS(ICRC2019)*. 36th International Cosmic Ray Conference. Madison, WI, U.S.A.: Sissa Medialab, 2019. 536. DOI: 10.22323/1.358.0536. (Cited on pp: 106, 124, 133, 143).

[296] A. D. Avrorin et al. *Dark matter constraints from an observation of dSphs and the LMC with the Baikal NT200*. J. Exp. Theor **125**, 80–90 (2017). DOI: 10.1134/s1063776117070135 (Cited on p: 106).

[297] A. D. Avrorin et al. *Neutrino signal at Baikal from dark matter in the Galactic Center*. Phys. Part. Nucl. **47**, 926–932 (2016). DOI: 10.1134/s1063779616060046 (Cited on p: 106).

[298] K. Frankiewicz and. *Dark matter searches with the Super-Kamiokande detector*. J. Phys. Conf. Ser. **888**, 012210 (2017). DOI: 10.1088/1742-6596/888/1/012210 (Cited on p: 106).

[299] Nicole F. Bell et al. *Searching for Sub-GeV dark matter in the galactic centre using Hyper-Kamiokande*. J. Cosmol. Astropart. Phys. **2020**, 019–019 (2020). DOI: 10.1088/1475-7516/2020/09/019 (Cited on p: 106).

[300] T. Bringmann et al. *DarkSUSY 6: an advanced tool to compute dark matter properties numerically*. J. Cosmol. Astropart. Phys. **2018**, 033–033 (2018). DOI: 10.1088/1475-7516/2018/07/033 (Cited on pp: 106, 107, 122, 131, 141).

[301] T. Sjöstrand et al. *PYTHIA 6.4 physics and manual*. J. High Energy Phys. **2006**, 026–026 (2006).
DOI: 10.1088/1126-6708/2006/05/026 (Cited on pp: 106, 107).

[302] J. Edsjö. *Nusigma 1.19*. URL: http://www.fysik.su.se/~edsjo/wimpsim. (Cited on pp: 106, 107).

[303] R. B. Davis et al. *Hypothesis Testing*. Circulation **114**, 1078–1082 (2006).
DOI: 10.1161/circulationaha.105.586461 (Cited on p: 119).

[304] G. Wikström et al. *Limits on the WIMP-nucleon scattering cross-section from neutrino telescopes*. J. Cosmol. Astropart. Phys. **2009**, 009–009 (2009).
DOI: 10.1088/1475-7516/2009/04/009 (Cited on p: 123).

[305] S. Adrián-Martínez et al. *Limits on dark matter annihilation in the sun using the ANTARES neutrino telescope*. Phys. Lett. B **759**, 69–74 (2016).
DOI: 10.1016/j.physletb.2016.05.019 (Cited on pp: 124, 133, 143).

[306] M. G. Aartsen et al. *Search for annihilating dark matter in the Sun with 3 years of IceCube data: IceCube Collaboration*. Eur. Phys. J. C **77**, 146 (2017).
DOI: 10.1140/epjc/s10052-017-4689-9 (Cited on pp: 124, 133, 143).

[307] K. Frankiewicz. "Searching for Dark Matter Annihilation into Neutrinos with Super-Kamiokande". In: *The Meeting of the American Physical Society Division of Particles and Fields (DPF 2015): Ann Arbor, Michigan, August 4-8, 2015*. 2015. (Cited on pp: 124, 133, 143).

[308] C. Amole et al. *Dark Matter Search Results from the PICO-60 C_3F_8 Bubble Chamber*. Phys. Rev. Lett. **118**, 251301 (2017).
DOI: 10.1103/PhysRevLett.118.251301 (Cited on pp: 124, 133, 143).